UNIVERSITY OF LIVERPOOL

New cathodes for intermediate temperature solid oxide fuel cells (IT-SOFCs).

Thesis submitted in accordance with the requirements of the University of Liverpool for the degree of Doctor in Philosophy by:

Darren Wayne Hodgeman

April 2014

Supervised by

Professor M. J. Rosseinsky

Dr J. B. Claridge

Abstract

The work presented in this thesis focuses on the synthesis of long axis *A*-site ordered perovskites, which have ordered oxygen vacancies. The materials discussed have also been assessed as potential cathodes for solid oxide fuel cells (SOFCs), targeting an intermediate temperature (IT) -SOFC operating range of 500 - 800 °C.

In chapter 3 of this thesis, a $16a_p$ phase (a_p = 1 perovskite unit, $ABO_{3-\delta}$), $Y_{2.24}Ba_{2.28}Ca_{3.48}Fe_{7.44}Cu_{0.56}O_{21-\delta}$, was first observed in a powder X-ray diffraction (PXRD) pattern that resulted from the attempted Cu doping of a $10a_p$ phase ($Y_{0.9}Ba_{1.7}Ca_{2.4}Fe_{5-x}Cu_xO_{13-\delta}$). This phase was indexed as $a_p\ \sqrt{2} \times 16a_p \times a_p\ \sqrt{2}$ by selective area electron diffraction (SAED). Mössbauer spectroscopy identified that Fe^{3+} existed in three different coordination environments and a Rietveld refinement was carried out using combined powder synchrotron (S) XRD and powder neutron diffraction (ND) data. High Angle Annular Scanning Transmission Electron Diffraction (HAADF-STEM) confirmed the *A*-site ordering from the refinement.

The $16a_p$ phase exhibited good thermal stability, CO_2 stability and chemical compatibility with state-of-the-art electrolytes (GDC, SDC and LSGM), as well as a close matching thermal expansion coefficient (TEC) with the same electrolytes. Although possessing low electronic conductivity, 3.5 $S.cm^{-1}$ at 750 °C, a good area specific resistance (ASR) of 0.12 $\Omega.cm^2$ at 750 °C was achieved, within the IT-SOFC operating range.

In chapter 4, a $10a_p$ phase, $Y_{0.9}Ca_{2.4}Sr_{1.7}Fe_5O_{13-\delta}$ (YCSFO), was discussed. The space group *Imma* was identified from SXRD data, while the structure was closely related to brownmillerite. A Rietveld refinement carried out with the addition of SXRD data collected at the K absorption edge for Sr determined *A*-site ordering. The ASR of YCSFO was three times higher than that of the $16a_p$ phase, highlighting the ordering of oxygen vacancies.

The final phases investigated in chapter 5 of this thesis belong to a family of Co doped $10a_p$ phases ($Y_{0.9}Ba_{1.7}Ca_{2.4}Fe_{5-x}Co_xO_{13-\delta}$). A range of compositions were synthesised by varying the cation ratios, in order to obtain high Co content phase pure samples. The highest Co content was x = 1.85 for compositions $Y_{1.24}Ba_{1.85}Ca_{1.91}Fe_{3.15}Co_{1.85}O_{13-\delta}$ (annealed in O_2) and $Y_{1.6}Ba_{1.8}Ca_{1.6}Fe_{3.15}Co_{1.85}O_{13-\delta}$. AC impedance measurements carried out showed that increased Co content reduced the ASR, with the values at 700 °C of 0.19 $\Omega.cm^2$ and 0.23 $\Omega.cm^2$ respectively.

Acknowledgements

Firstly, I would like to thank my supervisor Prof Matt Rosseinsky, who provided me with the fantastic opportunity to undertake my PhD within his research group. Throughout my time within the group, he has provided much valuable input and support for my research projects, for which I am grateful. I would also particularly like to thank my second supervisor Dr John Claridge for his help throughout my PhD, particularly enabling me to make use of his encyclopaedic knowledge in seemingly all areas.

With working in such a large research group, I have worked with many people, so I would like to thank them all for their part, but I will particularly highlight those that I worked most closely with.

At the outset of my PhD, Dr Antoine Demont showed me the ropes in terms of synthesis, powder diffraction and solid state chemistry, whilst Dr Ruth Sayers helped me get to grips with electrochemical measurements. As I progressed and Antoine left the group, I was lucky enough to work with Dr Phil Chater, who really helped me improve my Rietveld refinement skills. Most recently Dr Alex Corkett has been on hand for refinement discussions, though I have also enjoyed conversations with Dr Mike Pitcher and Dr Christophe Didier in this area.

I cannot forget Dr Hongjun Niu, who has always helped me with problems associated with the electrochemical instruments, as well as his humorous conversation style in the office. Another person to highlight is Dr Simon Romani, who carried out a lot of TEM work for me, as well as training me to use the TEM myself. Additionally my thanks goes to Dr Mike Thomas for Mössbauer analysis and Dr James Gallagher for SEM analysis. Last but not least, I would like to thank Dr Maria Tsiamtsouri, who amongst those listed above, has spent a lot of her time reading my chapters, providing valuable input.

Contents

1 Introduction

1.1 Energy concerns

A constant source and supply of energy is highly important, without which today's society would likely crumble without access for long periods of time. Access to a supply of electrical energy is particularly relied upon as it is used in all aspects of life, from powering hospital equipment to powering computers and light bulbs. Industrial economies are particularly reliant, as they contain 25 % of the world's population, which consumes 75 % of the world's energy supply. [1, 2]

Traditional power generation is based upon non-renewable fossil fuels such as coal, oil and natural gas. Although fossil fuel supplies are finite, they are still currently plentiful, nevertheless, in the long term it is inevitable that they will have to be replaced by sustainable resources. The problems for use of fossil fuels in the short term are linked to pollution, with their combustion releasing CO_2 among other things, which has been linked to global warming.[3-5] These factors lead to a search for alternative methods of power generation. It appears that while there are many alternative methods of power generation, each has its own disadvantages, such as solar power and wind farms, which although renewable, are very much "fair weather" technologies.[6] The ideal situation would likely be a good mix of energy generation methods, from renewable forms to high efficiency, reduced fuel consumption processes in order to fulfil demand.[7-10]

1.2 Fuel cells

Fuel cells convert chemical energy contained in a fuel directly into electrical energy, combining high efficiency (potentially > 60 %) with low emission of pollutants.[11] They can be viewed in a simplistic way as a cross between a battery, where chemical energy is converted directly into electrical energy, and a heat engine, which needs to be continuously fuelled. Fuel cells also have the advantage of not having any moving parts, which leads to quiet operation and components not needing to be replaced due to mechanical wear.[12]

Fuel cells have been known since 1838 when German scientist C. F. Schœnbein first demonstrated that energy can be produced through a combination of hydrogen and oxygen whilst conducting electrolysis of H_2O.[13] Sir William Grove built the first fuel cell, which he called "gas voltaic battery" after observing the generation of an electric current from the conversion of hydrogen and oxygen into water using a platinum electrode with a sulphuric acid electrolyte.[14] Ludwig Mond and Carl Langer are credited as the first to coin the term "fuel cell" in 1889, when they used coal gas and air in their cells, showing early fuel flexibility of fuel cells.[15]

Today there are many types of fuel cell under development, each with its own materials and mechanism for electrical energy generation, leading to advantages and disadvantages over other fuel cells in certain aspects of their operation. A selection of different types of fuel cell are summarised in Table 1.1. It is the electrolyte used in each case that primarily determines the operational temperatures used as well as the type of ion transport mechanism utilised for each fuel cell type.[11, 12, 16]

Fuel cell	**Operating temperature (°C)**	**Electrolyte**	**Ion**	**Catalyst**	**Fuel**
Proton exchange membrane (PEM)	30 - 100	Sulfonated PTFE membrane	H^+	Platinum	H_2, CH_3OH
Alkaline (AFC)	50 - 100	Potassium hydroxide	OH^-	Platinum, Nickel	H_2
Phosphoric acid (PAFC)	~ 200	Phosphoric acid	H^+	Platinum	H_2, CO
Molten Carbonate (MCFC)	~ 650	Alkali metal carbonate	CO_3^{2-}	Nickel	H_2, CO, CH_3OH
Solid Oxide (SOFC)	500 - 1000	Ceramic	O^{2-}	Metal oxide, Nickel	H_2, CO, CH_3OH

Table 1.1 Shows fuel cell types, along with their electrolyte, conducted ion and common operating temperatures, catalyst and fuel.[11, 12, 16]

Fuel cells also require an anode and a cathode, which are separated by the electrolyte. These electrodes display high electronic conductivity and catalytic activity. The first testing of a

"solid electrolyte fuel cell" was carried out in Westinghouse Electric Corporation in 1962, and has proved to be a landmark in fuel cell technology.[17] There has since been intense research into new materials suitable for the development of large scale devices. The focus of this thesis is the development of cathodes for solid oxide fuel cells (SOFCs), which are discussed next in section 1.3.

1.3 Solid Oxide Fuel Cells (SOFCs)

1.3.1 SOFC Overview

Solid oxide fuel cells (SOFCs) are all solid-state devices that operate at high temperatures and have great potential in the power generation industry due to having one of highest electrical energy conversion efficiencies of available technologies, reported from 45 - 65 %.[18] This is higher than is possible for conventional heat engines. An even higher efficiency is attainable with the additional use of turbines powered by the out flowing gas, as well as using them for combined heat and power, with a possible efficiency of up to 90 % suggested.[18, 19]

The power and voltage of a SOFC can be increased by stacking individual cells in a series, with an electrically conducting interconnect between adjacent cells to distribute reactants across the surface of the electrodes using flowing gas channels.[12]

As well as the promise of high efficiency, SOFCs have the flexibility of using a range of fuels, unlike many other types of fuel cell which require high purity hydrogen. For example, CO can be utilised as a fuel as opposed to a poison, as is the case with lower temperature fuel cells such as PEMs.[20] Hydrocarbon fuels can also be used directly due to the high operating temperatures, through internal reforming or direct oxidation.[21] When H_2 is used as the fuel, the main by-product is H_2O, hence they do not contribute to air pollution. Another advantage of SOFCs compared to other types of fuel cell is the use of solid electrolyte does not lead to corrosion problems caused when corrosive liquids are used for electrolytes.

SOFCs are made up from a ceramic electrolyte sandwiched between a ceramic cathode and a cermet anode. The basic operation of a SOFC is shown in the schematic diagram found in Figure 1.1. During the continuous operation of a SOFC, fuel is oxidised at the anode

producing electrons, which are passed through an external circuit to the cathode, where they are used to catalytically reduce oxygen. The oxygen ions are then transported across from the cathode, through the electrolyte (which exhibits high ionic and negligible electronic conductivity) to the anode to complete the circuit. The flow of electrons through the external circuit provides a source of electrical energy that can be used to do work.

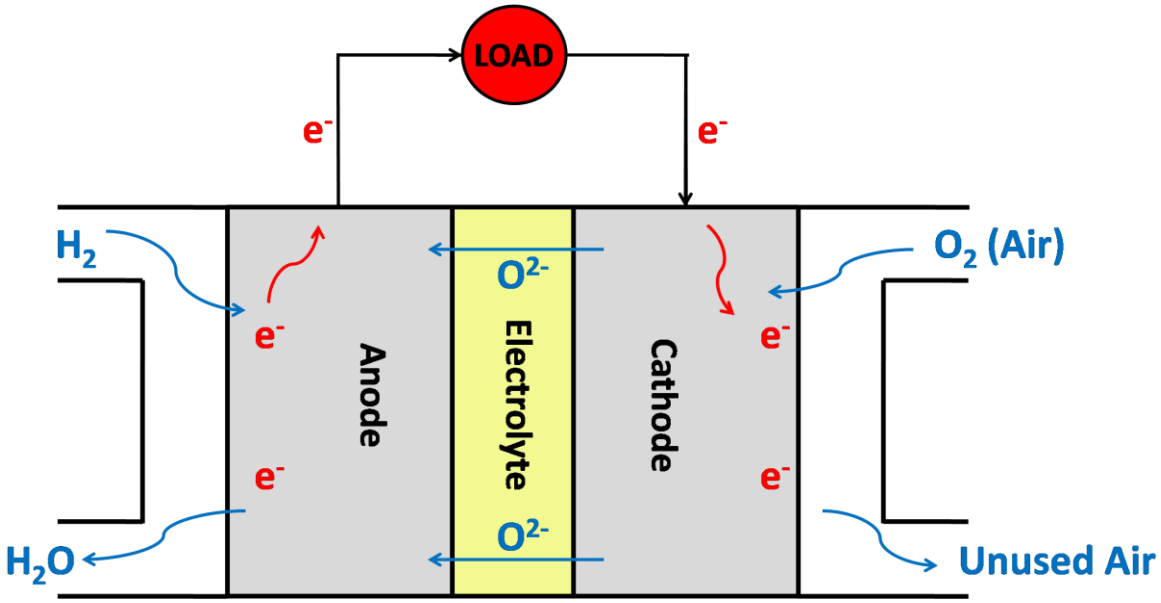

Figure 1.1 Schematic diagram of the basic workings of a SOFC, with oxygen reduced at the cathode, hydrogen oxidised at the anode and an external circuit transporting the generated electrons. H_2O is produced as the by-product.

The electrode reactions for a SOFC when using hydrogen as the fuel with oxygen from air are given below, together with the area of the SOFC where the reaction occurs:

$$O_2(g) + 4e^- \longrightarrow 2O^{2-}$$

Equation 1.1 Cathode reaction

$$2H_2(g) + 2O^{2-} \longrightarrow 2H_2O(g) + 4e^-$$

Equation 1.2 Anode reaction

$$2H_2(g) + O_2 \longrightarrow 2H_2O(g)$$

Equation 1.3 Overall reaction

As can be seen in the above equations, the migratory ions are oxygen anions. The ceramics in SOFCs do not become electrically and ionically active until they reach very high temperatures. This is in part due to the high charge and size of the oxygen ion species that is transported, consequently leading to an operating temperature range of 500 - 1000 °C. The high operation temperature does have the benefit of enabling internal reforming of fuels (such as hydrocarbons, CO and CO_2), resulting in the fuel flexibility discussed earlier. Thus SOFC technology is not so restricted by the hydrogen economy and its associated limitations (e.g. hydrogen storage problems), giving it advantages over other fuel cell.[22, 23]

Typically, SOFCs are operated at the high temperature region of 800 - 1000 °C in order to overcome low ionic conductivity of the electrolyte. For example, a typical electrolyte of a PEM, Nafion®, has a conductivity of ~ 0.1 $S.cm^{-1}$ at 100 °C, while a SOFC electrolyte yttrium stabilised zirconia (YSZ) achieves this same conductivity at 1000 °C.[24] In order to operate at high temperatures, there are stringent requirements for the components used in SOFC stacks, such as a high melting point, structural stability and compatibility of components at high temperatures, leading to the need for materials to be made from ceramics and high temperature stable alloys. For reduced scale applications, such as small electrical generators, lower operating temperatures are desirable, which moves operation into the intermediate operating temperature range of around 500 - 800 °C.[11] Reducing the operating temperature to the intermediate range (IT-SOFCs) of 500 - 800 °C provides an opportunity for cheaper materials to be used for components such as the interconnect.[12] Lower temperature operation also decreases the start-up and shut down time, reduces corrosion of metallic components, improves durability and enables a more robust construction.[12, 25]

In order to reduce the operating temperatures of SOFCs whilst maintaining the performance of the cell, the thickness of the electrolyte can be reduced, which would lower the overall ohmic losses from this component. New materials must be developed which have higher ionic conductivity for the electrolyte, while better performing electrodes are also required.[26] While recent material developments have led to the discovery of electrolytes that can operate with the desired ionic conductivity (> 0.1 S cm^{-1}) at much lower temperatures (materials discussed in section 1.7.1),[27] the main limitation comes from the cathode, which is discussed next in section 1.3.2.

1.3.2 SOFC Cathode limitation

Cathodes operating within the high temperatures region of 800 - 1000 °C have sufficiently rapid reaction kinetics that cell losses are only minor. As temperatures are reduced down to the intermediate range, there are increases in the polarisation losses related to the slow kinetics of the oxygen reduction reaction (ORR), which involves O_2 dissociation, subsequent reduction and incorporation and transport of the ions. The activation energy (E_a) of the ORR (often > 1.5 eV)[28-31] is high compared to other processes within a fuel cell, such as ionic conductivity (often < 1 eV)[32, 33] and electronic conductivity (< 0.5 eV),[34, 35] therefore the cathode requires particular attention. A significant amount of recent research has gone into the improvement of cathodes at reduced temperatures.[36-38] The key to this is to accelerate the ORR, which is quite complex and comprises of a number of steps. At a simplified level, the reactions involved are:

$$½O_{2(g)} + 2e^-_{(cathode)} \longleftrightarrow O^{2-}_{(cathode\ surface)}$$

Equation 1.4: O_2 dissociation

$$O^{2-}_{(cathode\ surface)} \longleftrightarrow O^{2-}_{(cathode\ bulk)}$$

Equation 1.5: O^{2-} Incorporation

$$O^{2-}_{(cathode\ bulk)} \longleftrightarrow O^{2-}_{(electrolyte)}$$

Equation 1.6: Transport of O^{2-} to the electrolyte

In Equation 1.4, there is the reduction of oxygen and subsequent adsorption onto the surface of the cathode. Equation 1.5 represents diffusion of the reduced oxygen ions into the bulk of the cathode, followed by Equation 1.6, where the oxygen ions are transported from the cathode to the electrolyte.[39]

There are two main paths that oxygen reduction and subsequent incorporation into a fuel cell can take, the "surface path" and the "bulk path". The path taken depends on the intrinsic properties of the cathode, with traditional cathodes such as $La_{1-x}Sr_xMnO_{3-\delta}$ (discussed later in section 1.7.3), which are good electronic conductors, but poor ionic conductors, thus

favouring the surface path. Accordingly and as shown in Figure 1.2 A, the reactive site for the ORR occurs at the triple phase boundary (TPB) where the gas, electrolyte and cathode all come into contact. Oxygen (gas) is reduced using electrons supplied by the cathode, before being incorporated into the electrolyte and transported away.

With the performance of a cathode limited by the kinetics of the ORR, which is significantly slowed at reduced temperatures, it makes sense to look for ways to improve it. Cathodes displaying mixed ionic-electronic conductivity (MIEC) are considered to be a viable solution to this as they allow incorporation of oxygen ions into the bulk of the cathode, as well as at the TPB, increasing the number of active sites and surface area for the ORR to occur (see Figure 1.2 B).[40-43] It has been shown that the ORR in a porous MIEC cathode is limited by oxygen surface exchange and oxygen diffusion within the cathode, meaning that a cathode needs high ionic conductivity for maximum bulk diffusion and a surface area as large as possible for greatest possible surface exchange, along with catalytic activity for the oxygen dissociation reaction.[42, 44]

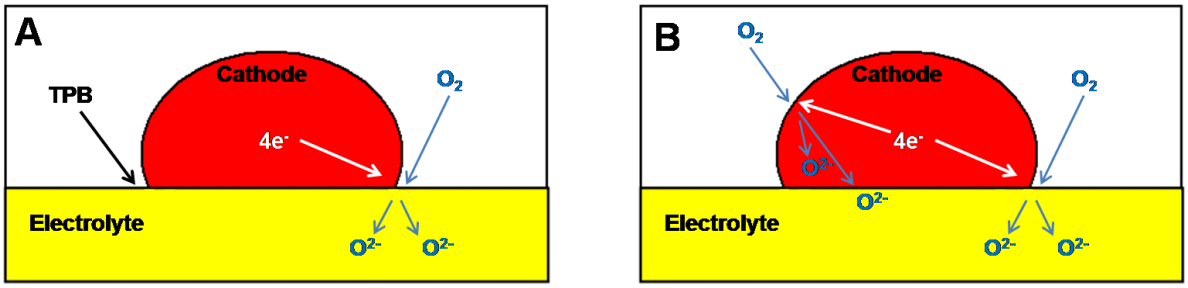

Figure 1.2 schematic representation of A) triple phase boundary (TPB) of oxygen, cathode and electrolyte and B) extended reaction surface for the ORR in a mixed ionic-electronic conductor (MIEC) cathode.

1.3.3 General SOFC component requirements

In order to assess the operational output and efficiency of a fully assembled fuel cell, numbers have to be put on the desired performance. The constraint for total resistance of a single fuel cell has been identified at around ~ 0.45 $\Omega.cm^2$, in order for power generation to occur with acceptable losses. This implies that the target should be < 0.15 $\Omega.cm^2$ for each component of a fuel cell.[41]

As well as the resistance, there are other properties that are required for fuel cell components. As components must function at high temperatures, the materials are required to be thermally stable at the desired operating temperature. The components are also in contact with each other, therefore reactivity between them needs to be negligible to prevent new, potentially insulating phase formation.[45] The thermal expansion coefficients (TEC) need to be close matching, otherwise thermal cycling can lead to stresses and delamination of layers, ultimately leading to failure of the device. All materials must possess enough mechanical and structural stability for the conditions required for fabrication into and operation as a SOFC device.

Component	**Ionic conductivity**	**Electronic conductivity**	**Atmospheric stability**	**Morphology**
Cathode	Desired	High	Oxygen/Air	Porous
Anode	Desired	High	Reducing/Fuel	Porous
Electrolyte	High	Negligible	Both above	Fully dense

Table 1.2 Desired properties of SOFC components.[38]

Additionally, as summarised in Table 1.2 above, each of the components needs to be stable in the atmospheres that they are exposed to. The cathode will operate in air (or oxygen), the anode will operate in the presence of the fuel and the fuel cell reaction products (i.e. water for hydrogen) and the electrolyte will need to be stable in both environments.

The electrolyte should be fully dense in order to prevent the direct passage of gas from one side of the cell to the other. It is required to be highly ionically conducting at the operating temperature, with a targeted conductivity of $> 10^{-2}$ S cm^{-1}. The electrolyte requires negligible electronic conductivity to prevent significant leakage current.[46]

The electrodes should be sufficiently electronically conducting to allow the flow of electrons to the active sites. As discussed earlier in section 1.3.2, ionic conductivity is a desired property of cathodes when operating at reduced temperatures, as well as for anodes. This allows a path of oxygen ions to be created from the cathode, through the electrolyte, to the anode. It also provides a greater surface area for the respective electrochemical reactions (see Equation 1.1 and Equation 1.2) to occur. The electrodes should also be catalytically active for their respective electrochemical reactions and be porous in order to maximise the surface area

of the electrochemically active sites. The combination of properties displayed by the electrodes is accounted for together in the area specific resistance (ASR).[38, 47] A description of how the ASR is measured is described later in section 2.10.2.

1.4 Mechanisms of conductivity in SOFC components

SOFC components are required to display electronic and/or ionic conductivity. Electronic conductivity in SOFC materials is often attributed to transition metals with mixed oxidation states, which provide a charge carrier. Ionic conductivity is attributed to point defects within the structure, commonly ion vacancies or interstitials. Through doping a material with aliovalent ions, vacancies/interstitials and charge carriers can be generated, due to the need to maintain charge neutrality. Below is a description of mechanisms of electronic and ionic conductivities.

1.4.1 Electronic conductivity

According to band theory, widely spaced orbital levels of free atoms combine in a molecule forming bonding and antibonding combinations. As the number of atoms increases, the orbitals become closer in energy, until they merge together to form continuous bands for a solid (infinity atoms).

In semiconductors and insulators, there is an energy gap (*Eg*) between the top filled energy level, the valence band, and the bottom empty energy level, the conduction band (see Figure 1.3). In a metal, there is a partially filled band of electrons, with a delocalised cloud of electrons that are free to move throughout the solid.

The electrical conductivity can be described by the number of electrons that are found in the conduction band and their mobility within the band. Figure 1.3 shows schematic diagrams of the band structures of a metal, a semi-conductor and an insulator.

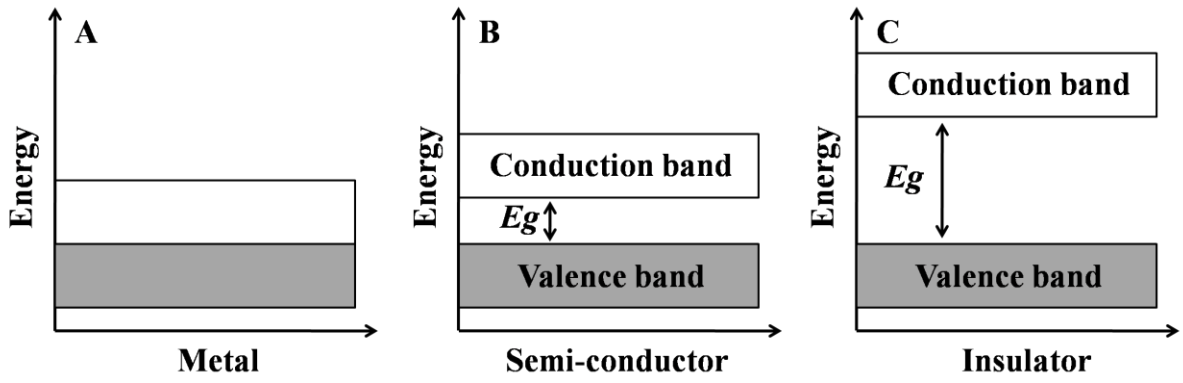

Figure 1.3 Schematic diagrams of band structures of A) a metal, B) a semi-conductor, C) an insulator.

In a metal (Figure 1.3 A), there are a large number of electrons that are completely delocalised, free to move throughout the structure. Band theory depicts a partially filled conduction band, allowing the electrons to move, which are responsible for the high electronic conductivity. For materials displaying insulating behaviour, electrons are localised and *Eg* is very large, meaning few electrons have sufficient energy to be promoted from the valence band to the conduction band (see Figure 1.3 B), thus electrical conductivity is negligible. In semi-conductors, the band structure is similar to that of insulators, however *Eg* is not so large, which allows more electrons with sufficient energy to be promoted to the conduction band (Figure 1.3 B).

When electrons are promoted into the conduction band, they are described as negative charge carriers. The vacant electron levels that are left behind are described as positive holes. The number of electrons that are promoted to the conduction band are dependent on the magnitude of *Eg*, as well as temperature. At 0 K, no electrons will have the thermal energy required to be promoted to the conduction band.

The electronic conductivity of a semi-conductor can be enhanced by doping. This can be done through doping with aliovalent ions, leading to p-type (positive) or n-type (negative) semiconducting behaviour. A p-type dopant is considered an electron acceptor, promoting the formation of holes in the valence band. The energy level is situated just above that of the valence band, accepting electrons from the valence band, thus decreasing the energy required to create a charge carrier (Figure 1.4 A). An n-type dopant is essentially the opposite, providing electrons for the conduction band. The dopant's energy level is found just below

the conduction band (Figure 1.4B), and hence electrons require less energy to be promoted from the valence band.

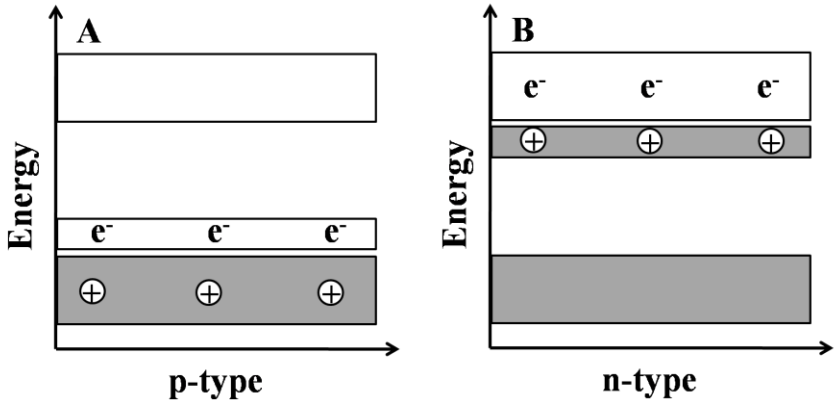

Figure 1.4 Schematic of the band structure of A) p-type and B) n-type semi-conductors.

A requirement of SOFC cathodes and anodes is the ability to transport electrons to and from an external circuit. Most cathodes used for SOFCs are semi-conductors, with more discussion in section 1.4.2.[48]

1.4.2 Electronic conductivity in transition metal oxides

The materials synthesised in this thesis all exhibit semi-conducting behaviour. They all contain at least one transition metal on the entirely transition metal occupied perovskite *B*-site. Simple band theory suggests that most transition metal oxides, such as NiO (Ni^{2+} $3d^8 4s^0$ and O^{2-} $2p^6$), should display electron delocalised metallic properties due to partially filled d-levels. However, many like NiO are insulators, as the d-electrons are localised with short range Coulomb repulsion of electrons preventing the formation of band states, instead stabilising localised electron states. These materials are known as Mott-Hubbard insulators.

The Coulomb repulsion is described by a correlation energy (Hubbard, *U*), which is the energy penalty for transferring an electron between adjacent sites. This is demonstrated in the schematic diagram in Figure 1.5.

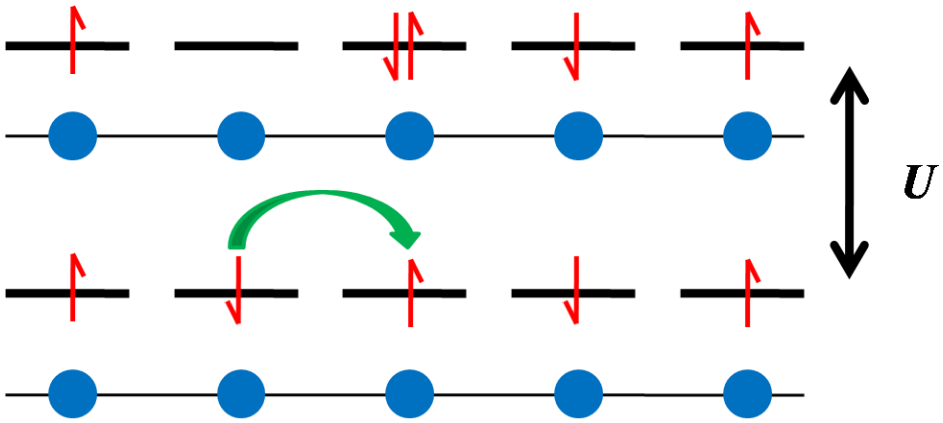

$$Ni^{2+} + Ni^{2+} \rightarrow Ni^{3+} + Ni^{+}$$
$$d^8 + d^8 \rightarrow d^7 + d^9$$

Figure 1.5 Schematic diagram showing the correlation energy (*U*) penalty for transferring an electron between two adjacent sites.

Figure 1.6 shows that electron repulsion can make even the half-filled band insulating when the interaction between (Bandwidth, *W*) atoms is small (i.e. when there is poor orbital overlap between atoms). When $U > W$, the d-band is split into sub-bands and an electron must overcome *U*, making the material a Mott-Hubbard insulator. When $U \approx W$, the bandwidth is sufficient for overlap to occur and the material is metallic as there is no energy gap.[49-52]

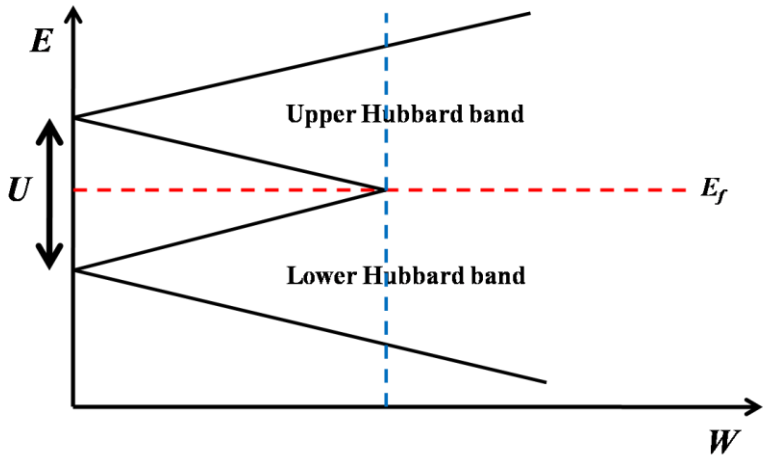

Figure 1.6 Schematic diagram demonstrating the relationship of Bandwidth (*W*) with *U* in a Mott-Hubbard insulator (E_f, Fermi energy).

1.4.3 Ionic conductivity

In ionic solids, ions will vibrate continuously, and if they have enough thermal energy to escape from their lattice sites into an adjacent site, they may be in the process of becoming an ionic conductor. Ionic conductivity is generally thermally activated, involving a defect structure. Ionic conductivity can proceed when an ion moves into a vacancy, into a vacant interstitial site, or exchanges with another ion. Figure 1.7 shows four types of ion migration; A) shows the ion moving into an equivalent neighbouring but vacant site, B) shows the ion move into an interstitial site, or vice versa C) shows the movement of an ion onto a site occupied by another ion, which is then displaced into an interstitial, D) shows the exchange of positions between two ions. The vacancy defects can also be thought of as Schottky defects, which are described by cation and anion vacancies in stoichiometric units in order to maintain charge neutrality, while the vacancy plus interstitial defect can describe a Frenkel defect.[48]

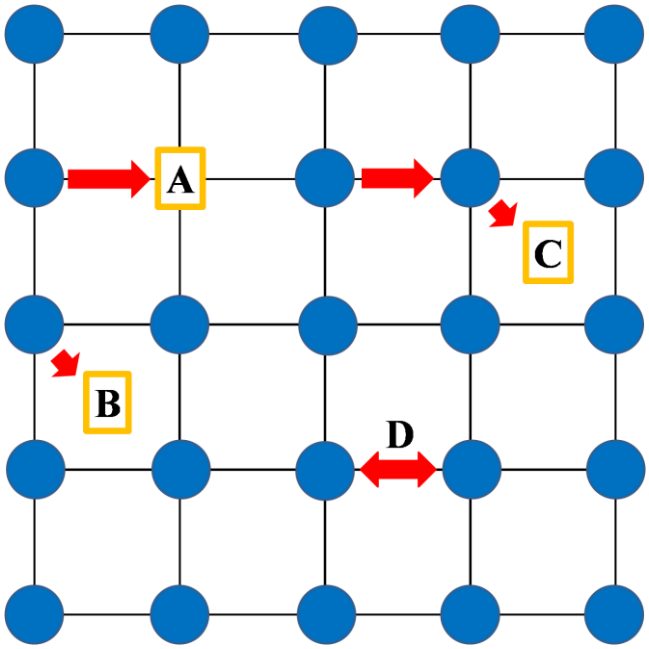

Figure 1.7 Schematic representation of ion migration mechanisms; A) vacancy, B) interstitial, C) interstitialcy, D) exchange.

Ionic conductivity is important for SOFC components, particularly for the electrolyte. The vacancy mechanism is predominant for a number of oxygen deficient fluorite materials

commonly used as electrolytes, as well as anion-deficient perovskites mainly used as both electrolytes and cathodes. The interstitial mechanism has been documented for some Ruddlesden-Popper phases used for electrode materials, as discussed later in section 1.7.3.4.[53]

1.5 Magnetic ordering

For a material to display paramagnetism, there must be unpaired electrons present, meaning many compounds containing transition metals or lanthanides are paramagnetic. In condensed matter, high concentrations of paramagnetic ions may interact with each other through covalent bonds to produce ordered magnetic states. Some of the more common magnetic ordering phenomena are described below.

When orientation is completely random on different atoms, a material is paramagnetic. When the electrons interact with each other, they can align parallel leading to an overall magnetic moment (ferromagnetic) or anti-parallel with zero overall magnetic moment (antiferromagnetic). If electrons align anti-parallel, but with unequal numbers, a net magnetic moment will result (ferrimagnetic). Schematic representations of these four effects are displayed below in Figure 1.8.[48]

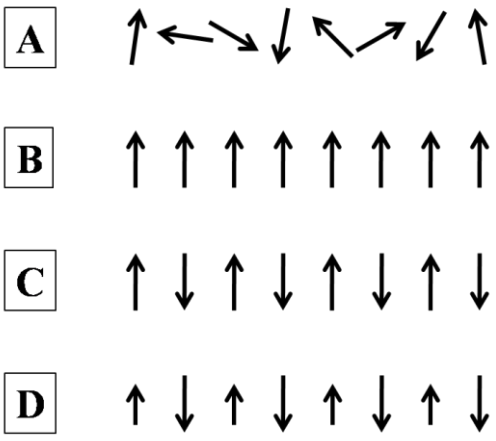

Figure 1.8 Schematic diagram of unpaired electrons aligned as A) paramagnetic, B) ferromagnetic, C) antiferromagnetic and D) ferrimagnetic.

The interaction of magnetic ions in a solid can be through direct exchange, where there is a direct coupling of magnetic ions, or superexchange, where coupling occurs via an intermediary ion.[54] This coupling requires overlap of the intermediary ions orbitals with both of the magnetic ions orbitals. In the case of Fe^{3+} (d^5) in octahedral coordination, the d orbitals are overlapping with oxygen 2p orbitals, which leads to an anti-parallel alignment and antiferromagnetic ordering as shown in Figure 1.9.

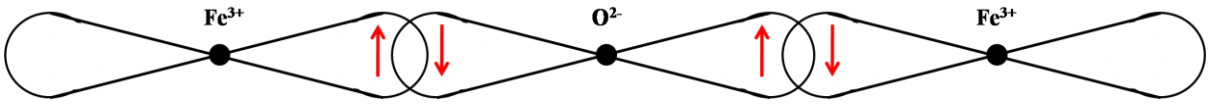

Figure 1.9 Antiferromagnetic coupling of spins of d electrons on Fe^{3+} ions through p electrons of O^{2-}.

In this thesis, the materials prepared mostly contain Fe^{3+} on the perovskite *B*-site, which formed magnetically ordered antiferromagnetic structures at room temperature. Neutron diffraction was used in the characterisation of these materials, and is able to detect magnetic ordering (see Chapter 2 section 2.2.4). Modelling of the magnetically ordered structure was required in order to obtain a good fit of the data. The fitting of the magnetic data is discussed in each of the results chapters.

1.6 Structures of Particular Interest

1.6.1 Fluorite

The fluorite structure gets its name from the mineral CaF_2. The structure is a cubic close packed (*ccp*) array of Ca^{2+} cations with F^- ions filling all the tetrahedral holes. The true lattice type of a fluorite is face-centred cubic (*fcc*), although it can alternatively be perceived as primitive cubic anions with the eight coordinate sites in the centre of the cell alternately occupied and vacant of a cation. The structure of the fluorite, as represented by CaF_2, is shown below in Figure 1.10.[48]

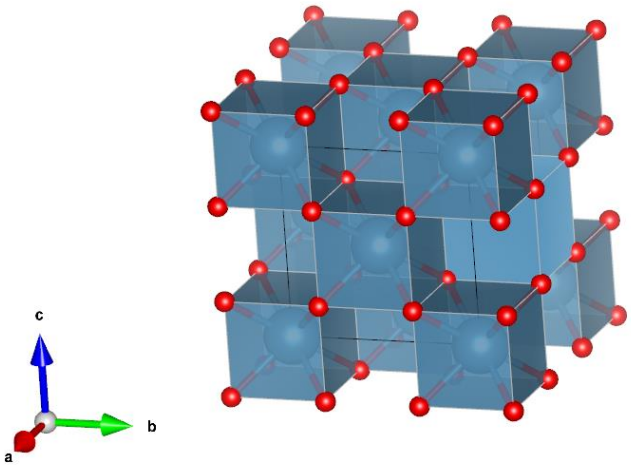

Figure 1.10 Fluor spar, CaF_2, representing the structure of the fluorite, with eight coordinate Ca cations (blue) and T_d coordinate F anions (red).[55]

Oxides adopting the fluorite structure with the general formula AO_2 (A^{4+}, O^{2-}), have shown great utility as oxide ion conductors. As discussed above, the fluorite has a number of interstitial body centred sites vacant of a cation, which gives it quite an open structure that may lend to rapid ion diffusion. However, the main mechanism of oxide ion conductivity comes from mobile oxygen vacancy defects. Further modification of the structure is possible, with the creation of more oxide vacancies through the substitution of trivalent and divalent cations. In order to maintain electroneutrality, the lower charge cation will be compensated for through the creation of oxide ion defects.[56-58] Some examples of fluorite oxide conductors are discussed in section 1.7.1.

1.6.2 Perovskite

$CaTiO_3$ was discovered by German mineralogist G. Rose in 1839 and named after Russian mineralogist L. A. Perovski. The name perovskite has since become the general description of a structural family, where the structure has the formula ABX_3 (A is usually a large

lanthanide or group II cation, B is usually a transition metal and X is an anion, usually O^{2-} or a halide). Perovskites can show great compositional diversity, forming with a combination of many elements, displaying the flexibility of the structure. Figure 1.11 below shows that the primitive unit cell of the perovskite contains *A*-site cations that are in the 12 coordinate cubo-octahedral sites, *B*-site cations in six coordinate corner sharing octahedral (O_h) sites, and X anions coordinated to four *A*-site cations and two *B*-site cations. The ideal structure adopts the cubic space group $Pm\bar{3}m$, which have a cell edge length a Å (usually ~ 4 Å), which can be donated as a_p.[48, 59]

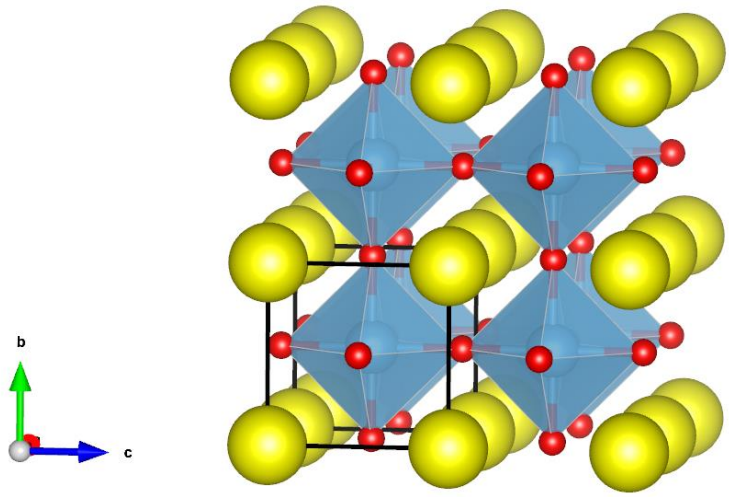

Figure 1.11 Perovskite structure, as displayed by the archetypal $SrTiO_3$,[60] with oxygen atoms (red), strontium atoms (yellow) and titanium atoms (blue) all represented in the primitive cubic unit cell $Pm\bar{3}m$ (highlighted in black box).

For a perovskite drawn with the origin centred on the *B*-site cation, in 1926 V. M. Goldschmidt observed that when anions and *A*-site cations are of equal size, the length of the line joining X-A-X would equal $\sqrt{2}$ times the edge of the unit cell or $(2r_X + 2r_A)$. The former equal$(2r_X + 2r_B)$s, and in an ideal case therefore:

$$(r_X + r_A) = \sqrt{2}(r_x + r_B)$$

Equation 1.7

Where r_X, r_A and r_B are the ionic radius of the anion, *A*-site cation and *B*-site cation respectively. In real systems, due the differences in sizes of X, A and B, the relationship is modified to include a tolerance factor, *t*:

$$t = \frac{(r_X + r_A)}{\sqrt{2}(r_x + r_B)}$$

Equation 1.8

For the ideal structure, $t = 1$, however perovskites are known to form with $t = 0.81$ - 1.11. The tolerance factor can give an indication whether a perovskite structure may form during synthesis, the further from unity, the less likely a perovskite structure will form.[59]

As the size mismatch between atoms increases and the tolerance factor moves away from 1, perovskites may form with distortions away from the ideal cubic structure. These distortions may arise from tilting or rotating of the O_h due to *A*-site cations being too large or small for the 12-coordinate environment. Also, *B*-site cations can be displaced from the centres of the O_h, or the distortions of the O_h could occur due to Jahn-Teller effects (not related to *t*).[59]

O_h tilting has been studied in detail by Glazer in 1972,[61] where he developed a notation to help explain the tilting system. The tilt system is described in terms of O_h rotations about the three orthogonal Cartesian axes. That is, tilts along *x*, *y* and *z* of the ideal cubic structure with the magnitude *a*, *b* and *c*. Positive superscripts are applied if the rotations of O_h are in the same direction in successive layers, whereas negative superscripts indicate rotation of neighbouring O_h in the opposite sense. A zero superscript is used for no rotation.

Tilting of O_h leads to a reduction in symmetry from the ideal $Pm\bar{3}m$ Glazer tilt system ($a^0a^0a^0$), creating sub-groups of lower symmetry. For example, the orthorhombic space group *Pnma* can be produced through tilting the original cubic cell O_h ($a^+b^-b^-$), giving $a \approx b \approx \sqrt{2a_p}, c \approx a_p$.[59]

Ordering within a perovskite can occur when *A*-site or *B*-site cations are partially substituted by cations of a different charge or size. Ordering is most common for *B*-site cations and can result in compounds with the general formula $A_2BB'X_6$, where B and B' are both in O_h coordination, but located on crystallographically distinct sites. The phase would be called a double perovskite, as with the example shown in Figure 1.12, K_2NaAlF_6.[62] *A*-site ordering can also occur, for $AA'B_2X_6$, the A and A' would also be located in distinct crystallographic sites.

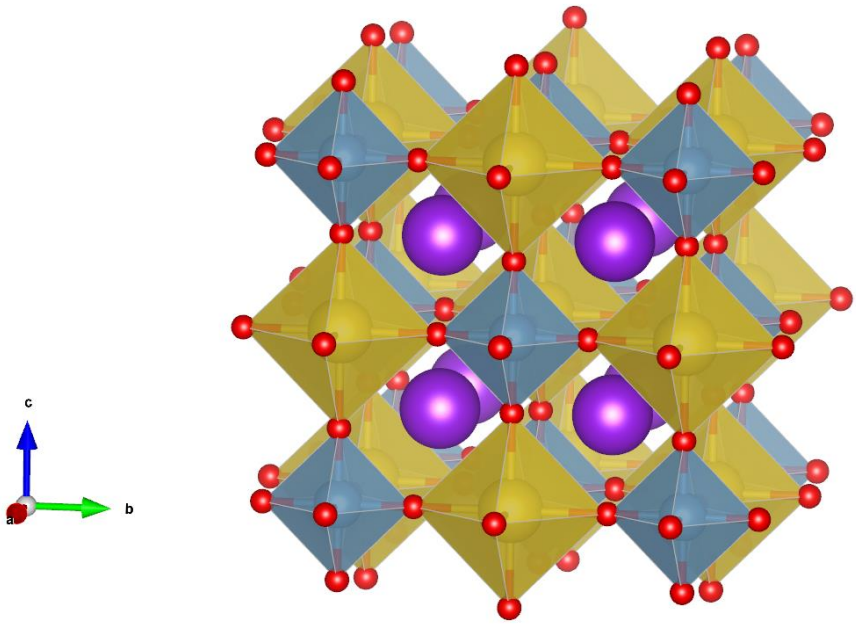

Figure 1.12 Crystal structure of the double perovskite K_2NaAlF_6,[62] with oxygen atoms (red), potassium atoms (purple), sodium (dark yellow) and aluminium (blue) all represented in the cubic unit cell $\boldsymbol{Fm\bar{3}m}$.

Non-stoichiometric perovskites can also form with vacancies and defect structures, such as the anion deficient brownmillerite family, with general formula $A_2B_2X_5$. They generally form through a reduction of the overall oxidation state of the cations, when compared to the ideal perovskite (ABX_3) with A + B = 6+. For example, in $Ca_2Fe_2O_5$, A + B = 5+ ($ABX_{2.5}$), therefore there are 0.5 O vacancies in the structure. Depending on the cations involved and synthesis conditions, the anion vacancy can be disordered (as for $Ba_{0.5}Sr_{0.5}Co_{0.8}Fe_{0.2}O_{3-\delta}$),[63] or in the case of the brownmillerite, ordered. When ordered, anion deficient tetrahedral (T_d) layers form either side of the corner sharing O_h, (as seen in Figure 1.13). In all cases, the O_h

are tilted, leading to the coordination of the *A*-site being either 7, 8 or 9 and generating conditions for *A*-site ordering.

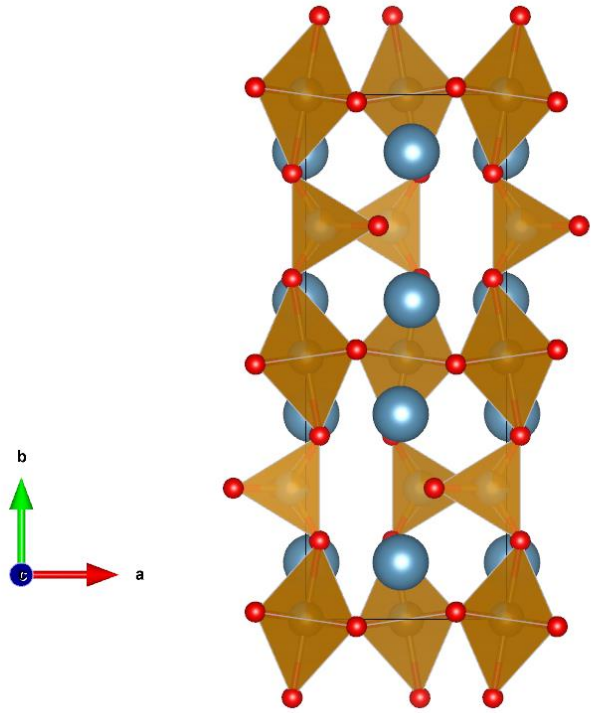

Figure 1.13 Crystal structure of brownmillerite phase Ca_2AlFeO_5,[64] with oxygen atoms (red), calcium atoms (blue), iron atoms (brown) and aluminium atoms (pale blue, within polyhedra) all represented in the orthorhombic unit cell ***Ibm2***.

Anion deficiency can also lead to different layered perovskite structures, particularly in addition to long range ordering, such as $YBa_2Fe_3O_8$,[65] shown in Figure 1.14, which is related to the superconducting material $YBa_2Cu_3O_{7-x}$. $YBa_2Fe_3O_8$ contains one anion vacancy for every perovskite unit (a_p), which presents itself between two square pyramidal (S_q) *B*-sites. The phase has two crystallographically distinct *A*-sites, an eight coordinate site occupied by Y and the two 12 coordinate sites are occupied by Ba. Fe occupies the two resultant *B*-site sites, the O_h BO_6 site and the two S_q BO_5 sites, resulting in a supercell of $a_p \times a_p \times 3a_p$ in the space group *P*4/*mmm*.[65]

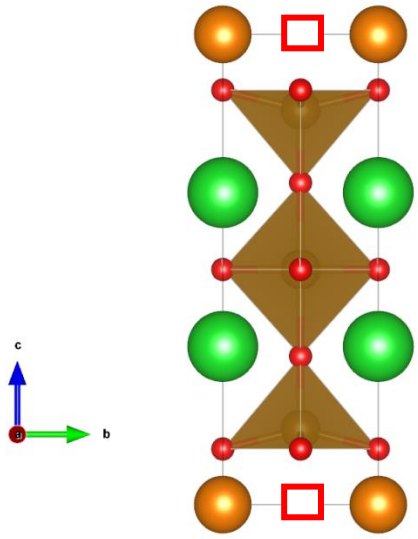

Figure 1.14 $YBa_2Fe_3O_8$ crystal structure,[65] displaying oxygen vacancies (red box), oxygen atoms (red), barium atoms (green), yttrium atoms (orange) and iron atoms (brown) represented in the tetragonal unit cell $P4/mmm$.

A-site ordering and brownmillerite structure types are important to the work carried out in this thesis, with the structures presented closely related to them. Intergrowths between these structure types are also possible, creating extended structures that are presented in the results chapters 3, 4 and 5.

1.7 SOFC Materials

1.7.1 Electrolytes

As discussed in section 1.3.3 for a SOFC, the electrolytes main property requirement is that of high ionic conductivity for the transport of oxygen ions from the cathode to the anode. Additionally, electrolytes should display negligible electronic conductivity, phase stability under air and fuel conditions at operating temperatures, and compatibility with both anode and cathode materials that it is in contact with, both chemically and in terms of thermal expansion (indicated by the thermal expansion coefficient, TEC). The electrolyte also needs to be able to be processed and fabricated into a thin dense ceramic that is both gas tight and

mechanically strong enough to prevent cracking.[66] Below are some examples of current electrolyte materials, with the main focus on those used in this thesis.

1.7.1.1 Stabilised ZrO_2

Yttria-stabilised zirconia (YSZ) is the most common electrolyte material used in SOFCs. Pure ZrO_2 adopts the cubic fluorite structure above 2300 °C,[67] with substitution of Y^{3+} for Zr^{4+} not only stabilising the structure in a cubic fluorite structure at room temperature (see section 1.6.1 and Figure 1.10), but also increasing the concentration of oxide vacancies through charge compensation, increasing the ionic conductivity.[68] YSZ shows its highest conductivity at 8 - 10 mol% Y_2O_3, with a value of 1.3 x 10^{-1} S.cm^{-1} achieved at 1000 °C.[69-71] YSZ is chemically stable in oxidising and reducing atmospheres in the oxygen partial pressure range of 1 - 10^{-17} atm.[72] The TEC of YSZ has been reported to be 10.5 x 10^{-6} K^{-1} between room temperature and 1000 °C.[73]

There are some potential compatibility issues for YSZ, as reactions with common cathode phase $La_{1-x}Sr_xMnO_{3-\delta}$ (LSM) have been reported at fabrication temperatures of 1250 °C, with the formation of pyrochlore phase $La_2Zr_2O_7$,[74-79] or perovskite $SrZrO_3$,[80-82] leading to degradation of cell performance due to the lower conductivities of the reaction products.[83]

An alternative doped zirconia is scandia-stabilised zirconia (ScSZ), which shows the higher conductivity than YSZ and the highest oxygen ion conductivity of all the zirconia based oxides, with a conductivity of 0.32 S.cm^{-1} at 1000 °C for 8 mol% Sc_2O_3 and a TEC of 10.7 x 10^{-6} K^{-1}.[84-86] The highly conducting cubic phase exists above 600 °C; below this, a rhombohedral phase exists with much reduced conductivity. It has been shown that the cubic phase can be stabilised at room temperature through co-doping with cations as Y.[87]

1.7.1.2 Doped CeO_2

The two most common dopants for ceria are samarium and gadolinium (SDC and GDC respectively) with the formula $Ce_{1-x}(Gd,Sm)_xO_{2-\delta}$, which form oxygen deficient cubic fluorite structures much like stabilised zirconia.[88-90] Doped ceria shows higher conductivity when

compared to YSZ, especially at reduced temperatures, as well as a lower polarisation resistance.[91] $Gd_{0.1}Ce_{0.9}O_{1.95}$ has been reported with a conductivity of 3.2×10^{-2} $S.cm^{-1}$ at 700 °C, higher than that observed for YSZ.[73]

The main problem with doped ceria is that it displays electronic conductivity at low oxygen partial pressures due to the partial reduction of Ce^{4+} to Ce^{3+}, making it only viable for a SOFC operating at ≤ 600 °C.[73, 91, 92] Doped ceria does however, shows improved chemical stability when compared to YSZ for LSM (in this case M = Mn, Co, Fe),[93-95] and has been used as a buffer layer between YSZ electrolyte and electrode.[96, 97] The TEC of doped ceria range around $11.5 - 12.5 \times 10^{-6}$ K^{-1}.[98]

In this thesis, $Gd_{0.1}Ce_{0.9}O_{1.95}$ and $Sm_{0.2}Ce_{0.8}O_{1.9}$ were used as electrolyte substrates for symmetrical cell fabrication.

1.7.1.3 Doped $LaGaO_3$

The perovskite lanthanum gallate, when suitably doped, has been shown to display very high oxide ion conductivity within the intermediate temperature range identified for SOFCs.[99] Sr and Mg co-doping (LSGM, $La_{1-x}Sr_xGa_{1-y}Mg_yO_{3-\delta}$) produce a material that has higher conductivity when compared to YSZ and ScSZ, but lower than that of doped ceria (0.11 $S.cm^{-1}$ at 800 °C).[100] The main advantage that LSGM possesses over doped ceria is that it does not contain any easily reduced cations, meaning that it displays negligible electronic conductivity, even at low partial pressures of oxygen.[99]

LSGM is more stable with La containing perovskites such as LSM compared to YSZ, with no new phase formation observed. There are however, reports of cation diffusion between LSGM and LSM ($La_{1-x}Sr_xMnO_{3-\delta}$) cathodes, though this is not necessarily detrimental to performance.[101, 102] There are some reactivity issues with Ni, when using the most common anode, Ni-YSZ. The formation of La_2NiO_4 has been observed, which resulted in decreased performance.[101] For the composition $La_{0.9}Sr_{0.1}Ga_{0.8}Mg_{0.2}O_{2.85}$, a TEC has been recorded at 11.9×10^{-6} K^{-1}, measured from room temperature to 1000 °C.[103, 104]

$La_{0.9}Sr_{0.1}Ga_{0.8}Mg_{0.2}O_{2.85}$, with its structure shown below in Figure 1.15, was used as an electrolyte substrate for symmetrical cell fabrication for this thesis.[105]

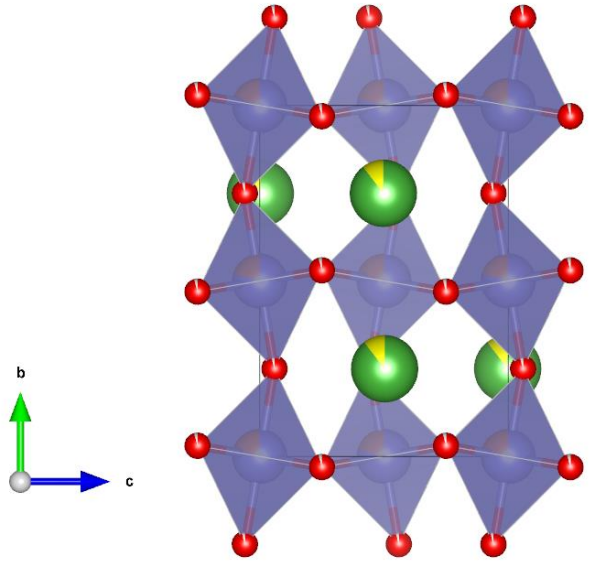

Figure 1.15 Crystal structure of $La_{0.9}Sr_{0.1}Ga_{0.8}Mg_{0.2}O_{2.85}$,[105, 106] with oxygen atoms (red), Lanthanum atoms (green), strontium atoms (yellow), gallium atoms (pale purple), magnesium atoms (orange, within polyhedra) all represented in the orthorhombic unit cell *Imma or monoclinic I2/a.*[105, 106]

1.7.2 Anodes

As a summary from section 1.3.3, SOFC anodes are required to display electronic conductivity in order to transport electrons that were generated by electrochemical reactions to an external circuit. They are also required to be catalytically active for the oxidation of fuels, chemically and thermally compatible with the electrolyte, thermally stable up to operating temperatures in the presence of the fuel. Ionic conductivity is also a desired property in order to transport oxygen ions from the electrolyte to the reactive sites. The anode should also be fabricated with high porosity in order to increase the number of electrochemically active sites.[107]

The most common SOFC anode is a material made up from metallic Ni mixed with the electrolyte YSZ, making a cermet. Since the anode side of a SOFC is exposed to a reducing atmosphere, Ni can be present in its metallic state. Ni has showed the highest activity for the oxidation of hydrogen when compared to Mn, Fe, Co, Ru and Pt when evaluated with electrolyte materials YSZ and SDC, meaning it is the ideal catalyst to use in the anode when

hydrogen is used as the fuel.[108] Although Ni has a higher TEC ($13.3 \times 10^{-6}\ K^{-1}$) when compared to YSZ, in a cermet the TEC is reduced and becomes comparable to that of YSZ. Ni also has a very high electronic conductivity of $\sigma \approx 2 \times 10^{4}\ S.cm^{-1}$.[109]

Ni/doped ceria cermets have also been used as anodes, using the same approach as for Ni/YSZ cermets. The CeO_2 however, become a MIEC under the reducing atmosphere at the anode, which leads to an enhancement of catalytic activity.[107]

As Ni cermets are a problem for LSGM electrolytes with the formation of La_2NiO_4, alternatives have been investigated. Such alternatives include the rhombohedral perovskite phase $La_{1-x}Sr_xCr_{0.5}Mn_{0.5}O_{3-\delta}$ seen below in Figure 1.16.[110, 111]

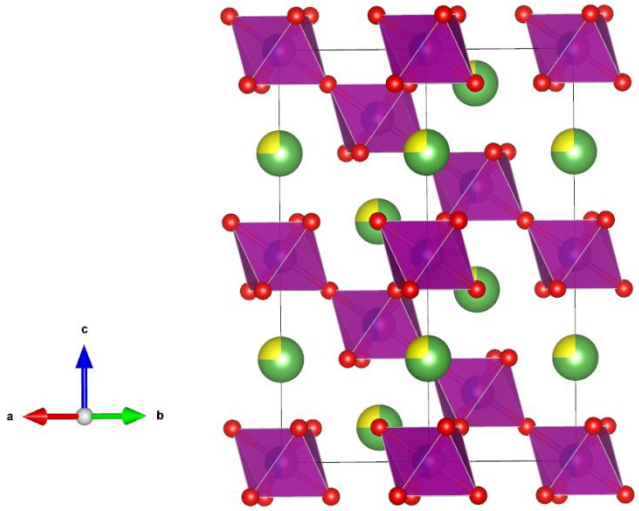

Figure 1.16 Crystal structure of $La_{0.75}Sr_{0.25}Cr_{0.5}Mn_{0.5}O_{3-\delta}$,[112] with oxygen atoms (red), lanthanum atoms (green), strontium atoms (yellow), manganese atoms (purple) and chromium atoms (blue, within polyhedra) all represented within the rhombohedral unit cell $\boldsymbol{R\bar{3}c}$.

1.7.3 Cathodes

Cathodes require similar properties to the anode, electronic conductivity for the transport of electrons, chemical compatibility with the electrolyte along with a close matching TEC and thermal stability under the atmosphere of the cathode (air). Cathodes also need to be catalytically active for the ORR, with ionic conductivity desirable, especially when operating

at intermediate temperatures. A porous microstructure is also required in order to maximise the surface area for the ORR to occur over.

In this next section, the most common cathodes will be discussed, as well as the more novel layered perovskite cathodes, which are structurally related to the materials studied in this thesis.

1.7.3.1 $La_{1-x}Sr_xMnO_{3-\delta}$ (LSM)

The perovskite LSM ($La_{1-x}Sr_xMnO_{3-\delta}$) is among the most widely investigated electrode materials for SOFCs.[113] The electronic conductivity of LSM is enhanced through the *A*-site substitution of Sr^{2+} for La^{3+}, which creates an electron hole on the *B*-site to maintain electroneutrality. Sr is the preferred alkaline earth dopant as it results in a stable perovskite that exhibits high electronic conductivity in oxidising atmospheres.[114, 115] A conductivity as high as 320 $S.cm^{-1}$ has been recorded for LSM at a temperature of 800 °C.[116] The TEC of LSM varies from between 11.2 - 12.7 x 10^{-6} K^{-1}, which is slightly higher than YSZ, but in close match with the doped ceria and LSGM phases.[117, 118] LSM has minimal oxygen vacancies within its structure, which leads to very low ionic conductivities, such as 5.9 x 10^{-8} $S.cm^{-1}$ at 800 °C for $La_{0.9}Sr_{0.1}MnO_{3-\delta}$.[119] The low ionic conductivity is considered to be the main cause for the high polarisation losses of LSM cathode for the ORR in IT-SOFCs, making only appropriate to use as a high temperature cathode.[120] Both the ionic and the electronic conductivity can be increased through increased substitution of Sr for La, however at levels of greater than 30 mol% Sr, insulating $SrZrO_3$ will form with YSZ.[37] Composites with ionic conductors YSZ and GDC have also been reported, which has been shown to enhance the performance of LSM.[121]

1.7.3.2 $La_{1-x}Sr_xCoO_{3-\delta}$ (LSC), $La_{1-x}Sr_xFeO_{3-\delta}$ (LSF) and $La_{1-x}Sr_xCo_{1-y}Fe_yO_{3-\delta}$ (LSCF)

$La_{1-x}Sr_xCoO_{3-\delta}$ (LSC) is a MIEC that displays high ionic and electronic conductivity. The ability of Co to alter its oxidation state (potentially 2+, 3+ and 4+), along with the presence of oxygen vacancies helps decrease the cathode polarisation losses. It is likely that the ORR is

not just limited to the TPB for this material.[37] LSC shows high oxygen diffusivity and high catalytic activity towards the dissociation of oxygen molecules,[122] and the electronic conductivity has been reported as high as 1600 $S.cm^{-1}$ at 800 °C. It does however, have a very large TEC, in the region of 20 x 10^{-6} K^{-1}, much higher than that of current electrolytes and likely to lead to delamination during operation.[123] The high TEC of this phase and other cobalt systems is related to the formation of oxygen vacancies, spin-state transitions associated to Co^{3+},[124] and the relatively weak Co-O bond.[125]

The total substitution of Fe for Co has the effect of lowering the TEC, but it also lowers the cathode performance. $La_{1-x}Sr_xFeO_{3-\delta}$ (LSF) has been shown to have a TEC of 12.2 x 10^{-6} K^{-1}, which is a good match for ceria based electrolytes.[126] An ASR of 0.1 $\Omega.cm^2$ at 800 °C has also been reported for LSF.[95]

Partial doping of LSC with Fe results in compounds with the general formula $La_{1-x}Sr_xCo_{1-y}Fe_yO_{3-\delta}$ (LSCF), which have a TEC around 15 - 20 x 10^{-6} K^{-1}, with the lower TEC attained for higher Fe content.[37, 127] An electronic conductivity in the order of 10^2 $S.cm^{-1}$ and an ionic conductivity in the order of 10^{-3} $S.cm^{-1}$ at 750 °C have been observed.[127, 128] There are also reports that show composites of LSCF with GDC not only reduce the TEC, but also lead to improved cathode performance.[94, 129] The main drawback of LSCF as a cathode is related to the reduced performance during long term operation, which is caused by Sr diffusion out of the cathode.[130, 131]

1.7.3.3 $Ba_{0.5}Sr_{0.5}Co_{0.8}Fe_{0.2}O_{3-\delta}$ (BSCF)

$Ba_{0.5}Sr_{0.5}Co_{0.8}Fe_{0.2}O_{3-\delta}$ (BSCF) is a simple cubic perovskite with the space group $Pm\bar{3}m$, with the same structure as seen in Figure 1.11. BSCF was initially used as an oxygen permeation membrane, but was first used as a cathode for SOFCs by Haile and Shao in 2004, where it displayed an ASR of less than 0.1 $\Omega.cm^2$ and power densities of ~ 1 $W\,cm^{-2}$ at 600 °C.[63] It currently displays the best cathode performance when measured under similar conditions at temperatures of 500 - 600 °C. The phase does have a number of major drawbacks however, such as a very high TEC as is common for Co rich phases, around 20 x 10^{-6} K^{-1} measured from 25 - 1000 °C.[132] Again, this can be problematic for cells using this material, with delamination of layers likely.

Another potential problem for this material is that it has a low tolerance for CO_2, readily decomposing in its presence to form carbonates of Ba.[133-136] This low tolerance appears to be an issue for many perovskite phases containing alkaline-earth elements.[137-139] A further drawback for BSCF is that the phase undergoes decomposition into insulating Co rich hexagonal phases and a cubic Sr rich phase at temperatures below 900 °C.[140-143] Much of the work being carried out on this phase involves attempts to improve the stability of the phase, whilst retaining as much of the performance as possible.[144]

1.7.3.4 $Ln_2NiO_{4+\delta}$

The general formula of a Ruddlesden-Popper (RP) material can be written as $A_{n+1}B_nO_{3n+1}$,[145] which consists of $n$$ABO_3$ perovskite layers sandwiched between AO rock-salt layers. The crystal structure of the n = 1 phase, as represented by Ln_2NiO_4,[146] is shown in Figure 1.17. RP phases have been studied as potential SOFC cathodes, as they have been shown to display oxygen non-stoichiometry, enabling a mechanism for fast ionic conductivity.[147] For n = 1, the most noted SOFC phase is based on $Ln_2NiO_{4+\delta}$ (Ln = La, Nd, Pr most common) with interstitial oxygen accommodation shown in the AO rock-salt layers, leading to fast ion conduction.[53]

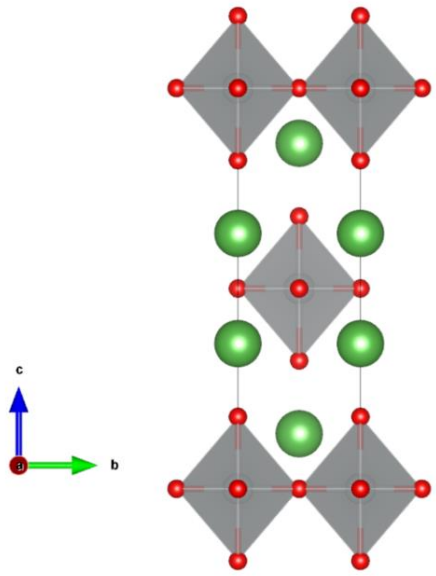

Figure 1.17 Crystal structure of Ruddlesden-Popper, represented by La_2NiO_4,[146] with oxygen atoms (red), Lanthanum atoms (green), Ni atoms (grey) all represented in the tetragonal unit cell $I4/mmm$.

$Ln_2NiO_{4+\delta}$ has shown electronic conductivity of ~ 65 S.cm^{-1} at 750 °C,[148, 149] and a TEC of 11 - 14 x 10^{-6} K^{-1}, within the range of common electrolytes.[37] An ASR of 0.5 Ω.cm^2 at 610 °C has been recorded for Ln = Pr, which is the lowest achieved for this phase.[150] $Ln_2NiO_{4+\delta}$ has however, been shown to react with electrolytes YSZ and GDC at temperatures above 800 °C,[151] as well as leading to phase segregation to n = 2, 3 RP phases when annealed at 950 °C for two weeks.[152]

1.7.3.5 $LnBaCo_2O_{5+\delta}$

Double perovskites, that form due to ordering of the *A*-site ($AA'B_2O_{5+\delta}$, where A = rare earth, A' = alkaline earth) are another structure type to have shown great promise as SOFC cathodes. With ordering of the *A*-site, ordered O vacancies are created in the rare-earth planes, forming channels that are known to enhance oxygen transport properties, which was demonstrated in $GdBaCo_2O_{5+\delta}$ (GBCO) and $PrBaCo_2O_{5+\delta}$ (PBCO).[153, 154] The crystal structure of $GdBaCo_2O_{5.5}$ is shown in Figure 1.18, which highlights the vacancy channels created in the lanthanide plane of the ordered phase.[155]

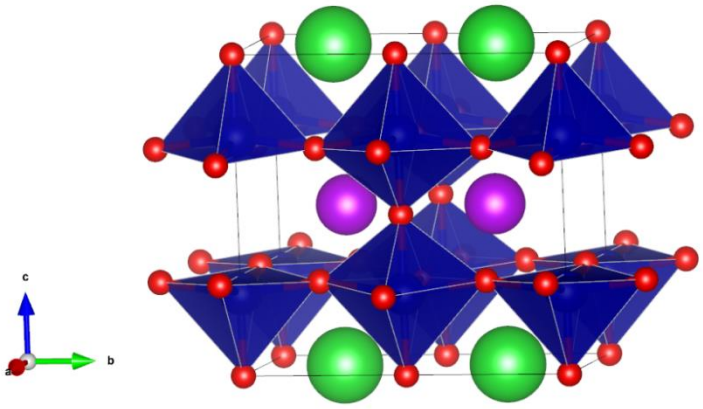

Figure 1.18 The structure of the ordered double perovskite $GdBaCo_2O_{5.5}$,[155] with oxygen atoms (red), gadolinium atoms (purple), barium atoms (green) and cobalt atoms (dark blue) all represented in the orthorhombic unit cell *Pmmm*.

In the case of GBCO, which can be formed ordered or disordered depending on preparation, it was showed that the ordered form had significantly enhanced oxygen diffusion.[130] An ASR

of 0.25 Ω.cm^2 at 625 °C for GBCO and at 550 °C for PBCO has been reported, with this material showing great promise as a cathode.[154, 156, 157] GBCO has also showed good stability in the presence of up to 500 ppm CO_2.[158] GBCO has also shown excellent stability with LSGM and doped ceria electrolytes, though it reacts with YSZ forming $BaZrO_3$.[158-161]

1.7.3.6 $Y_{0.9}Ba_{1.7}Ca_{2.4}Fe_5O_{13-\delta}$ (10a_p)

The 10a_p phase, $Y_{0.9}Ba_{1.7}Ca_{2.4}Fe_5O_{13-\delta}$, forms with a ~ 38 Å stacking axis due to *A*-site ordering, which leads to oxygen vacancy ordering and therefore *B*-site cations in three different coordination geometries, tetrahedral (T_d), octahedral (O_h) and Square pyramidal (S_q) in a 1:2:2 ratio. It has structural similarities with $LnBaCo_2O_{5+\delta}$, through the presence of channels of ordered oxygen vacancies forming between S_q sites. Figure 1.19 shows the structure and representations of the ordered oxygen vacancies for the 10a_p.

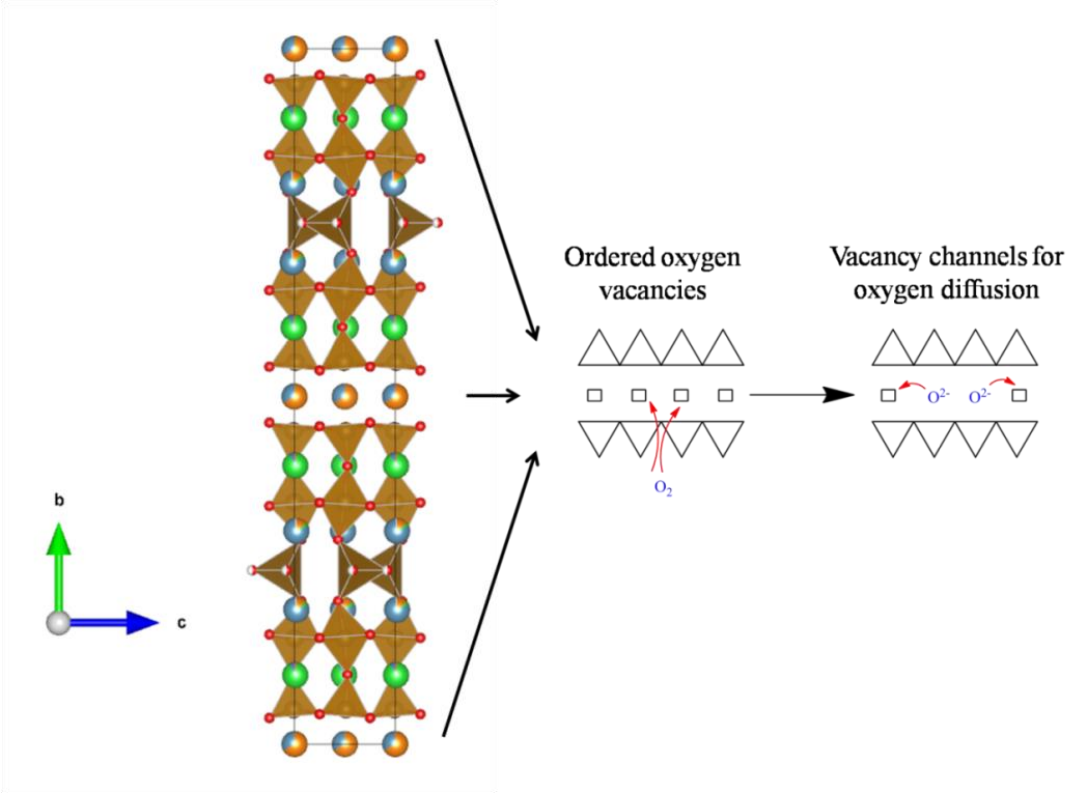

Figure 1.19 Structure of 10ap,[35] showing ordered oxygen vacancies that provide sites for oxygen dissociation and oxygen ion diffusion channels. Atoms of barium (green), calcium (blue), yttrium (orange), iron (brown) and oxygen (red) all represented in unit cell *Imma*.

This phase shows good performance as a SOFC cathode, attaining an ASR of 0.87 $\Omega.cm^2$ at 700 °C when first published,[35] then being lowered to 0.25 $\Omega.cm^2$ after some modifications to cathode processing.[162] The $10a_p$ phase is also thermally stable and chemically compatible with SDC and LSGM, although it reacts with YSZ forming $BaZrO_3$. The average linear expansion of the $10a_p$ phase is 11.8×10^{-6} K^{-1},[35] which matches well with doped ceria and LSGM. The main drawback for this material is its low electronic conductivity of 2.06 $S.cm^{-1}$, which is 10^2 $S.cm^{-1}$ lower compared to LSCF and 10^1 $S.cm^{-1}$ lower than BSCF.[37]

1.8 Aims of Thesis

The aims of this thesis have focused on work involving *A*-site ordered perovskites, leading to the formation of extended structures with ordered oxygen vacancies. The doping of a previously reported phase, $Y_{0.9}Ba_{1.7}Ca_{2.4}Fe_5O_{13-\delta}$ ($10a_p$),[35] was carried out in order to try to improve the performance of the material as a cathode. What follows in this thesis are the results from the attempted doping of this phase, which has led to the discovery of a new phase, as well as the successful doping of the aforementioned phase.

The isolation of phase pure samples was carried out, followed by crystal structure characterisation using both powder diffraction and microscopy techniques. The physical properties of the phases were also examined, in order to determine their potential as SOFC cathodes.

2 Experimental Methods

2.1 Synthesis

Solid state synthesis was the method used in this thesis for the preparation of target phases. The formation of thermodynamic products is achieved through the grinding of appropriate quantities of starting materials in an agate pestle and mortar, followed by subsequent reaction at high temperatures. Grinding reduces particle size and increases homogeneity within the sample, with mixing aided by the use of a solvent such as acetone. The mixed samples are typically contained within an Al_2O_3 crucible for reactions, due to its refractory properties and perceived inert nature, followed by annealing at high temperatures for a wide range of timescales, from hours to weeks depending on requirements. High temperatures are required, often exceeding 1400 °C, in order to enable ion diffusion to overcome kinetic barriers, along with long timescales due to the slow rate of diffusion in many cases. In order to decrease reaction timescales, the reactant powders are pressed into pellets to maximise contact between individual grains. Repeated grinding and annealing can be required to aid a reaction to completion, resulting in the formation of a thermodynamic product. Although there may be good mixing and contact between individual particles, on the atomic scale samples will generally be very inhomogeneous, meaning for reactions to reach completion, ions have to diffuse over long distances.[48]

Although solid state synthesis was the only method used in this thesis, some variations in the synthetic conditions were used. For all compounds, the required ratios of binary metal oxides or carbonates were weighed out and mixed by hand grinding in the presence of acetone, using an agate pestle and mortar, until an homogenous powder was obtained. All starting materials were heated before mixing in an oven at 200 °C (or a furnace at 950 °C for lanthanide oxides and Y_2O_3 due to them being highly hygroscopic), in order to ensure that all starting materials were dry so that accurate cation ratios could be determined. All samples were prepared on a 0.5 g scale for exploratory synthesis and annealed as powders during the first step in order to evolve CO_2 from the starting materials uninhibited. This was followed by pressing the reactant powders into pellets using a uniaxial press and subjecting to a second annealing step. Additional grinding and annealing cycles were carried out until the reactions reached

completion, indicated through the use of laboratory powder X-ray diffraction (PXRD) patterns, which stopped changing between cycles on reaction completion. After noticing that the starting materials had reacted with Al_2O_3 crucibles (discussed in Chapter 3), Pt foiled lined Al_2O_3 or Pt metal crucibles were used in the synthesis of all materials discussed in this thesis.

When scaling up synthesis of a previously isolated phase (typically on a 3 - 5 g scale), additional steps were undertaken to ensure homogeneity. The starting materials were milled in a Fritsch pulverisette planetary mill for at least 4 hours at 350 rpm in Yttrium Stabilised Zirconia pots using 8 5 mm ceramic balls made from the same material as grinding media with 4 ml isopropanol for every 1 g of sample. The resultant slurry had the solvent removed by evaporation from a Pyrex evaporating basin on a hot plate at ~ 60 °C in a fume hood. Hand grinding of the dried powder was carried out before undergoing identical annealing treatment as the same sample does on the 0.5 g scale.

Cooling rates are particularly important when considering the ordering of materials investigated in this thesis, particularly as discussed in chapter 3. Depending on the system in question, many phase transitions can occur at different temperature ranges, with systems often becoming more disordered at high temperature.[163-165] In order to access phases that form at higher temperatures, quenching can be a useful technique. For the $16a_p$ phase in Chapter 3, on the final annealing step, the sample was directly removed from the furnace at its synthesis temperature of 1200 °C and placed on a Al metal quenching block, which is highly thermally conducting,[166] enabling the sample to reach < 100 °C within a few seconds and room temperature within minutes. Quenching helped to preserve the metastable high temperature phase, preventing the formation of an unwanted secondary $10a_p$ phase.

The use of different atmospheres was also utilised during this thesis. Under "normal" synthesis conditions, a box furnace was used, subsequently samples were annealed under static air. For synthesis in an alternate atmosphere, a tube furnace was used that enabled flowing gas from a compressed gas cylinder to be used to deliver the chosen atmosphere.

The exact conditions of each synthetic preparation are described within Chapters 3, 4 and 5 for each phase synthesised.

2.2 Powder Diffraction Techniques

2.2.1 Diffraction and Crystal Symmetry

All phases prepared in this thesis are crystalline in nature, which has allowed the extensive use of powder diffraction for characterising their crystal structures. An ideal crystal structure can be described as a 3-dimentional lattice with a repeating structural motif made up of atoms or molecules ordered in a periodic way. The lattice can be described by choosing a parallelepiped unit cell with edges a, b and c and angles α, β and γ containing atoms in a specific spatial arrangement. Stacking of the unit cell in all three dimensions results in the crystal structure. It can be classified into seven different crystal systems depending on the geometry of the unit cell, which are summarised in Table 2.1.

Crystal system	Cell edge	Cell angle
Triclinic	$a \neq b \neq c$	$\alpha \neq \beta \neq \gamma \neq 90°$
Monoclinic	$a \neq b \neq c$	$\alpha = \gamma = 90°, \beta \neq 90°$
Orthorhombic	$a \neq b \neq c$	$\alpha = \beta = \gamma = 90°$
Tetragonal	$a = b \neq c$	$\alpha = \beta = \gamma = 90°$
Hexagonal	$a = b \neq c$	$\alpha = \beta = 90°, \gamma = 120°$
Trigonal	$a = b = c$	$\alpha = \beta = \gamma \neq 90°$
Cubic	$a = b = c$	$\alpha = \beta = \gamma = 90°$

Table 2.1 The seven crystal systems together with their characteristic unit cell parameters.

The Bravais lattice, combined with the unit cell, describes the translational symmetry of the crystal structure. The possible types of centring are; primitive (P), body centred (I), face-centred (A,B,C) and rhombohedral (R).

Due to symmetry constraints, not all centring types are compatible with all crystal systems. For example, any centred lattice can be reduced to a primitive lattice with a smaller unit cell volume for the triclinic system. When all five types of lattices are combined with the seven crystal systems, a total of 14 different Bravais lattices are presented. When the Bravais lattice

is combined with all possible symmetry elements for the unit cell, 230 unique space groups are defined.[167]

2.2.2 Diffraction

Due to the periodic nature of a crystalline material, structural characterisation by diffraction is a powerful tool. X-rays, neutrons and electrons can all be used in diffraction experiments due to their appropriate wavelength, which is in the order of magnitude of atomic radii and inter atomic spacing. Diffraction and the use of these radiation sources are described in the following sections.

2.2.3 X-ray Diffraction (XRD)

When a beam of X-rays propagates through a solid, they can interact leading to various processes occurring. One such process, fluorescence, occurs when photons are absorbed by ionising core electrons, with secondary photons emitted in random directions as the ions relax to their ground state. Although fluorescence contributes to the background signal of a diffraction experiment, it can be minimised through careful selection of wavelength.

Another process is the scattering of photons by electrons, caused by Coulombic interaction of the electron with the oscillating field of the X-ray beam. If energy is lost from a photon during collisions with core electrons, with an associated wavelength increase, the scattering process is inelastic. Elastic scattering occurs when a scattered X-ray beam is radiated by an oscillating electron at the same frequency and wavelength as the incident wave. This process gives rise to Bragg scattering and is used in crystallography.

Max von Laue developed the first theory of diffraction of X-rays by crystals in 1912, where he considered the crystal as a 3-Dimensional lattice with rows of regularly spaced atoms, although the theory is illustrated by a 1-Dimensional lattice, as shown in Figure 2.1. The atoms were considered a secondary source of X-rays with a spherical wavefront, each atom acting as a point scatterer.

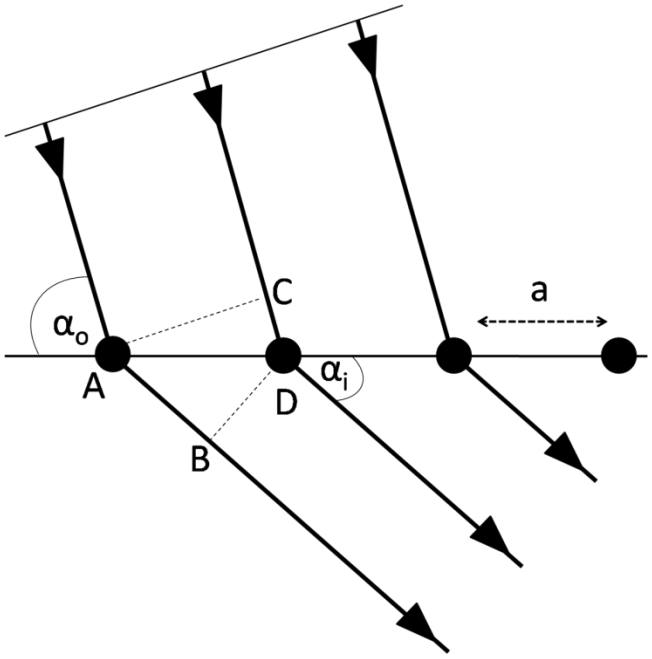

Figure 2.1 Schematic diagram showing Laue scattering by a 1-Dimensional lattice of monochromatic radiation from a single source. Labels of angle and distances used in construction of Laue equation (Equation 2.1).

The condition for constructive interference from a row of atoms along the *x*-axis is satisfied if, for a specific diffraction angle, the path length differs by an integer (n) of wavelength (λ) such that:

$$AB - CD = a(cos\alpha_i - cos\alpha_o) = n\lambda$$

Equation 2.1

For a real three dimensional system, three Laue equations for each of the *x*, *y* and *z*-axis must be simultaneously satisfied for constructive interference to occur. Due to the complexity of the Laue equation, which requires the determination of up to 12 variables, its practical use in crystallography is limited. A more useful law in powder diffraction was formulated by W. H. Bragg and W. L. Bragg. It considers diffraction occurring from a reflection of X-rays from planes within a crystal. These planes are defined by Miller indices (h, k and l), which intersect the unit cell at $\frac{a}{h}$, $\frac{b}{k}$ and $\frac{c}{l}$ respectively. Examples of Miller indices intersecting a unit cell are shown below in Figure 2.2.

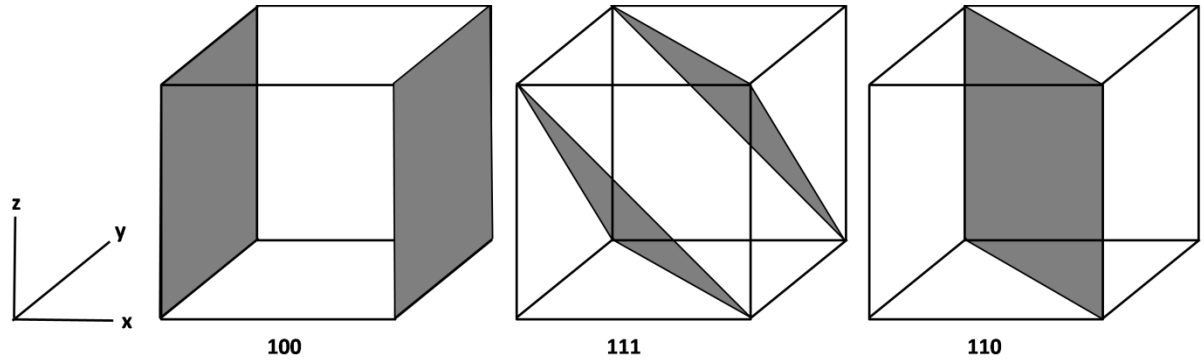

Figure 2.2 Examples of lattice planes with their corresponding Miller indices.

According to Figure 2.3, constructive interference occurs when the difference in path lengths (xyz = xy + yz, and from trigonometry xy = zy = $dsin\theta$) for beams A and A' is equal to an integer number (n) of wavelengths (λ). This is known as Bragg's law and is shown in Equation 2.2. Bragg's law is not satisfied when scattered beams are out of phase, leading to destructive interference.

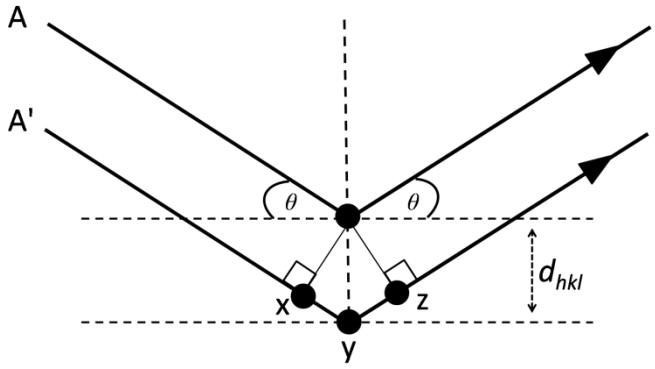

Figure 2.3 Bragg reflection of monochromatic radiation from a single source from regularly spaced planes of atoms. Labelled angles and distances used to construct Bragg equation (Equation 2.2).

$$n\lambda = 2d_{hkl}sin\theta$$

Equation 2.2

Bragg's law relates *d*-spacing to the angle of diffraction (θ) at a given wavelength (λ). This means that a diffracted beam, monitored at variable θ, only has constructive interference at discrete values of θ that is dependent on the d_{hkl} (spacing of diffracting planes). Assigning *hkl* Miller indices to observed reflections is known as indexing, and it allows determination of unit cell parameters and crystal system. Bravais lattice type can be deduced based on systematic absences identified, caused by translational symmetry within the unit cell.

Although information derived from Bragg's law is of importance, it is not able to describe the actual arrangement of atoms within a real crystal. The intensity of each reflection (I_{hkl}) needs to be considered, which is dependent on the structure factor (F_{hkl}), the Lorentz factor (L) which is dependent on instrument geometry, a polarisation correction (p) and a scale factor (s), which are related in Equation 2.3.

$$I_{hkl} = sLp|F_{hkl}|^2$$

Equation 2.3

As the structure factor dominates, the equation can be considered as follows:

$$I_{hkl} \propto |F_{hkl}|^2$$

Equation 2.4

The structure factor describes a number of crystal characteristics and can be defined by the complex mathematical function shown in the equation below:

$$F_{hkl} = \sum_{n=1}^{N} f_n(\theta) exp[2\pi i(hx_n + ky_n + lz_n)].q$$

Equation 2.5

Where $f_n(\theta)$ is the atomic form factor, which is the θ dependent scattering amplitude of an atom n. The coordinates of n are given by x_n, y_n, z_n and the temperature dependent Debye-Waller factor is q.

For X-rays, $f_n(\theta)$ is proportional to the electron count (Z) of the scattering atom, therefore heavy atoms are the strongest scatterers. The dependence on θ comes about due to a small amount of destructive interference introduced as photons are scattered from different regions of the same atom, giving slightly different path lengths.

The Debye-Waller factor, q, models temperature dependent vibrations of atoms about their equilibrium positions, with atoms existing at larger average distances from their equilibrium positions at higher temperatures. With a larger effective size, intensities observed decrease rapidly with increasing θ. Equation 2.6 for a simple isotropic thermal motion of atoms, with B_{iso} and U_{iso} experimentally determined isotropic temperature factors, is as follows:

$$q_{iso} = exp\left(\frac{-B_{iso}sin^2\theta}{\lambda^2}\right) \text{ and } B_{iso} = 8\pi^2 U_{iso}$$

Equation 2.6

If the scattering amplitudes of atoms within a unit cell are known, in principle the intensity of the observed Bragg reflections can be used to determine their coordinates and fully describe the crystal structure. This is used in the Rietveld method, as described in section 2.2.7.[167]

2.2.4 Neutron Diffraction (ND)

The de Broglie equation shown below describes the wave-like characteristics displayed by particles.

$$\lambda = \frac{h}{mv}$$

Equation 2.7

$$mv = p \; and \; so \; \lambda = \frac{h}{p}$$

Equation 2.8

Where *h* is Planck's constant, *m* is a particle's rest mass and *v* is the particle's velocity and *p* is particle momentum. Neutrons can therefore be diffracted by a crystal if they have suitable energy. Although the same conditions apply for the scattering of neutrons as those for the scattering of X-rays, the scattering mechanisms are somewhat different. Neutrons are scattered directly by the nucleus of an atom via nuclear force, which acts over a considerably shorter distance than that of the incident neutron wavelengths (10^{-15} m and 10^{-10} m respectively). As the scattering points for neutrons are so small, atomic form factors are independent of θ. It also means neutrons interact fairly weakly with matter, leading to generally large samples required (3 - 6 g) for neutron powder diffraction (ND) experiments if data collections are kept to reasonable timescales.

As neutron scattering factors are not related to their electron count (instead every isotope possesses a unique coherent scattering length), neutrons can be used to differentiate atoms that may have very similar Z number of electrons, as long as the scattering lengths are suitably contrasting, for example Fe and Co.[168] Neutrons are also an excellent tool for detecting light atoms in the presence of heavy atoms, which again X-rays has difficulty with, for example oxygen. Table 2.2 below shows the atomic number and neutron scattering lengths of all of the elements used in this thesis that were investigated by both X-rays and neutrons.

Element	Atomic number (*Z*)	Bound coherent scattering length (fm)
O	8	5.803
Ca	20	4.70
Fe	26	9.45
Co	27	2.49
Cu	29	7.718
Sr	38	7.02
Y	39	7.75
Ba	56	5.07

Table 2.2 Elements used in materials for this thesis, together with atomic number and coherent scattering lengths.[168]

Neutrons can also be diffracted by a lattice of ordered magnetic moments due to them being spin-½ particles. The intensity of the diffracted beam of neutrons is proportional to the square of the magnetic scattering factor and in turn, to the magnitude of the magnetic moment. When a beam of neutrons is incident upon a magnetically ordered crystal, two diffraction patterns, a structural and magnetic pattern are superimposed together. Neutron diffraction can be used to solve magnetic structures, with Shull et al first demonstrating this in 1951.[169] Magnetic scattering occurs from localised unpaired electrons, generally in the outermost orbitals, leading to strong θ dependency, with magnetic Bragg reflections appearing at appreciably greater intensities at low scattering angles.[167]

2.2.5 Electron Diffraction (ED)

Electrons, like neutrons in section 2.24, can also be described by de Broglie's ideas of wave-particle duality, as described by Equation 2.8. The momentum of an electron is created by accelerating it through a potential drop, *V*, which gives it potential energy, *eV*. With the kinetic energy equal to potential energy:

$$eV = \frac{mv^2}{2}$$

Equation 2.9

And when momentum is equated to mass through substitution for *v*:

$$p = mv = (2meV)^{1/2}$$

Equation 2.10

And substitution into Equation 2.8 gives:

$$\lambda = \frac{h}{(2meV)^{1/2}}$$

Equation 2.11

The inverse relationship between λ and V means that by increasing the accelerating voltage, the wavelength is decreased, therefore allowing wavelength to be controlled.

As the electron is a low mass negatively charged particle, it can be easily deflected when passing close to other electrons or the positive nucleus of an atom. These Coulomb interactions cause scattering of the electrons, which makes diffraction experiments possible. The probability of a scattering event can be related to the cross-section (σ_{atom}), or effective radius of a single isolated atom, *r*:

$$\sigma_{atom} = \pi r^2$$

Equation 2.12

The incident electron beam is scattered strongly by the electrons of an atom, giving rise to a very high scattering efficiency, ~ 10^6 - 10^7 times stronger than in XRD. This results in very intense diffraction when the electron beam constructively interacts, and according to Bragg's law, Equation 2.2. The Bragg scattering angles are very small when compared to XRD and ND, due to the smaller wavelengths, shown below in Table 2.3.

Radiation	**Wavelength, λ**
X-rays	Region of a few Å[48]
Neutrons	0.5 - 3 Å[48]
Electrons	0.0087 - 0.037 Å[170]

Table 2.3 Types of radiation and their usual associated wavelengths.

The elastic scattering of electrons can be described as:

$$\sigma_{atom} = \pi r^2 = \left(\frac{Ze}{V\theta}\right)^2$$

Equation 2.13

Where *e* is the elementary charge. Hence the heavier atoms more strongly scatter electrons than lighter atoms within a crystalline material, similar to the behaviour of X-rays.

Electron beams diffracted within a crystal may undergo a secondary diffraction event, resulting in secondary diffraction. As a consequence, additional reflections can appear, making analysis of the crystalline material more difficult. In order to alleviate this problem somewhat, very thin samples are required, reducing the chances of secondary diffraction occurring. Despite this, ED is a powerful technique, especially reliable for space group identification since kinematically forbidden reflections in XRD can be observed.

Electron radiation can also interact with matter inelastically, causing additional processes, which can be useful in other analytical techniques. Some of these techniques will be discussed in section 2.3.[170]

2.2.6 Powder Diffraction

Since it can be difficult to obtain single crystals for many materials, powder diffraction allows the determination of a crystal structure based on a polycrystalline material. Samples should have a narrow distribution of crystal size and be on the scale of a micron. With each

individual crystal within a sample ideally oriented in a random direction, *hkl* reflections will give a cone shaped diffraction beam, known as the Debye-Scherrer cone, with contribution coming from many crystals. This has been illustrated in the schematic diagram in Figure 2.4. Typically, in powder diffraction experiments, intensity of the diffracted beam is measured as a function of 2θ.

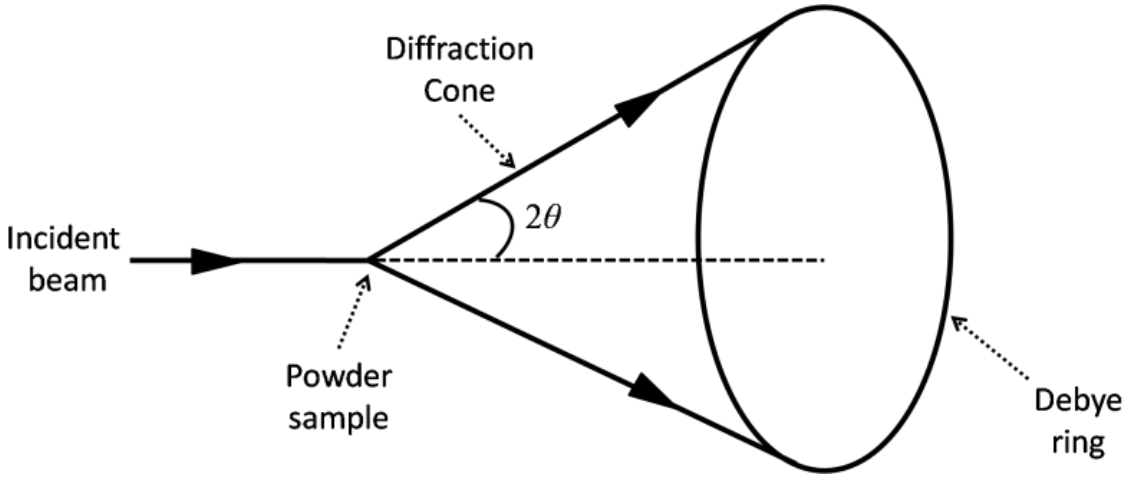

Figure 2.4 Schematic diagram of Debye-Scherrer cone arising through diffraction of incident beam by polycrystalline sample.

A powder diffraction experiment will provide a 1-Dimensional pattern for the 3-Dimensional crystal, which means that allowed reflections with the same (or close) *d*-spacing will lead to peak overlapping, and therefore the peaks will contain intensity contributions from all overlapped reflections.[167]

2.2.7 Rietveld Refinement

Powder (X-ray) diffraction is often used as a quick method for identifying phase purity of samples, with databases of known phases now containing a vast number of structures to be compared against, such as the Inorganic Crystal Structure Database (ICSD).[171] However, with high quality data, structural information can be derived in combination with the Rietveld method, which has been used extensively in this thesis.

The Rietveld method was first developed by H. M. Rietveld in the 1960s for use with neutron diffraction.[172, 173] In this thesis, refinements were carried out using the GSAS package,[174] and Topas Academic V5.[175] The Rietveld method allows structural variables to be refined against observed data, in order to generate a calculated diffraction pattern. A good fit between observed and calculated data can mean that the model is correct, although one has to be careful that the structure is physically and chemically sensible, as well as statistically significant. The method needs a starting model that is reasonably accurate in modelling the crystal structure. The difference between the experimental diffraction pattern and the theoretical pattern is expressed as a residual function, S_y:

$$S_y = \sum_i w_i \, (y_i^{obs} - y_i^{calc})^{\,2}$$

Equation 2.14

$$w_i = \frac{1}{\sigma^2(y_i^{obs})}$$

Equation 2.15

Where y_i^{obs} and y_i^{calc} are observed and calculated intensities at the *i*th step, w_i is the weight of the squared difference in intensities. σ is the uncertainty estimate of y_i^{obs},[176, 177] shown in Equation 2.15. The calculated intensity, y_i^{calc}, is determined by summing all contributions to the Bragg reflections for the structure factor, F_{hkl}, for the proposed structural model. This can be expressed as follows:

$$y_i^{calc} = y_i^b + s \sum_{hkl} L_{hkl} P_{hkl} A |F_{hkl}|^{\,2} \varphi(2\theta_i - 2\theta_{hkl})$$

Equation 2.16

Where y_i^b is the background intensity, typically generated by a separate polynomial function, s is a scale factor, L_{hkl} is a combined Lorentz factor for polarisation and multiplicity, P_{hkl}

describes preferred orientation, A is an absorption factor for the sample and $\varphi(2\theta_i - 2\theta_{hkl})$ is a profile function that describes peak shape.

When user defined parameters of a starting model are refined and good convergence is obtained between observed data and calculated model, the y_i^{calc} is incorporated into the residual function (see Equation 2.14), then minimised through least squares methods.

In a Rietveld refinement, firstly all non-structurally related parameters should be considered, such as zero shift, background and profile function, as well as lattice parameters. These parameters can be difficult to fit however, if the starting structural model is far from the actual structure, giving a poor fit. One way of temporarily ignoring the structural model is by fitting the data by Le Bail[178] or Pawley[179] procedures, with the latter used in this thesis. Peak positions can be fit by refining the lattice parameters and zero shift. The background intensity is usually fit with a polynomial function. The peak profile parameters can also be refined at this point before importing structural information for refinement by the Rietveld method, giving a better starting point. It is also one way to show the best fit that should be attainable for a particular data set prior to performing a Rietveld refinement, as it just fits intensity to peaks without considering structural parameters. When refining structural parameters that control peak intensities (fractional coordinates, thermal displacements, site occupancies) depending on the differences between starting model and observed data, parameters may need to be refined in different orders from refinement to refinement.

After each iteration, the quality of the fit should be scrutinised, with care being taken regarding the physical meaning of refined values for the structural model. The quality of the refinement can be evaluated through statistical outputs known as *R*-factors. The profile factor, R_P, is defined as:

$$R_P = \frac{\sum_i \left| y_i^{obs} - y_i^{calc} \right|}{\sum_i y_i^{obs}}$$

Equation 2.17

The weighted profile *R*-factor, R_{wp}, is the most straightforward statistical parameter that comes directly from the residual function seen in Equation 2.14:

$$R_{wp} = \sqrt{\frac{\sum_i w_i \, (y_i^{obs} - y_i^{calc})^{\,2}}{\sum_i w_i \, y_i^{obs\,2}}} = \sqrt{\frac{S_y}{\sum_i w_i \, y_i^{obs}}}$$

Equation 2.18

The best possible R_{wp} for a specific data set that can be obtained is called the expected *R*-factor, R_{exp}, which is given in the following equation:

$$R_{exp} \sqrt{\frac{N_{obs} - N_{var}}{\sum_i w_i (y_i^{obs})^2}}$$

Equation 2.19

Where N_{obs} is the number of observations and N_{var} is the number of refined parameters. In typical powder diffraction experiments, we expect N_{obs} to be much greater than N_{var}. If a refined model gave a perfect fit, with only difference occurring due to statistical variation, the R_{exp} would represent the R_{wp}. The parameter for goodness of fit, χ, can be defined in terms of R_{exp} and R_{wp}:

$$\chi^2 = \left(\frac{R_{wp}}{R_{exp}}\right)^2$$

Equation 2.20

Since the R_{exp} should not be greater than R_{wp}, the χ^2 should always be ≥ 1. Under certain conditions however, the χ^2 can be misleadingly low, such as when too many variables are being used. When a sufficient number of data points have been collected and counting time has been carried out so that the data is not dominated by a high background intensity, y_i^b (see Equation 2.16), a $\chi^2 < 2$ should be obtained for a good structural model.

Despite the importance of the statistical fit factors, it remains vitally important to inspect the refined pattern and compare it to the observed pattern, as it can show where the misfits occur, and what parameters need to be refined. The structural model also needs to be considered, making sure that the model is chemically sensible.[167]

2.2.8 Laboratory X-ray Sources

X-ray generation occurs when a tungsten metal filament is heated, which as a result produces electrons that are accelerated through a voltage of 40 kV towards a metal target, commonly Cu or Co. Only a Co target was utilised for samples analysed in this thesis. When the electrons that bombard the metal target are of sufficient energy, they ionise core 1*s* *K*-Shell electrons. An electron from an outer orbital will then fill the vacancy, which is accompanied by the emission of an X-ray photon with an energy corresponding to the energy gap between the two electronic states. A 2*p* electron filling in the 1*s* gives rise to K_α radiation, with 3*p* to 1*s* giving rise to K_β radiation. K_α radiation is in fact a doublet due to spin orbit coupling, which gives rise to radiation with two discrete wavelengths. A monochromator is used in order to select a specific wavelength.

For all newly synthesised samples produced for this thesis, initial characterisation was carried out by use of laboratory powder X-ray diffraction, PXRD. It was mostly utilised to investigate phase purity, as well as determine lattice parameters, especially for doped samples that may show variation on incorporation of dopant.

For this thesis, a Panalytical X'Pert Pro diffractometer was employed, with a Co source using a monochromator selecting K_α radiation of λ = 1.7890 Å. It was used in reflection Bragg Brentano geometry and operated at 40 kV and 40 mA. Samples were mounted on glass slides by applying small amounts of silicon grease.

2.2.9 Synchrotron Radiation

Synchrotrons are a source of very high flux electromagnetic radiation. Electrons produced by an electron gun are accelerated to relativistic speeds by particle accelerators, before entering a

huge storage ring. The electrons are turned and accelerated by huge bending magnets, emitting polarised radiation which is extracted to an experimental beamline.

Synchrotron data were collected from the I11 beamline at Diamond, the Rutherford Appleton Laboratories for materials investigated in this thesis.[180] The instrument produces its highest beam flux at between 0.6 - 1.1 Å. The X-ray beam is monochromated by a liquid nitrogen cooled Si(111) double crystal monochromator. The instrument operates in Debye-Scherrer geometry and features a Mythen position sensitive detector (PSD) that allows for the capture of a full resolution diffraction pattern in seconds. There is also a Multi-Analyser Crystal (MAC) detector for higher resolution data collection, although longer acquisition times are required (30 - 60 minutes for materials used in this thesis).

The beamline also features a hot air blower that enables the heating of a sample between room temperature and 1000 °C. This was used in chapters 3 and 4 of this thesis, to calculate lattice parameter evolution at variable temperatures.

2.2.10 Neutron Sources

The generation of neutrons for diffraction requires either a reactor source or spallation source, and therefore requires specialised facilities in order to carry it out. For the work carried out in this thesis, data were collected at the ISIS facility (Rutherford Appleton Laboratories), which uses a spallation source. Spallation does not produce a continuous beam due to the neutrons being generated through collisions of a high energy particle with a heavy metal target (ISIS uses W target). The collisions result in the destruction of the metal nucleus into a few smaller nuclei and high energy neutrons, which are extracted to experimental beamlines. Due to the pulsed neutron beam, diffraction experiments are conducted in energy dispersive mode with detectors at fixed angles. This is known as time of flight (TOF) diffraction.

The High Resolution Powder Diffractometer (HRPD)[181] has the highest resolution available at ISIS, with a $\Delta d/d$ resolution of ~ 4×10^{-4}, allowing peaks to be separated that result from small unit cell changes. As resolution increases with distance, HRPD is the furthest beamline from the target, situated 100 m away. At this distance however, slower neutrons from one pulse can be caught by faster neutrons from the next pulse, and therefore choppers are used to

only allow one in five neutrons to reach the instrument. This results in lower neutron flux compared to other beamlines at ISIS, and the experiment may need longer counting times.

For Chapter 3 of this thesis, ND data were collected from the backscattering ($2\theta = 168°$, *d*-spacing range 2.6 to 0.65 Å), $2\theta = 90°$ (*d*-spacing range 4.0 to 0.85 Å) and $2\theta = 30°$ (*d*-spacing range 10 to 2.6 Å) banks on the HRPD instrument.

POLARIS[182] is a medium resolution high intensity neutron beamline, which allows for faster data acquisition, or alternatively, the measurement of smaller samples. As well as collecting data on samples in Vanadium cans (as for HRPD), data were also collected on samples in glass capillaries for materials characterised in chapters 4 and 5, because of limited sample availability.

For Chapters 4 and 5, ND data were collected from the very low angle ($2\theta = 13° - 15°$, *d*-spacing range 0.5 - 21.0 Å), low angle ($2\theta = 28° - 42°$, *d*-spacing range 0.5 - 8.15 Å), $2\theta = 85° - 95°$ (*d*-spacing range 0.3 - 4.1 Å) and backscattering ($2\theta = 130° - 160°$, *d*-spacing range 2.6 to 0.65 Å) banks (or banks 2, 3, 4 and 5 respectively) on the POLARIS instrument.

Neutron powder diffraction (ND) is complementary to PXRD and has been used in combined refinements for materials studied in this thesis, taking advantage of the different scattering factors of neutrons and X-rays by atoms.

2.3 Electron Microscopy Techniques

2.3.1 General Electron Microscopy

Electron microscopy makes use of a beam of electrons to illuminate a sample and produce an image at much higher magnification and resolving power when compared to an optical microscope. This is possible as electrons have a much shorter wavelength ($\sim 10^{-12}$ m) when compared to that of visible light ($\sim 6 \times 10^{-7}$ m) used by optical microscopes. Resolution is the smallest distance we can distinguish two points. The shorter the wavelength, according to the Rayleigh criterion below, the greater the resolution that is possible:

$$\delta = \frac{0.61\lambda}{\mu sin\beta}$$

Equation 2.21

Where μ is the refractive index of a viewing medium and β is the semi-angle of the collecting lens. This explains why it should be possible to achieve higher resolution with electrons than with visible light.

The term electron microscope was first used in a paper by Knoll and Ruska in 1932, where they demonstrated the first electron images taken, for which Ruska received the Nobel Prize over 50 years later.[183] Electron microscopes use electromagnetic or electrostatic lenses to control the path of electrons. The basic lens would consist of a coil of wire around a tube, from which a current can be passed, inducing a magnetic field. Through changing the current, the magnetic field can be altered, enabling electrons to be controlled as they pass through as they possess a magnetic moment.

2.3.3 Scanning Electron Microscope (SEM)

An SEM produces images through the detection of secondary electrons and backscattered electrons, which are emitted from the surface due to excitation by the primary electron beam. SEM allows for the imaging of the topology of the surface of a sample. There is also the possibility of using other techniques such as energy dispersive X-ray spectroscopy (EDX) on an SEM, which can provide elemental compositions of samples (see section 2.3.7 for EDX).

For this thesis, a Hitachi S-4800 scanning electron microscope was used for analysis of symmetrical cells of cathode and electrolyte in chapter 3. EDX spectra were also collected on these same samples, with the experiments being carried out by J. Gallagher.

2.3.4 Transmission Electron Microscope (TEM)

The use of a TEM involves a high voltage electron beam illuminating a thin sample and being partially transmitted. The electron beam is a type of ionising radiation that will interact with a sample and produce a wide range of secondary signals. These have been summarised below in Figure 2.5.

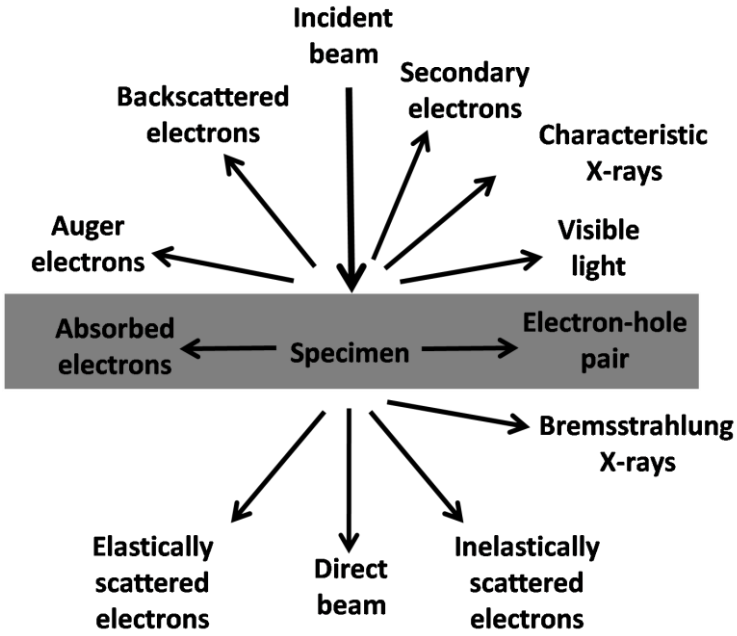

Figure 2.5 Signals generated when high energy beam of electrons interacts with a thin specimen (sample).

Many of the signals generated can be used analytically, such as EDX and electron energy loss spectroscopy (EELS). The resolution of TEM allows individual crystals to be imaged, allowing information to be collected for single phases even within multiphasic samples.[170]

In this thesis, TEM work has been carried out using a JEOL JEM 2000FXII TEM/STEM operating with a W electron source operated at 200 keV, a JEOL JEM 3010HR TEM/STEM with a LaB_6 electron source operated at 300 keV and a JEOL JEM 2100FCs 200 keV aberration corrected field emission TEM/STEM. All samples were prepared onto carbon coated Cu grids in through grinding in methanol to create a suspension, which was applied

drop wise onto the grid using a pipette. The grids were thoroughly dried before introducing them into the TEMs.

2.3.5 Selective Area Electron Diffraction (SAED)

For an electron diffraction (ED) experiment, diffracted electrons from the specimen are focused by the objective lens and a diffraction pattern is created in the back focal plane as seen in Figure 2.6. The electrons are then recombined to form an image in the image plane. This diffraction image gives direct crystallographic information about small areas of the specimen.

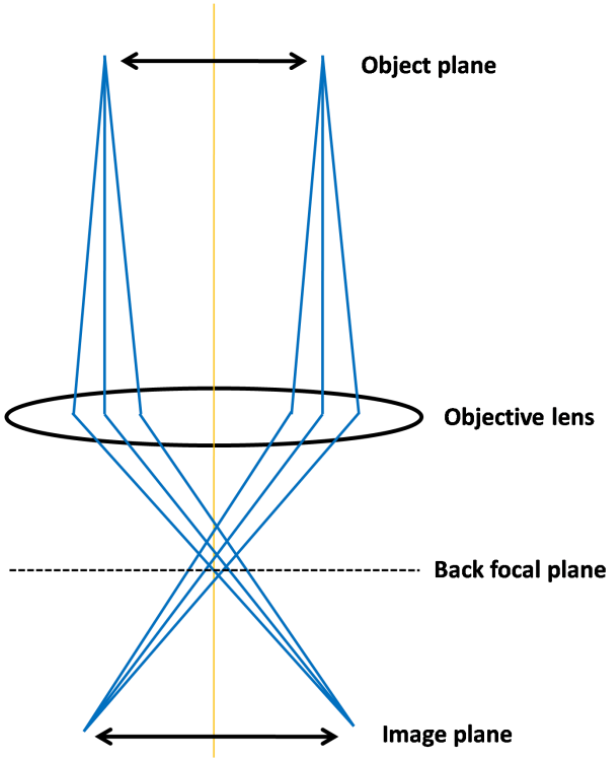

Figure 2.6 Path of diffracted electrons in a TEM.

In SAED, a selected area aperture is inserted into the image plane of the objective lens, which essentially excludes any electrons that do not pass through this aperture. Only electrons diffracted from a smaller area of the specimen will contribute to the diffraction pattern,

helping to improve the contrast of the image. Through rotating a crystal, and analysing the diffraction patterns from different planes, cell parameters, reflection conditions and consequently space groups in agreement with the conditions can be identified.[170]

2.3.6 High Angle Annular Dark Field Scanning transmission Microscopy (HAADF-STEM)

In scanning transmission electron microscopy (STEM), the specimen is scanned by a tiny electron beam. In the case of bright field (BF) imaging, a BF detector is inserted onto the axis of the microscope where it intercepts the direct beam electrons. For dark field (DF) imaging, scattered electrons, rather than direct beam electrons are collected. When the DF detector surrounds the BF detector, which allows for detection of scattered electrons, this is known as an annular (A)DF detector. The ADF image is complementary to the BF image in which it sits around. When using a high angle (HA)ADF detector, Z-contrast images of atoms can be collected, where the contrast of an atom is ~ Z^2. The general detector set up in an STEM is shown in Figure 2.7. [170] In chapter 3 of this thesis, HAADF has been used to confirm A-Site cation ordering of a long axis perovskite material.

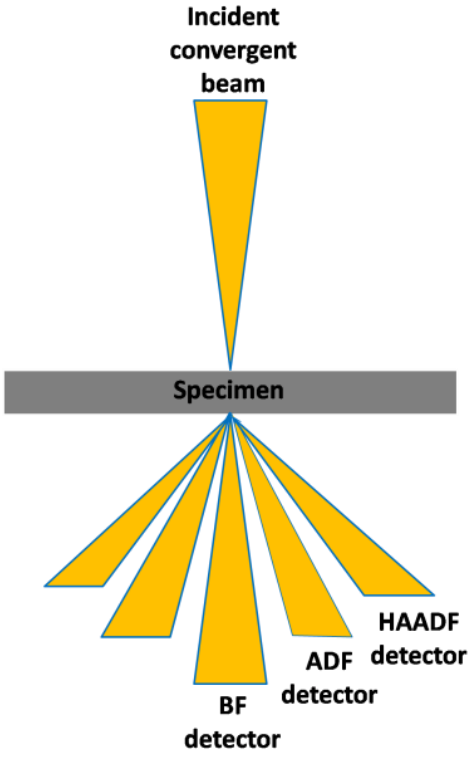

Figure 2.7 Schematic of detector set up for imaging in an STEM.

2.3.7 Energy Dispersive X-Rays (EDX)

As shown previously in Figure 2.5, when the ionising electron radiation interacts with a specimen, many secondary processes can occur. One is the emission of X-rays, with energy characteristic of the chemical element. Detection of these X-rays allows for the quantification of elements present by extraction of the relative intensities of the distinct X-ray energies.

EDX using a TEM has been used widely in this thesis for the determination of phase composition, as well as that of impurities that may be present. In order to improve the accuracy of the compositional measurement, many individual crystals had their composition analysed, so that a statistical average could be taken for a particular sample. EDX can also show up compositional inhomogeneities if elemental composition varied greatly from particle to particle.[170]

2.4 Thermogravimetric Analysis (TGA)

Thermogravimetric analysis (TGA) measures weight changes as a function of temperature and time. While a material undergoes heating, a loss of mass can occur due to dehydration, or the loss of compounds such as CO_2, which may have been adsorbed onto the surface of the material. For dry metal oxides such as those discussed in this thesis, TGA is a useful technique that can be used to monitor weight changes that can be related oxygen loss and therefore the related changes in oxidation state of transition metals present that would accompany this. TGA can be used as a complementary test to determine if a phase is stable, through the presence of a hysteresis, or not stable for a permanent weight change on thermal cycling. For example, if a dry metal oxide loses mass on heating but does not gain the same mass on cooling, this could indicate phase change due to reduction of the sample. It could also indicate the volatility of elements present depending on their nature.[48]

In this thesis, TGA measurements were carried out using a TA Instruments Q600 thermal analyzer. In each case, the experiment was undertaken using 100 - 200 mg of hand ground sample in a Pt crucible and heated from 50 °C to 800 °C with a dwell time of one hour at 800 °C with a gas flow rate of 100 ml per minute (10 % N_2, 90 % compressed air, instrument standard). Heating and cooling rates of 3 °C per minute were used and the experiments were

cycled at least twice to ensure reproducibility. Calibrations were run by measuring ZrO_2 as the standard material, which should not show any mass loss between 50 - 800 °C.

2.5 Mössbauer Spectroscopy

Mössbauer spectroscopy[184] is a technique that measures the absorption of γ-rays by atomic nuclei in a material. Where absorption is observed, information about the target nuclei can be discerned. Splitting of the nuclear energy levels can also be caused by the absorption of *γ*-rays. The effects of this can be observed in many nuclei, but sensitive information on the solid state environment can be observed only in a few cases (^{57}Fe, ^{119}Sn and ^{121}Sb). The most sensitive among these is ^{57}Fe, which has an abundance of ~ 2 % in natural Fe.

In a typical experiment, a beam of ^{57}Fe 14.4 keV *γ*-rays produced from a radioactive ^{57}Co source held in a solid state matrix are used to resonantly excite the 14.4 keV state in the nucleus of the ^{57}Fe isotope of the absorber (sample) under investigation. When the source moves into ranging velocity with respect to the absorber, the energy of the emitted *γ*-rays is modified according to the Doppler effect. The absorbance of the *γ*-rays, is typically quoted across a range of velocities of the source motion (mm/s) and the zero shift, known as the chemical shift.

The absorption of *γ*-rays is dependent on them having an appropriate energy to excite the target samples atomic nuclei. Mössbauer spectroscopy is typically calibrated with a standard, with bcc Fe metal used for spectra collected for this thesis. The chemical shift is influenced by the local environment of atoms, such as coordination number and oxidation state, which are refinable parameters from a Mössbauer spectra data set.

In a magnetically ordered material, hyperfine splitting of nuclear energy levels results in a spectrum containing a sextet, whereas for paramagnetic materials, only quadrupole coupling occurs resulting in a doublet being observed as shown in Figure 2.8.

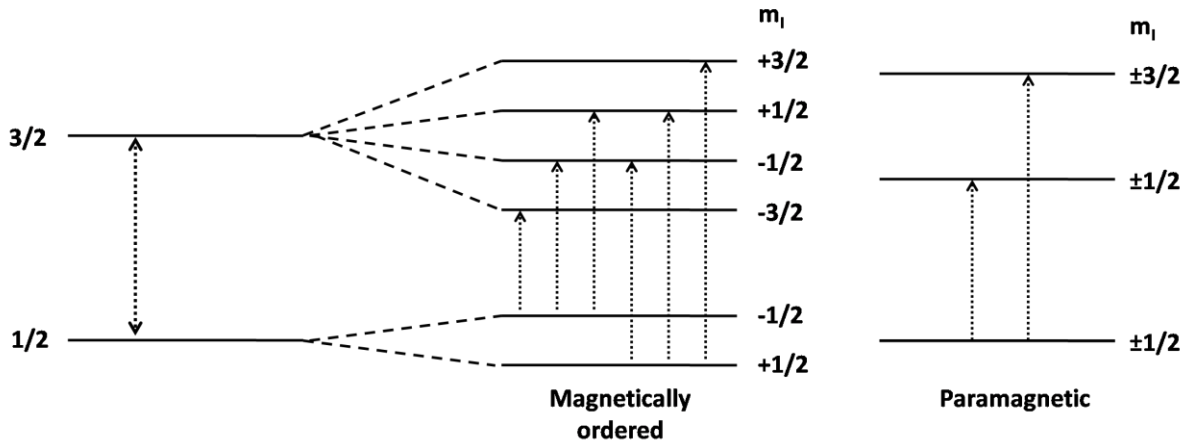

Figure 2.8 Schematic diagram of nuclear energy level splitting in magnetically ordered and paramagnetic materials, measured by Mössbauer spectroscopy.

Through fitting of data collected by Mössbauer spectroscopy, information can be discerned about the Fe oxidation state or even the coordination environment that it is found in. In this thesis (Chapter 3), Mössbauer spectroscopy was carried out at 300 K, using a conventional acceleration Mössbauer spectrometer incorporating a ≈25 mCi source of ^{57}Co in a Rh matrix. Data were collected and fitted by Dr M Thomas in the Department of Physics, University of Liverpool.

2.6 Iodometric Titrations

Titrations can provide quantitative information about a chemical substance under investigation. The technique is dependent on the addition of a precisely known quantity of standardised compound, indicated by such occurrences as a colour change or change in conductivity, defining the endpoint of a reaction. As a standard is required that is well characterised, information can be calculated for the sample due to the physical change that occurs in the sample, induced by the addition of the standard compound. [185]

In this thesis, iodometric titrations were performed to determine the oxygen content that corresponded to the sample prepared in chapters 3, 4 and 5. Approximately 50 mg of material was dissolved in 60 ml of 1 M hydrochloric acid with an excess of potassium iodide (Equation 2.22), in an argon atmosphere. Upon complete dissolution, the solution was titrated

with 0.1 M sodium thiosulphate (Equation 2.23). As sodium thiosulphate was added, the solution turned from orange to clear; starch was added just before the end point, turning dark purple before titrating to clear for the end point.

$$2B^{(n)+} + 2\mathrm{I}^- \longrightarrow 2B^{(\mathrm{n}-1)+} + \mathrm{I}_2$$

Equation 2.22

$$\mathrm{I}_2 + 2S_2\mathrm{O}_3^{2-} \longrightarrow 2\mathrm{I}^- + \mathrm{S}_4\mathrm{O}_6^{2-}$$

Equation 2.23

Prior to titrations, the sodium thiosulphate was standardised by titrating against potassium iodate (Equation 2.23 and Equation 2.24), which was dissolved in distilled water with potassium iodide and 1 M sulphuric acid. Titrations were repeated three times to ensure reproducibility, with the spread used to calculate a standard deviation.

$$\mathrm{IO}_3^- + 5\mathrm{I}^- + 6\mathrm{H}^+ \longrightarrow 3\mathrm{I}_2 + 3\mathrm{H}_2\mathrm{O}$$

Equation 2.24

The oxygen content (*O*) of a sample is calculated using the following equation:

$$O = \frac{M_{red}}{\frac{m_{MO}}{n_{ex}} - M_{oxy}} + O_{red}$$

Equation 2.25

Where M_{red} is the molecular mass of the reduced sample being titrated, m_{MO} is the starting mass of the sample, n_{ex} is the number of moles of oxygen generated, M_{oxy} is the molar mass

of oxygen (experimentally determined from the quantity of sodium thiosulphate used) and O_{red} is the oxygen content of the reduced sample.[185]

Iodometric titrations were carried out on samples discussed in chapters 3, 4 and 5 of this thesis.

2.7 Cathode Stability and Chemical Compatibility Testing

2.7.1 Thermal Stability

Thermal stability tests were performed on samples prepared in chapters 3, 4 and 5 of this thesis. Tests were carried out in order to determine how the phases change under thermal treatment. Around 50 mg of sample was pressed into 5 mm pellets using a uniaxial press, applying 0.5 tons force. Thermal treatment was then carried out by annealing at 750 °C for five days to simulate IT-SOFC operating temperatures. Annealing was also carried out at 950 °C for five hours to simulate temperatures required to get a cathode ink to adhere to an electrolyte substrate as required for measurement of the electrochemical properties (see section 2.10.2 for cathode inks). Post thermal treatment, the samples were hand ground and laboratory PXRD patterns were collected in order to determine if decomposition had occurred, or to evaluate if lattice parameters varied significantly. In order to "pass" the test, decomposition of the phase under investigation must not have occurred and lattice parameters should not vary significantly.

2.7.2 CO_2 Tolerance

The CO_2 stability tests can indicate if a phase is likely to react with CO_2 in the atmosphere and decompose over longer timescales. CO_2 tolerance is essentially an additional stability test that is complementary to the thermal stability test. In this thesis, this stability test was carried out for samples in chapters 3 and 4.

Powder samples (to ensure a large surface area is exposed) were annealed in a tube furnace at 750 °C under an atmosphere of 100 % flowing CO_2. Since the phases discussed in this thesis contain large amounts of Ba and Sr, there is the possibility for the formation of carbonates, which could lead to the loss of the main phase.[37] Samples were hand ground and analysed by laboratory PXRD post CO_2 treatment, with lattice parameters and any phase decomposition determined.

2.7.3 Chemical Compatibility

Chemical compatibility between a cathode and an electrolyte material is important for SOFCs as these components are in contact in the device. Reactivity between the phases under operating conditions must be determined as reaction could lead to phase decomposition or new phase formation that may be detrimental to performance.

In this thesis, chemical compatibility tests were carried out between the cathode materials prepared in chapters 3, 4 and 5, and state-of-the-art electrolytes $Ce_{0.9}Gd_{0.1}O_{1.95}$ (GDC, Fuel Cell Materials), $Ce_{0.8}Sm_{0.2}O_{1.9}$ (SDC, Fuel Cell Materials) and $La_{0.9}Sr_{0.1}Ga_{0.8}Mg_{0.2}O_{2.85}$ (LSGM, PI-KEM LTD). Cathode and electrolyte were mixed in a weight ratio 1:1 by hand grinding, pressed into 5 mm pellets using a uniaxial press (to increase particle contact and enhance potential reactivity) and annealed at 750 °C for five days and 950 °C for five hours. Again, post annealed samples were hand ground and analysed by laboratory PXRD in order to check for any eventual reaction between phases. Lattice parameter shifts are particularly important here as they may indicate cation diffusion between phases, although this may or may not be detrimental to performance.

2.8 Densification

In order to carry out DC conductivity and dilatometry measurements, firstly a dense pellet/bar of sample is prepared. To attain a sample of high relative density, ballmilled powder of decreased particle size was uniaxially pressed into pellets and isostatically pressed (Autoclave Engineers Cold Isostatic Press) at 200 MPa, before sintering. The achieved

density was greater than 95 % theoretical density for all materials discussed in this thesis. For AC impedance, electrolyte substrates were prepared by pressing commercially available powders of the respective oxides in a uniaxial press, followed by sintering at 1400 °C for 24 hours, resulting in greater than 98 % theoretical density.

Density measurements were carried out using an Archimedean balance, where the mass of a pelletized sample is collected "dry" (m_1), immersed in water (m_2) and after removal from the water, with the surface carefully dried with a non-absorbent material (m_3). The density (ρ) was calculated using the following equation:

$$\rho = \frac{m_1}{m_3 - m_2} \times \rho_{H_2O}$$

Equation 2.26

Where ρ_{H_2O} is the density of water, 0.997 g/cm^3 at 25 °C. This measured density was divided by the theoretical density of the phase in question in order to determine the percentage of theoretical density and therefore relative porosity of the pellet.

2.9 Thermal Expansion Coefficient (TEC) Measurements

2.9.1 VT-SXRD

In order to calculate the thermal expansion coefficient (TEC), variable temperature SXRD data were collected for samples on the I11 beamline at Diamond, the Rutherford Appleton Laboratories. The sample contained within a quartz capillary was heated in situ using a Cyberstar hot air blower, which has an operational temperature range of RT - 1300 K. SXRD data were collected every 50 °C from 200 °C, up to a maximum of 600 °C. The collected data were fitted using the Rietveld method, at each temperature. The linear TEC (α_L) can be calculated from the lattice parameters at each temperature using Equation 2.27 below:

$$\alpha_L = \frac{1}{L_o}\frac{\Delta L}{\Delta T}$$

Equation 2.27

Where L_o is initial length of lattice parameter, ΔL is change in length for a given change in temperature, ΔT. For anisotropic materials such as those studied in this thesis, it is necessary to calculate volumetric TEC (α_V) so that it can be compared with that of isotropic materials, such as many state of the art electrolytes that the TEC has to match closely with. The α_V of an isotropic material can be calculated using Equation 2.28, with that of anisotropic orthorhombic materials calculated using Equation 2.29.

$$\alpha_V = 3\alpha_L$$

Equation 2.28

$$\alpha_V = \alpha_{La} + \alpha_{Lb} + \alpha_{Lc}$$

Equation 2.29

Where α_{La}, α_{Lb} and α_{Lc} are the linear TEC for each axis of a material with an orthorhombic unit cell.

2.9.2 Dilatometry

Complementary to the TEC obtained by VT-SXRD data analysis, dilatometry has been used for the same purpose. A dilatometer measures the physical changes in length of a sample under heating and cooling.

In order to attain a sample with sufficient density, ballmilled powder was pressed into a 6 mm pellet, as described in section 2.8. The pellet was then sintered for 12 hours, which produced bar of ~ 7 mm long x 5 mm diameter. An Archimedean balance was used to confirm a sample

of greater than 98 % of the theoretical density. The thermal expansion of the pellet was then measured using a NETZSCH DIL 402 C dilatometer between 25 °C and 900 °C with a heating and cooling rate of 3 °C per minute. Prior to the sample measurement, a calibration was run using a known standard material with a known TEC (Al_2O_3), with the same length as the measured sample (± 5 %) in order to correct for instrumental factors and expansion. Crystals in the samples are considered to have random orientations, the TEC is then an average α_L for each axis of the orthorhombic material. Using Equation 2.28, the α_V can be calculated and compared to that obtained via VT-SXRD. This was carried out and discussed in chapter 4.

2.10 Electrochemical Characterisation

2.10.1 Four probe DC conductivity

The electrochemical properties of the materials studied in this thesis were determined by two methods. Here we discuss the four-probe direct current (DC) method for determination of the total electrical conductivity of a material.

The electrical conductivity (σ) is defined as the inverse of the electrical resistivity (ρ), which is the property that describes how a material resists the flow of an electric current. Equations describing σ and ρ are as follows:

$$\rho = \frac{R \times A}{l}$$

Equation 2.30

$$\sigma = \frac{1}{\rho}$$

Equation 2.31

Where R (Ω) is the measured resistance, A (m^2) is the area of the sample and l (m) is the length of sample. Where V is voltage experienced by an electric current, I, that flows through it, the resistance according to Ohm's law is as follows:

$$R = \frac{V}{I}$$

Equation 2.32

The four probe DC method requires only quite a simple set-up, with voltage measured as a current is passed through the sample. From the observed *R*, the conductivity can be easily calculated using Equation 2.30, Equation 2.31 and Equation 2.32. The four probe set up, shown in Figure 2.9, consists of two inner probes to measure *V* and two outer *I* probes. Separation of the *I* and *V* electrodes eliminates contribution from wiring and contact resistances.[186]

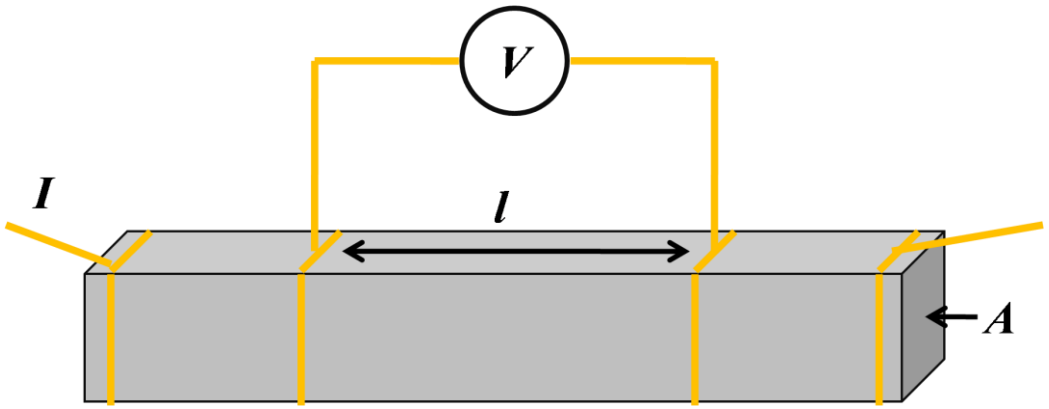

Figure 2.9 Schematic diagram of the arrangement of the electrical resistance measurements using the four probe DC conductivity technique.

As discussed in section 2.8, a dense pellet was first prepared in order to measure the DC conductivity. The dense sintered pellets were cut into bars, giving dimensions of roughly 2 × 2 × 10 mm, before attaching gold wire to the bar with gold paste (Koartan) to make the I-V probes with four-in-a-line contact geometry. DC conductivity was then measured using the standard four-probe method (Keithley 2182 Nanovoltmeter and Keithley 220 Current Source), with data for *R* versus temperature collected.

2.10.2 AC Impedance Spectroscopy

AC impedance spectroscopy was used to evaluate the electrochemical behaviour of a material, which takes into account many processes that contribute to the overall resistance of a material. It is usually measured by applying a single frequency sinusoidal AC voltage to a sample and measuring the current through the cell.

$$V(t) = V_m sin(\omega t)$$

Equation 2.33

$$I(t) = I_m sin(\omega t + \theta)$$

Equation 2.34

Where $V(t)$ and $I(t)$ are signals of voltage and current at time (t), V_m and I_m are their magnitude, θ is the phase difference and ω is the radial frequency (related to the frequency by $\omega = 2\pi f$). The impedance (Z) is then defined by relation to Ohm's law through a ratio between current (I) and voltage (V).

$$Z(\omega) = \frac{V(t)}{I(t)} = \frac{V_m sin(\omega t)}{I_m sin(\omega t + \theta)} = Z_m \frac{\sin(\omega t)}{sin(\omega t + \theta)}$$

Equation 2.35

Where Z_m is the impedance magnitude. Frequency dependant impedance, $Z(\omega)$, is expressed as a complex number with real (Z') and imaginary (Z'') parts:

$$Z(\omega) = |Z_m|e^{(-j\theta)} = |Z_m|cos(\theta) + j|Z_m|sin(\theta) = Z' + jZ''$$

Equation 2.36

For phase angle:

$$\theta = tan^{-1}\left(\frac{Z''}{Z'}\right)$$

Equation 2.37

And Magnitude:

$$|Z_m| = \sqrt{(Z')^2 + (Z'')^2}$$

Equation 2.38

Where j is an imaginary number = $\sqrt{-1}$. Using this nomenclature, the basic electrical elements of capacitor (C), inductor (L) and resistor (R) are defined as:

$$Z(\omega) = 0 + \frac{1}{j\omega C}$$

Equation 2.39

$$Z(\omega) = 0 + j\omega L$$

Equation 2.40

$$Z(\omega) = R + j0$$

Equation 2.41

In addition to these three basic elements, a constant phase element (CPE) can also be introduced to describe non ideal processes in real systems and is defined as:

$$Z(\omega) = 0 + \frac{A}{(j\omega)^{n}}$$

Equation 2.42

Where A and n are constants. If a *CPE* has $n = 1$ and $A = 1/C$ it is a capacitor, if $n = 0$ and $A = R$ then it is a resistor and if $n = 1$ and $A = L$, then it is an inductor.[187]

When $Z(\omega)$ is measured over a wide range of frequencies, a Nyquist plot of the Z' (x-axis) and Z'' (y-axis) can be produced to display the characteristic impedance arcs, which can be modelled using equivalent circuits based on the defined elements from Equation 2.39 to Equation 2.42.

Different regions of a ceramic sample can be characterised by a R and C, generally in parallel. Each *RC* element in parallel has a characteristic relaxation time (τ), which is related as follows:

$$\tau = RC$$

Equation 2.43

The *RC* elements are separable in the frequency domain due to the relationship of the *RC* element shown to its frequency of maximum loss (ω_{max}), within an impedance spectrum:

$$\omega_{max} RC = 1$$

Equation 2.44

As the *RC* elements can be identified separately, it is possible to assign them to appropriate regions of a sample, with individual R and C components quantifiable.[188]

An example of a typical impedance response from a solid electrolyte is shown below in Figure 2.10, which consists of three *RC* element arc assignments relating to the bulk electrolyte response (R_{bulk}), the grain boundary (R_{gb}) and the electrode blocking response ($R_{electrode}$).

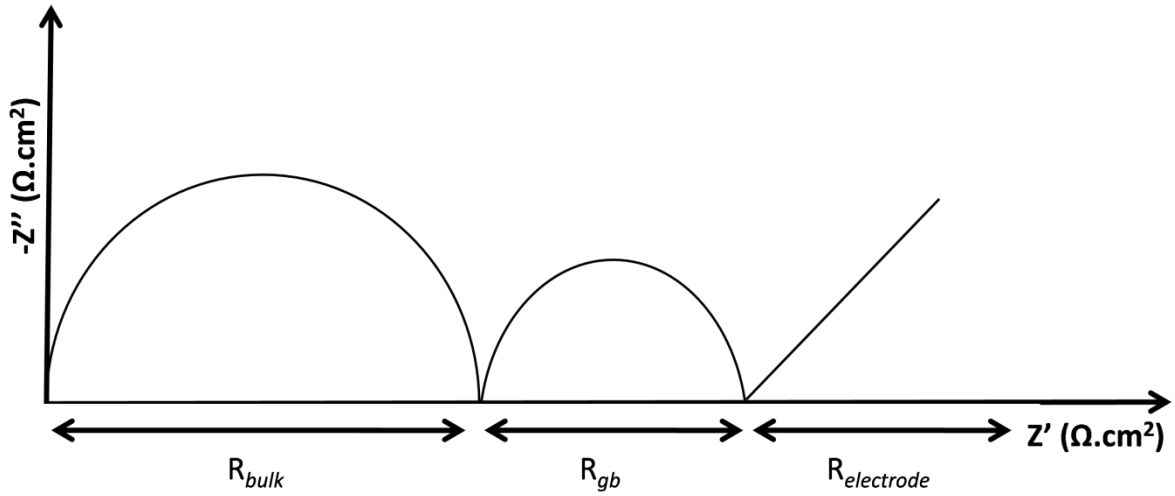

Figure 2.10 Typical Nyquist plot for a thick-film solid electrolyte symmetrical cell.[22]

As in the above example, the combination of a *R* and *C* in parallel is often used to describe the electrochemical behaviour of cathodes. The assignment to physical processes is based on the fact that physical phenomena can relax at very different frequencies, as discussed above. The capacitance can also have typical values for which physical properties can be assigned to, as displayed in Table 2.4.[188]

Capacitance (F)	Physical phenomenon
10^{-12}	Bulk
10^{-11}	Minor second phase
10^{-11} - 10^{-8}	Grain boundary
10^{-10} - 10^{-9}	Bulk ferroelectric
10^{-9} - 10^{-7}	Surface layer
10^{-7} - 10^{-5}	Sample-electrode interface
10^{-4}	Electrochemical reactions

Table 2.4 shows typical capacitance values for electrochemical phenomena.[188]

Often arcs cannot be fitted to a simple *RC* circuit because of deviation from a true capacitor behaviour in a real system. This is frequently the case for electrodes, as the electrodes resistance has a large dependence on the material and microstructure of the electrode. It is therefore fitted with a *CPE* instead of a simple *RC* model:

$$C = (R^{1-n}Q)^{1/n}$$

Equation 2.45

Where Q is the pseudo-capacitance and n is related to the depression angle. If $n = 1$, the *CPE* behaves as a true capacitor. If $n = 0.5$, the impedance spectrum is shown by a straight line, intersecting the real axis by 45°, which can be modelled by a Warburg element and is associated with semi-infinite diffusion.[22]

Once the electrochemical processes have been assigned for a cathode in a symmetrical cell format, the area specific resistance (*ASR*, Ω.cm^2) can be calculated:

$$ASR = \frac{R \times A}{2}$$

Equation 2.46

Where the resistance (R) is normalised for the cathodes surface area (A) and divided by 2 to take into account the cell symmetry. The ASR accounts for electronic conductivity, ionic conductivity, transfer of electrons and ions at interfaces and electrochemical activity per area of the cathode, and can therefore be scaled and directly compared to measured cells of different sizes.[187]

In order to carry out an AC impedance measurement on a cathode to obtain an ASR, symmetrical cells are produced by screen printing a cathode ink on either side of a dense electrolyte substrate, followed by attaching gold current collectors to either side, as shown in the schematic diagram and photograph below in Figure 2.11.

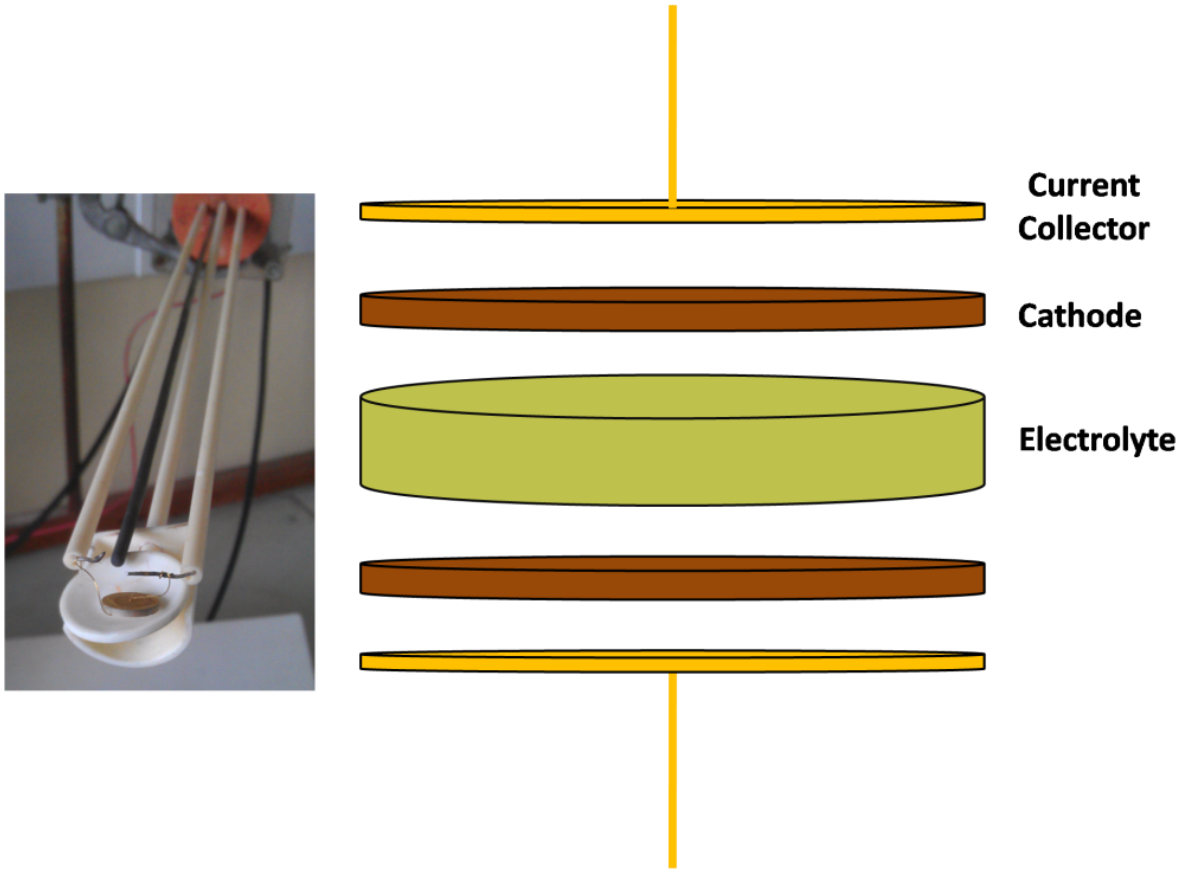

Figure 2.11 Left is a photograph of a symmetrical cell mounted on a holder in preparation for impedance measurement. Right is a schematic of the symmetrical cell formation.

For the preparation of cathode inks, powder samples were milled using a Fritsch pulverisette planetary mill at 350 rpm for 24 hours to reduce particle size and create a greater surface area. 8 5 mm zirconia balls were used as the grinding media in zirconia pots, along with 4 ml of isopropanol per 1 g of sample. Cathode inks were then prepared by ballmilling these powders with an organic binder (Fuel Cell Materials), in the weight ratio 67:33 powder to binder. The electrode ink was applied to both surfaces of the electrolyte substrate by screen printing in one layer. The cell was dried at 100 °C for 1 hour between the application of each layer followed by a final heating in air at 950 °C for 1 hour to achieve good adherence of the electrodes to the electrolyte surface. The contacts for the electrical measurement were gold wire and gauze fixed in position with gold paste, which were attached to the cell by heating to 600 °C for 1 hour.

AC impedance measurements were recorded over the frequency range 1 MHz to 0.01 Hz using a Solartron 1260 FRA with a modulation potential of 10 mV, in static air. The

symmetrical cell was held for 90 minutes at each temperature to allow thermal equilibration, and measurements were made using ZPlot v.2.9b (Scribner Associates) every 50 °C. The area specific resistance (ASR) of the cathode was calculated by fitting the data using ZView2.[189]

2.11 Extended Module Materials Assembly (EMMA)

2.11.1 General method

The Extended Module Materials Assembly (EMMA) approach is a computational method that was used in chapter 3 to identify new candidate structures, as outlined in Figure 2.12. First a set of extended layers (modules) must be chosen, such as Ba_4O_4 + Ca_4O_4 + Y_4 + Y_4O_4 + Fe_4O_8 + Fe_4O_4, based on the studied composition. Next the number of times each module appears within a single repeated unit cell is selected. At this point all possible permutations of the modules within the unit cell are created using chosen structure building operators.

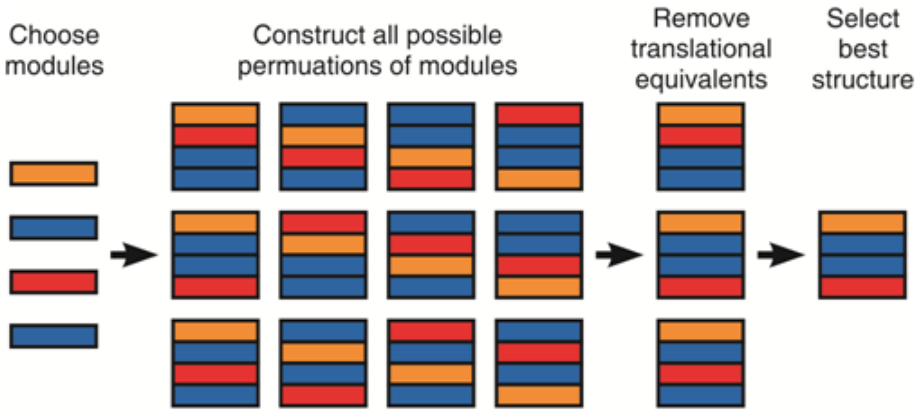

Figure 2.12 Schematic diagram of the EMMA approach.

The number of candidate structures is then reduced by removing structures which are related by translating the modules together within the unit cell. The remaining structures are then ranked according to some suitable selection criteria to give the most promising candidates for experimental isolation. In this case, a preliminary structural relaxation and ranking by energy of a large number of structures by classical force field methods followed by evaluation of the

best candidates using *ab* initio calculations to obtain a quantitative assessment of their relative stabilities was undertaken.

The extended modules encode bonding information directly into the candidate structures before force fields are applied, thus reducing the frequency of force field use in situations where they are not valid. There is no conceptual limit to the nature or size of the modules, although for this thesis it was concentrated on one atom thick metal oxide layers. A practical limit exists on the number of modules within a single repeat, since the total number of permutations becomes very large with more than 15-20 modules. This limitation could be circumvented by using methods such as evolutionary algorithms to search the space of permutations without generating every one. The EMMA method is applicable to the large number of structural families describable in this modular way. The use of modules allows the integration of crystal chemical understanding into the computational search for new structures, and permits the investigation of compositionally and structurally complex large unit cell structures.[197]

2.11.1 Searching a phase diagram

EMMA was used to investigate phase diagrams in chapter 3, where a phase diagram consisting of Y, Ba, Ca, Fe^{3+} and O was searched for layered phases with $7a_p$ long axis repeats using force fields within the EMMA method. The three lowest energy candidate structures for each of the compositions $YBa_2Ca_4Fe_7O_{18}$, $YBa_4Ca_2Fe_7O_{18}$ and $YBa_3Ca_3Fe_7O_{18}$ were chosen, which had the best stability calculated using force fields relative to the ternary oxides $YFeO_3$ + $x$$Ca_2Fe_2O_5$ + $y$$Ba_2Fe_2O_5$, and recalculated using DFT. The lowest energy structure for each composition, were structurally similar, with two T_d Fe layers with opposing orientations and one S_q Fe layer, all separated by O_h Fe layers.[197]

The EMMA method was carried out by M. Dyer, C. Collins and G. Darling for this thesis.

3 Synthesis and Characterisation of the 16a_P, $Y_{2.24}Ba_{2.28}Ca_{3.48}Fe_{7.44}Cu_{0.56}O_{21}$

3.1 Introduction

Previous work within the group carried out by Demont et al. led to the discovery of the compound $Y_{0.9}Ba_{1.7}Ca_{2.4}Fe_5O_{13}$ (10a_p).[35] This perovskite has an ordered *A*-site of Y, Ca and Ba with coordination numbers of 8, 9 and 12 respectively. This leads to Fe only *B*-sites in three different coordination geometries; tetrahedral (T_d), octahedral (O_h) and Square pyramidal (S_q) in a 1:2:2 ratio. The 10a_p phase can be thought of as an intergrowth between two known structures, $YBa_2Fe_3O_8$[65] and $Ca_2Fe_2O_5$,[190] which leads to the extended structure displayed in Figure 3.1.

It has been reported previously in the case of $GdBaCo_2O_{5-\delta}$ (GBCO) that ordering of the *A*-site and formation of oxygen vacancy channels can lead to enhanced cathode performance, through increased ionic conductivity.[191, 192] The structural similarity of GBCO with the 10a_p phase (both containing ordered oxygen vacancies), gave promise of similar properties being displayed.

The 10a_p phase does indeed show potential as a SOFC cathode, due in part to its thermal stability, CO_2 tolerance and chemical compatibility with state-of-the-art electrolytes $Sm_{0.2}Ce_{0.8}O_{1.9}$ (SDC) and $La_{0.8}Sr_{0.2}Ga_{0.9}Mg_{0.1}O_{2.85}$ (LSGM).[99, 193, 194] Additionally, the volumetric thermal expansion coefficient (TEC) of the 10a_p (α_v = 35.4 × 10^{-6} K^{-1}) is very similar to that of SDC ($\alpha_v \approx$ 37.5 × 10^{-6} K^{-1})[157] meaning that the cathode is unlikely to delaminate during operation due to the close match in rate of thermal expansion.

When first published, the 10a_p phase attained an ASR of 0.87 Ω cm^2 at 700 °C, which is a promising value when compared to 0.46 Ω cm^2 for cathode material $La_{0.6}Sr_{0.4}Co_{0.2}Fe_{0.8}O_{3-\delta}$ (LSCF).[94] It had been suggested that a limitation to the ASR of the 10a_p could be due to Fe^{3+} being the only oxidation state present for the transition metal, leading to a low electronic conductivity caused by a lack of charge carriers. As electronic conductivity is essential for cathodes, which are required to transport electrons from an external circuit to an electrochemically active site in order to reduce O_2, a low value could hinder performance.

The electronic conductivity of 2.06 S.cm^{-1} at 700 °C is two orders of magnitude lower when compared to 320 S.cm^{-1} for LSCF at the same temperature.[35, 195] The electronic conductivity of BSCF at 700 °C is ~ 40 S.cm^{-1},[34] and this phase displays the best cathode performance currently known. This suggests that electronic conductivity may not have to be as high that displayed by LSCF, although an increase on 2.06 S.cm^{-1} at 700 °C may still be required for improved performance.

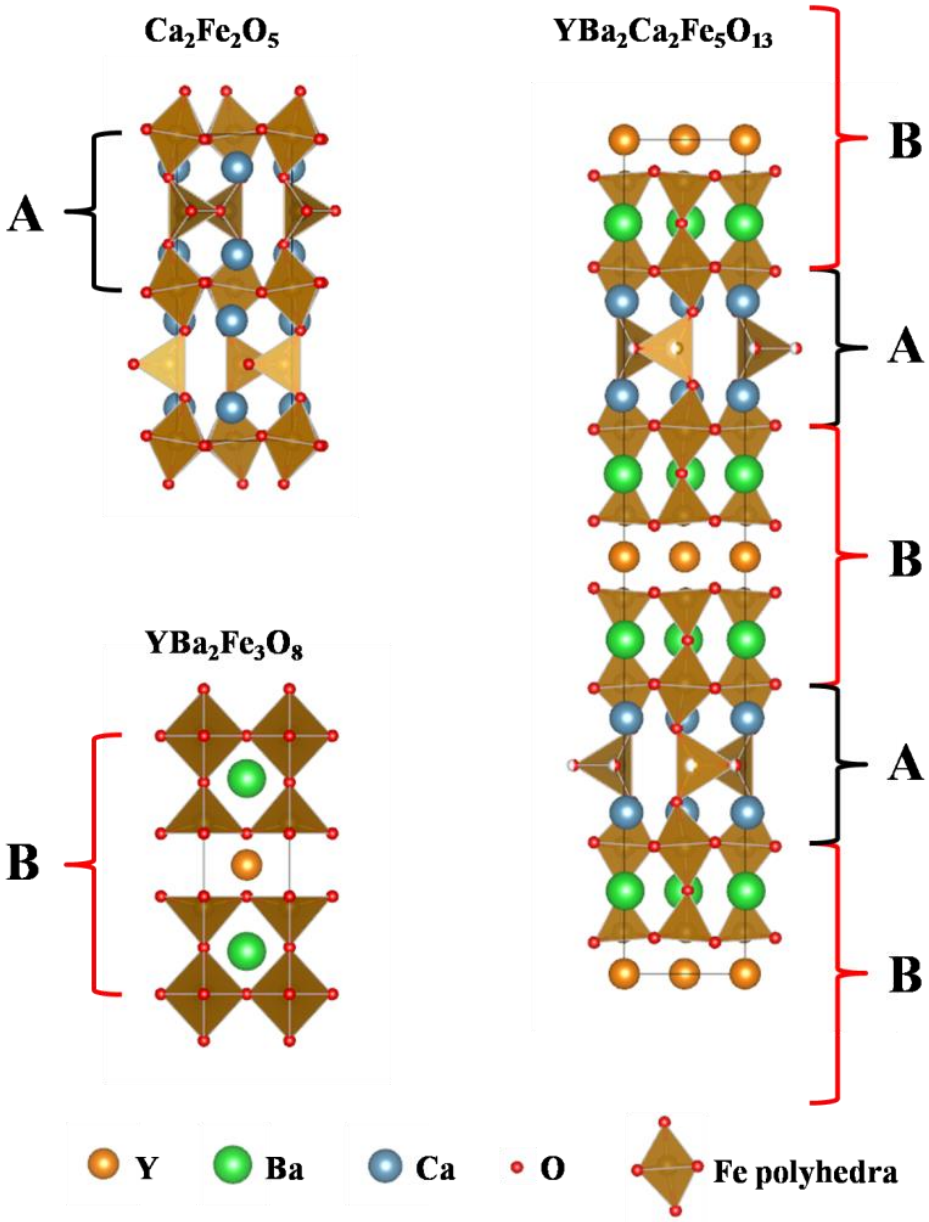

Figure 3.1 Structures of $Ca_2Fe_2O_5$,[190] $YBa_2Fe_3O_8$[65] and the ideal 10a_p intergrowth $YBa_2Ca_2Fe_5O_{13}$.[35] Building units A (from $Ca_2Fe_2O_5$) and B (from $YBa_2Fe_3O_8$) of the two former structures are regularly stacked in a 1:1 ratio to form the ideal 10a_p structure.

Whilst researching ways of increasing the DC conductivity of the 10a_p phase, Cu was considered as a dopant. It was proposed that substituting a small amount of Cu^{2+} for Fe^{3+} could lead to the formation of some charge carriers such as Fe^{4+} due the need to maintain electroneutrality, which would give a mechanism for the improvement of electronic conductivity. This has been demonstrated for the perovskite $LaFe_{1-x}Cu_xO_{3-\delta}$, where the resistance was significantly decreased with increased Cu content.[196] Initial Cu doping of the 10a_p phase however, resulted in a multiphasic sample that contained a previously unreported *A*-site ordered perovskite. Work on the identification and isolation (section 3.2), crystal structure characterisation (section 3.3) and evaluation as a cathode material (section 3.4) of the new phase are the main focus of this chapter.

3.2 Experimental

3.2.1 Discovery of the new phase

Using the solid state synthesis route, partial substitution of 10 % Cu^{2+} for Fe^{3+} ($Y_{0.9}Ba_{1.7}Ca_{2.4}Fe_{4.5}Cu_{0.5}O_{13\pm\delta}$) onto the *B*-site of the 10a_p phase $Y_{0.9}Ba_{1.7}Ca_{2.4}Fe_5O_{13\pm\delta}$ was attempted. 0.5 g was synthesised by hand grinding dried powders of Y_2O_3 (99.999 %), $BaCO_3$ (99.95 %), $CaCO_3$ (99.995 %), Fe_2O_3 (99.945 %) and CuO (99.995 %), all sourced from Alpha Aesar, in the required ratios in a pestle and mortar. The mixed powder was heated in a furnace to 1200 °C at a rate of 5 °C per minute in an Al_2O_3 crucible in static air. Power to the heating elements in the furnace was switched off after 12 hours, leaving it to cool to room temperature. The partially melted black crystalline material obtained was then hand ground using a pestle and mortar and a room temperature PXRD pattern was collected.

This synthesis afforded a multiphasic sample as observed in the PXRD pattern collected (Figure 3.2 A), while a low angle reflection with a *d*-spacing of 10.2 Å that could not be attributed to the 10a_p phase was identified. A second PXRD pattern was collected for this sample, this time only collecting data at low angle for a longer counting time in order to increase intensity and more fully resolve the low angle reflections.

Figure 3.2 B shows the presence of four low angle reflections observed in the diffraction pattern. Two, at 19 Å and 9.5 Å are indicative of the 020 and 040 reflections of the $10a_p$ phase that was the original target of the synthesis. The two non-indexed reflections found at 10.2 Å and 15.3 Å, appeared to be related by 10.2 being exactly 2/3 of 15.3, although this would have to be confirmed with further investigation.

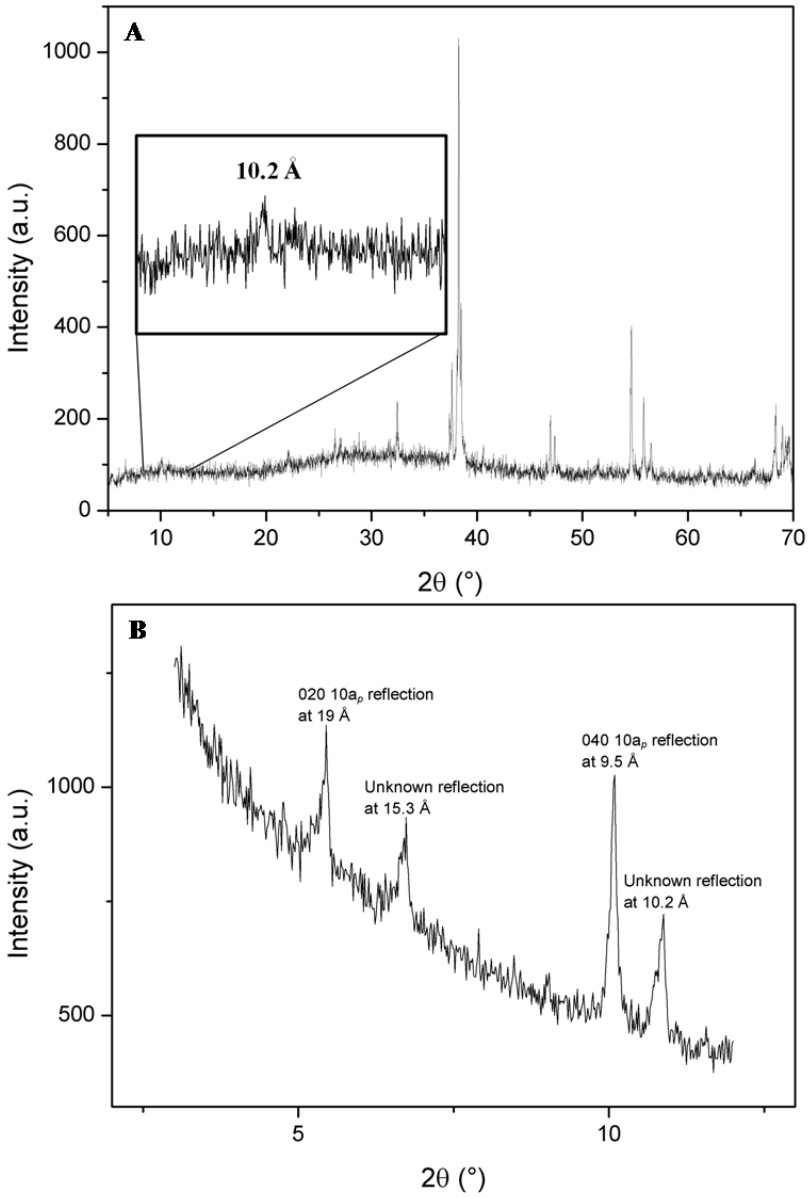

Figure 3.2 A) Shows initial multiphase PXRD pattern obtained for $Y_{0.9}Ba_{1.7}Ca_{2.4}Fe_{4.5}Cu_{0.5}O_{13\pm\delta}$, with low angle peak at 10.2 Å indicated in the insert. B) Shows the presence of four reflections observed in this low angle PXRD pattern, two at 19 and 9.5 Å indicative of 020 and 040 $10a_p$ reflections and two at 10.2 and 15.3 Å unknown.

In order to ascertain what these unknown low angle peaks were due to, preliminary TEM SAED was carried out by A. Demont on the sample, as well as compositional analysis using EDX. Figure 3.2 shows SAED of the unknown phase, which appears to have a stacking axis of $8a_p$. EDX analysis of five crystals with the $8a_p$ stacking axis gave an average composition of $Y_{2.08}Ba_{1.84}Ca_{4.08}Fe_{7.44}Cu_{0.56}O_x$, which was used as the starting point in the attempt to isolate this newly identified phase.

Additionally, a second phase observed from SAED was identified as a $10a_p$ phase, in concurrence with the identified phase from low angle peaks observed in the PXRD pattern in Figure 3.2.

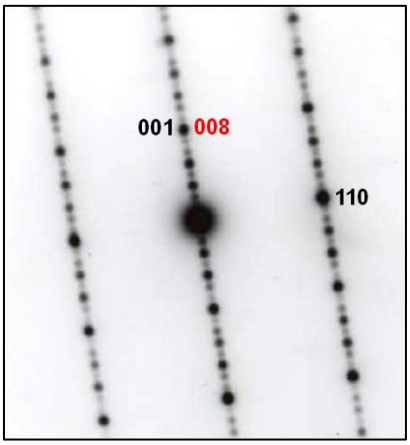

Figure 3.3 SAED shows the presence of an eight fold stacking axis for the unknown phase.

3.2.2 Reactivity with crucibles

As previously discussed in section 3.2.1, the multiphasic sample synthesised with starting molar ratio of $Y_{0.9}Ba_{1.7}Ca_{2.4}Fe_{4.5}Cu_{0.5}O_{13\pm\delta}$ was partially melted. The Al_2O_3 crucible that the sample was synthesised in was left discoloured, indicating that there may have been a reaction between the sample and the crucible. It was also noted during intermediate re-grinding and firing steps that phases present in a sample would change with each annealing step as observed in PXRD patterns (for reaction in ZrO_2 crucible, see Figure 3.4). The explanation for this change could be attributed to improvements in homogeneity with each step, kinetics to formation of each phase, or reactivity of the samples with the crucible,

changing the overall composition. In order to test these hypotheses, the synthesis of $Y_{1.8}Ba_{2.5}Ca_{3.7}Fe_{7.44}Cu_{0.56}O_{21}$ (or $Y_{1.13}Ba_{1.56}Ca_{2.31}Fe_{4.65}Cu_{0.35}O_{13}$) was carried out in Al_2O_3, ZrO_2 and Pt foil lined Al_2O_3 crucibles.

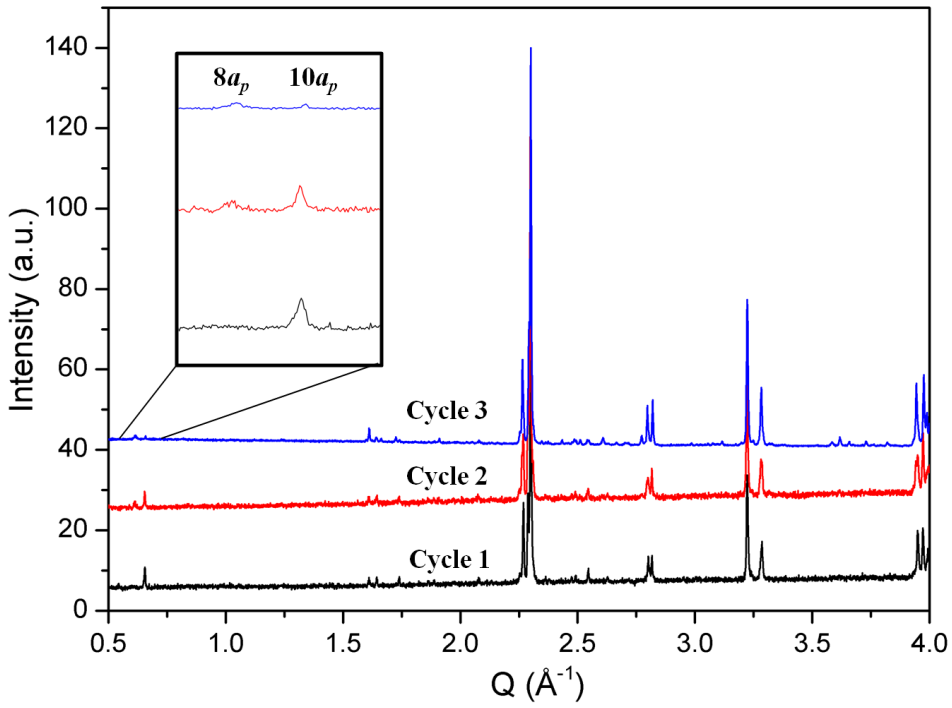

Figure 3.4 PXRD patterns showing changes in phases present between annealing cycles for $Y_{1.8}Ba_{2.5}Ca_{3.7}Fe_{7.44}Cu_{0.56}O_{21}$ when reacted in ZrO_2 crucible, particularly highlighted in low angle zoomed insert.

Figure 3.5 shows a comparison of PXRD patterns collected for $Y_{1.8}Ba_{2.5}Ca_{3.7}Fe_{7.44}Cu_{0.56}O_{21}$ synthesised in the three different crucible types listed above. Due to the composition used, a mostly 10a_p phase would be expected to form (as discussed in more detail in chapter 5), however, this was only observed in the synthesis using Pt foil as a barrier. Additionally, when synthesised using the Pt barrier, the reaction appeared to reach completion after two annealing cycles due to the lack of changes observed in the PXRD patterns after this point. Using Al_2O_3 and ZrO_2, there were further changes observed after two cycles, pointing to reactivity with the crucibles. From this point on, all synthesis of the 8a_p phase was carried out in Pt foil lined crucibles or Pt metal crucibles.

It is also worth noting that samples prepared in Al_2O_3 crucibles had significantly different compositions as determined by TEM EDX when compared to the starting composition. Also, there was no sign of Al in any of the samples, indicating that there was only cation loss to the crucible and not Al migration into the sample.

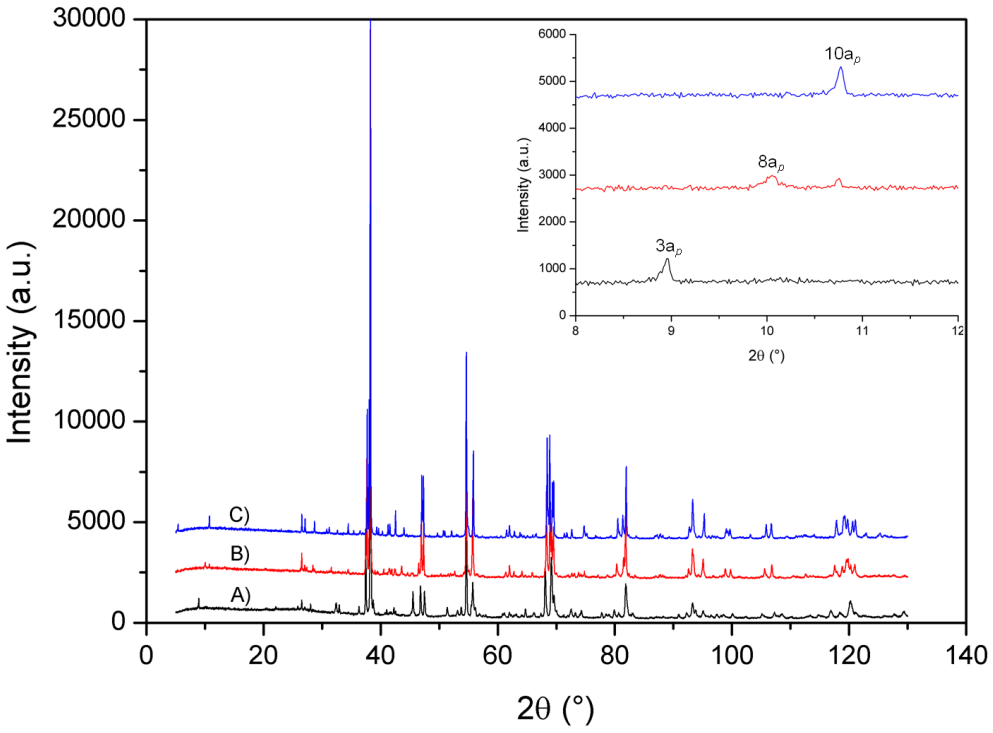

Figure 3.5 Comparison of phases present in PXRD patterns of $Y_{1.8}Ba_{2.5}Ca_{3.7}Fe_{7.44}Cu_{0.56}O_{21-\delta}$ reacted in A) Al_2O_3 crucible (black), B) ZrO2 crucible (red) and C) Pt foil lined Al_2O_3 crucible (blue).

3.2.3 Isolation using the phase diagram approach

Using the EDX given composition from section 3.2.1 ($Y_{2.08}Ba_{1.84}Ca_{4.08}Fe_{7.44}Cu_{0.56}O_x$) for the 8$a_p$ phase as a starting point, a range of new compositions were synthesised. A ternary phase diagram of *A*-site cation ratios (see Figure 3.6 A) was used to guide synthetic attempts. The Fe/Cu *B*-site ratios were also varied and could be considered as going into or coming out of the page, with each ratio having its' own ternary diagram of *A*-site compositions. The main

focus however, was the EDX obtained *B*-site composition of $Fe_{7.44}$ - $Cu_{0.56}$ in order to reduce the number of variations attempted.

All syntheses were carried out using standard solid state synthesis within Pt foil lined crucibles or Pt metal crucibles to prevent loss of cations to the crucible following the observtions described in section 3.2.2. Starting reagents were hand ground using a pestle and mortar and given the same heat treatment as described in section 3.2.1, as this had previously led to the formation of the $8a_p$ phase. The resultant black powders were then hand ground before being pressed into a pellets using a 13 mm die and a uniaxial press at 2 tons pressure. The samples underwent several heating and regrinding cycles to ensure a complete reaction and homogeneity of the sample. PXRD patterns were collected after each cycle in order to follow the reaction progress.

Synthesis of $Y_{2.32}Ba_{2.16}Ca_{3.52}Fe_{7.44}Cu_{0.56}O_{21-\delta}$ resulted in a weight fraction of 80 % $8a_p$, as determined by Rietveld analysis. This sample was then used for a more comprehensive SAED experiment than previously undertaken. Using this new sample, the phase was determined to have a $16a_p$ stacking axis and was indexed to $a_p \sqrt{2} \times 16a_p \times a_p \sqrt{2}$. Further discussion will be made about this analysis below in the crystal structure characterisation section 3.3. From this point onwards, the phase that forms with these parameters will be known as the $16a_p$ phase.

Continued variation of composition was carried out whilst attempting to isolate a phase pure $16a_p$ sample, leading to the discovery of two different $10a_p$ phases and a $3a_p$ phase, as well as the $16a_p$ phase within the compositional range explored. The presence of the two $10a_p$ phases are differentiated by $10a_p$' ($YBaCa_3Fe_5O_{13}$ type) and $10a_p$" ($YBa_2Ca_2Fe_5O_{13}$ type). The $10a_p$' phase was also identified from SAED and an average composition based on EDX of five crystals gave $Y_{1.15}Ba_{0.80}Ca_{3.05}Fe_{4.74}Cu_{0.26}O_x$. Figure 3.6 A below shows a ternary phase diagram for the ratios of the three *A*-site cations used, along with the regions of formation of the $16a_p$ (red), the $10a_p$' (blue), the $10a_p$" (orange) and the $3a_p$ (green) long axis phases.

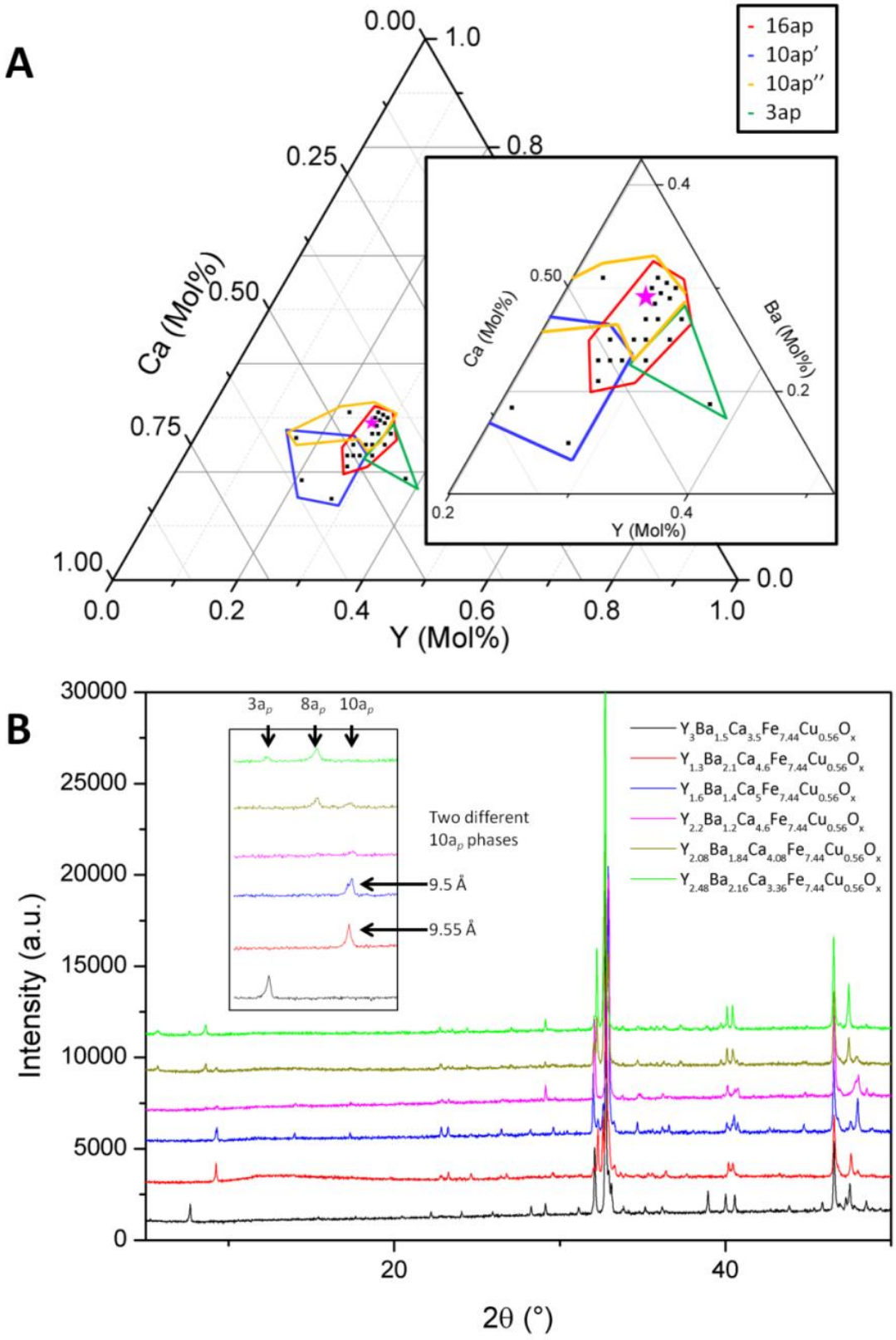

Figure 3.6 A) Ternary phase diagram showing variation in *A*-site cation ratios of synthesised samples. The presence of different perovskite phases is indicated within areas marked: red - 16a_p, blue - 10a_p', orange - 10a_p", green 3a_p. The magenta star indicates the sample with highest purity. B) A range of PXRD patterns from initial synthesis showing low angle peaks indicating the presence of four competing long axis phases.

Figure 3.6 B shows PXRD patterns for a range of compositions, displaying the low angle ordering reflections in the zoomed inserts that were used to identify which perovskite was present. As these long axis perovskites were all indexed as orthorhombic $a_p \sqrt{2} \times n\, a_p \times a_p \sqrt{2}$, without the low angle reflections it became exceedingly difficult to differentiate the phases through PXRD alone due to the peak overlap at higher angle. The sheer number of samples prepared did however allow for the changes in phase formation to be followed through careful examination of all PXRD patterns collected for near neighbour compositions.

3.2.4 Obtaining a Phase Pure Sample

In the starred region of Figure 3.6 A, the purity of the $16a_p$ phase seemed to reach its limit as further changes in composition appeared to show no further improvement. Reaction conditions were therefore investigated for this starred sample, $Y_{2.24}Ba_{2.28}Ca_{3.48}Fe_{7.44}Cu_{0.56}O_{21\pm\delta}$, which contained roughly > 85 % $16a_p$, < 10 % $10a_p$" and < 5 % Y_2O_3.

Many conditions were investigated in order to isolate a phase pure sample, including annealing in oxygen, nitrogen and argon atmospheres, variations in synthesis temperature above and below 1200 °C and cooling rates. None of which made an impact on the purity of the $16a_p$ phase, other than cooling rate. It was discovered that quenching from the synthesis temperature was required in order to isolate the $16a_p$ from the $10a_p$ phase (although a small amount of Y_2O_3 remained).

Taking the fully reacted sample and re-firing it at 1200 °C for 12 hours as two 5 mm pellets, one pellet was allowed to cool under normal conditions, whilst the other was rapidly quenched to room temperature by placing it directly onto an Al metal quenching block. The two samples were analysed by powder synchrotron X-ray diffraction, with their low angle reflections shown below in Figure 3.7.

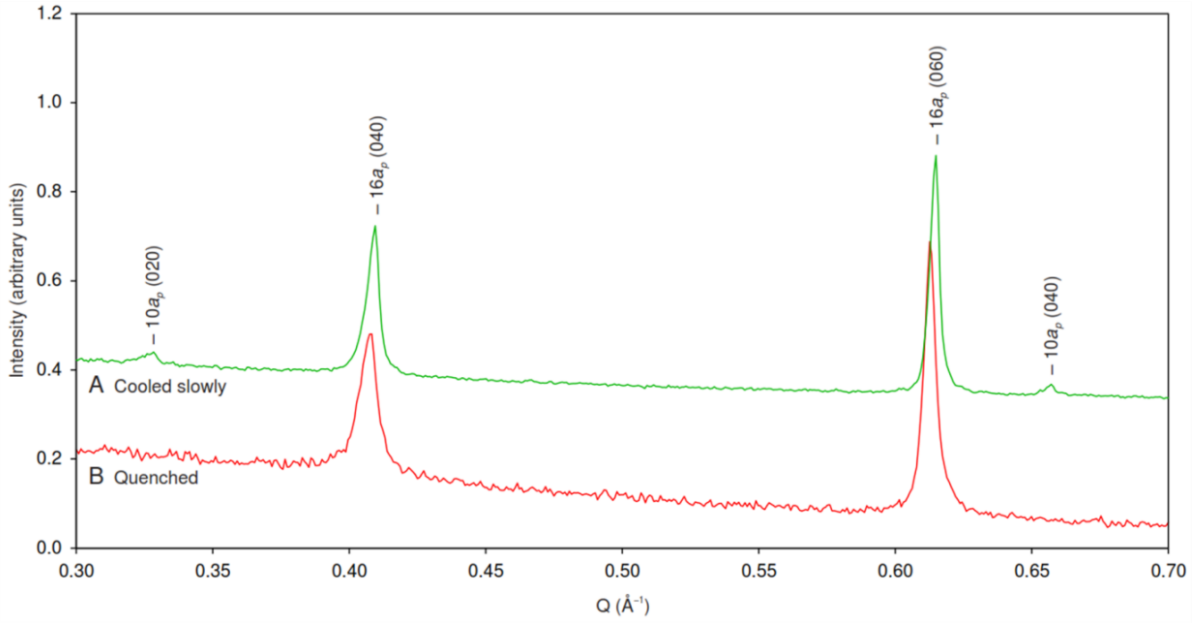

Figure 3.7 SXRD patterns of best 16a_p composition ($Y_{2.24}Ba_{2.28}Ca_{3.48}Fe_{7.44}Cu_{0.56}O_{21\pm\delta}$) produced by A) slow cooling and B) quenched rapidly to room temperature. Bragg reflections due to 16a_p phase and 10a_p phase are indicated.

As you can see, the diffraction pattern of the slowly cooled sample contains Bragg reflections for the 10a_p phase as well as the 16a_p phase. On quenching however, the 10a_p contribution is removed, leaving only Bragg reflections for the 16a_p phase. The requirement of quenching suggests that the 16a_p is a thermodynamic metastable phase. EDX on the quenched sample gave a composition of $Y_{2.07(15)}Ba_{2.49(20)}Ca_{3.44(5)}Fe_{7.63(18)}Cu_{0.37(7)}$, close to the as-made composition.

Before the 16a_p ($Y_{2.24}Ba_{2.28}Ca_{3.48}Fe_{7.44}Cu_{0.56}O_{21\pm\delta}$) was quenched and isolated from the 10a_p phase, SXRD and ND data were collected on the non-quenched samples. The crystal structure characterisation by combined Rietveld refinement was therefore carried out on a sample containing 10a_p and Y_2O_3 impurities. The quenched samples were used for the physical property measurements discussed in section 3.3.

3.2.4 Other *A*-site ordered synthesis attempts

After isolating the 16a_p phase, attempts were made to synthesise other *A*-site ordered perovskites, particularly one with a 7a_p stacking axis. Taking a *B*-site of entirely Fe, the *A*-site cations of Y, Ba and Ca were varied, as shown in the phase diagram displayed in Figure 3.8. Unfortunately, no 7a_p was observed in any of the diffraction patterns collected for these compositions.

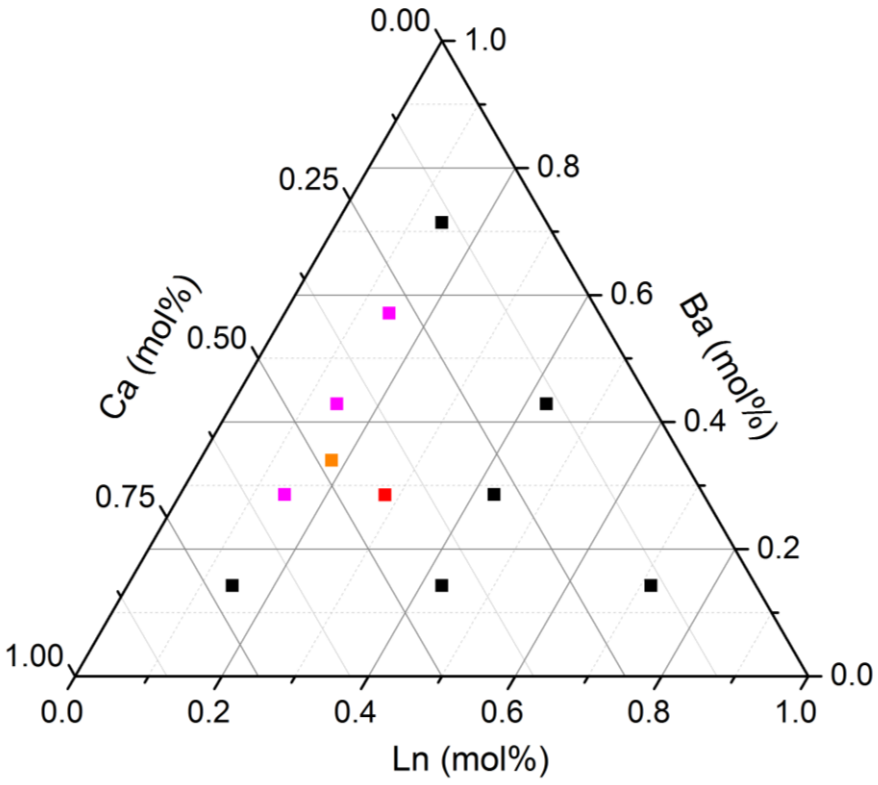

Figure 3.8 Ternary diagram of attempted 7a_p synthesis, with 10ap (red) 16ap (orange) and lowest energy EMMA compositions (magenta) highlighted.

The three lowest energy candidate compositions identified by the computation method EMMA,[197] and therefore determined the most likely compositions to form with the desired phase, $YBa_2Ca_4Fe_7O_{18}$, $YBa_4Ca_2Fe_7O_{18}$ and $YBa_3Ca_3Fe_7O_{18}$, were considered further. Total substitution of Y for a range of different sized lanthanides, *Ln* (*Ln* = La, Nd, Gd, Ho, Yb) was carried out at each composition. Synthesis was carried out at 1200 °C with normal cooling (3 °C per minute) under various atmospheres (air, O_2, N_2, Ar), as well as with quenching in

air. Again as for all other synthesis attempts, no 7ap phase was formed, with the main phases present being mixtures of $16a_p$, $10a_p$, $3a_p$ and cubic perovskites.

3.2 Crystal Structure Characterisation

3.2.1 Obtaining a Starting Model

Experimental SAED patterns of the $16a_p$ phase collected by A. Demont can be seen below in Figure 3.9. In the patterns, a set of subcell reflections characteristic of a cubic perovskite structure was observed. Additionally, sharp superstructure reflections show the existence of large inter-reticular distances along one of the directions, in agreement with low angle peaks observed by PXRD patterns. Reconstruction of the reciprocal space was carried out by rotation around this long axis, yielding a large perovskite superstructure with unit cell dimensions $a_p\sqrt{2} \times 16a_p \times a_p\sqrt{2}$, $\alpha = \beta = \gamma = 90°$, while the diffraction spots are controlled by the condition *hkl*: $h + k + l = 2n$, *hk*0: $h,k = 2n$ consistent with space groups *Imma* and *I*2*mb*.

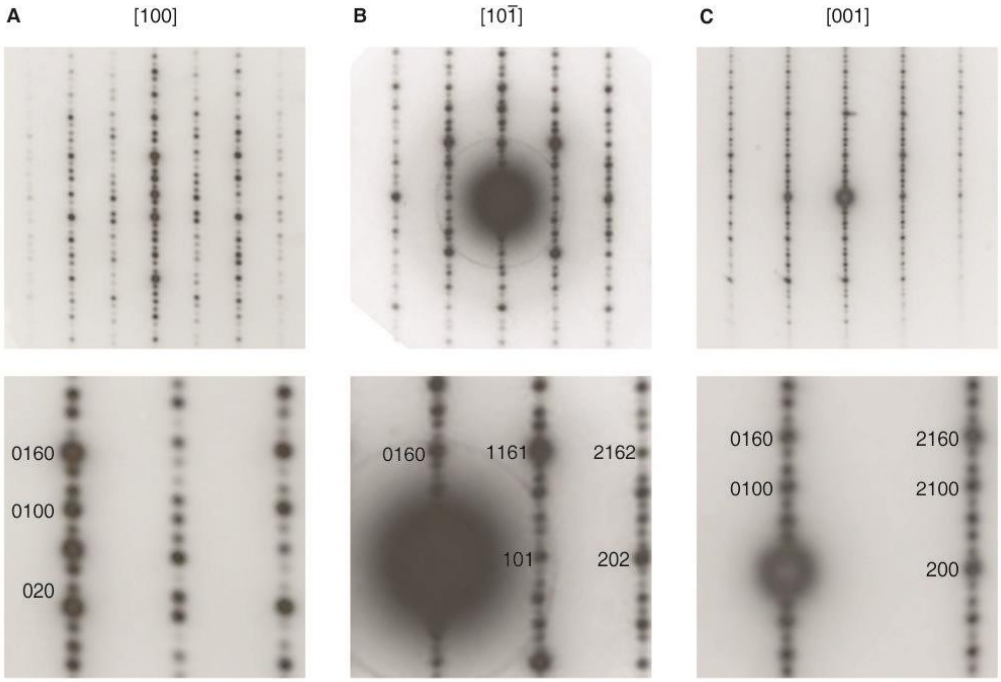

Figure 3.9 A) [100], B) [10$\bar{1}$], C) [001] experimental SAED patterns (above) with their respective selected portions (below) showing the indexing of the $16a_p$ unit cell.

The starting model for Rietveld refinement of the 16a_p phase was derived from the lowest energy 16a_p $Y_2Ba_2Ca_4Fe_8O_{21}$ structure identified by the computational method EMMA, which was carried out by M. Dyer, C. Collins and G. Darling.[197] The *P*1 structure generated from EMMA was transformed into the experimentally (SAED) determined symmetry of *Imma* using FindSym[198] to determine the unit cell origin and merge atoms within a tolerance of 0.25 Å, giving an observed symmetry of $P2_1/c$, and then Vesta[199] was used to impose *Imma* symmetry and remove duplicate atoms. The resulting *Imma* model contained disordering of oxygen positions around the tetrahedral Fe site (site *B*3) and one of the octahedral Fe sites (site *B*4). The labelled atomic sites can be seen in Figure 3.11 E.

Mössbauer data were obtained (on $Y_{2.32}Ba_{2.16}Ca_{3.52}Fe_{7.44}Cu_{0.56}O_{21-\delta}$) at 300 K using a conventional acceleration Mössbauer spectrometer incorporating a ≈25 mCi source of ^{57}Co in a Rh matrix. The observed data seen in Figure 3.10 were fitted by M. Thomas and indicated that only Fe^{3+} was present, which was found in octahedral (O_h), tetrahedral (T_d) and square pyramidal (S_q) environments (from chemical shifts) in a 2:1:1 ratio (relative area), consistent with the calculated structure. This fitting gave a χ^2 = 9.78 for 15 variables and the data for this can be seen in Table 3.1.

Fe^{3+} coordination	Chemical shift	Quad	Wdth	DWid	Fild	Relative Area
O_h	0.3453(9)	-0.414(2)	0.457(3)	-0.075(3)	504.06(8)	1000
S_q	0.309(2)	-0.280(4)	0.453(5)	0.099(5)	482.8(2)	500
T_d	0.184(2)	0.738(4)	0.507(4)	0.103(5)	392.76(15)	500

Table 3.1 Shows refined Mössbauer parameters for the 16ap, which presents Fe^{3+} only in O_h, S_q, and T_d coordination geometries in a ratio of 2:1:1.

Iodometric titrations were performed to determine the oxygen content that corresponded to a quenched sample with a composition of $Y_{2.24}Ba_{2.28}Ca_{3.48}Fe_{7.44}Cu_{0.56}O_x$ as detailed in section 2.6. Assuming reduction to Fe^{2+} and Cu^+ species,[185] and using the nominal composition for the cations, the oxygen content was calculated giving a full composition of $Y_{2.24}Ba_{2.28}Ca_{3.48}Fe_{7.44}Cu_{0.56}O_{20.92(2)}$. This corresponds to an average Fe/Cu charge state of 2.95+ and is in good agreement with the fact that attempts to refine oxygen content away

from full site occupancy during Rietveld refinement were unsuccessful and the observation of only Fe^{3+} environments in the Mössbauer data. Formal charge states of Fe^{3+} (consistent with Mössbauer spectra) and Cu^{2+} would yield an oxygen content of $O_{20.84}$, which agrees well with the observed value.

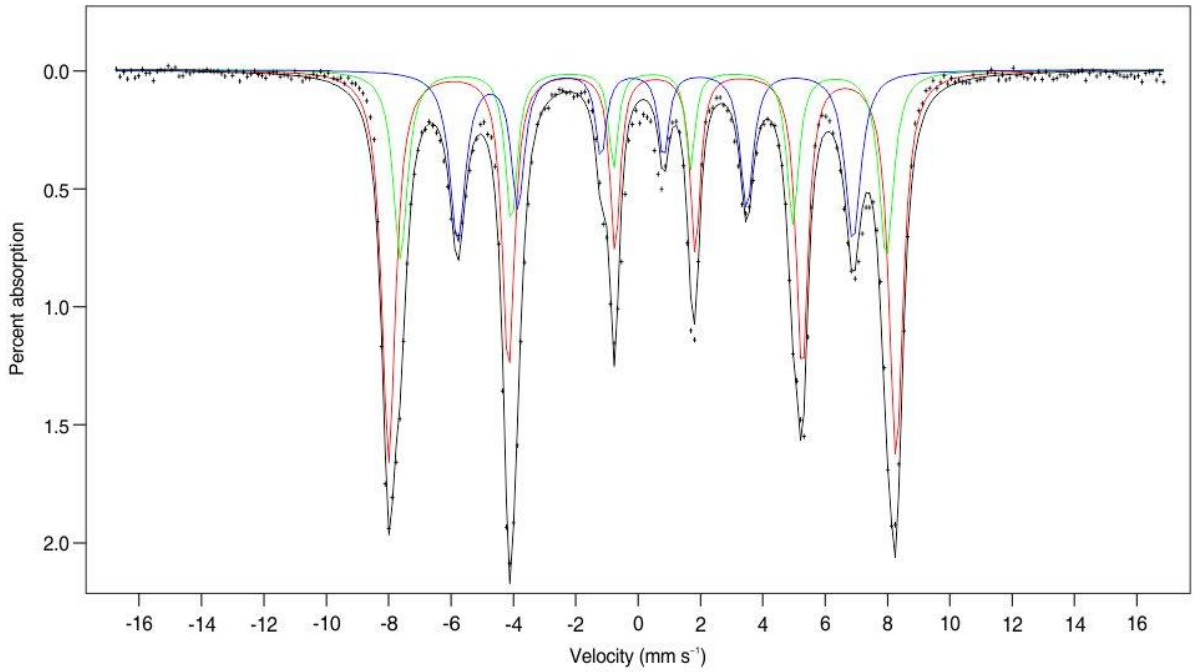

Figure 3.10 ^{57}Fe Mössbauer spectrum of 16a_p, $Y_{2.32}Ba_{2.16}Ca_{3.52}Fe_{7.44}Cu_{0.56}O_{20.92}$, showing the observed data (black crosses) and calculated fit (black line). Individual components of the calculated fit corresponding to octahedral (red line), square pyramidal (green line) and tetrahedral (blue line) Fe^{3+} are shown.

3.2.2 Crystal Structure Refinement

Time-of-flight neutron diffraction (ND) data were collected on the HRPD instrument as detailed in section 2.2.10. SXRD data were obtained on Beamline I11 as detailed in section 2.2.9, at a wavelength of 0.826145(3) Å over a 2θ range of 2 to 150° and a step size of 0.003°. Powder diffraction data were analysed by P. Chater in a combined X-ray and neutron Rietveld refinement using the GSAS suite.[174]

Using the starting model determined by EMMA,[197] a Rietveld refinement was carried out on the SXRD and ND data (collected for $Y_{2.24}Ba_{2.28}Ca_{3.48}Fe_{7.44}Cu_{0.56}O_{20.92}$ non-quenched

samples) by P. Chater. Within the ND data, there were peaks present that could not have intensity assigned to them, although their *d*-spacing was characteristic of the unit cell. The peaks were attributed to magnetic Bragg scattering.

Possible *B*-site magnetic structures were determined by co-representational analysis using the computer program SARAh[200] and were screened against the observed neutron scattering data. The best fit was observed for a G-type antiferromagnetic structure (propagation vector **k** = 0,0,0) with moments (anti)parallel to the *a*-axis. This type of magnetic structure is common for perovskites with an Fe^{3+} B-Site, with examples including the 10a_p phase,[35] $YBa_2Fe_3O_8$[65] and the brownmillerite $Ca_2Fe_2O_5$.[190] The magnitude of the magnetic moment along the *a*-axis on each *B*-site was refined in magnetic space group *Pmn′a*; sites *B*2 and *B*3 (see Figure 3.11 E) refined to a moment consistent with occupation by Fe^{3+} (3.89(8) μ_B and 3.97(6) μ_B, respectively), while sites *B*1 and *B*4 refined to a significantly lower moment (2.89(10) μ_B and 2.48(11) μ_B, respectively). As Cu (also only present in small amounts) and Fe are practically indistinguishable by X-ray and neutron atomic scattering (bound coherent scattering lengths: Fe - 9.45, Cu - 7.718 fm)[168], the Cu position was inferred on sites *B*1 and *B*4 from the refined magnetic moment, as Cu^{2+} has a significantly lower magnetic moment than Fe^{3+}. The experimental Cu composition was shared equally between the two identified Cu positions (sites *B*1 and *B*4) to give two sites with occupancies of $Fe_{0.86}Cu_{0.14}$ which were not refined.

For the combined Rietveld refinement, the ND time-of-flight diffractometer *zero* offset was refined for the 168° bank, all three constants (*difc*, *difa* and *zero*) were refined for the 90° and 30° banks 2 and 3, and the *zero* point was refined for the SXRD data giving a total of 8 refined diffractometer parameters. A total of 42 background parameters were refined; 4 for each ND histogram; 24 for SXRD high 2θ; 6 for SXRD low 2θ. Lattice parameters for the 16a_p were refined separately for ND and SXRD data as the data were collected on different samples. Bragg reflections matching 10a_p and Y_2O_3 impurities were also observed in the sample. Structures for 10a_p $Y_{0.9}Ba_{1.7}Ca_{2.4}Fe_5O_{13}$ (including the magnetic structure)[35] and Y_2O_3[201] were included in the Rietveld refinement and determined to be present at 15.0(2) weight% and 3.67(14) weight%, respectively, alongside the dominant 16a_p phase. Only the lattice parameters, scale factors and profile of the impurity phases were refined.

In order to improve the peak profile fitting of the broad, asymmetric low order Bragg reflections, the SXRD data-set was split into two histograms covering low 2θ and high 2θ ranges with a *d*-spacing range of 0.90 to 6.76 Å and 6.76 to 36 Å, respectively. Anisotropic strain broadening[202] was refined for the $16a_p$ phase in the high 2θ SXRD data-set and the highest resolution (168°) ND data-set to account for slight differences in peak shape for reflections corresponding to the long stacking axis. Stacking faults are quite common for similar phases, such as the brownmillerite $SrFeO_{2.5}$[203, 204] and long axis phase $Ca_4Fe_2Mn_{0.5}Ti_{0.5}O_9$,[205] which could be the cause of the peak shape differences. A total of 39 profile parameters were used in the refinement for all histograms and phases; 11 for ND 168°; 6 for ND 90°; 3 for ND 30°; 15 for SXRD high 2θ; 4 for SXRD low 2θ.

The relative occupancy of Y, Ba and Ca for each *A*-site were refined while penalties were applied to force a total occupancy of unity on each *A*-site. A soft chemical composition restraint was implemented to drive the refinement towards the experimental *A*-site composition of $Y_{2.24}Ba_{2.28}Ca_{3.48}$. A single isotropic displacement parameter was refined for each atom type; *A*-site (Y/Ba/Ca), *B*-site (Fe/Cu) and O. The atomic coordinates of each atom was refined within the symmetry allowed by each Wyckoff position. During the refinement, six of the disordered O positions from the EMMA structure moved close to a higher symmetry Wyckoff position. These atoms were moved onto the higher symmetry sites to reduce the number of refined atomic coordinates. A χ^2 of 10.87 was obtained for the refined parameters seen in Table 3.2.

Figure 3.11 A - D shows the fits from the combined Rietveld refinement using GSAS[174] for A) ND 168°, B) ND 90°,C) ND 30° and D) SXRD data sets. E) and F) show the EMMA calculated structure for $Y_2Ba_2Ca_4Fe_8O_{21}$ and the refined structure from this starting model with composition $Y_{2.25(1)}Ba_{2.29(1)}Ca_{3.47(2)}Fe_{7.44}Cu_{0.56}O_{21}$ respectively. It is evident that the refined structure remains remarkably close to the starting model, only deviating to any major extent on the oxygen sites. There is also a significant amount of Ba on the *A*5 Y site, likely due to the composition difference between the EMMA calculated structure and the experimental structure.

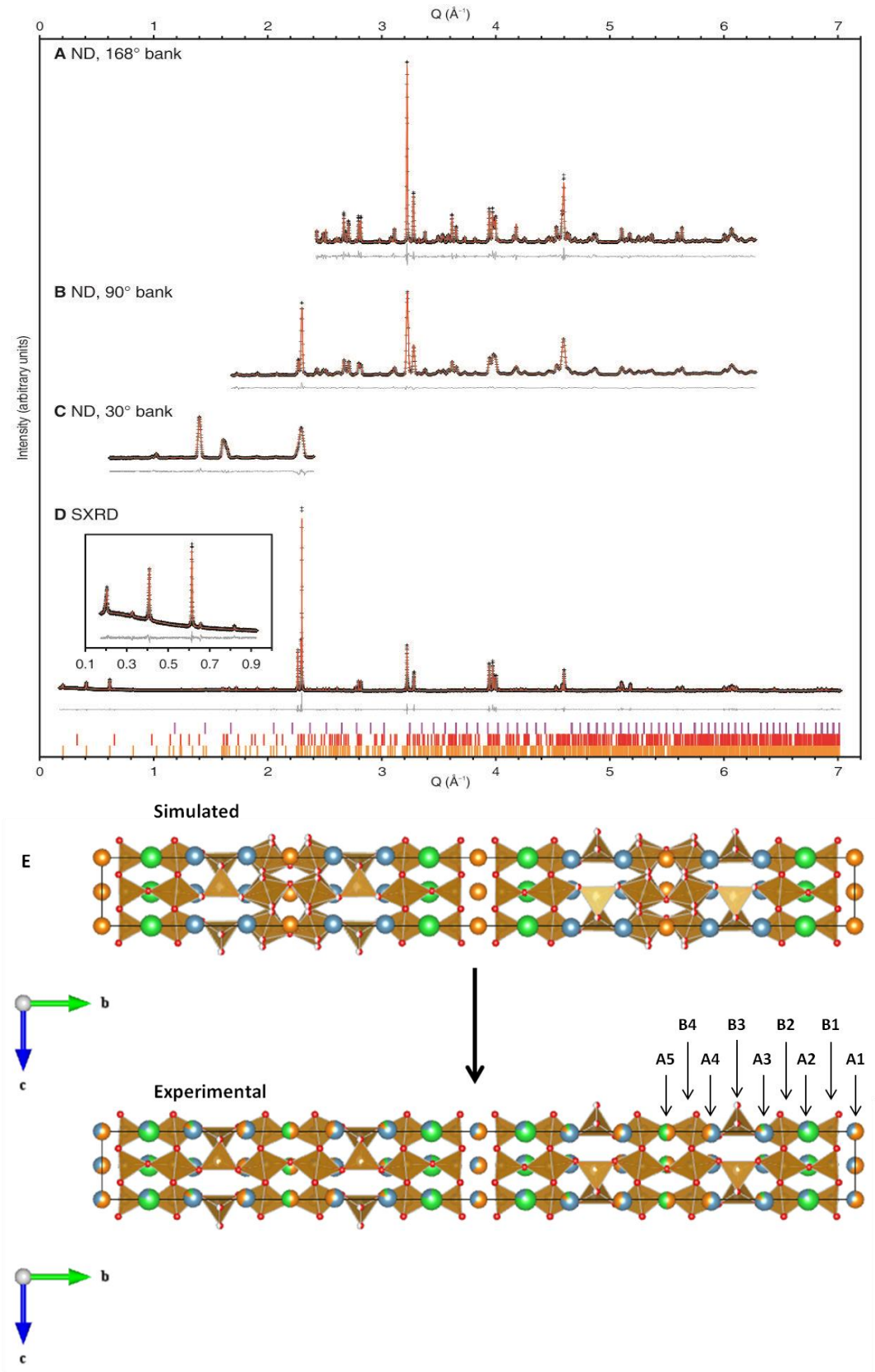

Figure 3.11 Fit data from combined refinement of A) ND 168°, B) ND 90°, C) ND 30° and D) SXRD together with insert of zoomed low angle region. E) Shows structures of EMMA[197] simulated and experimentally refined structure, with labels for each of the *A* and *B*-sites.

	Unit cell parameters					
	a (Å)	5.484964(25)				
	b (Å)	61.25901(32)				
	c (Å)	5.550477(25)				
Site	**Multiplicity**	**Occupancy**	**x**	**y**	**z**	**Uiso (Å^2)**
A1	4*a*	$Y_{0.627(4)}Ca_{0.373(4)}$	0	0	0	0.0196(2)
A2	8*h*	$Ba_{0.787(2)}Ca_{0.213(2)}$	0	0.062392(28)	0.9977(7)	0.0196(2)
A3	8*h*	$Ca_{0.768(9)}Y_{0.132(7)}Ba_{0.100(5)}$	0	0.12077(5)	0.9756(8)	0.0196(2)
A4	8*h*	$Ca_{0.566(1)}Y_{0.434(1)}$	0	0.19120(5)	0.9770(7)	0.0196(2)
A5	4*e*	$Y_{0.488(2)}Ba_{0.512(2)}$	0	1/4	0.9868(9)	0.0196(2)
B1	8*h*	$Fe_{0.86}Cu_{0.14}$	0	0.030041(31)	0.5008(6)	0.0123(2)
B2	8*h*	Fe_1	0	0.09470(4)	0.4891(8)	0.0123(2)
B3	16*j*	$Fe_{0.5}$	0.9450(4)	0.15521(5)	0.43229(32)	0.0123(2)
B4	8*h*	$Fe_{0.86}Cu_{0.14}$	0	0.217745(29)	0.4867(6)	0.0123(2)
O1	8*g*	1	1/4	0.02180(8)	1/4	0.0254(2)
O2	8*g*	1	3/4	0.02445(7)	3/4	0.0254(2)
O3	8*h*	1	1/2	0.06107(8)	0.034(4)	0.0254(2)
O4	8*g*	1	3/4	0.09480(7)	3/4	0.0254(2)
O5	8*h*	1	1/2	0.12861(7)	0.9347(9)	0.0254(2)
O6	4*e*	1	1/2	1/4	0.0500(14)	0.0254(2)
O7	8*g*	1	1/4	0.28288(8)	3/4	0.0254(2)
O8	8*g*	1	1/4	0.28929(9)	1/4	0.0254(2)
O9	8*h*	1	1/2	0.31872(5)	0.9354(8)	0.0254(2)
O10	16*j*	0.5	0.9024(7)	0.34338(11)	0.1161(7)	0.0254(2)
O11	8*g*	1	3/4	0.40037(8)	1/4	0.0254(2)

Table 3.2 Refined crystallographic data for $16a_p$ from combined data set of ND and SXRD. Space group - *Imma.* Refined composition $Y_{2.25(1)}Ba_{2.29(1)}Ca_{3.47(2)}Fe_{7.44}Cu_{0.56}O_{21}$, including soft chemical composition restraint.

High-angle Annular Dark Field (HAADF) images were acquired by S. Romani using inner and outer collection semi angles of 74 and 196 mrad, respectively. Environmental noise sources were removed by using an annular filter in the FFT of the raw image, which improves the image qualitatively, while flattening the intensity response across the image field. The beam convergence semi angle was 14mrad and spherical aberration (C_s) was controlled to within +/− 10 microns.

Simulated HAADF-STEM images were produced using the computer program QSTEM[206] using the same instrumental parameters as those used in the experiment. In order to produce a representative image, a 10a × b × 10c super-cell of the 16a_p unit cell was constructed from the structure determined by Rietveld refinement using Vesta.[199] Within each *A*-site layer, individual *A*-sites were randomly assigned an atom type (Y, Ba or Ca), which were consistent with the experimentally determined atomic composition for that layer.

A comparison of the simulated and observed HAADF-STEM images can be seen below in Figure 3.12. As viewed down A) [001] and B) [100], the simulated images match up with the experimentally observed images both in terms of intensity and atom positions. This is good confirmation that the refined model is indeed a good match for the actual 16a_p structure. Site *A*5, which changed from Y only in the starting model to 50:50 with Ba in the refined model also matches up well, with brighter spot intensity seen than if the site was occupied only by the lighter Y atom (red box). The T_d *B*-site, *B*3, can also be seen quite clearly by the displacement observed when viewed down the [100] (blue box).

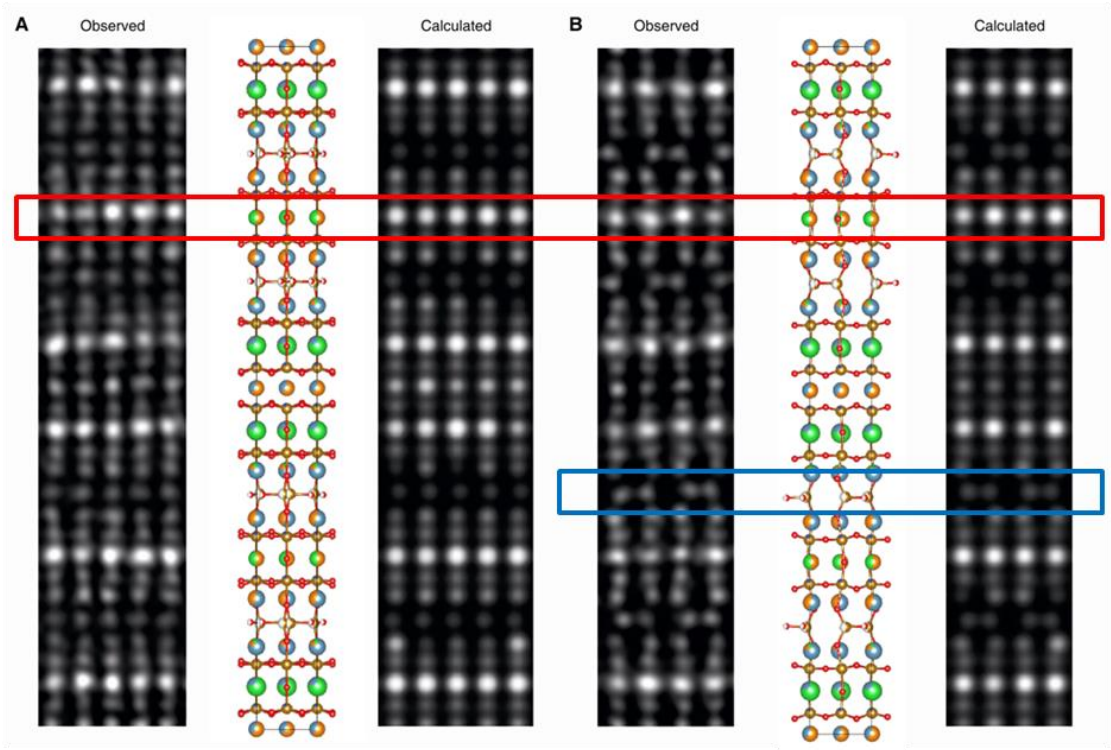

Figure 3.12 Observed and calculated HAADF-STEM images of 16a_p, as viewed down the A) [001] and B) [100] axes. The refined crystal structure is shown for comparison. An *A*5 Y/Ba site highlighted in red box and a T_d *B*3 site highlighted in blue box.

3.2.3 Cu Free 16a$_p$

It was also possible to form the 16a_p phase with a pure Fe only *B*-site, indicating that Cu was not requisite for its formation. At a composition of $Y_{1.95}Ba_{2.1}Ca_{3.95}Fe_8O_{21\pm\delta}$, a majority 16$a_p$ phase was produced, with rough weight fractions obtained by Rietveld analysis leading to 80 % 16a_p, 10 % 10a_p and 10 % 3a_p (see Figure 3.13). Further attempts were not made to isolate a phase pure Fe only sample, with the focus remaining on $Y_{2.24}Ba_{2.28}Ca_{3.48}Fe_{7.44}Cu_{0.56}O_{20.92}$.

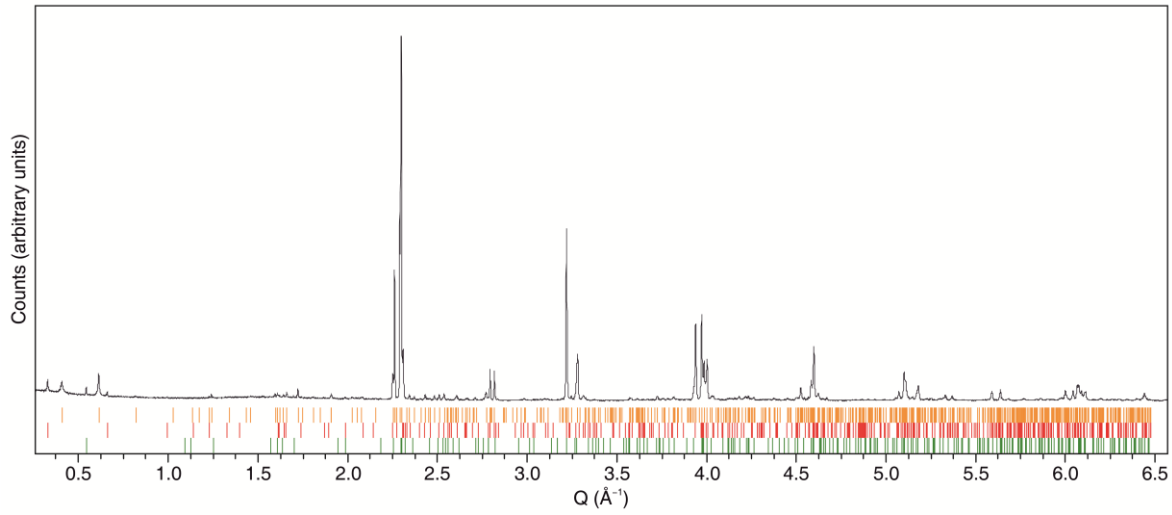

Figure 3.13 SRXD pattern of the Cu free 16a_p, $Y_{1.95}Ba_{2.1}Ca_{3.95}Fe_8O_{21}$. The tick marks represent: the 16ap phase, 2, as the majority phase (≈ 80 %, orange), a phase with a 10ap repeat (≈ 10 %, red) and one with a 3ap repeat (≈ 10 %, green). Estimated weight fractions were determined for each phase present by Rietveld refinement.

3.3 Physical Properties

In order to determine if the 16a_p phase had potential to perform as a cathode in a SOFC, many properties had to be determined, which are discussed in this section. High structural stability at high temperatures, as well as chemical compatibility with other components, especially the electrolyte in which it is in contact with, needs to be demonstrated in order for the material to be considered a viable candidate (see section 3.3.1). The electrochemical

performance of the 16a_p phase is discussed in section 3.3.2, and some post electrochemical analysis is examined in section 3.3.3.

3.3.1 Stability and Compatibility

Thermal stability tests were performed in air on the as-synthesised powder and on powder which was ballmilled in isopropanol for 20 hours. Ballmilling reduces the particle size and increases the surface area, which should increase the number of electrochemically active cathode sites for improved electrochemical performance. Stability tests were therefore carried out on samples that resembled the processed cathode as much as possible. Samples were then annealed in air at 750 °C for five days (to simulate intermediate SOFC operating temperatures) and 950 °C for five hours (cathode processing temperatures) and subsequent phase stability was characterised by PXRD, as seen in Figure 3.14. No new phase formation or decomposition of the 16a_p phase was observed. According to Table 3.3, lattice parameters do not change significantly.

To study chemical compatibility with the state-of-the-art electrolytes $Ce_{0.9}Gd_{0.1}O_{1.95}$ (GDC, Fuel Cell Materials), $Ce_{0.8}Sm_{0.2}O_{1.9}$ (SDC, Fuel Cell Materials) and $La_{0.9}Sr_{0.1}Ga_{0.8}Mg_{0.2}O_{2.85}$ (LSGM, PI-KEM LTD), milled powder of the 16a_p phase and electrolyte were mixed in a weight ratio 1:1 by hand grinding, pressed into 5 mm pellets and annealed as for the stability test. The pellets were then ground into powders for characterization by PXRD, as seen in Figure 3.14. Again, as for the thermal stability test, there was no detectible degradation of the 16a_p phase. No new reflections were observed within the PXRD patterns, suggesting new phase formation through reactivity with the electrolyte did not occur. Lattice parameters, seen below in Table 3.3, also remained mostly constant with only small deviations, indicating a small amount of cation diffusion between electrolyte and 16a_p was likely. The 16a_p lattice parameter deviations were most pronounced when combined with LSGM. It has been reported that for LSGM, rather than new phase formation cation diffusion between cathode and electrolyte are favoured, with transition metals Mn, Fe and Co in particular rapidly diffusing into LSGM.[207, 208] It is likely that in this case, there is some exchange in cations between the 16a_p phase and LSGM.

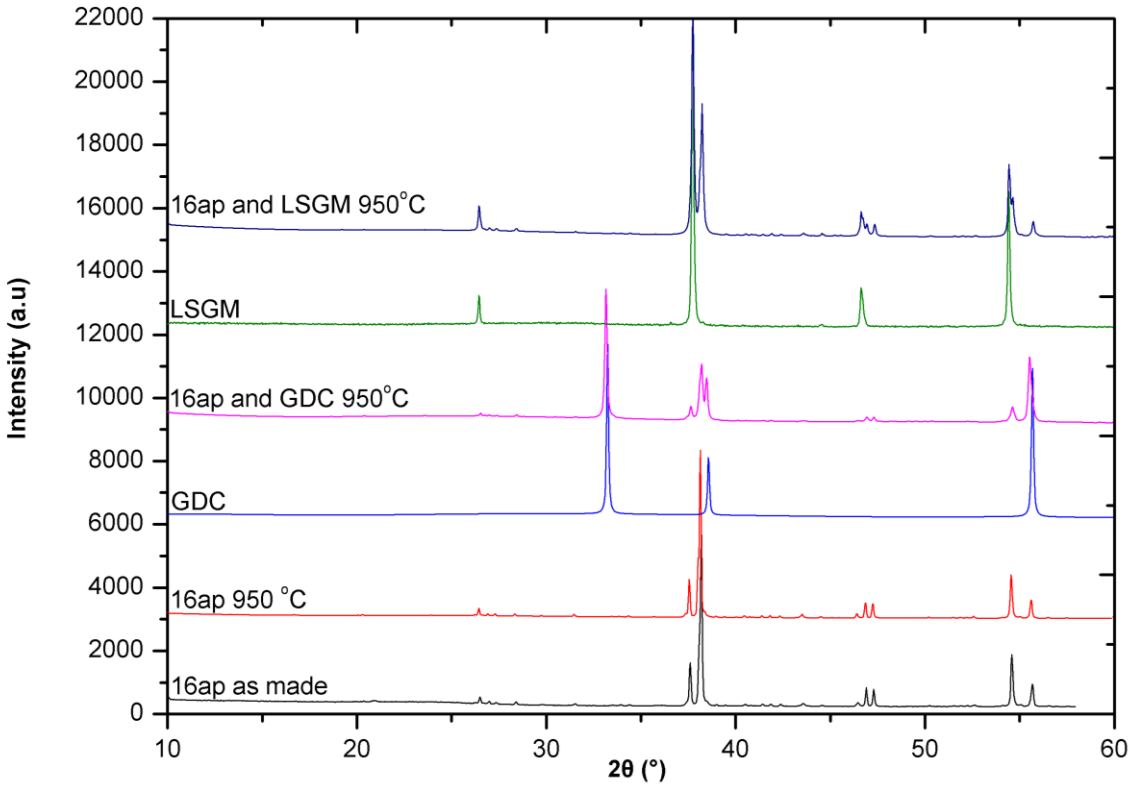

Figure 3.14 X-ray diffraction patterns showing the stability of the synthesised 16a_p material. The patterns show that the material is both thermally stable and compatible with the two common electrolyte materials, $Ce_{0.9}Gd_{0.1}O_{2-\delta}$ (GDC) and $La_{0.9}Sr_{0.1}Ga_{0.8}Mg_{0.2}O_{3-\delta}$ (LSGM).

Under the same thermal treatment investigated for the 16a_p phase, BSCF decomposes into an insulating hexagonal perovskite[140, 142, 143, 209-211] and a second phase with plate-like morphology that is rich in Co and poor in Sr compared to cubic $Ba_{0.5}Sr_{0.5}Co_{0.8}Fe_{0.2}O_{3-\delta}$.[141, 142] BSCF also reacts with SDC under these conditions.[212]

Phase(s) / Axis	*a* (Å)	*b* (Å)	*c* (Å)
16a$_p$ as-made	5.4824(1)	61.291(1)	5.5497(1)
	Tests carried out at 950 °C for five hours		
16a$_p$ 950 °C	5.4800(1)	61.279(3)	5.5457(1)
16a$_p$ with GDC 950 °C	5.4808(3)	61.311(8)	5.5478(3)
16a$_p$ with SDC 950 °C	5.4836(4)	61.35(1)	5.5490(4)
16a$_p$ with LSGM 950 °C	5.4772(3)	61.226(8)	5.5465(5)
	Tests carried out at 750 °C for five days		
16a$_p$ 750 °C	5.4814(1)	61.242(3)	5.5452(1)
16a$_p$ with GDC 750 °C	5.4840(3)	61.255(9)	5.5472(4)
16a$_p$ with SDC 750 °C	5.4826(4)	61.25(1)	5.5474(4)
16a$_p$ with LSGM 750 °C	5.4789(4)	61.193(8)	5.5440(7)

Table 3.3 Lattice parameters of 16a_p phase before and after thermal stability and chemical compatibility tests at 950 °C for five hours and 750 °C for five days with electrolytes GDC, SDC and LSGM.

Phase stability is essential for a functional material used within a device under operating conditions, therefore these first results were a promising start. However, to study the long term stability of the 16a_p phase, samples were annealed under the quite extreme conditions of a flowing atmosphere of 100 % CO_2 at 750 °C for 24 hours. The stability was characterised by PXRD and it was observed that there was no degradation of the 16a_p phase and no new phase formation, as seen in Figure 3.15. This is another promising property exhibited by the 16a_p, with the lattice parameters also remaining constant before and after the treatment. Many other cathodes containing alkaline-earth elements have a low tolerance for CO_2,[137-139] particularly those that contain Ba, decomposing into carbonates in its presence.[133-136] This then leads to the requirement of CO_2 removal from air before it reaches the cathode, reducing the viability and flexibility of the fuel cell.[37] The tolerance that the 16a_p phase shows for such a high concentration of CO_2 is another case where this material shows promise.

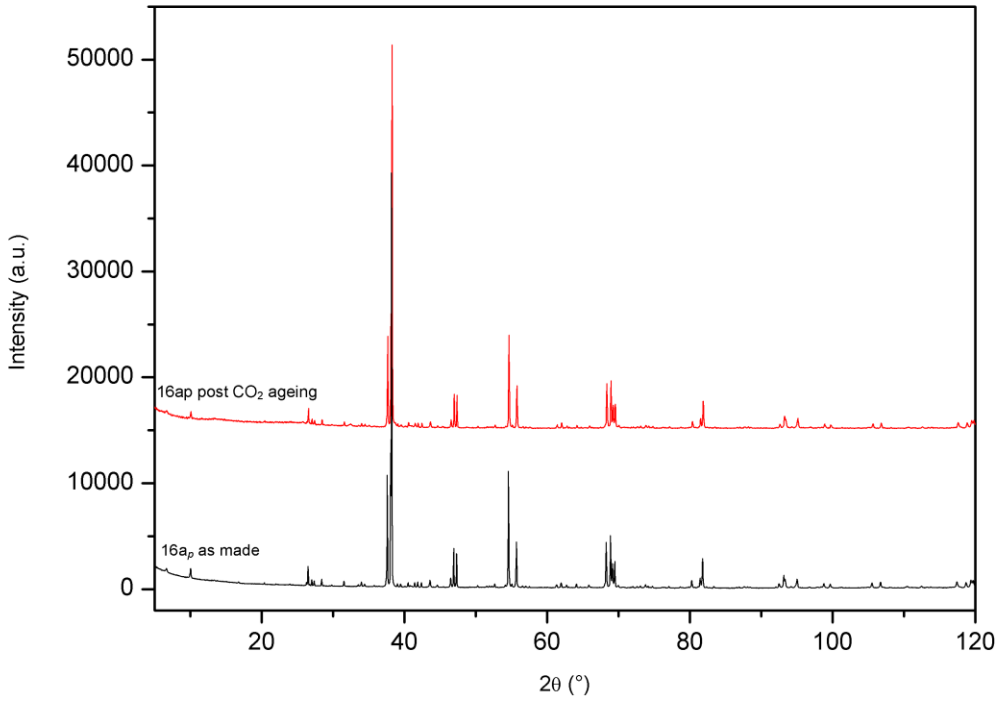

Figure 3.15 PXRD of as made 16a_p and after aging in 100 % CO_2 for 24 hours at 750 °C.

The TEC for each lattice parameter of the 16a_p phase was determined by variable temperature SXRD from 200 °C to 600 °C with increments of 50 °C. Each data set had the lattice parameters determined by Rietveld refinement, with each of the data points plotted below in Figure 3.16 A and B. The 16a_p phase shows anisotropic expansion, with expansion along *a* (11.3×10^{-6} K^{-1}) and *c* (9.0×10^{-6} K^{-1}) being similar, but along *b*, the stacking direction thermal expansion coefficient is roughly 1.5 times greater (16.9×10^{-6} K^{-1}). This anisotropic behaviour is not unusual for layered materials and has been reported before, with examples including the 10a_p[35], $YBa_2Cu_3O_7$[213] and Na_xCoO_2.[214]

Over the measured temperature range there appeared to be no significant change to the structure, with SXRD patterns remaining remarkably similar throughout heating. Lattice parameters were the only significant change with temperature (see Figure 3.17). This change in lattice parameters occurs linearly with temperature, also indicating no structural change or significant oxygen evolution occurs, which was backed up by a TGA measurement that showed no significant weight change (see Figure 3.16 C). The volumetric expansion of

$\alpha_v = 37.2 \times 10^{-6}$ K^{-1} (see Figure 3.16 C) as calculated from lattice parameter evolution, is comparable to state-of-the-art electrolytes GDC ($\alpha_v \approx 36.5 \times 10^{-6}$ K^{-1}),[215] SDC ($\alpha_v \approx 37.5 \times 10^{-6}$ K^{-1}),[157] LSGM ($\alpha_v \approx 33 \times 10^{-6}$ K^{-1}).[216] The close matching thermal expansion means that delamination of the 16a_p as a cathode printed onto the electrolyte would be unlikely during operation. This is a well-known problem for many other cathodes, especially Co rich phases such as LSC, BSCF and $Sm_{0.5}Sr_{0.5}CoO_{3-\delta}$ (SSC), which have volumetric TECs in the region of 60×10^{-6} K^{-1}.[37]

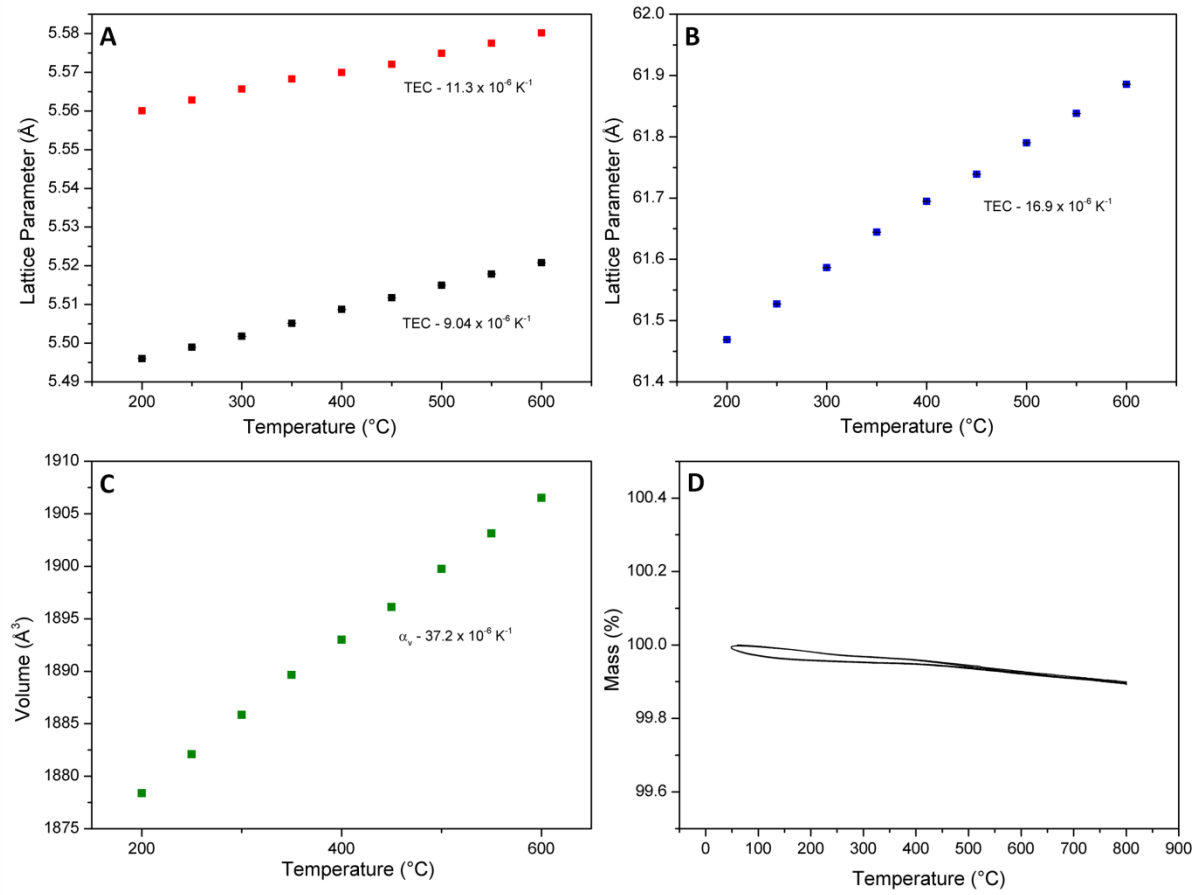

Figure 3.16 Plots of the expansion of lattice parameters versus temperature (error bars within points) together with TEC for lattice parameters A) *a* (black), *c* (red), B) *b* (blue) and C) Volume (olive). D) shows TGA experimental results of mass versus temperature.

The TGA experiment was undertaken using ~ 100 mg hand ground sample inside a Pt crucible. The measurement was undertaken using a TA Instruments Q600 thermal analyzer

with a 100 ml per minute gas flow rate (10 % N_2, 90 % atmospheric air), heating rate of 3 °C per minute from 50 °C to 800 °C, a dwell time of 1 hour at 800 °C and cycled twice.

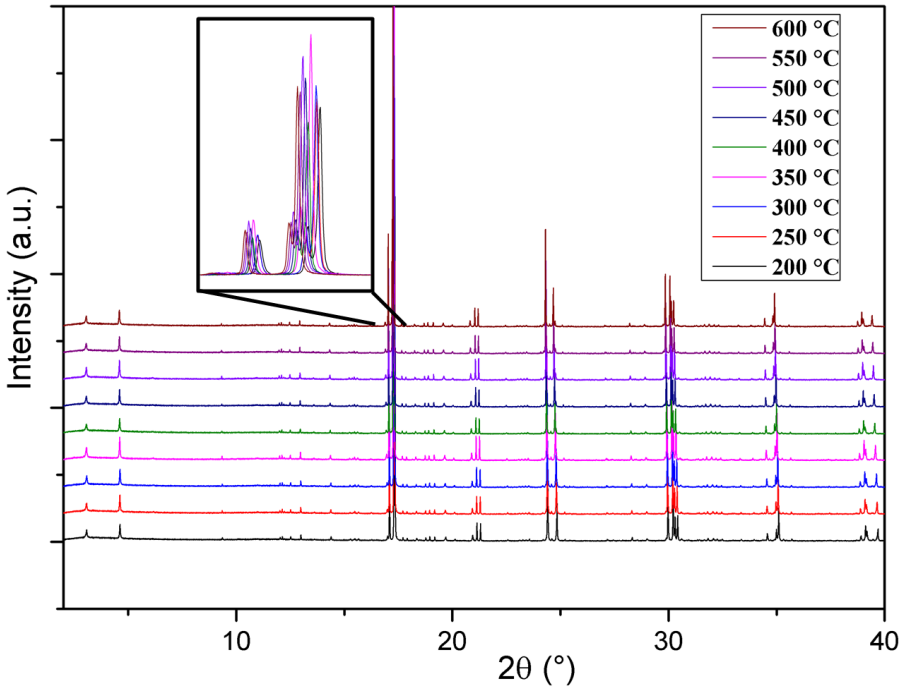

Figure 3.17 VT-SXRD patterns of the 16a_p, $Y_{2.24}Ba_{2.28}Ca_{3.48}Fe_{7.44}Cu_{0.56}O_{21-\delta}$, taken at 50 °C increments over a range of 200 - 600 °C. Patterns show no significant change other than lattice parameter evolution.

3.3.2 Electrochemical behaviour

Electronic conductivity is an important property for a cathode to display, as it is required for the transport of electrons to the triple phase boundary (TPB) in order to reduce O_2 into $2O^{2-}$. DC conductivity of the 16a_p phase was measured in order to obtain its electronic conductivity. Ionic conductivity is usually assumed to have such a small contribution (1 - 2 orders of magnitude lower) under these conditions, the measured value can be assumed to be only electronic.[217] Measurement was carried out as detailed in section 2.10.1.

DC conductivity was then measured using the standard four-probe method from 800 °C to 350 °C on cooling at 50 °C increments. The results from this measurement can be seen below

in Figure 3.18. The 16a_p phase displayed semi conducting behaviour, with a low electronic conductivity comparable to the 10a_p phase. At 800 °C the 16a_p phase has a conductivity of 3.68 S.cm^{-1}, similar to 2.33 S.cm^{-1} for the 10a_p phase and around 10^{-2} smaller than LSCF of 333 S.cm^{-1}.[218] This low conductivity can be attributed to, as with the 10a_p phase, a lack of charge carriers. This is indicated by the Mössbauer and iodometric titration analysis in section 3.2.1, which both confirmed Fe^{3+} was the only form present. The activation energy E_a, calculated for conductivity between 500 - 800 °C is 0.111(4) eV, which is close to that of $Ca_2Fe_2O_5$, and is associated to the small polaron mechanism.[219]

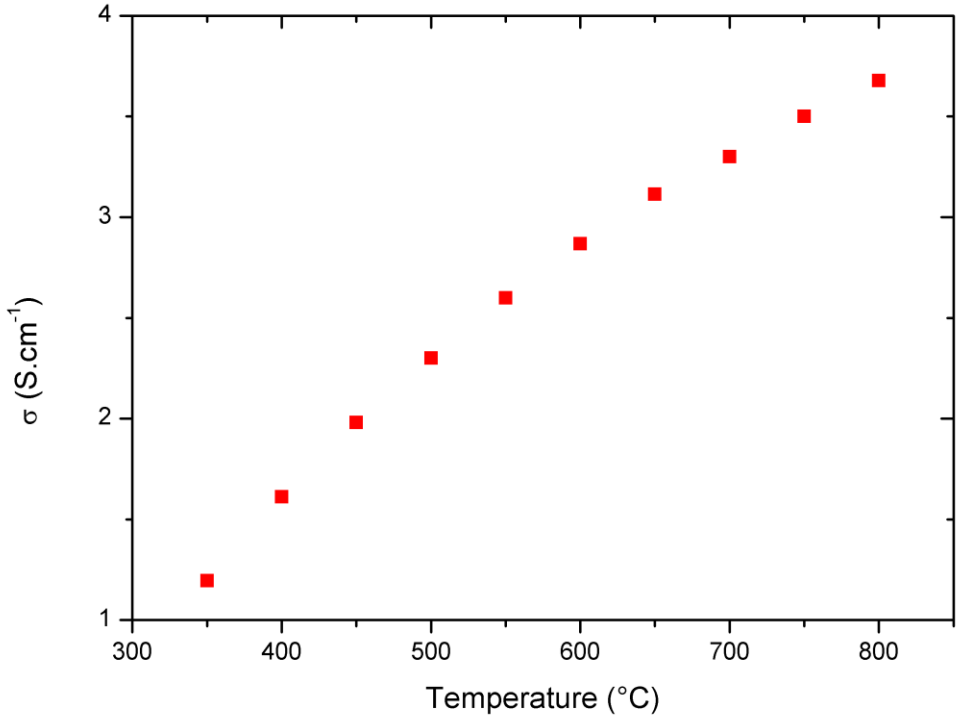

Figure 3.18 Electronic conductivity of the 16a_p $Y_{2.24}Ba_{2.28}Ca_{3.48}Fe_{7.44}Cu_{0.56}O_{21}$ as measured via DC conductivity, collected upon cooling from 800°C to 500°C.

Although the electronic conductivity of the 16a_p phase is quite low, it is not necessarily the defining property for a cathode as long as it is not too low as to become the limiting factor to performance. BSCF is a prime example of a cathode with relatively low electronic conductivity (although higher than the 16a_p) compared to other well-known cathodes such as LSCF. It has an electronic conductivity 10^{-1} worse than LSCF, at around 45 S.cm^{-1}, but

despite this, it has the best known cathode performance at the intermediate temperature range.[34] The defining measurement that is used to determine a cathodes performance is AC impedance of a symmetric cell, which enables the determination of the Area Specific Resistance (ASR), which takes all properties into account, such as electronic conductivity, ionic conductivity, and electrochemical activity of the cathode.[220]

The cathode performance of the 16a_p phase was consequently investigated by AC impedance of a symmetrical cell fabricated with 16a_p cathode on each side of a GDC electrolyte substrate, as detailed in section 2.10.2. Cathode inks were then prepared by ballmilling this powder with an organic binder for 18 hours, in the weight ratio 67:33 powder to binder. The electrode ink was applied to both surfaces of the electrolyte substrate by screen printing in one layer. The cell was dried at 100 °C for 1 hour between the application of each layer followed by a final heating in air at 950 °C for 1 hour to achieve good adherence of the electrodes to the electrolyte surface. This was used as the temperature for stability tests discussed in section 3.3.1. The contacts for the electrical measurement were gold wire and gauze fixed in position with gold paste, which were attached to the cell by heating to 800 °C for 1 hour.

AC impedance measurements were recorded over the frequency range 1 MHz to 0.01 Hz using a Solartron 1260 FRA with a modulation potential of 10 mV, over the temperature range of 500 °C to 800 °C in static air. The symmetrical cell was held for 90 minutes at each temperature to allow thermal equilibration and measurements were made using ZPlot v.2.9b (Scribner Associates) every 50°C. The area specific resistance (ASR) of the cathode was calculated by fitting the data using ZView.[189] The data were fitted with an Inductor (I) and two Resistors (R) in series with associated Constant Phase Elements (CPE) in parallel with each resistor. The ASR was then calculated by normalizing the measured resistance for the electrode area and dividing by two to take into account the symmetry of the cell.

Figure 3.19 A below displays a Z'-Z'' plot of the data obtained for the 16a_p cathode on a GDC electrolyte substrate. The 16a_p phase has an ASR of 0.27 $\Omega.cm^2$ at 700 °C and compares favourably to well-known cathode LSCF (0.46 $\Omega.cm^2$)[218] prepared in a similar way and the original 10a_p published data (0.88 $\Omega.cm^2$).[35] Table 3.4 shows the values of ASR and DC conductivity for the 16a_p phase between 500 and 800 °C. The ASR of the 16a_p phase falls below 0.15 $\Omega.cm^2$ at 750 °C, a target suggested by Steele for each of the three main

components of a fuel cell, the cathode, anode and electrolyte.[221] It could therefore be suggested that the potential operating temperature of a cathode produced from the 16a_p phase would be 750 °C, within the commonly quoted 500 - 800 °C intermediate operating temperature range.[38] The E_a of the ASR for the 16a_p phase is 1.57(4) eV, slightly higher than was reported for the 10a_p phase (1.43 eV). This could be due to the lower frequency of S_q sites per polyhedra within the structure, which are thought to be the electrochemically active site.[35] The error on the E_a of the ASR was calculated from a linear regression using the computer software Excel. An R^2 = 0.9963 obtained for data suggests that the limiting step for the performance of the 16a_p phase as a cathode is dominated by one single process, or processes of a similar E_a.

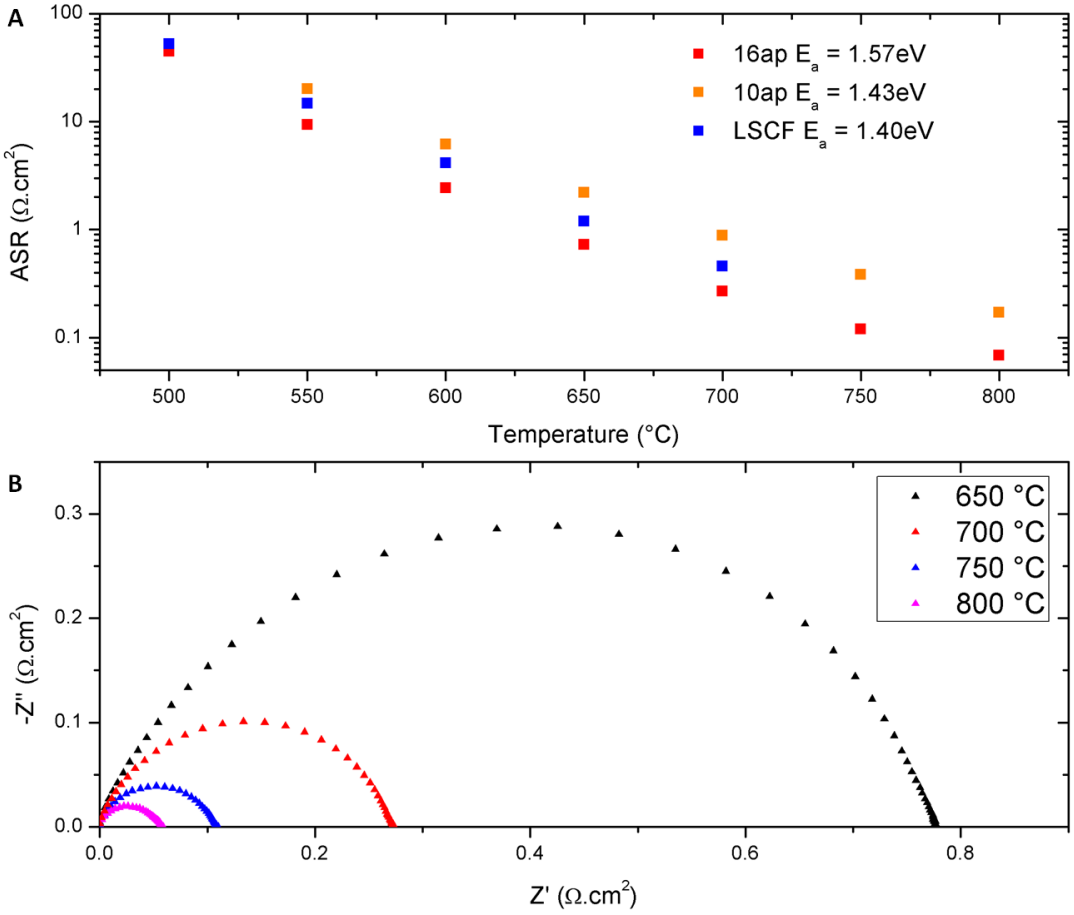

Figure 3.19 A) comparison of ASR versus temperature for the 16a_p (red), 10a_p[35] (orange) and LSCF[218] (blue) together with their E_a B) Z'-Z'' plot showing cathode performance of the 16a_p in a symmetrical cell on a GDC electrolyte at temperatures between 650 °C and 800 °C.

Temperature (°C)	ASR ($\Omega.cm^2$)	Conductivity ($S.cm^{-1}$)
500	44.56	2.30
550	9.40	2.60
600	2.43	2.87
650	0.73	3.11
700	0.27	3.30
750	0.12	3.50
800	0.068	3.68

Table 3.4 Values of ASR measured for a symmetrical cell on a GDC electrolyte and electronic conductivity measure by DC conductivity on a dense bar.

3.3.3 Post Impedance analysis

Cathode microstructure was examined using a Hitachi S-4800 field-emission scanning electron microscope. Figure 3.20 shows an SEM image taken at the surface of the cathode that was printed to create a symmetrical cell. The surface appears to show a large amount of porosity, which should aid the diffusion of O_2 onto the surface of the cathode. It should be noted that considerable time was not spent attempting to optimise the cathode microstructure, through imaging cathodes under different conditions.

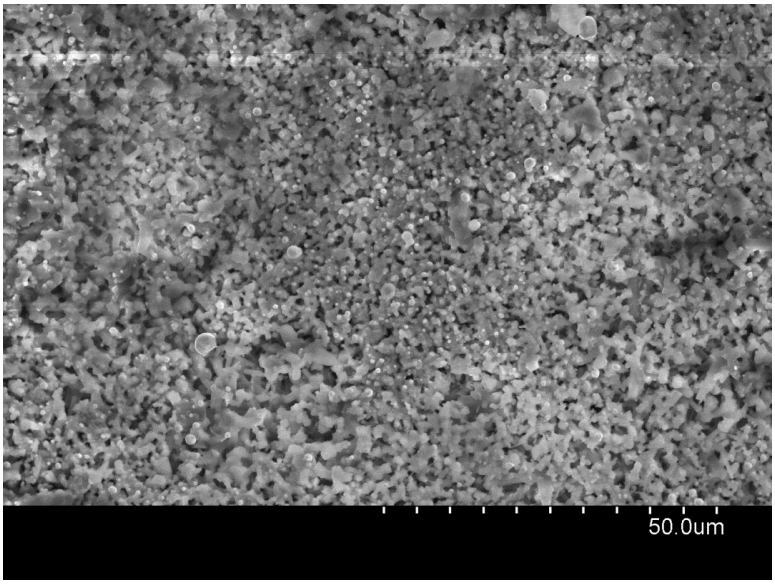

Figure 3.20 SEM image of the porous cathode surface printed onto a GDC substrate.

SEM was used to analyse symmetrical cells post AC impedance measurement. The cells were firstly broken into smaller pieces to obtain a sheared face, before the gold contacts were removed from the cathodes surface. The fractured edge of the cell was then imaged, with the composition also analysed from the electrolyte across to the cathode via EDX line scanning. Figure 3.21 shows an image of the region in which the EDX line scan was performed upon, with the electrolyte/cathode interface highlighted. Below this is the relative abundance of each element that corresponds to the above SEM image.

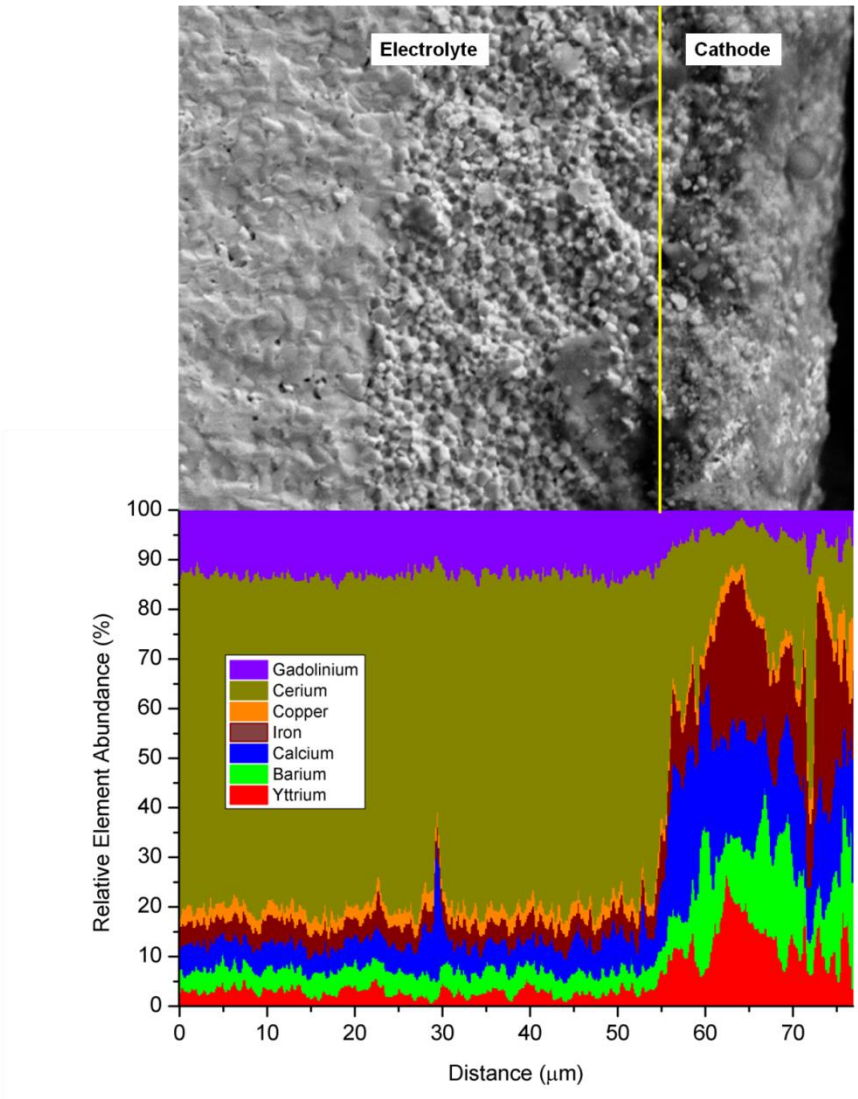

Figure 3.21 SEM image of electrolyte/cathode interface together with EDX data obtained from line scan across region shown.

From the start point of the data collection, there is a very high relative abundance of the cations that the electrolyte substrate consists of, Ce and Gd, from 0 to 55 μm. At this point, there is a sharp decrease in the presence of Ce and Gd and an increase in Y, Ba, Ca and Fe, the main constituents of the cathode. Due to the small percentage of Cu that makes up the cathode, it is unsurprising that the amount detected throughout the scan changes little.

The EDX analysis matches up well with the image above, highlighting more clearly the interface between the electrolyte and the cathode. The cathode has a slightly darker contrast than the electrolyte in the image and is roughly 20 μm thick. The EDX analysis also shows that there is little reactivity between the electrolyte and cathode due to the sharp decrease in electrolyte cations Ce/Gd and increase of cathode cations Y/Ba/Ca/Fe at 55 μm, the interface. Together with the small deviations in lattice parameters for the chemical compatibility tests shown in Table 3.3, this provides further evidence for that cation diffusion between cathode and GDC electrolyte must be on a small scale.

3.4 Discussion

This chapter focused on the discovery and isolation of a new *A*-site ordered perovskite with ordered oxygen vacancies and a 16a_p stacking axis, which we refer to as "the 16a_p". The first evidence of its existence was observed whilst attempting to dope a 10a_p, $Y_{0.9}Ba_{1.7}Ca_{2.4}Fe_5O_{13-\delta}$,[35] with 10 % Cu, which was substituted for Fe on the *B*-site in order to try to introduce charge carriers to increase the electronic conductivity. However in doing so, a multiphasic sample was produced (see PXRD pattern in Figure 3.2), which contained a 10a_p phase and the 16a_p phase, which was identified from TEM SAED and EDX as seen in Figure 3.9.

In order to isolate the 16a_p phase, a range of compositions were prepared. During these synthetic attempts, four long axis perovskites were identified; two different 10a_p phases, a 3a_p phase and the 16a_p phase, which were all differentiated by the low angle reflections indicative of each phase observed in PXRD patterns (see Figure 3.6 B). The 16a_p phase was finally isolated by quenching a sample with composition $Y_{2.24}Ba_{2.28}Ca_{3.48}Fe_{7.44}Cu_{0.56}O_{21-\delta}$,

from its synthesis temperature of 1200 °C, cooling it close to room temperature within seconds. This shows the $16a_p$ phase to be a thermodynamically accessible metastable phase.

The $16a_p$ phase was fully indexed using SAED to $a_p\sqrt{2} \times 16a_p \times a_p\sqrt{2}$, $\alpha = \beta = \gamma = 90°$, with the space group *Imma*. With this information available, a starting model was developed using the computational approach known as EMMA.[197] The model developed using the composition $Y_2Ba_2Ca_4Fe_8O_{21}$, was then used as the starting point for a combined ND and SXRD Rietveld refinement for data collected on the non-quenched experimental composition $Y_{2.24}Ba_{2.28}Ca_{3.48}Fe_{7.44}Cu_{0.56}O_{21-\delta}$. The structure remained largely the same, with only oxygen positions moving significantly (see Figure 3.11), although the coordination geometries of Fe-O remained the same, with Mössbauer confirming Fe^{3+} coordination environments of Oh, Sq, and Td in a 2:1:1 ratio (Figure 3.10). HAADF-STEM images taken for the experimental sample also matched up well to simulated images based upon the refined structure, giving further confirmation that the obtained structure was correct for the $16a_p$ phase.

As seen in Figure 3.1, the $10a_p$ phase can be thought of as an intergrowth between $YBa_2Fe_3O_8$[65] and $Ca_2Fe_2O_5$,[190] leading to an extended structure. The $16a_p$ phase can also be seen as an extended structure arising from the intergrowth of two phases. In this case it is between $YBa_2Fe_3O_8$[65] and $YCa_4Fe_5O_{13}$[222] as demonstrated in Figure 3.22 below. Considering the $16a_p$ and $10a_p$ extended structures exist as intergrowths from other smaller building blocks, it may be possible to combine other building blocks to produce new extended structures.

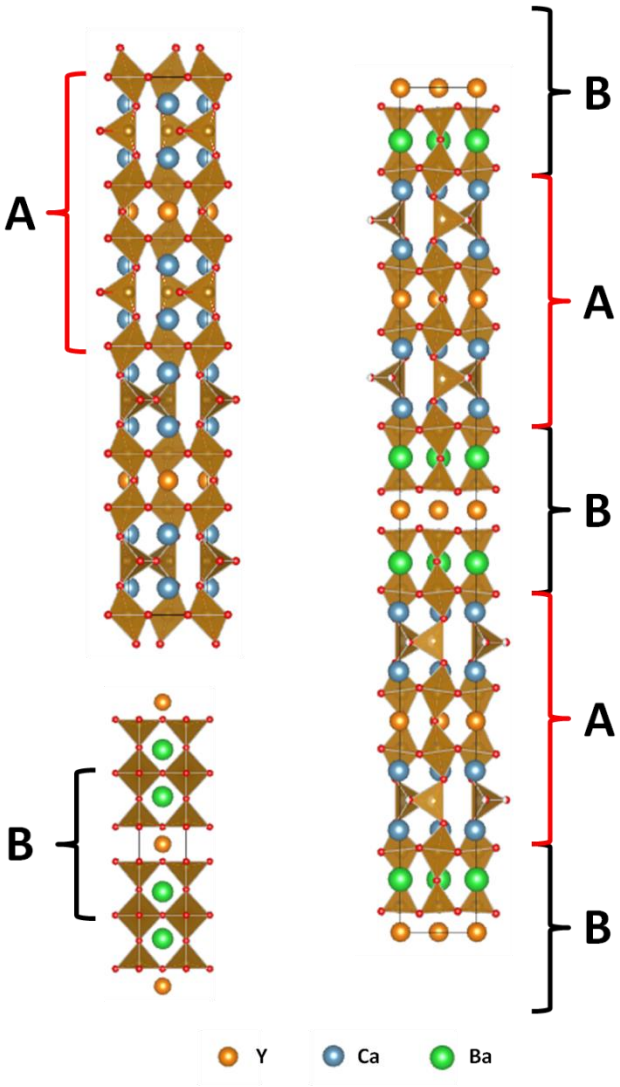

Figure 3.22 Structures of $YCa_4Fe_5O_{13}$,[222] $YBa_2Fe_3O_8$[65] and the ideal 16a_p intergrowth $Y_2Ba_2Ca_4Fe_8O_{21}$. Building units A and B of the two former structures are regularly stacked in a 1:1 ratio to form the ideal structure.

When considering the 16a_p phase as a potential cathode, there are specific requirements that it must possess. Figure 3.14 demonstrates the excellent thermal stability and chemical compatibility of the 16a_p phase, through the lack of detectible degradation or new phase formation. The lattice parameters in Table 3.3, together with the SEM EDX analysis, displayed in Figure 3.21, show the 16a_p phase displays chemical compatibility with state-of-the-art electrolytes GDC, SDC and LSGM, although a small amount of cation diffusion may occur between phases, indicated by the small changes in lattice parameters. Under the same conditions, BSCF both decomposes into an insulating hexagonal perovskite[140, 142, 143, 209-211] and a morphologically plate-like phase[141, 142] and reacts with SDC.[212] The 16a_p phase also

displays excellent stability in the presence of 100 % flowing CO_2 at 750 °C for 24 hours (see Figure 3.15), whereas other Ba rich cathodes such as GBCO decompose into $BaCO_3$.[158] The stability displayed by the 16a_p phase is not something to be taken lightly when considering the large Ba (almost 1/3 of the total *A*-site) content in the phase. The cathode BSCF, $Ba_{1-x}Sr_xCo_{0.8}Fe_{0.2}O_{3-\delta}$, shows carbonate formation not only for well know composition at x = 0.5,[223] but also for up to x = 0.8 (1/5 Ba content on *A*-site).[224]

The rate that component materials of a SOFC expand on heating is important, as if components of a single device expand at a very different rate, delamination can occur, at the very least deteriorating the operational efficiency.[225-227] The volumetric TEC of the 16a_p phase was determined to be $\alpha_v = 37.2 \times 10^{-6}$ K^{-1} and is highly comparable to state-of-the-art electrolytes GDC ($\alpha_v \approx 36.5 \times 10^{-6}$ K^{-1}),[215] SDC ($\alpha_v \approx 37.5 \times 10^{-6}$ K^{-1}),[157] and LSGM ($\alpha_v \approx 33 \times 10^{-6}$ K^{-1}).[216] This is a further advantage that this material possesses over some of the Co rich phases such as GBCO ($\alpha_v \approx 60.3 \times 10^{-6}$ K^{-1})[157] and $Sm_{0.5}Sr_{0.5}CoO_{3-\delta}$ (SSC $\alpha_v \approx 61.5 \times 10^{-6}$ K^{-1}).[228]

In the 16a_p phase, Fe is only found in its Fe^{3+} oxidation state, as determined by iodometric titration and Mössbauer spectroscopy (see Figure 3.10), which leads to a lack of charge carriers. Due to this, the electronic conductivity of the 16a_p phase, as measured by DC conductivity, is two orders of magnitude lower than LSCF, which has charge carriers in the form of Fe^{3+}/Fe^{4+} and Co^{3+}/Co^{4+}.[218, 229] However despite this, the overall electrochemical performance, as indicated by the ASR, compares favourably. The 16a_p phase achieves an ASR of 0.27 Ω.cm^2 at 700 °C (see Table 3.4), whereas LSCF prepared and measured in a comparable fashion is 0.46 Ω.cm^2 at the same temperature, despite the much larger electronic conductivity. The ASR of LSCF has been reported at much lower values, which required preparation of a cell under different fabrication conditions such as composites,[94] and wet infiltration.[230] The 10a_p phase has also seen improvement in performance, through alterations in milling and fabrication temperatures, which has led to the ASR being equivalent to that of the 16a_p phase, also below 0.15 Ω.cm^2 at 750 °C.[162] This may also be possible to duplicate for the 16a_p phase. The 16a_p phase achieved an ASR of below 0.15 Ω.cm^2 at 750 °C, showing its potential to operate at an intermediate range. It is appropriate to compare cathodes with similar stabilities to the 16a_p phase such as LSCF and the 10a_p phase, however, in terms of cathode performance the 16a_p phase falls behind the leading materials such as BSCF, SSC

and GBCO, especially at lower temperatures.[63, 231, 232] Obtaining a viable cathode may require a trade-off of improved phase stability for lower cathode performance.

3.5 Conclusion

In summary, the work presented in this chapter shows the discovery, isolation and characterisation of a new *A*-site ordered perovskite phase. The discovery was made whilst attempting to synthesise $Y_{0.9}Ba_{2.4}Ca_{2.4}Fe_{4.5}Cu_{0.5}O_{13-\delta}$, a doped 10$a_p$ phase. Low angle reflections were observed in PXRD patterns that were not related to the 10a_p phase, which was followed up by carrying out SAED in order to identify the unknown phase. The unknown phase was eventually identified as the 16a_p phase, which was subsequently isolated and characterised.

The structure consists of *A*-site ordering of Y, Ba and Ca, with Fe and Cu found on the *B*-site in three different coordination environments: O_h, S_q and T_d in a 2:1:1 ratio. The extended structure can be thought of as an intergrowth between $YBa_2Fe_3O_8$ and $YCa_4Fe_5O_{13}$, leaving the question, are there other extended structures waiting to be unearthed? This discovery also shows the importance of scrutinising all data and following up on unknowns, as new breakthroughs can happen by chance as much as by design.

Future work on the 16a_p phase could include investigating symmetrical cell preparation and cathode processing conditions in order to try and reduce the ASR. Doping studies could also be considered, with the same goal of a reduced ASR in mind. Due to the anisotropic nature of the structure, it would also be interesting to look into thin film growth of this material, as for the 10a_p phase, which has been grown as a thin film on $SrTiO_3$ via pulsed laser deposition resulting in an order of magnitude higher conductivity than for the bulk.[233]

4 Synthesis and Characterisation of $Y_{0.9}Ca_{2.4}Sr_{1.7}Fe_5O_{13\pm\delta}$, YCSFO

4.1 Introduction

Following the discovery of the 16a_p phase described in chapter 3, identified alongside the previously reported 10a_p phase ($YBa_2Ca_2Fe_5O_{13}$ type) a second unreported 10a_p phase ($YBaCa_3Fe_5O_{13}$ type) and a 3a_p phase, the potential for discovering other long axis perovskites became apparent. Calculations using EMMA were performed by M. Dyer and C. Collins that suggested potential compositions with a 7a_p structure may form (described in SI of paper)[197]. The three lowest energy compositions identified were $YBa_2Ca_4Fe_7O_{18}$, $YBa_4Ca_2Fe_7O_{18}$ and $YBa_3Ca_3Fe_7O_{18}$.

Synthesis carried out using these compositions only produced samples with 10a_p and 16a_p phases identified, therefore new compositions were considered. A complete substitution of the smaller Sr cation (1.44 pm) for the larger Ba cation (1.61 pm)[234] was considered, as after normalisation of O content down to one single perovskite unit, the 7a_p (O = 2.57) would be less oxidised than the 10a_p (O = 2.6) or 16a_p (O = 2.63). Sr^{2+} is less electropositive than Ba^{2+} and is therefore more likely to be stable in a lower oxidised phase such as the proposed 7a_p structure.

On synthesis of $YCa_4Sr_2Fe_7O_{18}$, $YCa_2Sr_4Fe_7O_{18}$ and $YCa_3Sr_3Fe_7O_{18}$, although no 7a_p was formed, another long axis phase was identified by PXRD. This long axis phase was investigated and is reported in this chapter.

4.2 Experimental/Synthesis

4.2.1 Discovery

Using the standard solid state synthesis route, samples with compositions $YCa_4Sr_2Fe_7O_{18}$, $YCa_2Sr_4Fe_7O_{18}$ and $YCa_3Sr_3Fe_7O_{18}$ were produced. 0.5 g was synthesised by hand grinding

dried powders of Y_2O_3 (99.999 %), $SrCO_3$ (99.995 %), $CaCO_3$ (99.995 %) and Fe_2O_3 (99.945 %), all sourced from Alpha Aesar, in the required ratios in a pestle and mortar. The mixed powder was heated in a furnace to 1200 °C at a rate of 5 °C per minute in an Al_2O_3 crucible in static air. After dwelling at 1200 °C for 12 hours, the furnace was cooled at 3 °C per minute down to room temperature. The black crystalline material obtained was then hand ground using a pestle and mortar and a room temperature PXRD pattern was collected. The sample was then pressed into 13 mm pellets using a uniaxial press and the heat treatment was repeated, with the resultant sample hand ground in a pestle and mortar and analysed by PXRD.

This synthesis afforded a $10a_p$ phase (at $YCa_4Sr_2Fe_7O_{18}$), a cubic phase (at $YCa_2Sr_4Fe_7O_{18}$) and a mix of these two phases (at $YCa_3Sr_3Fe_7O_{18}$) as identified in PXRD patterns collected for each composition. The PXRD patterns of these samples are given in Figure 4.1, together with an insert showing a zoomed in region, which clearly displays reflections at low angle indicative of a long axis phase.

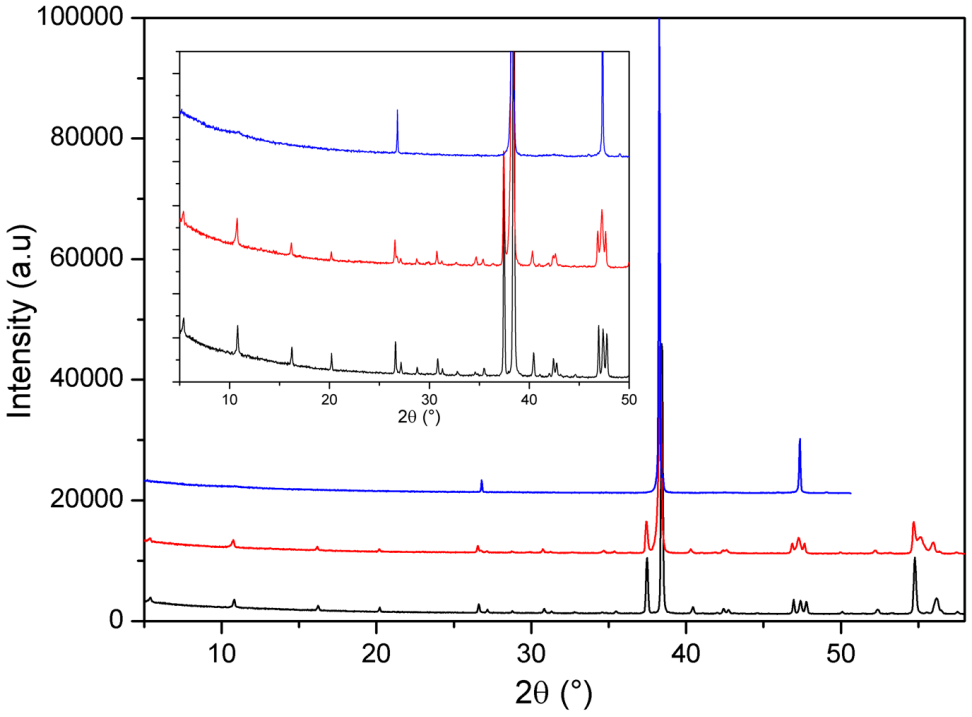

Figure 4.1 PXRD patterns collected for $YCa_4Sr_2Fe_7O_{18}$ (black), $YCa_3Sr_3Fe_7O_{18}$ (red) and $YCa_2Sr_4Fe_7O_{18}$ (blue) samples. The Insert shoes a zoomed in region more clearly displaying long *d*-space reflections and gradual pattern changes with composition.

As was also described for the $16a_p$ phase in section 3.2.2, the samples appeared to react with the Al_2O_3 crucibles that they were synthesised in, as staining of the crucibles was observed. EDX composition analysis was carried out on the phase pure sample, $YCa_4Sr_2Fe_7O_{18}$, in order to determine the cation ratio and to establish if Al incorporation from the crucible into the $10a_p$ phase occurred. This analysis showed that although no Al was incorporated, there was a significantly different *A*-site cation molar ratio compared to the starting values, whilst the standard perovskite the A/B ratio of 1:1 was retained. Normalising the composition to $A_5B_5O_x$, the EDX attained composition based on an average of four particles was $Y_{1.0(1)}Ca_{2.2(1)}Sr_{1.8(1)}Fe_5O_x$, compared to the $Y_{0.7}Ca_{2.9}Sr_{1.4}Fe_5O_x$ (in $A_5B_5O_x$ form) nominal composition.

From this point in the chapter, the $10a_p$ phase that forms with this $YCa_{2.2}Sr_{1.8}Fe_5O_x$ composition will now be referred to as YCSFO.

4.2.2 Isolation using the phase diagram approach

In order to carry out physical property measurements on YCSFO, large sample batches were needed. However, the problem of reactivity with the crucible had to be addressed prior the measurements in order to synthesise reproducibly large amounts of a phase pure $10a_p$ sample. New syntheses at various compositions were carried out in Pt foil lined Al_2O_3 or Pt metal crucibles, using the conditions described in section 4.2.1. A ternary phase diagram of *A*-Site cation ratios was constructed to guide synthesis, using the EDX given composition ($YCa_{2.2}Sr_{1.8}Fe_5O_x$) as the starting point, and selecting compositions around this in order to map the phase space.

PXRD patterns collected for each of the compositions were carefully analysed so that the main phases formed could be mapped onto the ternary phase diagram shown in Figure 4.2. Within the phase space explored, the formation of four readily identifiable main phases was observed. Two long period phases were observed, the YCSFO target $10a_p$ (a = 5.43424(6), b = 38.0147(4), c = 5.56989(5)), and a second $10a_p$ phase with smaller lattice parameters (a = 5.4277(2), b = 37.783(2), c = 5.5649(2)) found in a region poorer in Sr and richer in Ca. As there was no gradual change in lattice parameters to the smaller cell $10a_p$ that would be

expected from a solid solution, it appears to be a different phase. Full identification of this phase has not been carried out for this thesis however. The other two major phases observed in the PXRD patterns of samples rich in Sr and poor in Ca were a $3a_p$ phase and a cubic phase.

Within the region labelled as $10a_p$ formation in Figure 4.2, impurities were observed that could not be identified. The impurity peaks were observed partially overlapping with the highest intensity $10a_p$ perovskite reflections, the [1,10,1], [2,0,0] and [0,0,2]. It is likely that these impurities were perovskite related, possibly the $3a_p$ or cubic perovskites already identified previously, which have reflections in similar regions.

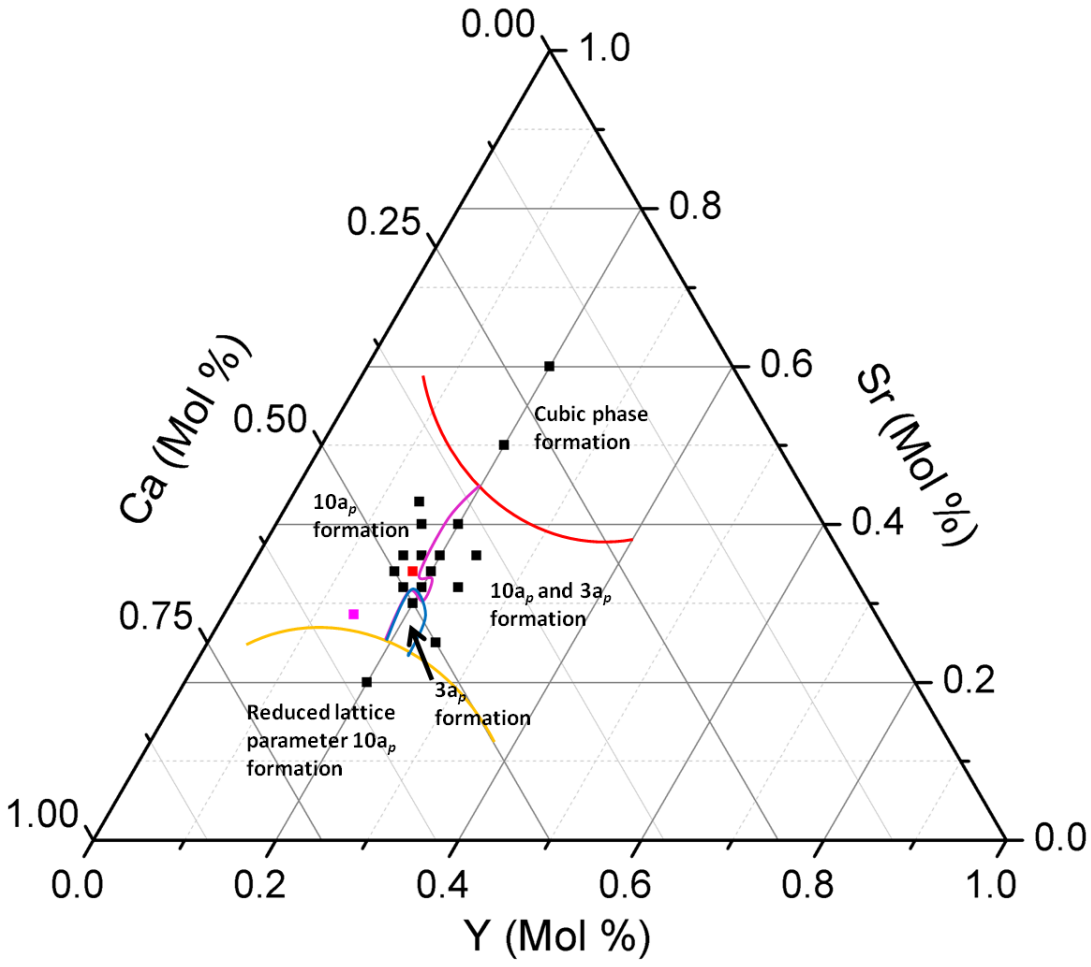

Figure 4.2 Ternary phase diagram showing variation in *A*-site cation ratios (Y, Ca and Sr) and displaying regions of phase formation of two $10a_p$ phases, a $3a_p$ phase and a cubic phase. Pure phase at $Y_{0.9}Ca_{2.4}Sr_{1.7}$ (red) and original composition synthesised YCa_4Sr_2 (magenta) highlighted.

Isolation of a phase pure sample was finally achieved through varying the *A*-site ratio and arriving at the required composition. No further variations to the reaction conditions were necessary and the final composition found was $Y_{0.9}Ca_{2.4}Sr_{1.7}Fe_5O_{13-\delta}$. Whilst this sample was being isolated, SXRD and ND data were collected on the original $YCa_2Sr_4Fe_7O_{18}$ sample ($YSr_{1.8}Ca_{2.2}Fe_5O_x$ EDX composition), which will be referred to as YCSFO(I). Crystal structure characterisation was carried out for this sample, which is described in section 4.3, together with TEC a measurement based on VT-SXRD data (section 4.4.1). Samples with the composition $Y_{0.9}Ca_{2.4}Sr_{1.7}Fe_5O_{13}$, appeared the same as the nominal $YCa_2Sr_4Fe_7O_{18}$ sample by PXRD. It was samples prepared at the composition $Y_{0.9}Ca_{2.4}Sr_{1.7}Fe_5O_{13}$ that were subsequently used for physical property measurements described in section 4.4. They will be referred to as YCSFO(II) when distinction is required from YCSFO(I).

4.3 Crystal Structure Characterisation

4.3.1 Testing models

Time-of-flight neutron diffraction (ND) data were collected on the POLARIS instrument, as detailed in section 2.2.10. SXRD data were obtained on Beamline I11 at Diamond Light Source, detailed in section 2.2.9, at a wavelength of 0.827153 Å over a 2θ range of 2 to 90° and a step size of 0.001°, using the PSD detector for a 0.2 mm capillary. A second wavelength was collected at the Sr K absorption edge of 0.770056 Å (ASXRD) over a 2θ range of 2 to 150° and a step size of 0.001°, using the MAC detector for a 0.1 mm capillary. Powder diffraction data were analysed in a combined X-ray and neutron Rietveld refinement using the computer program Topas Academic v5.[175]

Originally the crystal structure of YCSFO(I) was treated as a $Y_{0.9}Ba_{1.7}Ca_{2.4}Fe_5O_{13}$ $10a_p$ type phase.[35] As discussed in chapter 3, $Y_{0.9}Ba_{1.7}Ca_{2.4}Fe_5O_{13}$ ($10a_p$) can be considered as an intergrowth between $YBa_2Fe_3O_8$ and $Ca_2Fe_2O_5$.[35] For YCSFO, we considered that an intergrowth between $YSr_2Fe_3O_8$ and $Ca_2Fe_2O_5$ may give the same structure, as $YSr_2Fe_3O_8$ is isostructural to $YBa_2Fe_3O_8$.[235] Pawley fitting of SXRD data in the $10a_p$ space group, *Imma*, gave a good fit to the data with all peaks indexed (see Figure 4.3). YCSFO(I) was also

attempted to be indexed using a $5a_p$ stacking axis in *P*1 as the first observed reflection [0,2,0] is seen at ~ 19 Å, equivalent to a $5a_p$. However, with a unit cell of ~ 5.43 × 19 × 5.57 Å, several superstructure reflections could not be indexed and so this unit cell arrangement was disregarded. An orthorhombic unit cell of ~ 5.43 × 38 × 5.57 Å indexed all observed reflections for YCSFO(I), including those missed by the $5a_p$ such as the [0,3,1], [0,9,1] and [0,11,1].

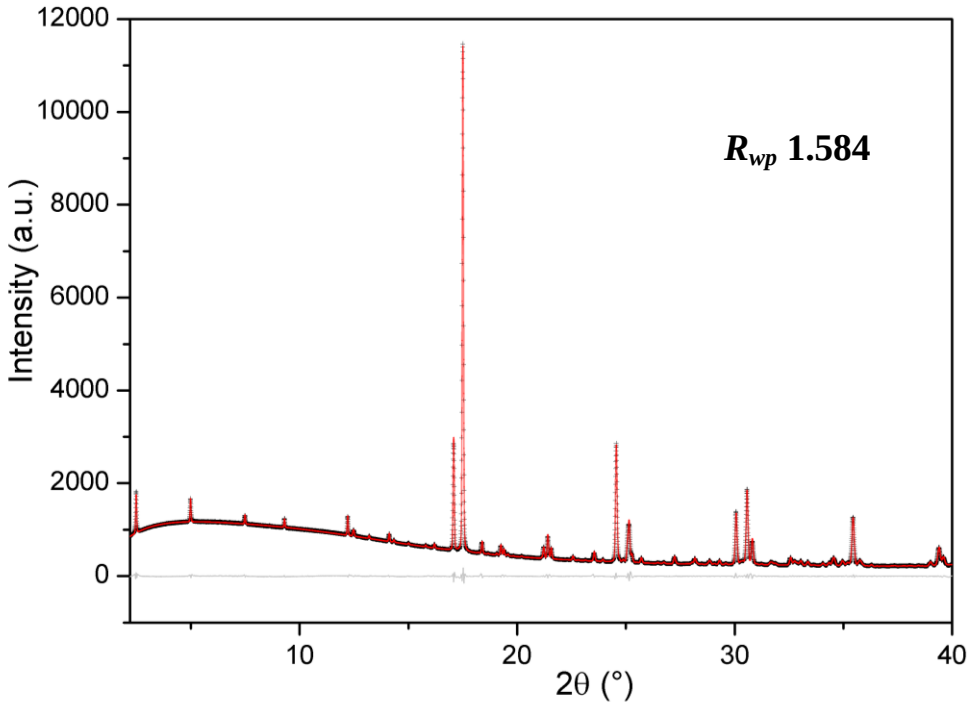

Figure 4.3 Pawley fit YCSFO(I) of SXRD data in *Imma* space group with observed data (black), calculated fit (red) and difference (grey) all shown together with the R_{wp}.

When performing a Rietveld refinement using the $Y_{0.9}Ba_{1.7}Ca_{2.4}Fe_5O_{13}$ $10a_p$ structure as the starting model, there were some significant misfits observed. A second starting model based on the known phase $YCa_4Fe_5O_{13}$[222] was considered. Both models are based on an orthorhombic a_p $\sqrt{2}$ × $10a_p$ × a_p $\sqrt{2}$, α = β = γ = 90°, *A*-site ordered perovskite. The models mainly differ in the Fe-O coordination geometries, with S_q-O_h-T_d-O_h-S_q ordering for the $Y_{0.9}Ba_{1.7}Ca_{2.4}Fe_5O_{13}$ $10a_p$ and O_h-T_d-O_h-O_h-T_d ordering for $YCa_4Fe_5O_{13}$. The structures of the

two described phases are shown below in Figure 4.4 as inserts within Rietveld plots from SXRD refinements using each model.

The two potential models can be distinguished by diffraction, as in the example shown in Figure 4.4, where SXRD data were used. ND would normally be the most appropriate method to screen the difference between the models due to the increased scattering from oxygen positions, which are the main difference between the models. However, peaks were also present due to magnetic ordering, making initial refinements of the different models more complicated. Fe in T_d sites particularly can be used to differentiate between the models due to its shifted position within the unit cell when compared to its position when in O_h or S_q coordination. For this purpose, SXRD data proved adequate to differentiate between the models.

Figure 4.4 shows that a better Rietveld refinement fit is achieved when using the $YCa_4Fe_5O_{13}$ model, particularly highlighted by the greater mismatch seen at high angle for the $Y_{0.9}Ba_{1.7}Ca_{2.4}Fe_5O_{13}$ model (see insets in Figure 4.4). Occupancy of the mixed *A*-site was initially allowed to refine as just Y, in order to represent the electron density of each *A*-site. Using the $YCa_4Fe_5O_{13}$ model, an R_{wp} of 2.182 was obtained for the SXRD data compared to 3.469 for the $Y_{0.9}Ba_{1.7}Ca_{2.4}Fe_5O_{13}$ model.

The models were also tested using ND data as well, once magnetic space groups could be determined (discussed later in section 4.3.2), with the best fit obtained again for the $YCa_4Fe_5O_{13}$ model. An R_{wp} for ND bank 5 data in this model was 7.654, compared to 10.187 for the $Y_{0.9}Ba_{1.7}Ca_{2.4}Fe_5O_{13}$ model. The fits were good indications that the correct model to use for this phase was based on $YCa_4Fe_5O_{13}$.

Iodometric titrations were carried out for YCSFO(II) made at the composition $Y_{0.9}Ca_{2.4}Sr_{1.7}Fe_5O_{13}$ in order to determine the oxygen content, as detailed in section 2.6. Assuming reduction to Fe^{2+},[185] and using the nominal composition for the cations, the oxygen content was calculated giving a full composition of $Y_{0.9}Ca_{2.4}Sr_{1.7}Fe_5O_{12.95(2)}$. This corresponds to an Fe^{3+} oxidation state. This oxidation state commonly obtained for pure Fe *B*-site perovskites made in air, with examples such as the $10a_p$ phase,[35] $Ca_2Fe_2O_5$[236] and $YFeO_3$.[237] This oxygen content could then be used to inform the Rietveld refinements, giving confidence that each O site was fully occupied.

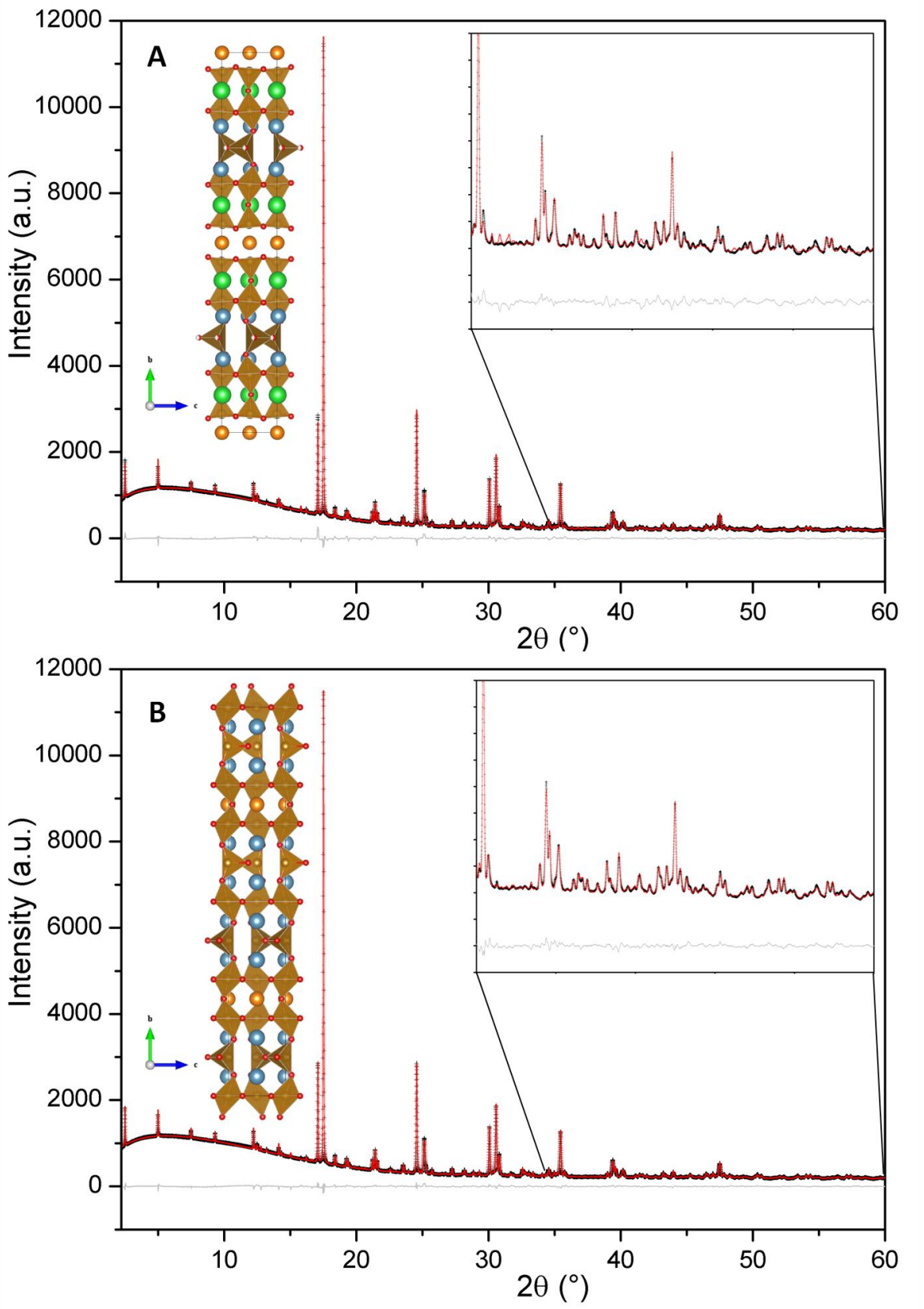

Figure 4.4 SXRD data refined with A) $Y_{0.9}Ba_{1.7}Ca_{2.4}Fe_5O_{13}$ $10a_p$ model and B) $YCa_4Fe_5O_{13}$ $10a_p$ model. Each starting structural model is shown as an insert within the refined histogram using it together with a zoomed high angle region highlighting the difference between the fits using the two models.

4.3.2 Magnetic model

Using the determined starting model, a Rietveld refinement was carried out using the SXRD and ND data. Within the ND data, peaks were present that could not have intensity assigned to them, although their *d*-spacing was characteristic of the unit cell. On heating from room temperature to 350 °C, the peaks diminished in intensity indicating that they could be attributed to magnetic ordering. The peaks did not disappear entirely at this temperature, suggesting that the magnetic ordering temperature, or Néel temperature (T_N), had not been reached (see Figure 4.5).

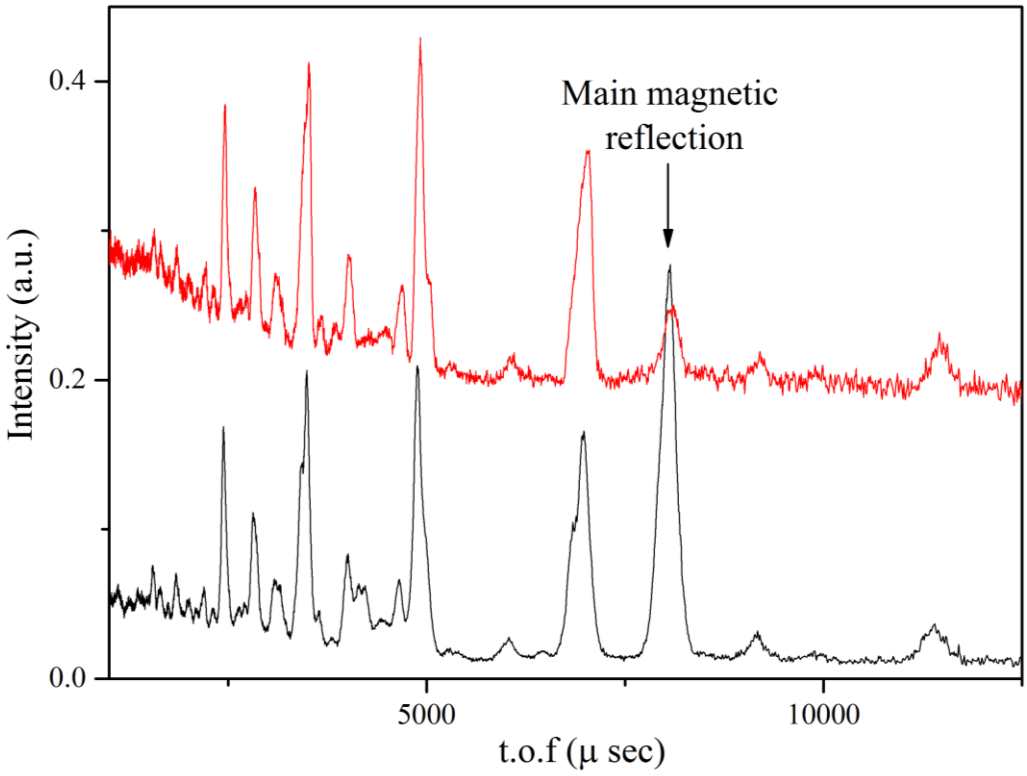

Figure 4.5 Bank 2 POLARIS ND data collected at room temperature (black) and 350 °C, which shows diminished intensity of the main magnetic reflection indicated with arrow (note, also a nuclear reflection due to **k** = 0,0,0 but of comparatively low intensity).

Possible *B*-site magnetic structures were determined by co-representational analysis using the computer program SARAh[200] and were screened against the observed neutron scattering data. The YCSFO(I) working model was imported into GSAS[174] together with ND banks 2 and 5 data sets in order to test magnetic models. The best fit was observed for a G-type antiferromagnetic structure (propagation vector **k** = 0,0,0) with moments oriented along the *a*-axis. This type of magnetic structure is common for related perovskites, as discussed in chapter 3.2.2.[35, 65, 190, 197] The magnitude of the magnetic moment along the *a*-axis on each *B*-site was refined using the SARAh determined magnetic space group *Pnma*, with moments of the three *B*-sites constrained to the same value. The magnetic moment refined to 3.390(7) μ_B, which compares very closely to Fe pure *B*-site perovskites the $10a_p$ 3.638(9) μ_B,[35] and $LaCa_2Fe_3O_8$ 3.4(2) μ_B.[238] The respective T_N of these phases are ~ 480 °C and 460 °C, meaning YCSFO is likely to have a T_N close to these temperatures based on the observed same magnetic ordering and similar magnitude of magnetic moment at room temperature.

The magnetic space group *Pnm'a* was also identified for the other potential structural model based on the $Y_{0.9}Ba_{1.7}Ca_{2.4}Fe_5O_{13}$ structure in order to fully examine it using ND as well as SXRD data as stated in section 4.3.1. As already discussed, a much inferior fit was obtained using this model, therefore it was taken no further.

4.3.3 Combined refinement

Now that the magnetic structure had been identified as well as the nuclear structure model, a complete combined Rietveld refinement was carried out using SXRD and ND data using Topas Academic v5.[175]. As the *A*-site contained three possible cations (Y, Ca and Sr), initially occupancies were refined using Y and Ca summed to a total of one on each *A*-site. This is because Y^{3+} and Sr^{2+} are indistinguishable by X-rays (both have 36 electrons) and have poor contrast in neutrons (bound coherent scattering lengths: Y 7.75 fm, Sr 7.02 fm).[168] A small compositional restraint was given for the *A*-site, set as the EDX given composition of $Y_{2.8}Ca_{2.2}$, with Sr included in the Y total.

Combined refinements were carried out in the space group *Pnma*, as well as an alternative space group $Pn2_1a$, which was also identified for the reported $YCa_4Fe_5O_{13}$ phase and has the

same reflection conditions.[222, 239] Though the best fit was obtained for the space group *Pnma*, during the refinement, it became obvious that the structure was not quite right due to differences in the fit and observations made from difference maps created from the observed − calculated fit. The Fourier difference maps showed that the T_d sites contained a mismatch, indicating that the site should be split along the *a*-axis (see Figure 4.6) creating disordered T_d Fe and O sites. This disordering is not possible using the *Pnma* space group with the $YCa_4Fe_5O_{13}$ structure without adding additional atoms.

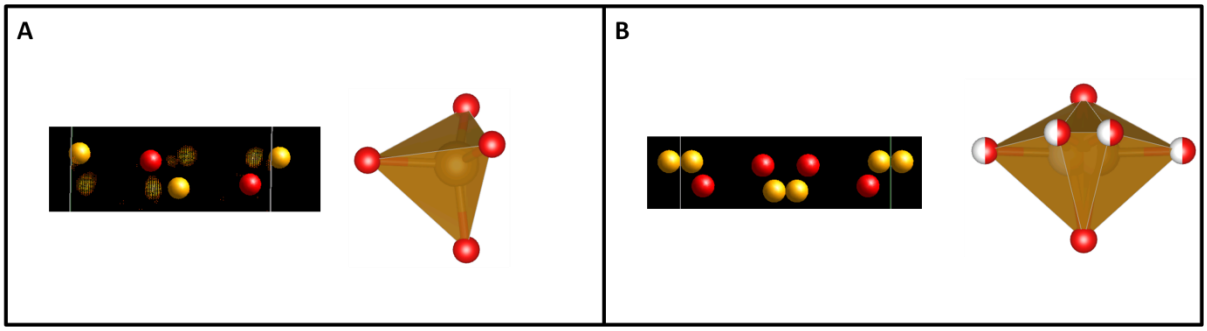

Figure 4.6 A) Using space group *Pnma*, left shows a Fourier map with Fe atoms (solid yellow), O atoms (solid red) and missing electron density (yellow pixels) for an ordered T_d site shown right. B) Using space group *Imma*, right shows disordered T_d site with split Fe and O sites (half white) due to presence of a mirror plane, also represented in Fourier map on left, which has no relative missing electron density. Difference Fourier maps generated from ND bank 5 data set.

It was decided to attempt to find an appropriate space group using the SXRD data rather than the ND data as this contained the additional complication of the presence of magnetic reflections. The lattice parameters and unit cell geometry were already identified, therefore the *hkl* reflections observed were listed where possible in order to obtain the reflection conditions. The reflection conditions are listed in Table 4.1 together with examples of reflections observed obeying the conditions. No reflections contradicting the conditions were observed and none were left without being indexed.

Reflection Conditions							
	hkl	0*kl*	*h*0*l*	*hk*0	*h*00	0*k*0	00*l*
	h+*k*+*l* = 2n	*k*+*l* = 2n	?	*h*,*k* = 2n	*h* = 2n	*k* = 2n	*l* = 2n
Examples of observed reflections	1 4 1	0 3 1		2 6 0	6 0 0	0 2 0	002
	1 6 1	0 7 1		2 10 0		0 4 0	
	1 1 2	0 9 1		2 12 0		0 6 0	
	1 3 2	0 6 2		2 14 0		0 12 0	
	2 5 1	0 8 2					

Table 4.1 Showing the reflection conditions and examples of the conditions observed in SXRD data. The "?" signifies unknown conditions due to overlap of potential *h*0*l* reflections with known reflections.

Due to overlap with other allowed reflections, *h*0*l* conditions could not be assigned. Based on the observed reflection conditions, the highest symmetry space groups allowed are *Imma*, *Immb*, *Im*2*a* and *I*2*mb* for $h + l$ = 2n, and *Imcb* and *I*2*cb* for *h*, *l* = 2n for *h*0*l* ambiguity. Combined refinements were carried out in all space groups, with the best fit obtained for the space group *Imma*, which also allowed for the modelling of the disordered T_d site. Together with *I*2*mb*, which has ordered T_d chains, they are not uncommon space groups to find for related structures. Brownmillerite phases such as $Sr_2Al_{1.07}Mn_{0.93}O_5$,[240] $Sr_2Co_2O_5$,[241], and $Ca_2Fe_2O_5$[242] have been reported in *Imma*. The Brownmillerite structure $Ca_2Fe_2O_5$ has also been reported to undergo a phase transition from *Pnma* at room temperature, to *I*2*mb* at ~ 700 °C,[190, 219, 243] and *Imma* at ~ 1300 °C.[244] The transition between the space groups occur due to changes in T_d ordering along the *a*-axis, where the two T_d in the unit cell point in opposite directions for *Pnma*, in the same direction for *I*2*mb*, and disordered in *Imma*.

As with the brownmillerite, the difference between the between the space groups *Pnma*, *I*2*mb* and *Imma* for the YCSFO structure is down to the T_d ordering. For *Pnma*, the T_d chains point right-right-left-left when looking down the *c*-axis, whereas in *I*2*mb*, the T_d chains all point in the same direction. Finally, for *Imma*, the T_d are disordered, as shown in Figure 4.7 along with the YCSFO structure represented in *Pnma* and *I*2*mb*. The T_d have been highlighted within the black boxes for ease of comparison.

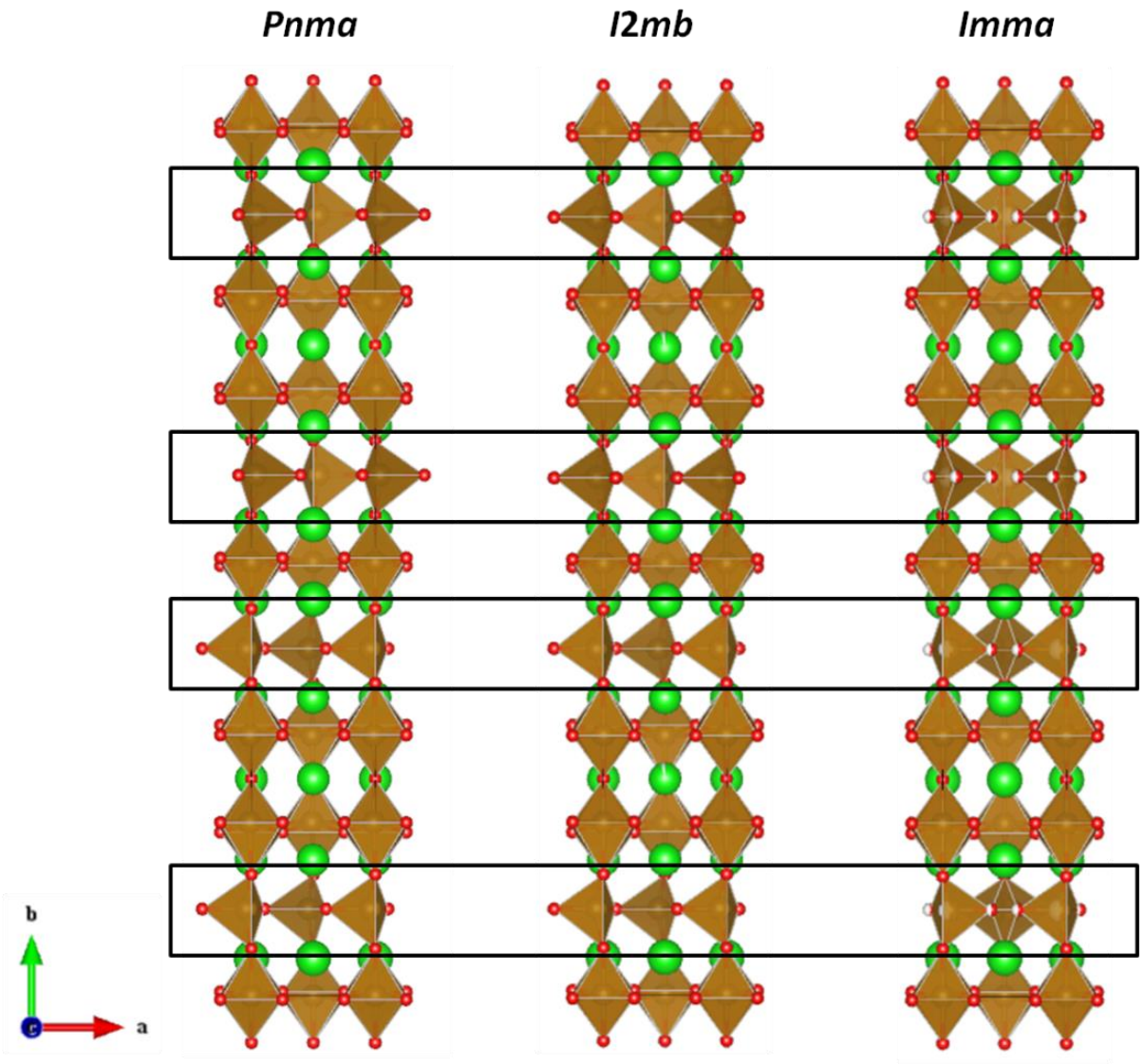

Figure 4.7 Representation of the YCSFO structure in *Pnma*, *I2mb* and *Imma* space groups for comparison, with the main difference found in the ordering of T_d chains (highlighted within black boxes). *A*-site atoms (green), O atoms (red) and *B*-site polyhedra (brown).

For the combined Rietveld refinement, the ND time-of-flight diffractometer constants were all refined for the ND banks 2, 3, 4 and 5. The zero point was refined for the SXRD data giving a total of 13 refined diffractometer parameters. A total of 36 background parameters were refined; 6 for each ND histogram; 12 for SXRD histogram. Refined lattice parameters for YCSFO were constrained to the same value for ND and SXRD data. Structures for YCSFO (including the magnetic structure) were included in the Rietveld refinement.

In order to improve the peak profile fitting, anisotropic strain broadening[202] was refined for YCSFO in the SXRD data-set and the highest resolution (banks 4 and 5) ND data-sets to account for slight differences in peak shape for reflections corresponding to the long stacking axis. A total of 29 profile parameters were used in the refinement for all histograms; 3 for ND bank 2; 3 for ND bank 3; 8 for ND bank 4; 8 for ND bank 5; 7 for SXRD.

The relative occupancy of Y and Ca for each *A*-site were refined while the total occupancy of unity on each *A*-site was enforced. A soft chemical composition restraint was implemented to drive the refinement towards the EDX *A*-site composition of $Y_{2.8}Ca_{2.2}$, with Sr accounted for in Y total. A single isotropic displacement parameter was refined for each atom type; *A*-site (Y/Ca), B-site (Fe) and O. The atomic coordinates of each atom was refined within the symmetry allowed by each Wyckoff position.

Figure 4.8 below shows the fits from the combined Rietveld refinement of SXRD and ND data discussed above. A good fit was obtained for all data with an R_{wp} = 1.812, R_{exp} = 0.258.

A refinement was also carried out in *Pnma*, with the addition of a second O and Fe atom with 1/2 occupancy in order to model the disordered T_d site. The additional atoms refined to the same positions as they appear using the space group *Imma*. The fit was not improved when compared to the refinement in *Imma*, despite the extra freedom of the atoms to move within *Pnma*. It was therefore decided to retain the higher symmetry space group *Imma*.

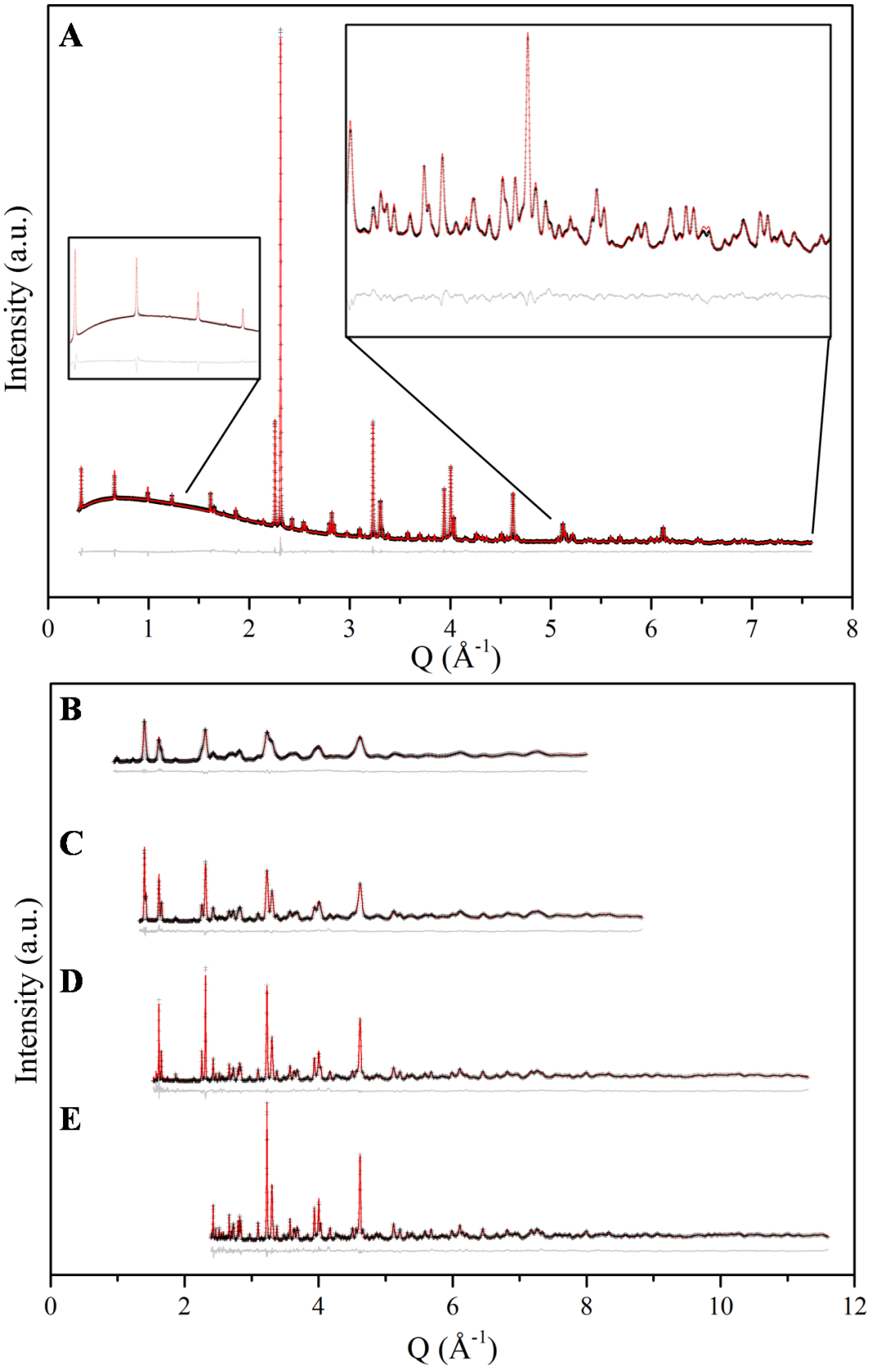

Figure 4.8 Fit data from a combined refinement including only A-Site cations Y and Ca of A) SXRD data together with zoomed in regions of low and high angle, B) ND bank 2, C) ND bank 3, D) ND bank 4 E) ND bank 5 data.

Before the anomalous scattering ASXRD data were added to the refinement, Sr was added to the three *A*-sites and refined. Each site had a large penalty, restraining the total occupancy to unity, as well as having a soft penalty to keep the total *A*-site cation ratio close to the EDX given ratio of $YCa_{2.2}Sr_{1.8}$. Simulated annealing was carried out with *A*-site occupancy, fractional coordinates, thermal parameters, lattice parameters and scale factors refined. This was to allow the refinement some freedom to change parameters that may affect the calculated intensities along with occupancy. This led to refined parameters with large errors, especially for Y and Sr occupancies, as well as very large errors for the refined composition. Ca occupancies refined with only small errors by comparison. This demonstrated the difficulty in distinguishing Y and Sr, and showed the need to use additional data for this purpose. These data are shown in Table 4.4. The next refinement to be set up was to contain the ASXRD data set.

4.3.4 Combined refinement including anomalous data set

Anomalous scattering takes advantage of the changes in the scattering cross section of an atom near to its X-ray absorption edge.[245] It has long been used for characterisation of proteins and other biological macromolecules. Through reducing a complex structure of thousands of atoms down to solving a few centres of anomalous scattering, these centres can then be used as reference points for mapping the rest of the structure.[246-248] Anomalous scattering can also be used to differentiate atoms that are located on the same site, where normal diffraction fails. Such a case was reported for $Bi_2Sr_{2-x}CaCu_2O_8$ where wavelengths at the immediate vicinity of the Bi L_{III} edge was used for Bi location within the structure.[249] Other examples of similar uses include the superconductor system $YBa_2Cu_{3-x}M_xO_{7-\delta}$ (M = Fe, Co, Ni, Zn) where the location of the dopant was required,[250] and $Fe_{0.53}Cr_{0.47}$, where the local order was investigated.[251] It is the differentiation of atoms that potentially share sites that YCSFO required an anomalous data set for.

The theoretical Sr K absorption edge is 16115.26 eV (0.769359 Å); this is shown in Figure 4.9.[252] As the theoretical absorption edge does not account for the effect of neighbouring

atoms, which can cause great influence near an absorption edge, the experimental absorption edge of Sr was measured for YCSFO(I). This was carried out on the I11 beamline at Diamond by Professor Chiu Tang and Doctor Stephen Thompson. The measured value of 16.122 keV (0.769037 Å), was then set 10eV below the edge at 16.112 keV (0.769515 Å), and was calibrated via SXRD of a Si standard to be 16.10067 keV (0.770056 Å). The data set collected at this wavelength was then added to the other data sets (SXRD at 0.827153 Å and ND banks 2, 3, 4 and 5) and used in the combined refinement to locate Sr.

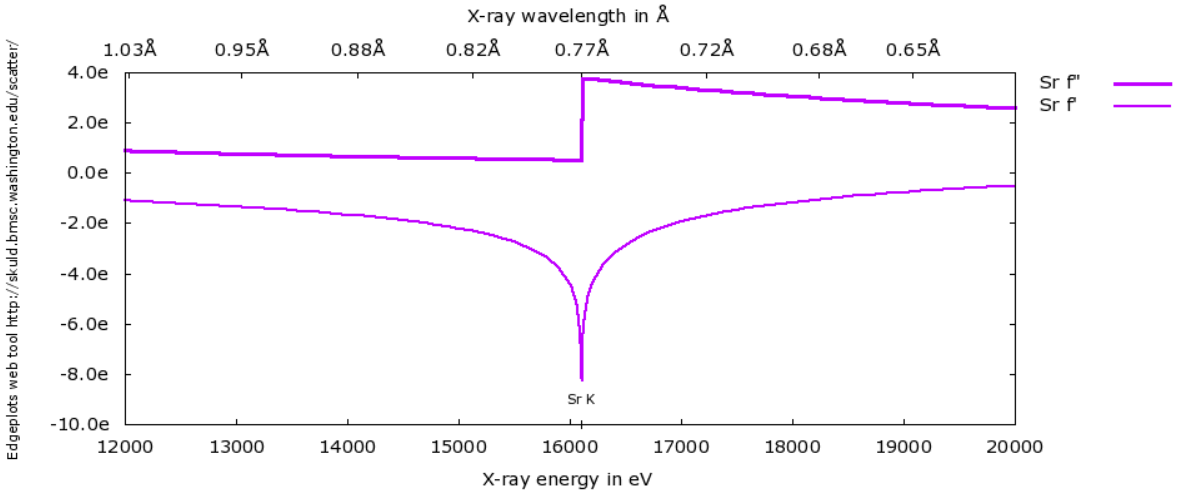

Figure 4.9 Plot of theoretical Sr K absorption edge, showing f' and f" form factors.

On addition of the anomalous wavelength data, simuated annealing was carried out starting with the addition of Sr to the refined data that previously only contained Y and Ca. The *A*-site occupancy, fractional coordinates, thermal parameters, lattice parameters and scale factors refined. This was to again allow the refinement freedom to change parameters that may affect the calculated intesnities along with occupancy. For each *A*-site, penalties were applied to force a total occupancy of unity, whilst the overall composition had a soft penalty to keep the total *A*-site cation ratio close to the EDX given ratio of $YCa_{2.2}Sr_{1.8}$.

In addition to the refined parameters for the other data sets, the zero point was refined for the ASXRD data and 12 background parameters were refined for the ASXRD data. A peak

profile including anisotropic strain broadening[202] was refined for YCSFO in the SXRD data-set in order to improve the fit, with 7 profile parameters refined in all. The Sr form factors for the ASXRD data set were also refined, and an absorption correction was applied. The combined refinement from all data sets can be seen in Figure 4.10, which had an R_{wp} = 1.828, R_{exp} = 0.480. The refined parameters that gave the fit seen in this figure can be seen in Table 4.2. The refined composition of $Y_{0.95(3)}Ca_{2.48(9)}Sr_{1.57(4)}Fe_5O_{13}$ is notably close to the as-made composition of $Y_{0.9}Ca_{2.4}Sr_{1.7}Fe_5O_{13}$.

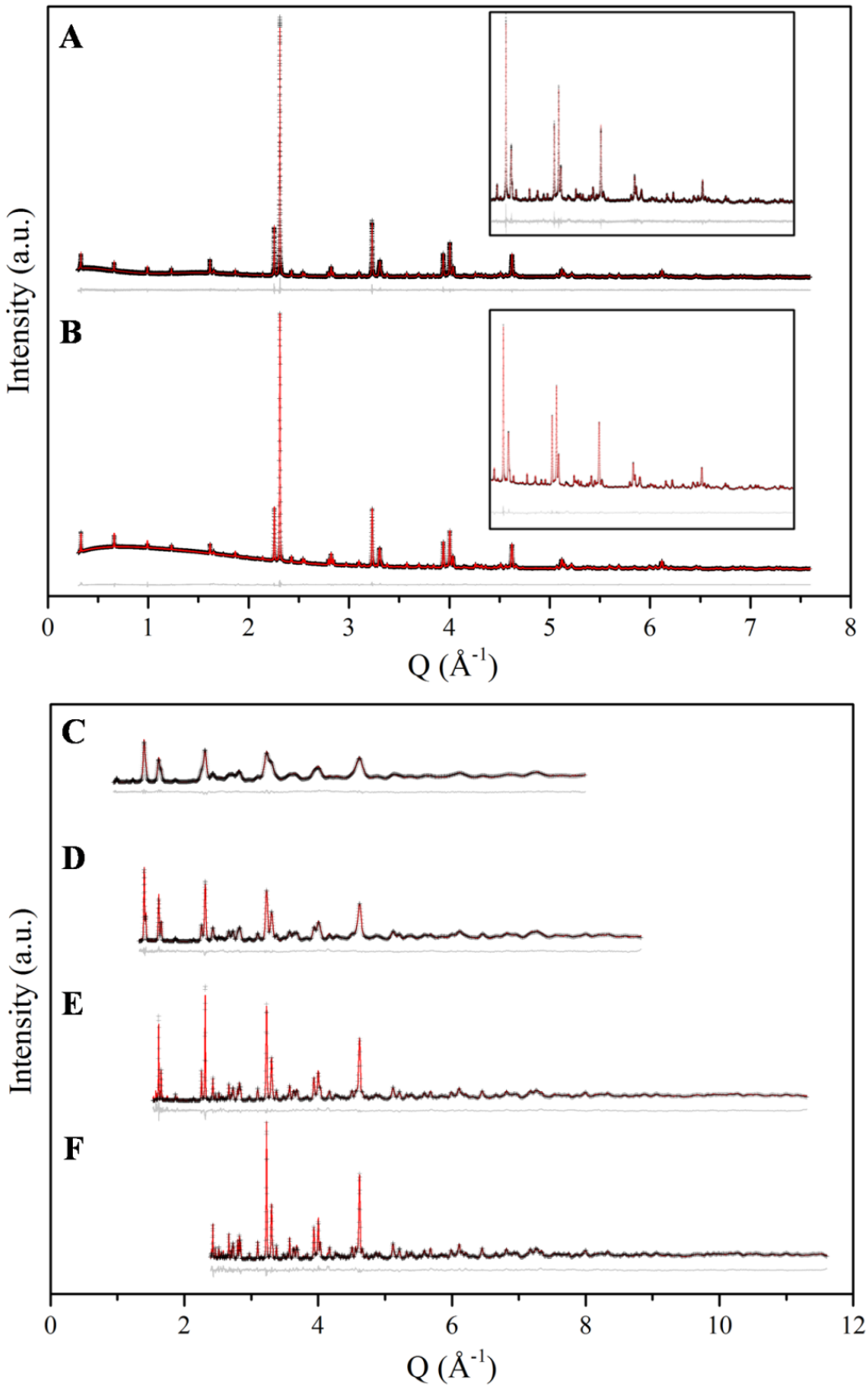

Figure 4.10 Fit data from a combined refinement including all *A*-site cations Y, Ca and Sr of A) SXRD data together with zoomed in region of high angle, B) Anomalous wavelength SXRD data together with zoomed in region of high angle, C) ND bank 2, D) ND bank 3, E) ND bank 4 F) ND bank 5 data.

	Unit Cell Parameters					
	a (Å)	5.43424(6)				
	b (Å)	38.0147(4)				
	c (Å)	5.56989(5)				
Site	**Multiplicity**	**Occupancy**	***x***	***y***	***z***	***Biso* (Å^2)**
A1	8*h*	$Ca_{0.640(5)}Sr_{0.360(5)}$	1/2	0.04416(3)	0.0221(2)	0.623(9)
A2	8*h*	$Y_{0.30(2)}Ca_{0.52(4)}Sr_{0.18(2)}$	1/2	0.15682(2)	0.0306(2)	0.623(9)
A3	4*e*	$Y_{0.35(3)}Ca_{0.15(6)}Sr_{0.50(2)}$	1/2	1/4	0.0128(3)	0.623(9)
B1	4*a*	Fe_1	0	0	0	0.231(5)
B2	16*j*	$Fe_{0.5}$	0.0537(2)	0.09930(3)	0.9340(1)	0.231(5)
B3	8*h*	Fe_1	0	0.19944(2)	0.9912(2)	0.231(5)
O1	8*g*	1	1/4	0.99531(5)	1/4	0.825(9)
O2	8*h*	1	0	0.05444(5)	0.0566(5)	0.825(9)
O3	16*j*	0.5	0.3924(5)	0.09977(9)	0.8780(4)	0.825(9)
O4	8*h*	1	0	0.13850(5)	0.0750(4)	0.825(9)
O5	8*g*	1	1/4	0.19972(6)	1/4	0.825(9)
O6	8*g*	1	1/4	0.81163(5)	1/4	0.825(9)
O7	4*e*	1	0	1/4	0.9381(6)	0.825(9)

Table 4.2 Refined crystallographic data for YCSFO(I) from combined data set of ND, SXRD and ASXRD. Space group - *Imma*. Refined composition $Y_{0.95(3)}Ca_{2.48(9)}Sr_{1.57(4)}Fe_5O_{13}$, including soft chemical composition restraint.

Each of the *A* and *B*-sites have been labelled in Figure 4.11A so that the location that each site is found in is more clear. From the refinement, Y has refined to the *A*2 and *A*3 positions equally, with none present on the *A*1 site. Y refined to essentially zero on the *A*1 site and was therefore removed from this site to reduce the number of parameters refined. *A*1 refined to a mostly Ca site, with ~ 1/3 of the rest of the site Sr. *A*2 was again a mostly Ca site at around 1/2 occupancy, with the rest made up of Y a smaller amount of Sr. *A*3 had the lowest Ca occupancy, with roughly 1/2 Sr occupancy and 1/3 Y occupancy. A comparison with the parent $YCa_4Fe_5O_{13}$ can be made,[222, 239] although the structure was not refined, but derived from high resolution TEM. The general similarities can be seen, with the retention of the O ordering, together with sites *A*1 and *A*2, which were allocated as a Ca site for the parent structure, containing the highest occupancy of Ca for YCSFO.

The Y site for $YCa_4Fe_5O_{13}$[220] (*A*3), becomes mostly a Sr site for YCSFO, with Y present in equal amounts on *A*2 and *A*3. Apart from the addition of Sr for YCSFO, the main difference between the structures is the space group, with *Pnma* used for $YCa_4Fe_5O_{13}$,[220] meaning that the T_d chains point right-right-left-left when looking down the *c*-axis. For YCSFO, *Imma* is used, which contains disordered T_d, as depicted in Figure 4.7.

The refined bond lengths of each *A*-site to O and *B*-site to O for YCSFO(I) are shown below in Table 4.3, together with the bond valence sums of the *B*-site. Considering that Sr is the largest cation present (in 9 coordinate site; Sr^{2+} 1.31 pm, Ca^{2+} 1.18 pm, Y^{3+} 1.075 pm),[234] it follows the expected trend that it is the predominant cation in the highest coordination site (*A*3). This site also has on the whole, the longest bond lengths, enabling it to accommodate the larger Sr cation. The lower coordination sites *A*1 and *A*2 (9 coordinate) with generally shorter bond lengths, as discussed earlier, are occupied mostly by Ca, as is the case with the parent structure.

The *B*-site also contains sensible bond lengths for an Fe^{3+} cation, as shown by the bond valences calculated for each site based on the Fe-O bond lengths. As we know from titrations that Fe^{3+} is the only oxidation state present on the *B*-site, the calculated bond valence sums of 3.07, 3.10 and 3.18 for Site *B*1, *B*2 and *B*3 respectively match up well with this. As discussed earlier, the *B*-site geometries remain ordered as O_h-T_d-O_h-O_h-T_d, as with the parent structure. The $10a_p$,[35] contains *B*-site geometries of S_q-O_h-T_d-O_h-S_q, with Ba occupying the 12 coordinate site almost on its own, Ca the 9 coordinate site and Y the 8 coordinate site,

although with relatively large disorder between Ca and Y on their respective sites. The same coordination number preference is also observed in the $16a_p$ phase.[197] The greater overall mixing of the *A*-site cations in YCSFO in comparison to the $10a_p$ phase is due to the smaller size of the Sr cation compared to that of the Ba cation, which leads to the formation of the $YCa_4Fe_5O_{13}$ structure[220] rather than the $10a_p$[35] structure.

A-Site Bond	***n* × distance (Å)**	**B-Site Bond**	***n* × distance (Å)**
A1 – O1	2 × 2.628(2)	B1 – O1	4 × 1.9535(1)
A1 – O1	2 × 2.529(2)	B1 – O2	2 × 2.093(2)
A1 – O2	2 × 2.7518(4)	B2 – O2	1 × 1.860(2)
A1 – O2	1 × 2.379(3)	B2 – O3	1 × 1.947(2)
A1 – O3	2 × 2.336(3)	B2 – O3	1 × 1.867(3)
A2 – O3	2 × 2.402(3)	B2 – O4	1 × 1.710(2)
A2 – O4	2 × 2.8158(5)	B3 – O4	1 × 2.363(2)
A2 – O4	1 × 2.304(2)	B3 – O5	2 × 1.9810(6)
A2 – O5	2 × 2.449(2)	B3 – O6	2 × 1.9563(8)
A2 – O6	2 × 2.393(1)	B3 – O7	1 × 1.9446(8)
A3 – O5	4 × 2.692(2)		
A3 – O6	4 × 3.079(2)	**Site**	**Bond Valence**
A3 – O7	1 × 2.511(4)	B1	3.07
A3 – O7	2 × 2.7488(5)	B2	3.10
A3 – O7	1 × 3.058(4)	B3	3.18

Table 4.3 Refined *A*-site to O and *B*-site to O bond lengths for YCSFO(I) from combined refinement of ND, SXRD and ASXRD data. Also shown are the calculated bond valences for each of the *B*-sites using bond-valence model.[253]

Figure 4.11 displays the refined structures of YCSFO(I), with A) showing the refined structure using only the ND and SXRD data sets and containing only Y and Ca on the *A*-site. B) shows the structure after the addition of the ASXRD data set along with the incorporation of Sr into the refinement C) shows the G-type magnetic ordering, with the directions of the refined magnetic moments on each of the sites (left). Also present are the positions of the refined *B*-site cations, which the magnetic sites were constrained to.

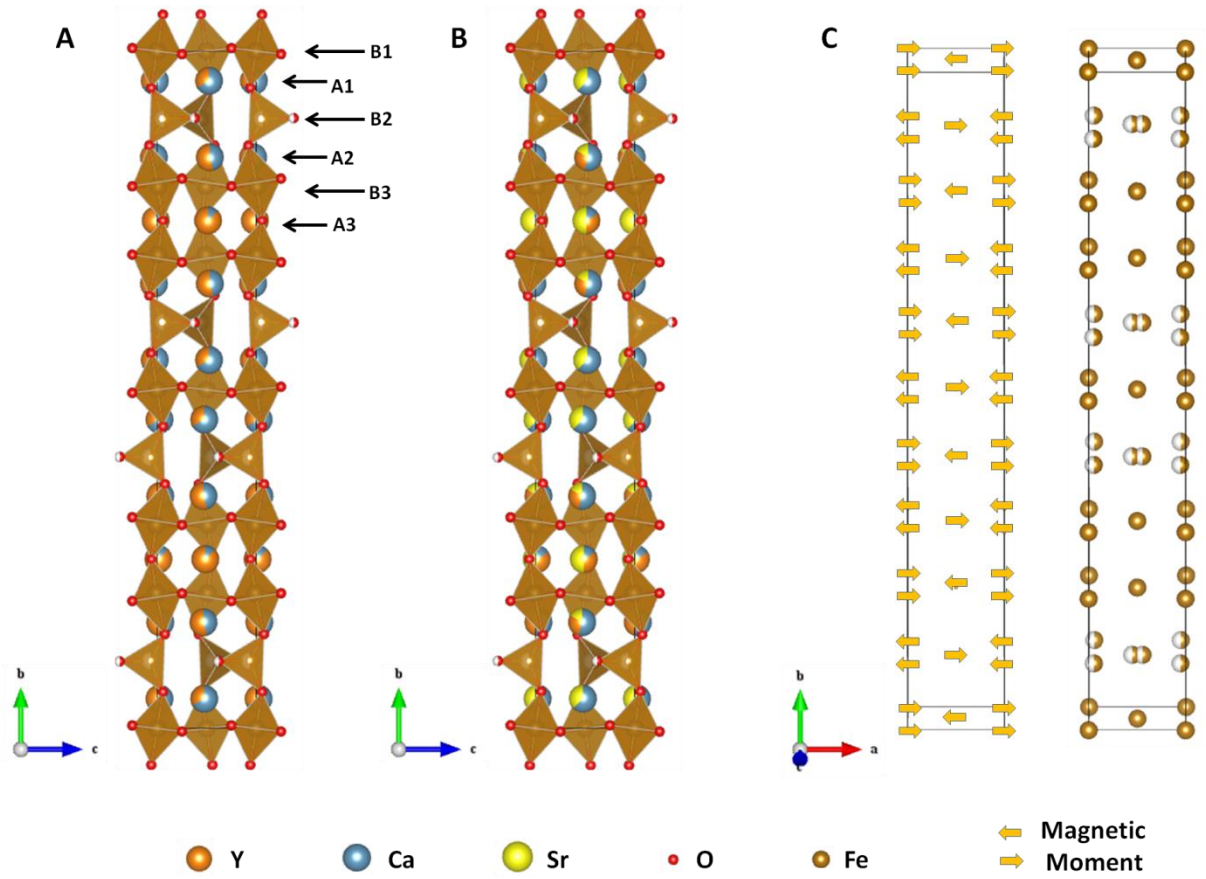

Figure 4.11 Refined crystal structures of YSCFO(I) A) from ND and SXRD data with only Y and Ca A-site cations, B) from ND, SXRD and ASXRD data with all *A*-site cations and C) direction of refined magnetic moments (left) together with refined positions of *B*-site (right), also constrained as position of moment within unit cell.

Table 4.4 shows a comparison of refined compositions and *A*-site occupancies from ND and SXRD data for only Y and Ca, ND and SXRD for Y, Ca and Sr, and finally ND, SXRD and ASXRD for Y, Ca and Sr. As can be seen from the data, the final composition and *A*-site occupancies of "Y, Ca" and "Y, Ca, Sr + ASXRD data" are remarkably similar when considering Y in the first case also accounts for Sr, giving strength to the refined values. For the "Y, Ca, Sr" case, the values obtained for *A*-site occupancy are markedly different from the other data set. The values also contain much larger errors, as is the case with the refined composition. This analysis shows the importance of the ASXRD data set in determining realistic refined parameters involving Sr and Y within the same phase.

Site	Y, Ca	Y, Ca, Sr	Y, Ca, Sr + ASXRD data
A1	$Y_{0.347(4)}Ca_{0.653(4)}$	$Ca_{0.517(8)}Sr_{0.483(8)}$	$Ca_{0.640(5)}Sr_{0.360(5)}$
A2	$Y_{0.532(5)}Ca_{0.467(5)}$	$Y_{0.02(14)}Ca_{0.55(8)}Sr_{0.42(12)}$	$Y_{0.30(2)}Ca_{0.52(4)}Sr_{0.18(2)}$
A3	$Y_{0.884(7)}Ca_{0.116(7)}$	$Y_{0.83(18)}Ca_{0.17(10)}Sr_{0.00(14)}$	$Y_{0.35(3)}Ca_{0.15(6)}Sr_{0.50(2)}$
Refined composition	$Y_{2.64(1)}Ca_{2.36(1)}$	$Y_{0.88(34)}Ca_{2.30(18)}Sr_{1.82(27)}$	$Y_{0.95(3)}Ca_{2.48(9)}Sr_{1.57(4)}$

Table 4.4 comparison of refined *A*-site occupancies and compositions for YCSFO with ND and SXRD data for only Y and Ca, with ND and SXRD for Y, Ca and Sr and with ND, SXRD and ASXRD data for Y, Ca and Sr.

4.4 Physical Properties

4.4.1 Stability and Compatibility

In order to determine the potential of YCSFO as a cathode in a SOFC, thermal stability and chemical compatibility tests were carried out on the as-synthesised YCSFO(II) powder as detailed in section 2.7.1 and 2.7.3 respectively. Figure 4.12 shows PXRD patterns collected after thermal treatment, and show no new phase formation or decomposition of the YCSFO(II) phase , with the phase showing the similar robust stability to ordered perovskites the $10a_p$ and $16a_p$ phases.[35, 197]

Chemical compatibility tests, also, as for the thermal stability test, showed no detectible degradation of the YCSFO(II) phase and no new reflections were observed within the PXRD patterns, suggesting new phase formation through reactivity with the electrolyte did not occur.

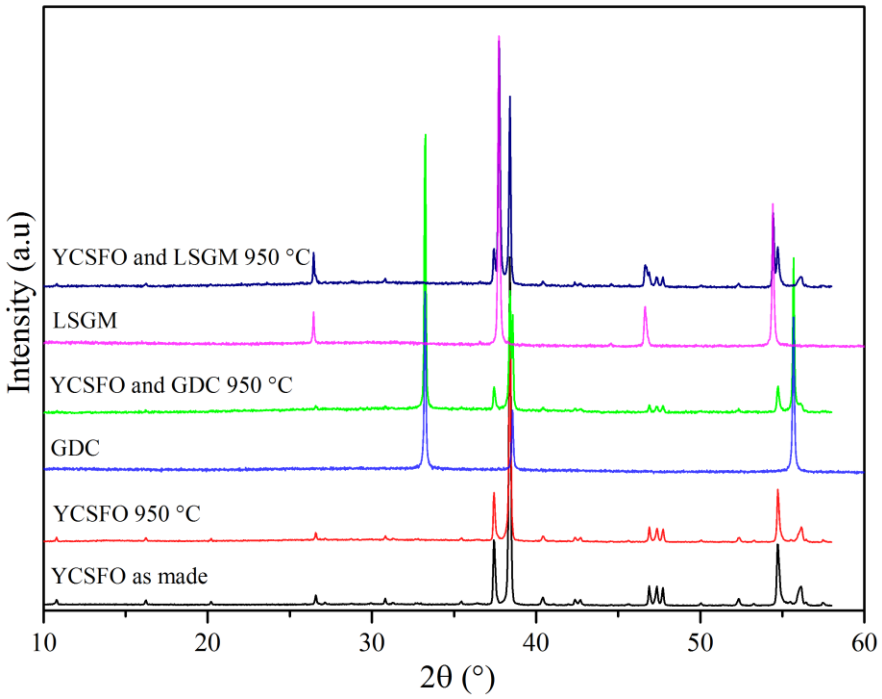

Figure 4.12 PXRD patterns showing the stability of the synthesised YCSFO(II) material. The patterns show that the material is both thermally stable and compatible with the two common electrolyte materials, $Ce_{0.9}Gd_{0.1}O_{2-\delta}$ (GDC) and $La_{0.9}Sr_{0.1}Ga_{0.8}Mg_{0.2}O_{3-\delta}$ (LSGM).

Refined YCSFO(II) lattice parameters from the thermal stability and chemical compatibility tests are shown below in Table 4.5. Only a slight change in lattice parameters can be observed on the fourth significant figure. This indicates that not only did the phases not react to form additional phases, but also in the case of the chemical compatibility tests, cation diffusion between phases must have been negligible. The stability of lattice parameters with LSGM is particularly impressive given that cation diffusion between this electrolyte and many well-known cathodes commonly occurs, as discussed for the $16a_p$ phase in section 3.3.1.[207, 208]

Phase(s) / Axis	*a* (Å)	*b* (Å)	*c* (Å)
YCSFO as-made	5.4400(3)	38.027(1)	5.5719(1)
950 °C anneal for 5 hours			
YCSFO	5.4392(4)	38.016(1)	5.5736(2)
YCSFO with GDC	5.4393(6)	38.019(3)	5.5729(3)
YCSFO with SDC	5.4397(7)	38.021(3)	5.5733(3)
YCSFO with LSGM	5.4399(5)	38.018(2)	5.5742(3)
750 °C anneal for 5 days			
YCSFO	5.4383(3)	38.013(1)	5.5738(1)
YCSFO with GDC	5.4397(6)	38.014(2)	5.5746(3)
YCSFO SDC	5.4367(8)	38.018(3)	5.5736(3)
YCSFO LSGM	5.4399(5)	38.018(2)	5.5742(3)
750 °C anneal for 24 hours in 100 % CO_2			
YCSFO	5.4379(2)	38.021(1)	5.5719(1)

Table 4.5 Refined lattice parameters of YCSFO(II) before and after thermal stability, chemical compatibility with state-of-the-art electrolytes and CO_2 stability.

A complimentary stability test was carried out by heating as-made YCSFO(II) powder to 750 °C for 24 hours in a flowing atmosphere of 100 % CO_2. The powder was then hand ground and characterised by PXRD. As with the previous stability and compatibility tests, no degradation of the phase occurred and there was no formation of new phases detected in the PXRD patterns (see Figure 4.13 and Table 4.5). This CO_2 stability test shows the robust nature of YCSFO(II), indicating it to be a very stable phase. As discussed in the introduction of this chapter, YCSFO lacks Ba, which readily forms $BaCO_3$ in the presence of CO_2. This is a well-documented occurrence for Ba containing phases, causing decomposition of several notable cathodes, such as BSCF.[224] Nevertheless, as discussed in section 3.3.1, many other alkaline-earth containing perovskites are susceptible to CO_2 reactivity, making the stability of YCSFO noteworthy.[137-139]

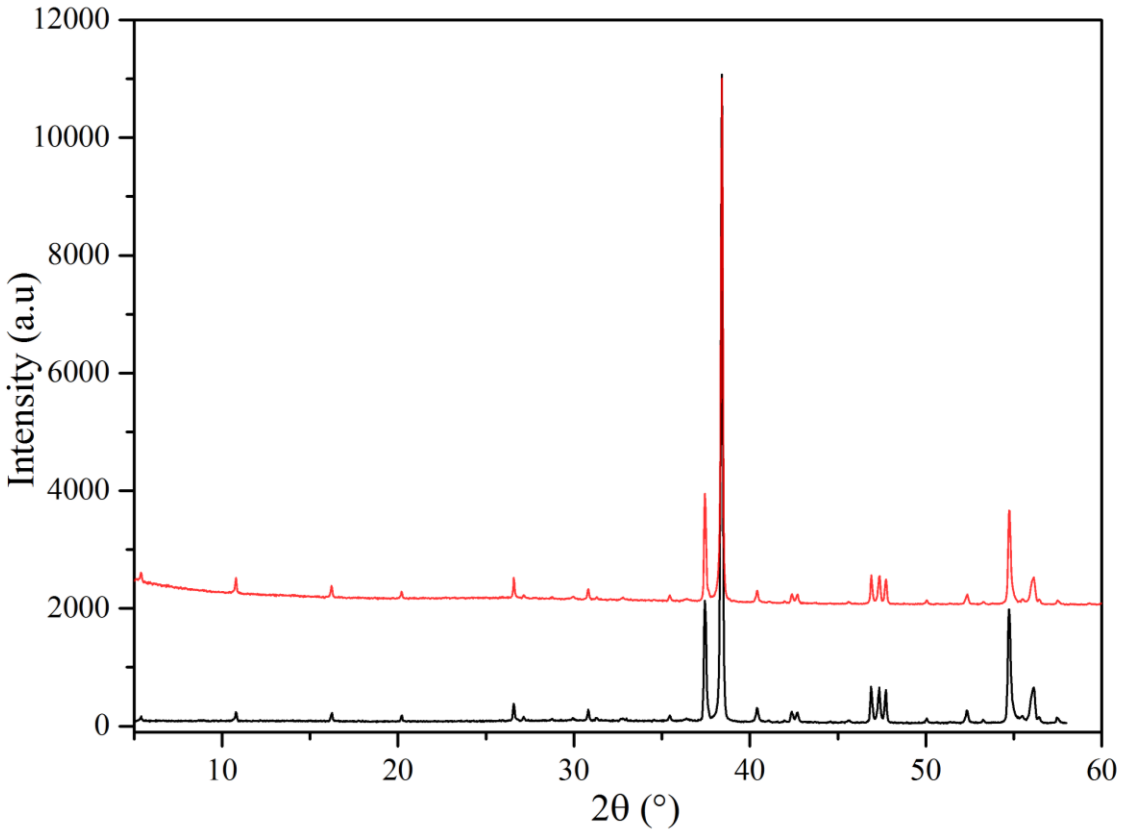

Figure 4.13 PXRD of as made YCSFO(II) before and after aging in 100 % CO_2 for 24 hours at 750 °C. The PXRD patterns show YCSFO has a high tolerance for CO2, as it remains unchanged after treatment.

The TEC of YCSFO(I) was determined *via* VT-SXRD, as well as by the use of a dilatometer, using YCSFO(II). For the VT-SXRD method, the lattice parameters were determined by Rietveld refinement of each SXRD data set, from 200 °C to 550 °C with increments of 50 °C. The *abc* lattice parameters for each refinement are given in Figure 4.14, A). Although YCSFO(I) shows slight anisotropic expansion, the difference in expansion down each axis is not significantly different, showing the structure is constrained similarly in all directions, unlike the layered $10a_p$ and $16a_p$ materials.[35, 197] The TEC along each axis were calculated from each data set and are as follows; a = 16.8 × 10^{-6} K^{-1}; b = 14.9 × 10^{-6} K^{-1}; c = 18.3 × 10^{-6} K^{-1}.

Also in Figure 4.14, B) is the TEC as measured by a dilatometer, with the measurement carried out as detailed in section 2.9.2. The thermal expansion of the pellet was measured between 25 °C and 900 °C with a heating and cooling rate of 3 °C per minute. A calibration was run using a known standard (Al_2O_3) with the same length as the measured sample

(± 5 %) in order to correct for instrumental factors and expansion. A TEC of 16.61×10^{-6} K^{-1} was calculated on cooling between 200 °C and 550 °C so as to compare to the VT-SXRD data over the same temperature range, although extending the range made little difference to the value calculated. The dilatometer measured TEC of 16.61×10^{-6} K^{-1} closely matches the VT-SXRD TEC, especially when taken as an average *a*, *b* and *c* (16.67×10^{-6} K^{-1}), giving more confidence to the measurements.

YCSFO(II) undergoes a linear expansion on heating from 25 °C to 900 °C as shown by the dilatometer measurement. There also appears to be no significant changes to the YCSFO(I) structure between room temperature and 550 °C as observed in the SXRD data. The linear expansion also indicates that there is not a significant loss of oxygen from the structure. TGA also confirms this, as no significant change in mass on heating between 50 °C and 800 °C is observed (see Figure 4.14, C). This is to be expected for a stable air synthesised perovskite with an entirely Fe^{3+} *B*-site, as Fe^{3+} is unlikely to be reduced to Fe^{2+} whilst being heated in air in order to accommodate O^{2-} loss.

The TGA measurement was performed using a TA instruments Q600 thermal analyser on ~ 200 mg of sample, which was heated from 50 - 800 °C at 3 °C per minute, with a dwell at 800 °C of 2 hours. The measurement was cycled three times, showing no changes between each cycle.

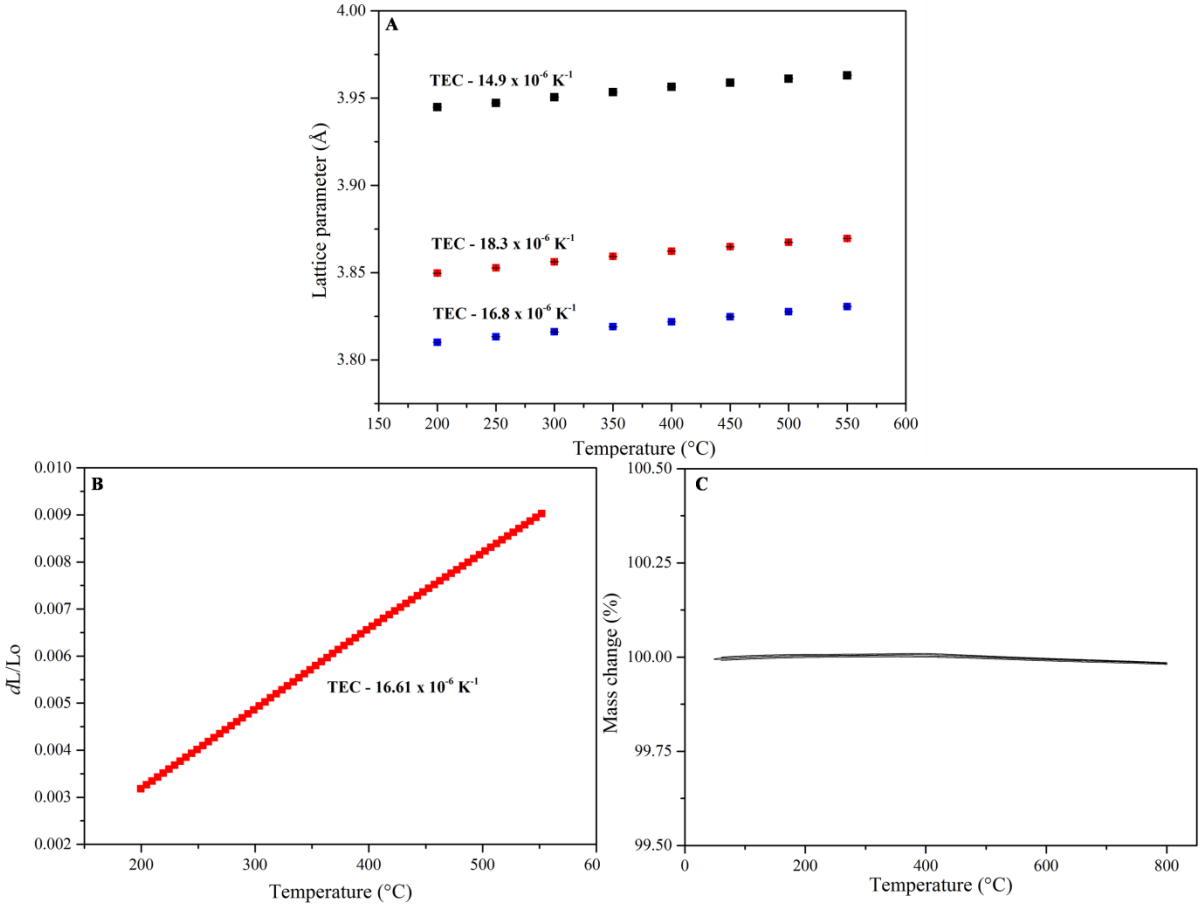

Figure 4.14 For YCSFO(I/II) plots show A) *a* (blue), *b* (red) and *c* (black) lattice parameter changes taken versus from refined VT-SXRD data, normalised to one a_p unit, B) TEC data measured using a dilatometer and C) TGA plot of % mass change versus temperature.

4.4.2 Electrochemical behaviour

The electronic conductivity of YCSFO(II) was measured by four probe DC conductivity (detailed in section 2.10.1). DC conductivity was then measured from 800 °C to 500 °C on cooling at 50 °C increments, with isotherms of one and a half hours at each temperature. The results from this measurement can be seen below in Figure 4.15. YCSFO(II) displays semi conducting behaviour, with a conductivity of 2.86 to 4.57 $S.cm^{-1}$ between the measured temperatures. Iodometric titrations (analysis in section 4.3.1) showed that Fe^{3+} was the only oxidation state present for the transition metal. This accounts for the low electronic conductivity displayed as there are a lack of charge carriers available that would lead to a higher conductivity. The E_a for YCSFO(II) conductivity is 0.111(1) eV, which is similar to

that of related structure $Ca_2Fe_2O_5$, 0.28 eV, which was reported to relate to the small polaron mechanism.[219]

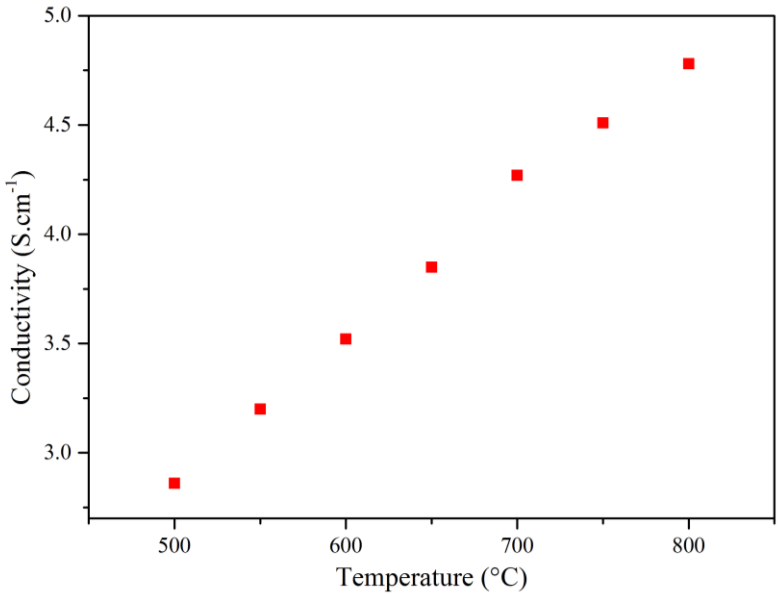

Figure 4.15 The electronic conductivity of YCSFO(II) versus temperature measured via four probe DC conductivity.

The cathode performance of YCSFO(II) was investigated by measuring the AC impedance of a symmetrical cell of the material on a GDC electrolyte substrate, as detailed in section 2.10.2. Cathode inks were then prepared by ballmilling this powder with an organic binder for 12 hours, in the weight ratio 67:33 powder to binder. The electrode ink was applied to both surfaces of the electrolyte substrate by screen printing in one layer. The cell was dried at 100 °C for 1 hour between the application of each layer followed by a final heating in air at 950 °C for 1 hour to achieve good adherence of the electrodes to the electrolyte surface. The contacts for the electrical measurement were gold wire and gauze fixed in position with gold paste, which were attached to the cell by heating to 600 °C for 1 hour.

AC impedance measurements were recorded over the frequency range 1 MHz to 0.01 Hz with a modulation potential of 10 mV, over the temperature range of 500 °C to 800 °C in static air. The symmetrical cell was held for 90 minutes at each temperature to allow thermal equilibration and measurements were made using ZPlot v.2.9b (Scribner Associates) every 50 °C. The ASR of the cathode was calculated by fitting the data using ZView2.[189] The data

was fit with an Inductor (I) and two Resistors (R) in series with associated Constant Phase Elements (CPE) in parallel with each resistor. The ASR was then calculated by normalizing the measured resistance for the electrode area and dividing by two to take into account the symmetry of the cell.

Figure 4.16 below displays a Z'-Z" plot of the data obtained for the YCSFO(II) cathode on a GDC electrolyte substrate, whilst Figure 4.17 displays a plot of ASR versus temperature. YCSFO(II) had an ASR of 0.18 Ω.cm^2 at 800 °C, which is quite a high resistance for a SOFC cathode to display when compared to other comparably stable materials such as the 10a_p[35] 16a_p[197] and LSCF.[94] The ASR is also higher than the required maximum value aimed for of 0.15 Ω.cm^2.[29] The ASR values, together with the electronic conductivity measured between 500 - 800 °C can be seen in Table 4.6. The E_a of the ASR for YCSFO(II) is 1.58(2) eV, which compares closely to the 16a$_p$ $Y_{2.24}Ba_{2.28}Ca_{3.48}Fe_{7.44}CuO_{21-\delta}$, 1.57(4) eV, although it also has a lower ASR, suggesting that the 16a_p phase is the more promising cathode.[35, 162]

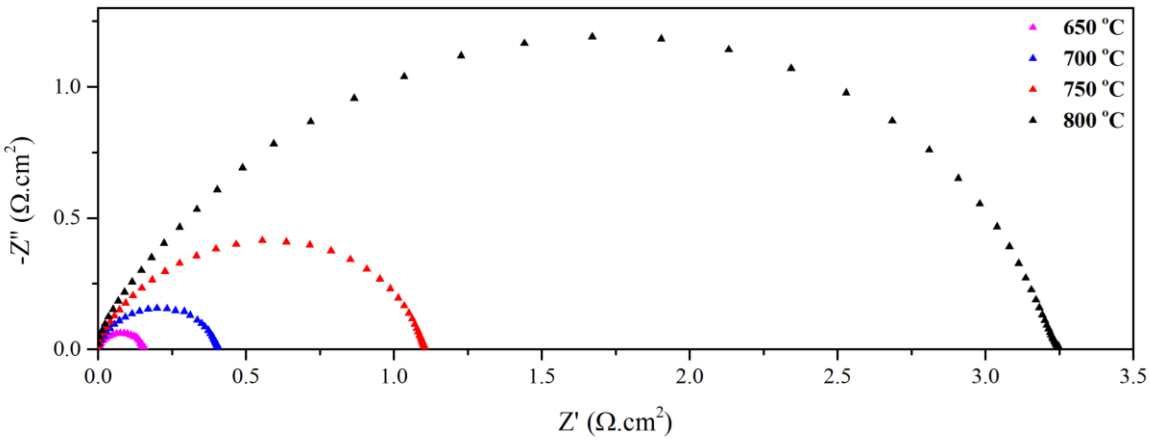

Figure 4.16 Z'-Z" plot showing cathode performance of YCSFO(II) in a symmetrical cell on a GDC electrolyte at temperatures between 650 °C and 800 °C.

Temperature (°C)	ASR ($\Omega.cm^2$)	Conductivity ($S.cm^{-1}$)
500	133.57	2.86
550	34.90	3.2
600	10.09	3.48
650	3.20	3.76
700	1.10	4.05
750	0.42	4.32
800	0.18	4.57

Table 4.6 ASR values together with the electronic conductivity of YCSFO(II) against temperature.

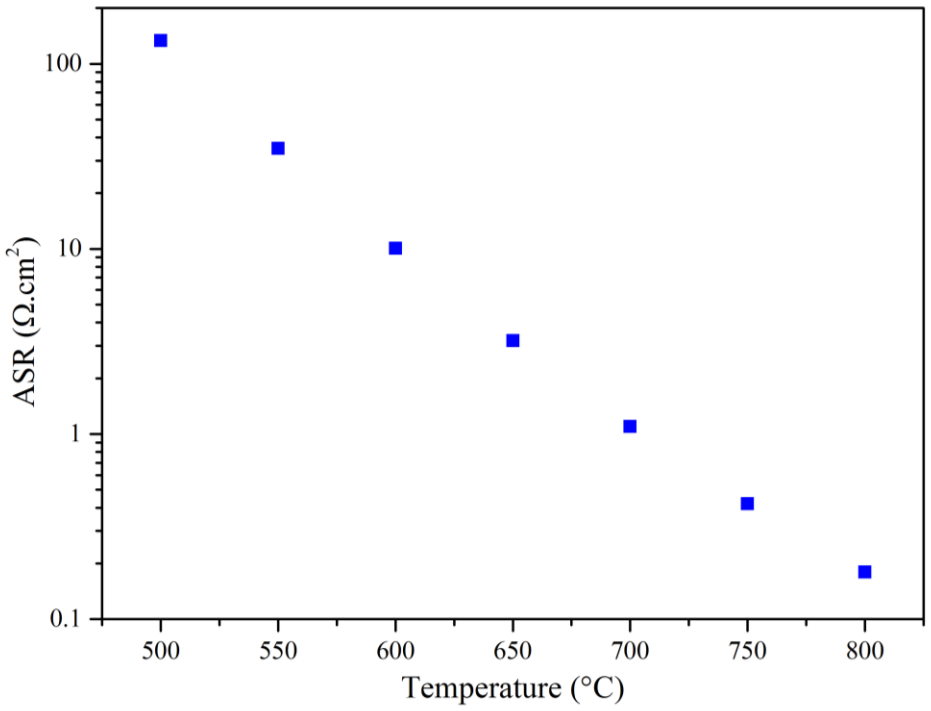

Figure 4.17 ASR versus temperature for YCSFO(II) fabricated on a GDC electrolyte.

4.5 Discussion

In this chapter we have shown the isolation, structural characterisation and physical property measurements of the $10a_p$ phase $Y_{0.9}Ca_{2.4}Sr_{1.7}Fe_5O_{12.95(2)}$, or YCSFO. The phase discovery was a case of the formation of an unexpected phase observed in a PXRD pattern that was followed up in detail. As discussed in chapter 3, Al_2O_3 crucibles showed their ability to incorporate cations at elevated temperatures, changing the cation ratios left in reacted samples, which led to the formation of YCSFO.

Although YCSFO is not a completely new phase, it was a new (unintended) doping of known phase $YCa_4Fe_5O_{13}$,[222, 239] with significant substitution of Sr for Ca. Synthesis of this phase proved to be quite straightforward with the use of a ternary diagram to vary *A*-site cation ratios. As well as the phase discussed in this chapter, within the phase space explored, there appeared to be at least one other $10a_p$ phase with a composition of roughly $YCa_3SrFe_5O_{13}$, a $3a_p$ phase and a cubic phase when in the Sr rich region, as seen in Figure 4.2

YCSFO was indexed to an orthorhombic $a_p\sqrt{2} \times 10a_p \times a_p\sqrt{2}$, $\alpha = \beta = \gamma = 90°$ cell using PXRD data. Indexation to this geometry was quick as initially the phase was compared to the $10a_p$ structure $Y_{0.9}Ba_{1.7}Ca_{2.4}Fe_5O_{13}$, which is also an orthorhombic $a_p\sqrt{2} \times 10a_p \times a_p\sqrt{2}$, $\alpha = \beta = \gamma = 90°$.[35] As the lowest angle reflection present with intensity in the PXRD pattern had a *d*-spacing equivalent to a $5a_p$ stacking axis (~ 19 Å), YCSFO was also tested as such, however not all reflections could be indexed therefore the $10a_p$ repeat was retained.

During the crystal structure refinement using the $Y_{0.9}Ba_{1.7}Ca_{2.4}Fe_5O_{13}$ $10a_p$ structural model, a mismatch in intensity that could not be solved through refining parameters was observed. A second structural model was then tested, based on $YCa_4Fe_5O_{13}$,[222] which gave a much improved fit, leading to it being identified as the most appropriate structural model for YCSFO.

As was discussed in chapter 3, it seems many long axis phases can be considered as intergrowths between smaller phases. As long as they are compatible, the smaller phases become building blocks in the formation of extended structures. In the case of the $16a_p$ and $10a_p$ phases, intergrowths form between $YBa_2Fe_3O_8$ for both, combined with $Ca_2Fe_2O_5$ and $YCa_4Fe_5O_{13}$ for the two phases respectively.[35, 197] As it happens $YCa_4Fe_5O_{13}$ can also be

thought of as an intergrowth, as has already by discussed in the publications of $YCa_4Fe_5O_{13}$,[222, 239] A combination of $Ca_2Fe_2O_5$ and $YFeO_3$ in a 2:1 ratio can be considered the building blocks, as seen in Figure 4.18: Note, oxygen sites O5 and O6 in slightly unphysical positions from published data,[222] leading to strange looking O_h polyhedra. These sites can move along *b* stacking axis within the symmetry of *Pnma*, which leads to more realistic polyhedra.

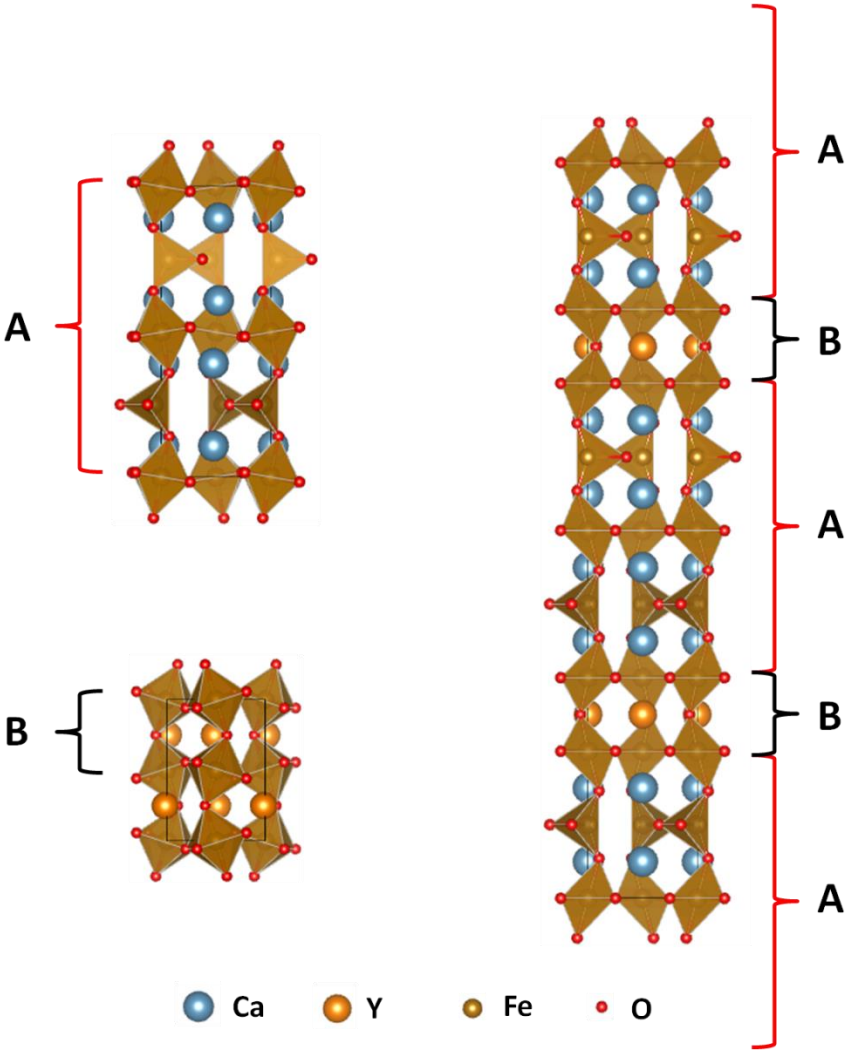

Figure 4.18 Structures of A) $Ca_2Fe_2O_5$, B) $YFeO_3$ and the ideal $YCaFe_5O_{13}$ intergrowth (right). Building units A and B of the two former structures are regularly stacked in a 2:1 ratio to form the ideal structure.

Even with this model, there were some misfits in intensity observed, most noticeably seen in Fourier difference maps. Along the *a*-axis, a mismatch was observed suggested a disordering

of the T_d sites was required at Site B2 and O3. As this is not possible using the space group *Pnma* for the structure, new space groups were identified based on observed reflection conditions seen in the SXRD data. The space group *Imma* was eventually selected as it gave the best fit out of the highest symmetry space groups allowed based on the reflection conditions. The major constituent of YCSFO, $Ca_2Fe_2O_5$, which has the space group *Pnma* at room temperature (as does $YCa_4Fe_5O_{13}$)[222], has also been reported in *Imma* at a temperature of 1300 °C.[244] Another transition to *I*2*mb* has been reported for this phase at 700 °C, with the main differences seen in the T_d chain ordering when looking down the *c*-axis, which orient themselves in the same direction for *I*2*mb*, but in alternating directions for *Pnma*. *Imma* is differentiated from *I*2*mb* by the T_d chain disorder that was observed in Fourier maps for YCSFO(I). The observations noted about the differences seen in the T_d chains for the space groups *Pnma*, *I*2*mb* and *Imma* are represented for the YCSFO structure in Figure 4.7.

$Sr_2Fe_2O_5$, which may also contribute as significantly as $Ca_2Fe_2O_5$ to the structure of YCSFO due to its overall composition, forms at room temperature in the body centred space group *Ibm*2.[254, 255] The body centring of $Sr_2Fe_2O_5$ combined with $Ca_2Fe_2O_5$ (and $YFeO_3$) could combine to form the YCSFO phase in *Imma* as opposed to *Pnma* for $YCa_4Fe_5O_{13}$.[222]

ND data collected for YCSFO(I) showed that it was magnetically ordered based on the presence of peaks that could not be assigned intensity from the structural model. Also on heating in situ to 350 °C, these peaks diminished in intensity, although not completely. This

suggested that the T_N temperature is a little over 350 °C. This would follow a common trend, as the T_N of its building blocks are ~ 450 °C for $Ca_2Fe_2O_5$,[256, 257] and ~ 370 °C for YFeO3.[258] The magnetic reflections were fit by Rietveld refinement in the magnetic space group *Pnma*, and to a magnetic moment of 3.390(7) μ_B.

The refined *A*-site cation order from ND, SXRD and ASXRD located Sr mostly on site *A*3, which is the highest coordination site (12 coordinate) with the longest bond lengths. As Sr is a larger cation than either Y or Ca, it is reasonable that it would occupy this site. Y is found in equal amounts across sites *A*2 and *A*3, with Ca present on all sites, although with preference shown for Site *A*1, followed closely by *A*2. This preference is also shown by the parent structure $YCa_4Fe_5O_{13}$.[222]

YCSFO(II) displayed very robust thermal stability, chemical compatibility and CO_2 tolerance. Under the test conditions, no decomposition occurred at any time, nor did any reactivity occur as shown by the lack of new peaks observed in PXRD patterns post-test (see Figure 4.12). The lattice parameters remained remarkably unchanged (see Table 4.5), indicating that cation diffusion between phases was negligible. This shows improved stability even over the $16a_p$ phase, where small lattice parameter shifts were observed after these same tests.[197]

The thermal stability is further demonstrated by no changes to the structure being observed by TEC or TGA measurements shown in Figure 4.14. VT-SXRD shows a linear increase in lattice parameters with temperature, along with the structure remaining the same as observed by the similarities in the SXRD patterns at different temperatures. The main differences were due to the change in lattice parameters. TGA also showed that there was no change in mass from 50 - 800 °C, indicating that the phase does not lose any oxygen between these temperatures.

The electronic conductivity of YCSFO is governed by the Fe^{3+} oxidation state, with the low DC conductivity attributed to the Mott-Hubbard energy gap produced by inter-electron repulsion. The conductivity is of the same magnitude as other Fe^{3+} perovskites, such as the $10a_p$,[35] $YFeO_3$,[259] and $Ca_2Fe_2O_5$.[219] LSCF on the other hand, with its conductivity around 10^2 times higher, has mixed valence *B*-site cations, enabling it to display much higher conductivity.[218]

The ASR of YCSFO(II) as measured by AC impedance of a symmetrical cell on a GDC substrate is a little high when compared to current cathodes. At 800 °C it is around three times more resistive than other long axis *A*-site ordered perovskites, the $16a_p$ or the $10a_p$ phases.[162, 197] YCSFO does not possess an oxygen vacancy channel between two S_q coordinated *B*-sites, as the $16a_p$ and $10a_p$ possess. It is the oxygen ordering channels that are thought to enhance the performance of these cathodes, so as YCSFO lacks this site, performance also suffers.

4.6 Conclusion

To summarise, this chapter shows the discovery of a Sr doped $YCa_4Fe_5O_{13}$ type phase[222] that was subsequently isolated for crystal structure characterisation and physical property measurements.

The crystal structure was based on that of $YCa_4Fe_5O_{13}$, with the space group *Imma* being determined as an appropriate space group due to it being the highest symmetry space group to fit the observed data with good statistics. This space group also modelled the disordered T_d site observed in Fourier difference maps.

Anomalous scattering SXRD data was collected at the wavelength of the Sr absorption K-edge in order to differentiate between Y and Sr, which are both found sharing the same sites within the structure. The use of the ASXRD and SXRD data together enabled the cation ordering to be reliably refined giving the occupancies of the three *A*-sites.

YCSFO has proved to be a robust phase, showing very good stability and chemical compatibility with state-of-the-art electrolytes. It does however have a significantly worse ASR when compared to current cathode materials, meaning that it is probably a poor candidate.

Further work on this phase could include doping studies, in an attempt to improve its cathode performance, whilst hopefully retaining its stability. It would also be useful to carry out electron diffraction or convergent beam electron diffraction using a TEM in order to confirm the space group assignment. High angle annular dark field imaging would also be useful to compare the cation refined structure to the experimentally observed structure. Annular bright field imaging would also be interesting, as the oxygen ordering can be observed, which could then be compared to the structure used.

It would be interesting to carry out in-situ VT diffraction studies on the parent phase, $YCa_4Fe_5O_{13}$,[222] to see if there is a transition from *Pnma* to *I*2*mb* or *Imma*, as there is for $Ca_2Fe_2O_5$.[243] Also the smaller unit cell $10a_p$ phase identified in section 4.3.2 could be investigated to determine if it forms in *Pnma*, *I*2*mb* or *Imma*. It may show if the role Sr plays is to stabilise a higher temperature phase of $YCa_4Fe_5O_{13}$.

5 Doping studies of the 10a_p, $Y_{0.9}Ba_{1.7}Ca_{2.4}Fe_5O_{13-\delta}$

5.1 Introduction

As described in section 1.7.3.6 and section 3.1, the 10a_p, $Y_{0.9}Ba_{1.7}Ca_{2.4}Fe_5O_{13-\delta}$, shows great potential as a cathode for an IT-SOFC.[35] However, despite the stability of the phase and its moderate cathode performance, it lags behind some of the Co rich state-of-the-art cathodes that have been reported in the literature at lower temperatures in terms of ASR, such as BSCF, GBCO and $Sm_{1-x}Sr_xCoO_3$ (SSC).[63, 122, 153, 260]

$LaCoO_3$ (LCO) for example, displays marked electrocatalytic activity for the reduction of oxygen, which is associated with the electron occupation of the crystal field d state near the Fermi level (E_F). Electron transfer is consequently enhanced due to the build-up of surface charge between cation and catalysed species.[261] $La_{1-x}Sr_xCoO_{3-\delta}$ (LSC) displays significant cathode performance due to pronounced oxygen ion diffusivity and pronounced dissociation ability for oxygen molecules.[3] However, the Co only *B*-site perovskites generally have high TECs, which become problematic during fabrication of SOFC devices or thermal cycling.[122, 262]

Fe doping of Co based cathode materials is a common approach in trying to reduce the TEC and improve phase stability. For instance, $La_{0.6}Sr_{0.4}Co_{1-x}Fe_xO_3$ has a TEC of 20.1×10^{-6} K^{-1} for $x = 0.2$,[263] but for $x = 0.8$,[127] the TEC is reduced to 15.4×10^{-6} K^{-1}, closer to that of state-of-the-art electrolyte materials. The Co to Fe ratio in this material has also shown to influence the electronic conductivity, with a larger Co content giving rise to higher conductivity.[263,127]

In this chapter the approach of Co doping of the highly stable 10a_p phase is discussed in order to try and improve its performance as a cathode at temperatures below 800 °C. Other dopants will also be briefly discussed, showing how flexible the 10a_p structure is to incorporation of various dopant elements.

5.2 Co doping $Y_{0.9}Ba_{1.7}Ca_{2.4}Fe_{5-x}Co_xO_{13-\delta}$

5.2.1 Synthesis

Initial non-published synthetic work carried out by A. Demont targeted the composition $Y_{0.9}Ba_{1.7}Ca_{2.4}Fe_{5-x}Co_xO_{13-\delta}$ for x = 2.5 in order to try and determine the limit of Co doping. The synthesised sample was analysed by PXRD, which showed it to be multiphasic (see Figure 5.1). Analysis of the diffraction pattern indicated that the highest intensity reflections could be related to at least one orthorhombic perovskite. EDX analysis was carried out to obtain the compositions of the phases that were present. A potential $10a_p$ composition was determined to be $Y_{1.23(6)}Ba_{1.60(7)}Ca_{2.17(5)}Fe_{3.10(4)}Co_{1.90(4)}O_z$ based on the analysis of four particles showing a grouped composition.

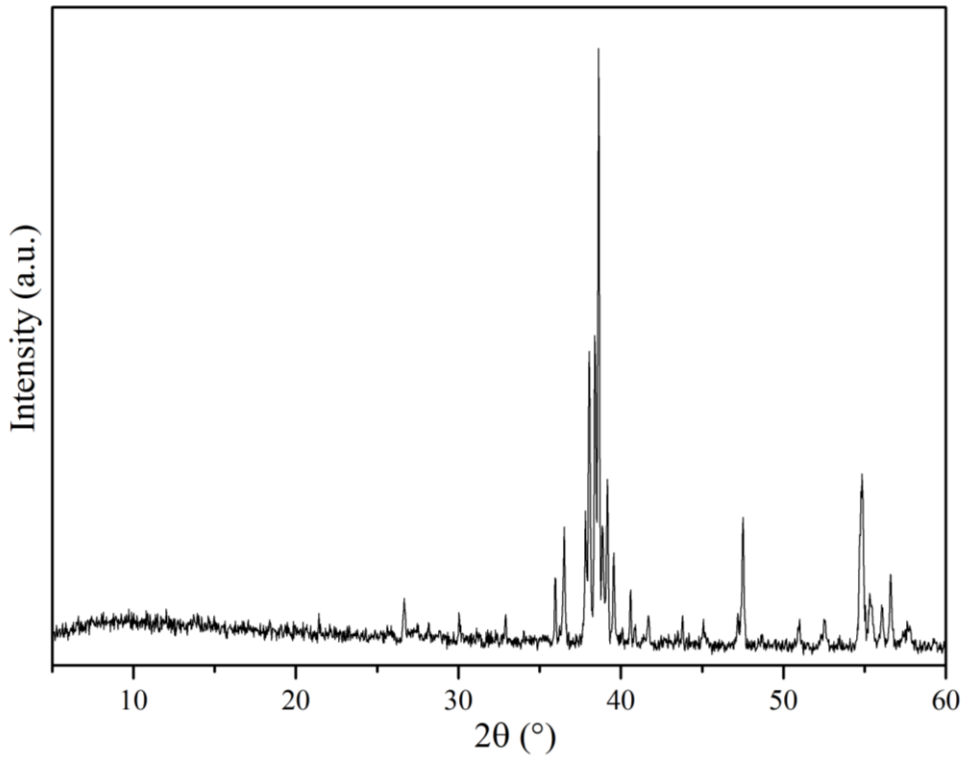

Figure 5.1 PXRD pattern showing multiphase sample obtained through synthesis of $Y_{0.9}Ba_{1.7}Ca_{2.4}Fe_{2.5}Co_{2.5}O_{13-\delta}$.

In order to isolate a phase pure material of high Co content, multiple samples were prepared using the EDX given composition of $Y_{1.23}Ba_{1.60}Ca_{2.17}Fe_{3.10}Co_{1.90}O_z$ as the starting point, fixing the *B*-site at $Fe_{3.1}Co_{1.9}$. Additional synthesis of lower Co content (x = 0.5, 1 and 1.5) was carried out, with the aim to obtain a range of Co contents that would enable potential trends in cathode performance and structure to be observed. Ternary phase diagrams of *A*-site cation ratios were used to direct the synthesis at each fixed Co content, leading to the isolation of phase pure samples for x = 0.5 ($YBa_{1.8}Ca_{2.2}Fe_{4.5}Co_{0.5}O_{13-\delta}$) and x = 1 ($Y_{1.15}Ba_{1.75}Ca_{2.1}Fe_4CoO_{13-\delta}$). For x = 1.5, it was not possible to isolate a pure sample at this point, therefore properties and structural characterisation have not been carried out in this thesis.

In order to isolate phase pure samples, 0.5 g batches were synthesised by hand grinding dried powders of Y_2O_3 (99.999 %), $BaCO_3$ (99.997 %), $CaCO_3$ (99.95 %), Fe_2O_3 (99.9985 %) and Co_3O_4 (99.9998 %), all sourced from Alpha Aesar, in the required ratios in a pestle and mortar. The mixed powders were heated in a furnace to 1100 °C at a rate of 5 °C per minute in a Pt metal crucible in static air. After dwelling at 1100 °C for 12 hours, the furnace was cooled to room temperature at 3 °C per minute. The black crystalline materials obtained were hand ground and room temperature PXRD patterns were collected. The samples were then pressed into 13 mm pellets, with 2 tons force applied, before undergoing the same heat treatment as for the first cycle, before being ground and having PXRD patterns collected. This process was repeated until PXRD patterns stopped changing, indicating that the reaction had reached completion.

5.2.2 Highest Co content synthesis

Synthesis of the highest Co content, using the EDX attained ratio as the starting point led to a majority $10a_p$ phase, which had the composition $Y_{1.2}Ba_{1.8}Ca_2Fe_{3.1}Co_{1.9}O_{13-\delta}$. A Pawley fit using PXRD data collected for this sample is shown in Figure 5.2. There were some difficulties in identifying the impurity phase(s) shown in the PXRD pattern (marked with *), although a good match for the observed impurity reflections was obtained using $BaCaCo_2Fe_2O_7$.[264] EDX was carried out on this sample in order to give further indication of the composition required for a phase pure sample. It was of particular interest to determine if

the Fe/Co ratio within the 10a_p phase varied from the starting ratios, possibly due to reaching the limit of Co doping.

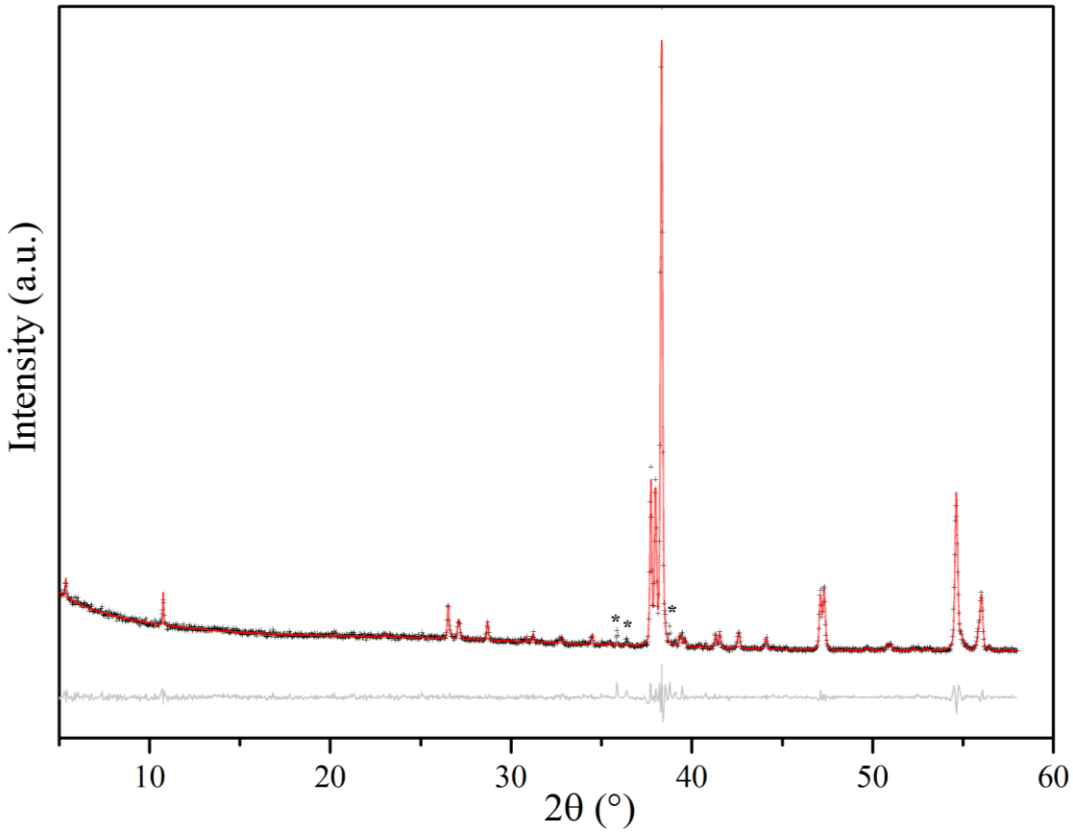

Figure 5.2 Pawley fit of PXRD data collected for $Y_{1.2}Ba_{1.8}Ca_2Fe_{3.1}Co_{1.9}O_{13-\delta}$, with impurity peaks highlighted with *.

Further EDX of the $Y_{1.2}Ba_{1.8}Ca_2Fe_{3.1}Co_{1.9}O_{13-\delta}$ sample resulted in the composition $Y_{1.24(11)}Ba_{1.85(9)}Ca_{1.91(13)}Fe_{3.15(9)}Co_{1.85(9)}O_{13-\delta}$ being observed from an average of 15 crystals. Further synthetic work was continued, with the Fe/Co content varied, as well as making small changes to the *A*-site ratio. High purity samples were obtained, however, impurity peaks became apparent from higher quality PXRD data sets. The impurities were also difficult to identify due to peak overlap within PXRD patterns, but were later identified as (*Ln*,Ca)BaM_4O_7 (*M* = Co,Fe) from synchrotron data.[265]

An iodometric titration was carried out on a high purity sample ($Y_{1.18}Ba_{1.89}Ca_{1.93}Fe_{3.17}Co_{1.83}O_{13-\delta}$), using the same protocols described in chapters 3 and 4, in order to obtain the oxygen content and thus the average oxidation state of the *B*-site cations. Assuming reduction to Fe^{2+} and Co^{2+},[185] the titration determined a content of $O_{12.54(5)}$, indicating that the sample was deficient in oxygen when compared to the expected O_{13} for a pure Fe *B*-site 10a_p. It appears that the oxygen deficiency is a result of the lower average oxidation state of Co compared to pure Fe^{3+} found in the parent material, with significant amounts of Co^{2+} likely present. Using this information, approaches for the isolation of a phase pure sample were then considered. Two successful approaches discussed in section 5.2.3 and 5.2.4.

5.2.3 O_2 annealing of high Co content 10a_p

In the case of a related 3a_p phase, $YBa_2(Fe_{1-x}Co_x)_3O_8$, annealing under a flowing atmosphere of O_2 enabled the preparation of samples up to $x = 0.47$.[266] Therefore, in order to compensate for oxygen deficiency in $Y_{1.24}Ba_{1.85}Ca_{1.91}Fe_{3.15}Co_{1.85}O_{13-\delta}$, the highest purity composition prepared thus far, the sample was annealed in a flowing atmosphere of 100 % O_2 at 1100 °C for 12 hours. The resultant powder was hand ground and analysed by PXRD, which can be seen in Figure 5.3. The PXRD pattern showed that the sample was now phase pure, containing only the desired 10a_p phase. The saturated O_2 atmosphere appeared to have compensated for the oxygen deficiency in the sample, allowing a pure 10a_p sample to form. The oxidation of Co^{2+} to Co^{3+} is the most probable explanation, as was the case with $YBa_2(Fe_{1-x}Co_x)_3O_8$.[266]

The sample was then scaled up for acquisition of ND and SXRD data, as well as for the measurement of AC impedance to obtain an ASR. This sample with composition $Y_{1.24}Ba_{1.85}Ca_{1.91}Fe_{3.15}Co_{1.85}O_{13-\delta}$, will be referred to as $x = 1.85$(I) from this point onwards.

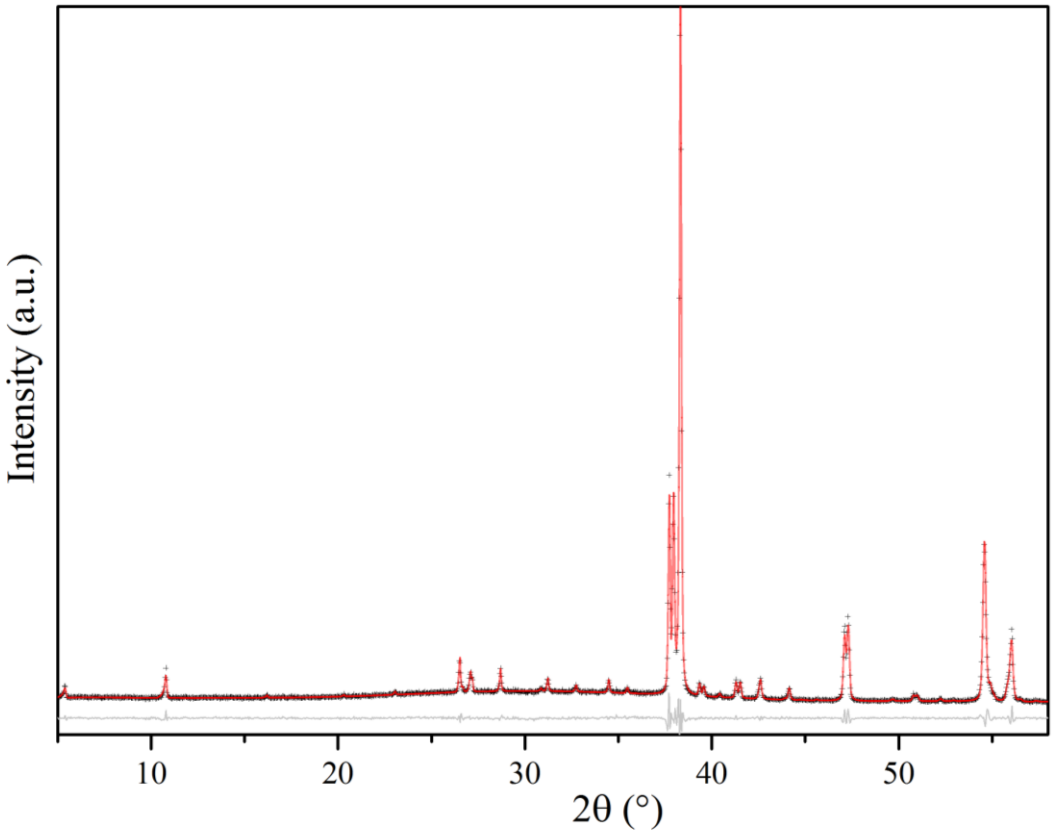

Figure 5.3 Pawley fit of PXRD data for O_2 annealed $Y_{1.24}Ba_{1.85}Ca_{1.91}Fe_{3.15}Co_{1.85}O_{13-\delta}$.

5.2.4 Variation in Y to Ca/Ba ratio, forming a solid solution for $Fe_{3.15}Co_{1.85}$

The determined oxygen deficiency of $Y_{1.18}Ba_{1.89}Ca_{1.93}Fe_{3.17}Co_{1.83}O_{12.54(5)}$, led to a simultaneous second approach for the attempted isolation of a phase pure Co rich sample. The incorporation of increased Y^{3+} content, substituting for Ca^{2+}/Ba^{2+}, was investigated in an attempt to introduce a greater overall charge to the sample, which was hoped would compensate for a lower overall *B*-site oxidation state due to the presence of Co^{2+}. It was envisioned that this method would introduce a greater oxygen content, which is required in order to maintain charge neutrality, allowing synthesis of this sample in air.

Starting with ca. $Y_y(Ba,Ca)_{5-y}Fe_{3.15}Co_{1.85}O_{13-\delta}$ (although Ba usually ≈ 1.8), a range of Y content samples were prepared from y = 0.8 - 3, with PXRD data collected on all samples

synthesised as discussed in 5.2.1. A representative selection of PXRD patterns are displayed in Figure 5.4, which indicates that at this high Co content, the $10a_p$ phase forms as a solid solution with Y versus Ba/Ca ratio. This observation is particularly noteworthy as this phenomenon is not possible for the Fe pure $10a_p$, which required an exact *A*-site cation ratio to form single phase due to Fe being particularly stable at 3+.

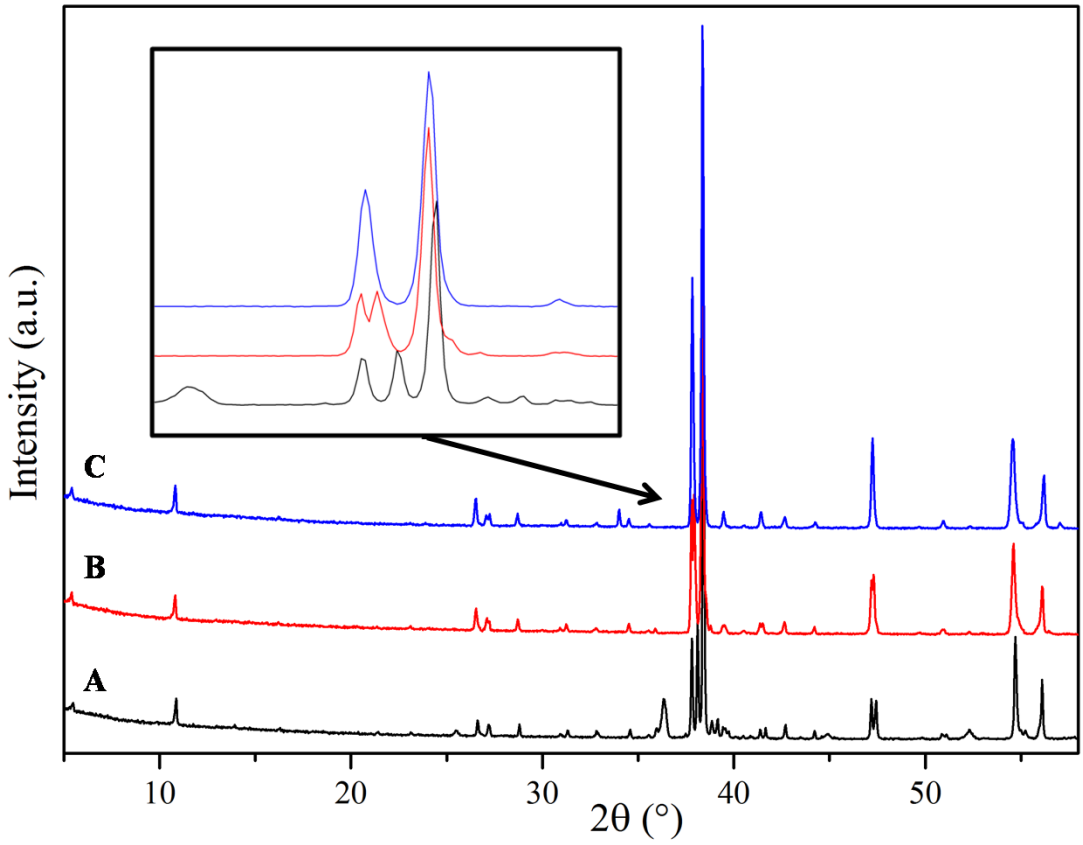

Figure 5.4 Changes in PXRD patterns observed with Y substitution for Ca, A) $YBa_{1.8}Ca_{2.2}Fe_{3.15}Co_{1.85}O_{13\pm\delta}$, B) $Y_{1.4}Ba_{1.8}Ca_{1.8}Fe_{3.15}Co_{1.85}O_{13\pm\delta}$, C) $Y_{1.6}Ba_{1.8}Ca_{1.6}Fe_{3.15}Co_{1.85}O_{13\pm\delta}$.

Interestingly at high Y content ($Y_{1.6}Ba_{1.8}Ca_{1.6}Fe_{3.15}Co_{1.85}O_{13\pm\delta}$), as is apparent in Figure 5.4 C), the $10a_p$ phase that forms appears to be almost tetragonal, with the *a* and *c* lattice parameters moving close together. The lower the Y content, the $10a_p$ phase becomes more orthorhombic, with the *a* and *c* lattice parameters moving further apart. The trend in lattice parameters is shown in Figure 5.5. The *a* lattice parameter increases up to $y \sim 1.8$, while the *b* and *c* lattice parameters both decrease up to $y \sim 1.8$, leading to an overall volumetric unit cell

decrease. The lower limit for Y content is not as clear, however it appears to be $y \sim 1$. It should be noted that at this point, none of the samples were single phase, meaning there may have been some variation from the as-made *A* and *B*-site ratios, possibly giving rise to some slight deviations in lattice parameters. Despite this, the obvious trend observed was interesting behaviour for the $10a_p$ phase.

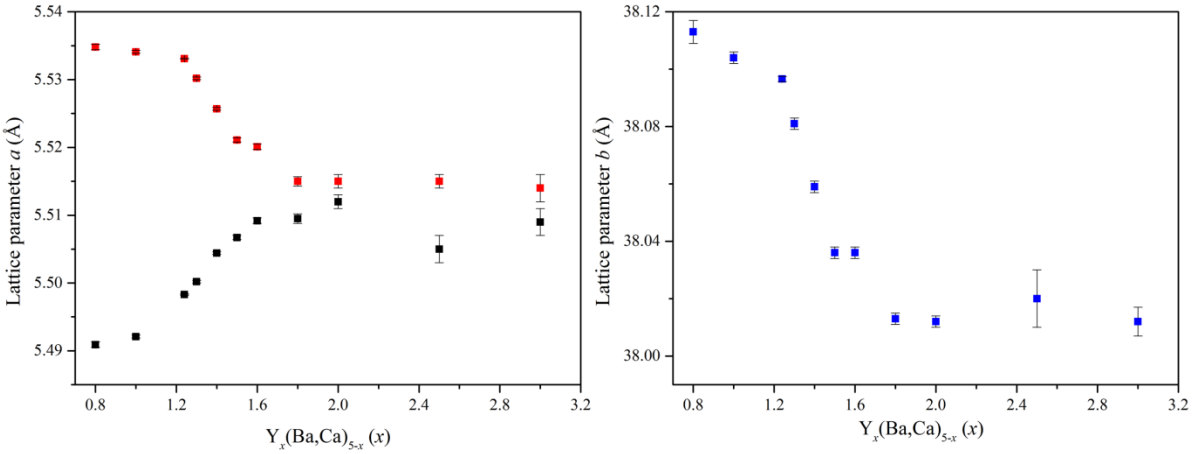

Figure 5.5 Plots of lattice parameter evolution with Y content for $Y_y(Ba,Ca)_{5-y}Fe_{3.15}Co_{1.85}O_{13\pm\delta}$. Showing *a* (black), *b* (blue) and *c* (red).

Attempts were made to isolate a range of Y contents, with y = 1, 1.4 and 1.6 focused upon. For each Y content, the Ba to Ca ratios were varied in order to achieve this, whilst Fe and Co content remained fixed at 3.15 and 1.85 respectively. Although y = 1 and 1.4 samples were prepared with high purity, they were not isolated phase pure at his point and therefore have not been structurally characterised or tested as a cathode for this thesis. For y = 1.6, a sample was isolated phase pure as identified by laboratory PXRD, and formed with the composition $Y_{1.6}Ba_{1.8}Ca_{1.6}Fe_{3.15}Co_{1.85}O_{13-\delta}$. SXRD and ND data were collected for crystal structure characterisation, and AC impedance was measured in order to evaluate cathode performance. This composition will be referred to as x = 1.85(II) from this point onwards to distinguish it from x=1.85(I) made by O_2 annealing and with a different *A*-site composition.

All of the *A*-site cation ratios synthesised for $Fe_{3.15}Co_{1.85}$ are shown in Figure 5.6, with the two isolated phases x = 1.85(I) and 1.85(II) represented by green and red points respectively.

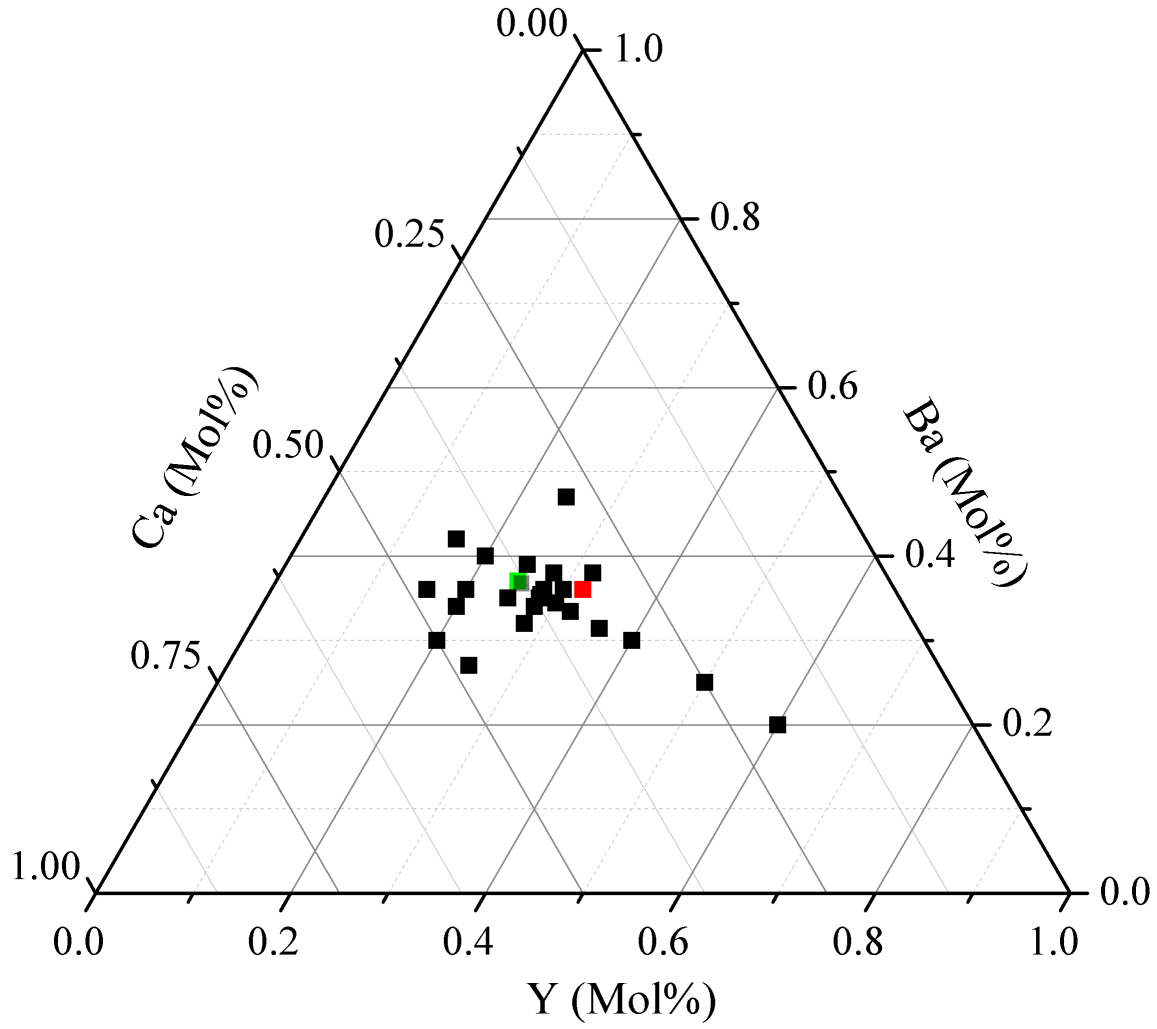

Figure 5.6 Phase diagram of *A*-site compositions synthesised for $(Y,Ba,Ca)_5Fe_{3.15}Co_{1.85}O_{13-\delta}$, with x = 1.85(I) represented with green point and x = 1.85(II) represented with red point.

All samples characterised in this thesis, or parent materials used as reference are listed in Table 5.1 along with what they are referred to for this chapter.

Two references are used for the parent material, x = 0(I) is the original publication that contains the structural characterisation and initial ASR.[35] The second, x = 0(II), contains an improved ASR measurement following changes to cathode processing, including different milling protocols and cathode adherence temperatures.[162]

Composition	Referred to as	Comment
$Y_{0.9}Ba_{1.7}Ca_{2.4}Fe_5O_{13-\delta}$ [35]	x = 0(I)	Original synthesis
$Y_{0.9}Ba_{1.7}Ca_{2.4}Fe_5O_{13-\delta}$ [162]	x = 0(II)	New cathode preparation
$YBa_{1.8}Ca_{2.2}Fe_{4.5}Co_{0.5}O_{13-\delta}$	x = 0.5	
$Y_{1.15}Ba_{1.75}Ca_{2.1}Fe_4CoO_{13-\delta}$	x = 1	
$Y_{1.24}Ba_{1.85}Ca_{1.91}Fe_{3.15}Co_{1.85}O_{13-\delta}$	x = 1.85(I)	O_2 annealed
$Y_{1.6}Ba_{1.8}Ca_{1.6}Fe_{3.15}Co_{1.85}O_{13-\delta}$	x = 1.85(II)	

Table 5.1 Shows how the compositions studied in this chapter are referred to in this chapter for clarity.

5.3 Crystal Structure Characterisation

Although Co and Fe cannot be distinguished by PXRD (electron count), there is a good contrast in ND (bound coherent scattering lengths: Fe = 9.45, Co = 2.49 fm)[168], which allows the Co and Fe distribution within the *B*-sites of the structure to be determined. It is important to establish the sites that Co is found in for these structures as it is believed that the ordered oxygen vacancies between the S_q (*B*1) polyhedra are the active sites in the ORR, as well as being the main source of ionic mobility, as was reported for $LnBaCo_2O_{5.5+\delta}$.[153, 154]

Time-of-flight neutron diffraction (ND) data were collected for all samples on the POLARIS instrument as detailed in section 2.2.10. SXRD data were obtained on Beamline I11 as detailed in section 2.2.9, at a wavelength of 0.82699 Å over a 2θ range of 2 to 90° and a step size of 0.001°, using the PSD detector for 0.1 mm capillaries for x = 1, x = 1.85(I) and x = 1.85(II). Data were also collected at a wavelength of 0.825623 Å (ASXRD) over a 2θ range of 2 to 90° and a step size of 0.001°, using the PSD detector for a 0.1 mm capillary for x = 0.5. Powder diffraction data were analysed in a combined X-ray and neutron Rietveld refinement using the computer program Topas Academic v5.[175]

5.3.1 Modelling magnetic structures

Using the parent $10a_p$ starting model, combined Rietveld refinements were carried out on the SXRD and ND data. Within the ND data sets, magnetic reflections with a *d*-spacing that was characteristic of the unit cell were observed, as was the case for $Y_{0.9}Ba_{1.7}Ca_{2.4}Fe_5O_{13}$.[35]

Magnetic structures of the Co doped $10a_p$ phases were created using the computer program SARAh[200] and were screened against the observed neutron scattering data. The working models were then imported into GSAS software[174] together with banks 2 and 5 POLARIS to confirm that the magnetic models fit well in each case. The best fits was observed for G-type antiferromagnetic structures (propagation vector **k** = 0,0,0) with moments (anti)parallel to the *a*-axis. This is the same magnetic structure found for the parent $10a_p$ $Y_{0.9}Ba_{1.7}Ca_{2.4}Fe_5O_{13,}$[35] and is a common type of magnetic structure for perovskites with an Fe^{3+} *B*-site, as discussed in chapter 3.2.2.[35, 65, 190, 197] The magnitude of the magnetic moment along the *a*-axis on each *B*-site was refined in magnetic space group *Pnm'a*, with the moments of the three *B*-sites initially fixed to the same value until a good fit was achieved for the data. The moments were then allowed to refine freely from each other.

5.3.2 Combined refinements using SXRD and ND data

For each Rietveld refinement carried out, the x = 0(I) structure was used as the starting model,[35] with lattice parameters, peak shape, scale and zero shift refined for SXRD data initially. *A*-site occupancy was then allowed to refine as Ba only, in order to represent electron density, while *B*-site occupancy was fixed as wholly occupied by Fe, which is indistinguishable from Co by X-rays. Once a good fit was obtained, the POLARIS ND data sets from banks 2, 3, 4 and 5 were added to the refinement, Co added equally to the *B*-sites and for the *A*-site, Ca and Y were added as for x = 0(I).[35] The relative occupancies of each of the *A* and *B*-sites contained soft chemical composition restraints to drive the refinements towards each of the as-made compositions. A total occupancy of unity was also enforced on each site. The determined magnetic models were added to the refinements at this point.

Single isotropic displacement parameters were refined for each atom type, while the atomic coordinates were refined within the symmetry allowed by each Wyckoff position.

Other phases were added when required, such as Vanadium for $x = 1$ and $x = 1.85$(II), which was observable in each case in the POLARIS data as the samples were measured in Vanadium cans (~ 3 g samples). The Vanadium peaks were not observed for $x = 0.5$ (very large sample > 5 g) or $x = 1.85$(I) (sample measured in glass capillary). The Y_2O_3[201] and $Ca_2Fe_2O_5$[190] impurities were added to the refinement of $x = 1.85$(II), which were observed most noticeably in the SXRD data. Only lattice parameters, scale and peak shape were refined for the vanadium and impurity phases.

For all Rietveld refinements, in order to improve the fitting of the broad, asymmetric low angle Bragg reflections, the SXRD data-set was split into two histograms covering low 2θ (d spacing 10.75 Å - 4.74 Å) and high 2θ (d spacing 4.74 Å - 0.72 Å). Anisotropic strain broadening[202] was refined for the Co doped $10a_p$ phase in the high 2θ SXRD data-set. The probable cause of the observed broadening in the long axis is stacking faults, which are common for the similar brownmillerite phases, as discussed in section 3.2.1.[203, 204] All of the ND time-of-flight diffractometer constants were all refined for ND banks 2, 3, 4 and 5. The zero point was refined for the SXRD data giving a total of 13 refined diffractometer parameters. A total of 42 background parameters were refined; 6 for each ND histogram; 6 for the low 2θ and 12 for the high 2θ SXRD histogram.

The results of the Rietveld refinements for each of the four phases are shown in the sections below, followed by a comparison of the refined structures. All refinements were carried out using Topas Academic v5.[175]

5.3.3 $x = 0.5$ Rietveld refinement

The fitted data for $x = 0.5$ can be seen below in Figure 5.7, with a table of all the refined parameters shown in Table 5.2. Co did not show marked *B*-site preference, although the T_d coordination site was slightly favoured (*B*3 ~ 20 % Co occupancy), compared to the O_h site (*B*2 ~ 10 % Co occupancy) and S_q site (*B*1 ~ 5 % Co occupancy).

The magnetic moments when fixed to the same value were 3.625(7) μ_B, which is equivalent to the moment determined for $x = 0$ of 3.638(9) μ_B.[35] Although high spin Co^{3+} has one less unpaired electron than high spin Fe^{3+}, and therefore a smaller magnetic moment, the difference is not great. With the small amount of Co substitution for Fe in $x = 0.5$, there is only a small change in the magnitude of the moment observed.

As the Co content on each site varied slightly, the magnetic moments were then allowed to refine freely from each other, leading to moments of; $B1$ = 3.66(4) μ_B, $B2$ = 3.64(4) μ_B and $B3$ = 3.22(7) μ_B. The lower moment found on the T_d $B3$ site is likely due to the presence of greater amounts of Co compared to the other sites.

The refined composition $Y_{0.98(9)}Ba_{1.80(2)}Ca_{2.22(9)}Fe_{4.50(1)}Co_{0.50(1)}O_{13}$, is the same as the as-made composition, giving strength to the results. After a stable refinement and good fit of the data were achieved, the oxygen occupancies were allowed to refine in order to determine if any vacancies were present. However, they remained wholly occupied within error. A good fit of the data was achieved (Figure 5.7) with an R_{wp} = 2.404, R_{exp} = 0.648. The refined structure for $x = 0.5$ is displayed in Figure 5.8.

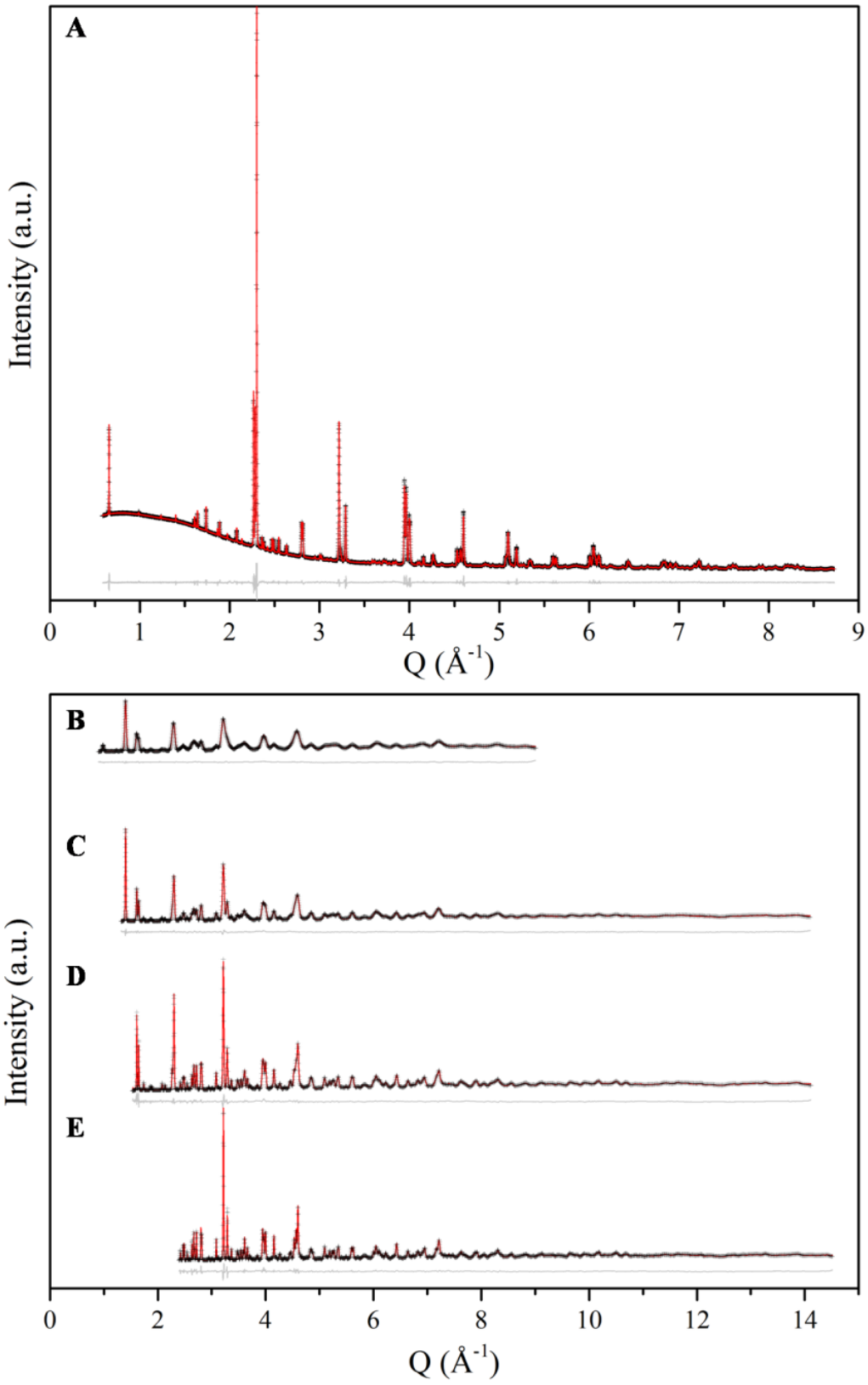

Figure 5.7 Fit data from a combined refinement of SXRD and ND data for x = 0.5, showing A) SXRD data together with B) ND bank 2, C) ND bank 3, D) ND bank 4 E) ND bank 5 data.

	Unit Cell Parameters					
	a (Å)	5.50323(2)				
	b (Å)	38.1956(2)				
	c (Å)	5.54730(2)				
Site	**Multiplicity**	**Occupancy**	***x***	***y***	***z***	***Biso* (Å^2)**
A1	4*a*	$Y_{0.615(4)}Ca_{0.385(4)}$	0	0	0	0.537(7)
A2	8*h*	$Ba_{0.859(2)}Ca_{0.141(2)}$	0	0.59971(2)	0.9964(2)	0.537(7)
A3	8*h*	$Y_{0.182(46)}$ $Ba_{0.041(8)}Ca_{0.777(68)}$	0	069335(2)	0.9761(3)	0.537(7)
B1	8*h*	$Fe_{0.955(4)}Co_{0.045(4)}$	0	0.04896(2)	0.5019(3)	0.260(7)
B2	8*h*	$Fe_{0.901(4)}Co_{0.099(4)}$	0	0.15300(2)	0.5024(3)	0.260(7)
B3	8*i*	$Fe_{0.394(4)}Co_{0.106(4)}$	0.0586(3)	1/4	0.5691(3)	0.260(7)
O1	8*g*	1	1/4	0.03923(6)	1/4	0.693(9)
O2	8*g*	1	1/4	0.96345(6)	1/4	0.693(9)
O3	8*g*	1	1/4	0.15140(6)	1/4	0.693(9)
O4	8*g*	1	1/4	0.65777(6)	1/4	0.693(9)
O5	8*i*	0.5	0.4058(8)	1/4	0.6120(8)	0.693(9)
O6	8*h*	1	0	0.09807(6)	0.5071(6)	0.693(9)
O7	8*h*	1	0	0.20762(6)	0.4329(4)	0.693(9)

Table 5.2 Refined crystallographic parameters from combined data set of ND, SXRD. Space group - *Imma*. Refined composition $Y_{0.98(9)}$ $Ba_{1.80(2)}Ca_{2.22(9)}Fe_{4.50(1)}Co_{0.50(1)}O_{13}$ (referred as x=0.5), including soft chemical composition restraint.

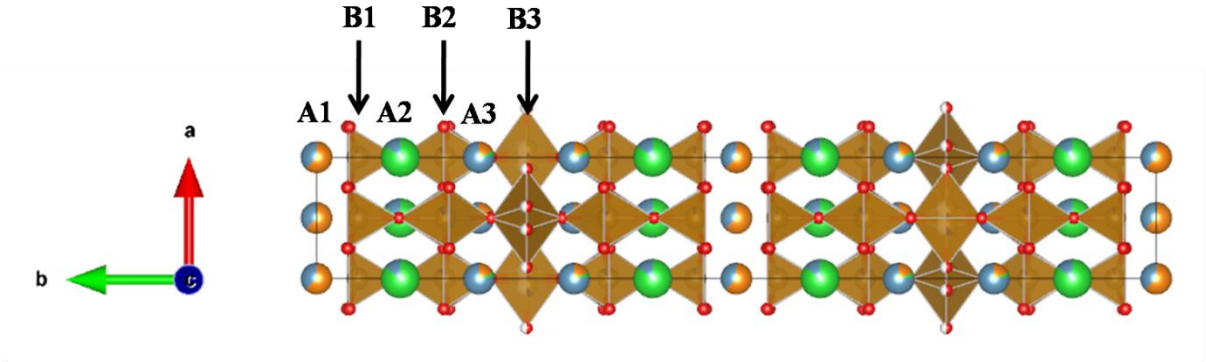

Figure 5.8 Refined structure of $x = 0.5$ in *Imma* with *A*-sites and *B*-sites labelled.

5.3.4 x = 1 Rietveld refinement

The fitted data for x = 1 can be seen below in Figure 5.9, with a table of all the refined parameters shown in Table 5.3. Co substituted onto the *B*-site with a similar preference as for x = 0.5, with the T_d coordination site favoured (*B*3 ~ 30 % Co occupancy), compared to the O_h site (*B*2 ~ 15 % Co occupancy) and S_q site (*B*1 ~ 20 % Co occupancy).

The magnetic moments when fixed to the same value were 3.550(9) μ_B, which is reduced when compared to x = 0.5 and x = 0.[35] The reduction observed is due to the difference in number of unpaired electrons found in Fe^{3+} compared to $Co^{2+/3+}$. As the Co content on each site varied slightly, the magnetic moments were then allowed to refine freely from each other, leading to moments of; *B*1 = 3.80(8) μ_B, *B*2 = 3.52(9) μ_B and *B*3 = 3.1(1) μ_B. The lower moment found on the T_d *B*3 site is again likely due to the presence of greater amounts of Co compared to the other sites.

The refined composition $Y_{1.14(9)}$ $Ba_{1.76(2)}Ca_{2.10(9)}Fe_{4.04(2)}Co_{0.96(2)}O_{13}$, is notably close to the as-made composition. Once a stable refinement with a good fit of the data was achieved, the oxygen occupancies were allowed to refine. They remained wholly occupied within error, as in the case of x = 0.5.

An additional oxygen site was then added to the vacancy channel position between the S_q *B*1 sites due to the presence of increased Y^{3+} for Ba^{2+}/Ca^{2+} compared to x= 0(I), which could lead to increased O. The refined occupancy of this site was 0.021(9), indicating that there is negligible oxygen found there at room temperature at which the data were collected, hence this site was removed from the final refinement. Due to the additional Y^{3+} content in this sample compared to x = 0,[35] along with the same O occupancies, the transition metal *B*-site will have to compensate to maintain charge neutrality. Assuming that Fe^{3+} is the only oxidation state that it is found in as Fe^{2+} is uncommon in air (although possible),[267] Co would be required to have an average charge state of +2.85. A good fit of the data was achieved with an R_{wp} = 1.387, R_{exp} = 0.759. The refined structure of x = 1 is displayed in Figure 5.10.

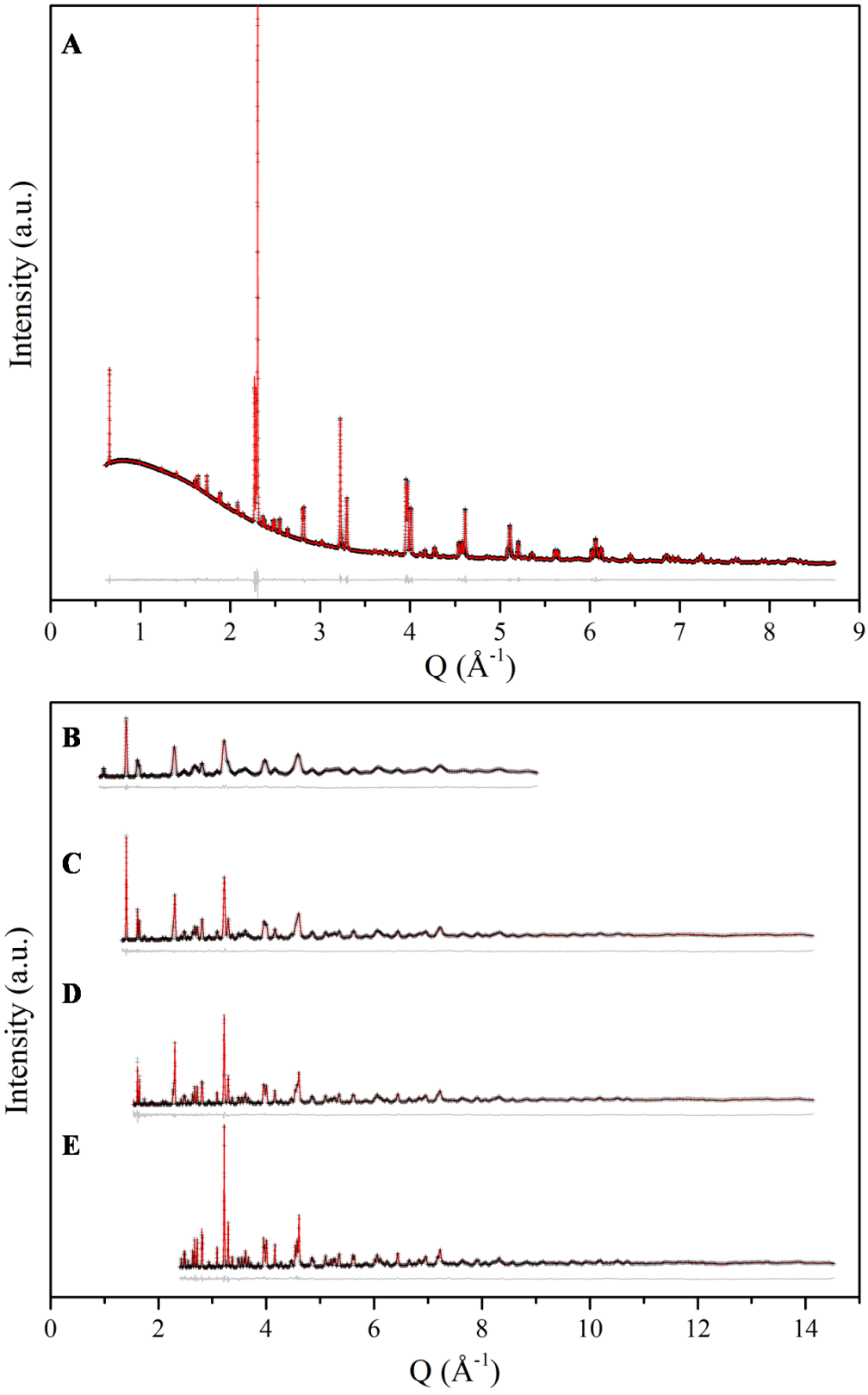

Figure 5.9 Fit data from a combined refinement of SXRD and ND data for x = 1, showing A) SXRD data together with B) ND bank 2, C) ND bank 3, D) ND bank 4 E) ND bank 5 data.

	Unit Cell Parameters					
	a (Å)	5.49546(2)				
	b (Å)	38.1385(2)				
	c (Å)	5.53769(2)				
Site	**Multiplicity**	**Occupancy**	***x***	***y***	***z***	***Biso* (Å^2)**
A1	4*a*	$Y_{0.601(4)}Ca_{0.399(4)}$	0	0	0	0.389(7)
A2	8*h*	$Ba_{0.834(2)}Ca_{0.166(2)}$	0	0.59971(2)	0.9964(2)	0.389(7)
A3	8*h*	$Y_{0.270(40)}$ $Ba_{0.044(8)}Ca_{0.686(58)}$	0	069335(2)	0.9761(3)	0.389(7)
B1	8*h*	$Fe_{0.810(7)}Co_{0.190(7)}$	0	0.04896(2)	0.5019(3)	0.287(5)
B2	8*h*	$Fe_{0.850(5)}Co_{0.150(5)}$	0	0.15300(2)	0.5024(3)	0.287(5)
B3	8*i*	$Fe_{0.357(5)}Co_{0.143(5)}$	0.0586(3)	1/4	0.5691(3)	0.287(5)
O1	8*g*	1	1/4	0.03923(6)	1/4	0.88(1)
O2	8*g*	1	1/4	0.96345(6)	1/4	0.88(1)
O3	8*g*	1	1/4	0.15140(6)	1/4	0.88(1)
O4	8*g*	1	1/4	0.65777(6)	1/4	0.88(1)
O5	8*i*	0.5	0.4058(8)	1/4	0.6120(8)	0.88(1)
O6	8*h*	1	0	0.09807(6)	0.5071(6)	0.88(1)
O7	8*h*	1	0	0.20762(6)	0.4329(4)	0.88(1)

Table 5.3 Refined crystallographic parameters from combined data set of ND, SXRD. Space group - *Imma*. Refined composition $Y_{1.14(9)}$ $Ba_{1.76(2)}Ca_{2.10(9)}Fe_{4.04(2)}Co_{0.96(2)}O_{13}$, including soft chemical composition restraint.

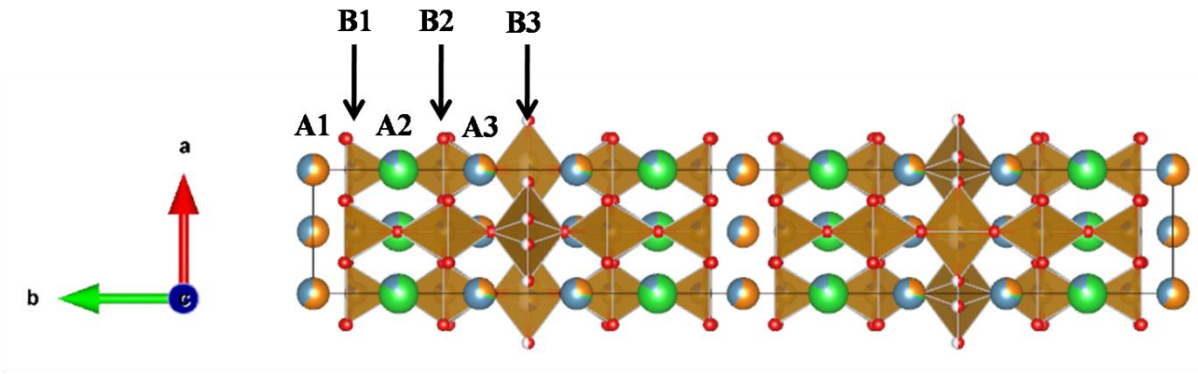

Figure 5.10 Refined structure of $x = 1$ in *Imma* with *A*-sites and *B*-sites labelled.

5.3.5 x = 1.85(I) Rietveld refinement

The fitted data for x = 1.85(I) can be seen below in Figure 5.11, with a table of all the refined parameters shown in Table 5.4. As with x = 0.5 and 1, Co showed a preference for the occupation of the T_d coordination *B*-site. A little under 50 % Co occupancy was determined for the T_d (B3) site, with O_h site *B*2 having 30 % Co occupancy and the S_q site *B*1 has just under 40 % Co occupancy.

The magnetic moments when fixed to the same value were 3.30(2) μ_B, reduced further compared to x = 0,[35] 0.5 and 1. The difference between the magnetic moments is again attributed to the number of unpaired electrons/spin state of Fe^{3+} (S = 5/2) compared to Co^{3+} (S = 2) and Co^{2+} (S = 3/2). As the Co content on each site varied slightly, the magnetic moments were then allowed to refine freely from each other, leading to moments of; *B*1 = 3.4(2) μ_B, *B*2 = 3.3(2) μ_B and *B*3 = 3.2(3) μ_B. Although the moment found on the T_d *B*3 site is lower, it is easily within error of the moments on the other sites, making them all essentially the same, with no difference clearly discernable.

The refined composition $Y_{1.26(13)}$ $Ba_{1.81(3)}Ca_{1.93(14)}Fe_{3.18(4)}Co_{1.82(4)}O_{13}$, is the same as the as-made composition. The relatively large error present on the composition is related to the ND data set, which was collected on a very small sample in a glass capillary (< 0.5 g). The oxygen occupancies were allowed to refine, however they remained wholly occupied within error, as was the case for x = 0.5 and 1. An additional oxygen site was added to the vacancy channel position between the S_q *B*1 sites, this time not only taking into account the increased Y^{3+} content, but also the fact that this sample was annealed in O_2. However, the oxygen atom would not remain in the channel, instead moving into a chemically non sensible position. When fixed, the occupancy stayed at zero. Due to the additional Y^{3+} content in this sample compared to x = 0,[35] along with the same oxygen occupancies, the *B*-site will again have to compensate to maintain charge neutrality. Assuming that the Fe^{3+} is the only oxidation state that it is found in, Co would be required to have an average charge state of +2.87. A good fit of the data was achieved with an R_{wp} = 2.544, R_{exp} = 0.817. The refined structure of x = 1.85(I) is displayed in Figure 5.12.

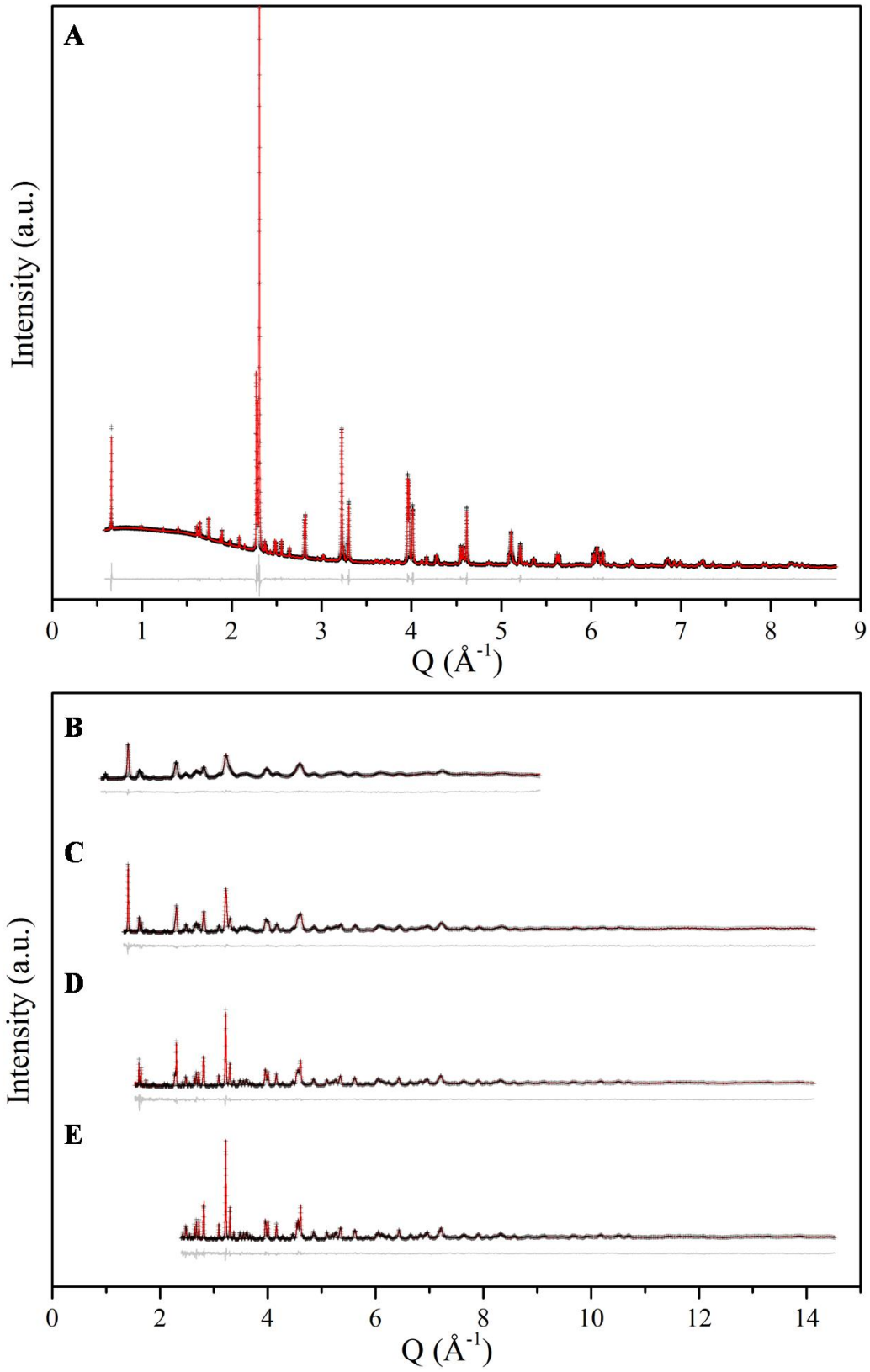

Figure 5.11 Fit data from a combined refinement of SXRD and ND data for x = 1.85(I), showing A) SXRD data together with B) ND bank 2, C) ND bank 3, D) ND bank 4 E) ND bank 5 data.

	Unit Cell Parameters					
	a (Å)	5.50292(1)				
	b (Å)	38.10134(9)				
	c (Å)	5.53609(1)				
Site	**Multiplicity**	**Occupancy**	***x***	***y***	***z***	***Biso* (Å^2)**
A1	4*a*	$Y_{0.668(4)}Ca_{0.332(4)}$	0	0	0	0.583(6)
A2	8*h*	$Y_{0.05(4)}Ba_{0.86(1)}Ca_{0.09(5)}$	0	0.59924(1)	0.9972(2)	0.583(6)
A3	8*h*	$Y_{0.25(6)}$ $Ba_{0.05(1)}Ca_{0.70(8)}$	0	069385(2)	0.9778(3)	0.583(6)
B1	8*h*	$Fe_{0.61(1)}Co_{0.39(1)}$	0	0.04937(3)	0.5029(4)	0.252(8)
B2	8*h*	$Fe_{0.71(1)}Co_{0.29(1)}$	0	0.15315(3)	0.5036(4)	0.252(8)
B3	8*i*	$Fe_{0.27(1)}Co_{0.23(1)}$	0.0549(4)	1/4	0.5680(4)	0.252(8)
O1	8*g*	1	1/4	0.0390(1)	1/4	0.84(1)
O2	8*g*	1	1/4	0.9634(1)	1/4	0.84(1)
O3	8*g*	1	1/4	0.1515(1)	1/4	0.84(1)
O4	8*g*	1	1/4	0.6581(1)	1/4	0.84(1)
O5	8*i*	0.5	0.396(2)	1/4	0.615(1)	0.84(1)
O6	8*h*	1	0	0.0982(1)	0.503(1)	0.84(1)
O7	8*h*	1	0	0.2079(1)	0.4384(1)	0.84(1)

Table 5.4 Refined crystallographic parameters from combined data set of ND, SXRD. Space group - *Imma*. Refined composition $Y_{1.26(13)}$ $Ba_{1.81(3)}Ca_{1.93(14)}Fe_{3.18(4)}Co_{1.82(4)}O_{13}$, including soft chemical composition restraint.

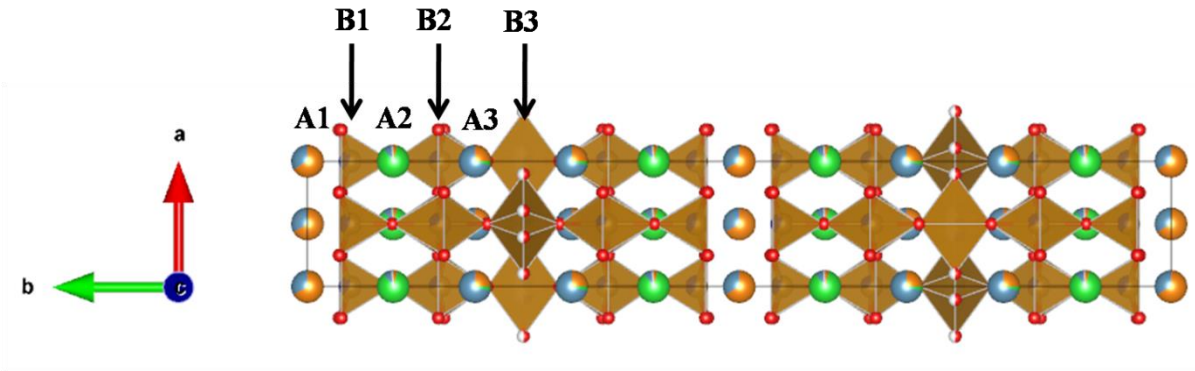

Figure 5.12 Refined structure of x = 1.85(I) in *Imma* with *A*-sites and *B*-sites labelled.

5.3.6 x = 1.85(II) Rietveld refinement

The final set of fitted data for a Co doped $10a_p$ sample, x = 1.85(II), can be seen below in Figure 5.14, with a table of all the refined parameters shown in Table 5.5. Refinements in the space group *Imma* produced unphysical bond lengths between *B*3 and O5 at the T_d site of 1.587(9) Å and 2.371(9) Å, which are unlikely for Co-O or Fe-O. A refinement was carried out in the space group *I*2*mb*, which has the same reflection conditions as *Imma*, however it differs from *Imma* by having ordered T_d chains, as opposed to disordered. The refinement in *I*2*mb* produced a good fit of the data. as well as giving chemically sensible bond lengths between *B*3 and O5 of 1.854(10) Å and 2.046(11) Å. Fourier difference maps did not show any mismatch around the T_d site that would suggest it should be split as would be the case in *Imma*, meaning the model identified described the structure well.

From the refinement in *I*2*mb*, Co occupied the *B*-site with the same preference as for x = 1.85(I), with the T_d coordination site again favoured with *B*3 having little under 50 % Co occupancy. The O_h site *B*2 has 30 % Co occupancy, while the S_q site *B*1 has just under 40 % Co occupancy.

The magnetic moments when fixed to the same value were 3.24(1) μ_B, which is slightly lower than x = 1.85(I), which has the same amount of Co present. This lower value is likely due to the presence of greater amounts of Co^{2+} (S = 3/2) and smaller amounts of Co^{3+} (S = 2) for x = 1.85(II) compared to x = 1.85(I). The magnetic moments were allowed to refine freely from each other, leading to moments of; *B*1 = 3.4(2) μ_B, *B*2 = 3.2(3) μ_B and *B*3 = 3.3(4) μ_B, with the moments all the same within error.

The refined composition $Y_{1.61(16)}$ $Ba_{1.70(3)}Ca_{1.69(22)}Fe_{3.15(3)}Co_{1.85(3)}O_{13}$, is close to the as-made composition ($Y_{1.6}Ba_{1.8}Ca_{1.6}Fe_{3.15}Co_{1.85}O_{13}$), although Ba is a little lower and Ca is a little higher than expected. The impurities identified and added to the refinement were Y_2O_3[201] (1.86 weight%) and $Ca_2Fe_2O_5$[190] (2.81 weight%), which only had lattice parameters and peak shape refined. Due to the number of cations present, it is likely that the $Ca_2Fe_2O_5$ present was doped, which would have affected its contributions to the observed reflections somewhat, most of which are overlapped with the $10a_p$ reflections. Although this could lead to some ambiguities in the refinement, the model remained chemically sensible.

At the end of the refinement the oxygen occupancies were allowed to refine, however they remained wholly occupied within error, as was the case for all Co doped $10a_p$ samples. An additional oxygen site was added to the vacancy channel position between the S_q *B*1 sites, however, the oxygen atom refined to zero. Due to the much increased Y^{3+} content in this sample compared to $x = 0$,[35] along with the same oxygen occupancies, in order to maintain charge neutrality, the *B*-site cations would have to compensate through changing their oxidation state. Assuming that the Fe^{3+} is the only oxidation state that it is found in, Co would be required to have an average charge state of +2.68. A good fit of the data was achieved with an $R_{wp} = 2.742$, $R_{wp} = 0.556$.

The structure of $x = 1.85$(II) refined in *I*2*mb*, displaying ordered T_d chains is shown in Figure 5.13, together with the structure of $x = 0$,[35] which has disordered T_d chains in the space group *Imma*, for comparison.

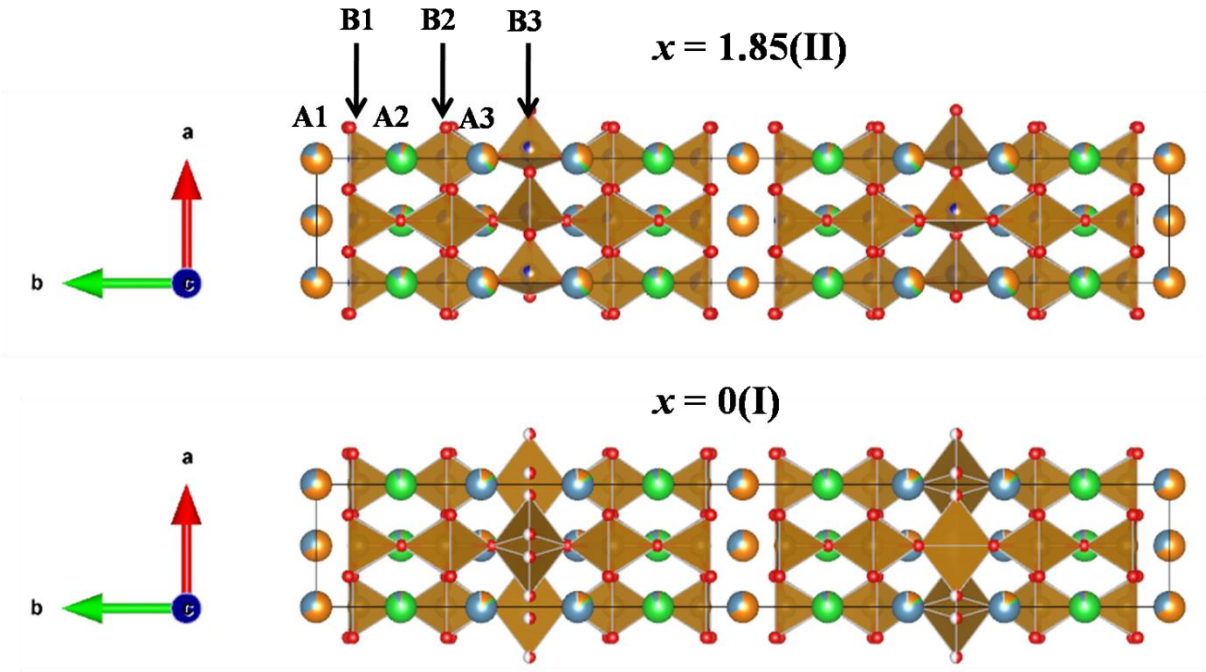

Figure 5.13 Refined structure of $x = 1.85$(II) in *I*2*mb* with *A*-sites and *B*-sites labelled, together with $x = 0$,[35] in *Imma* for comparison.

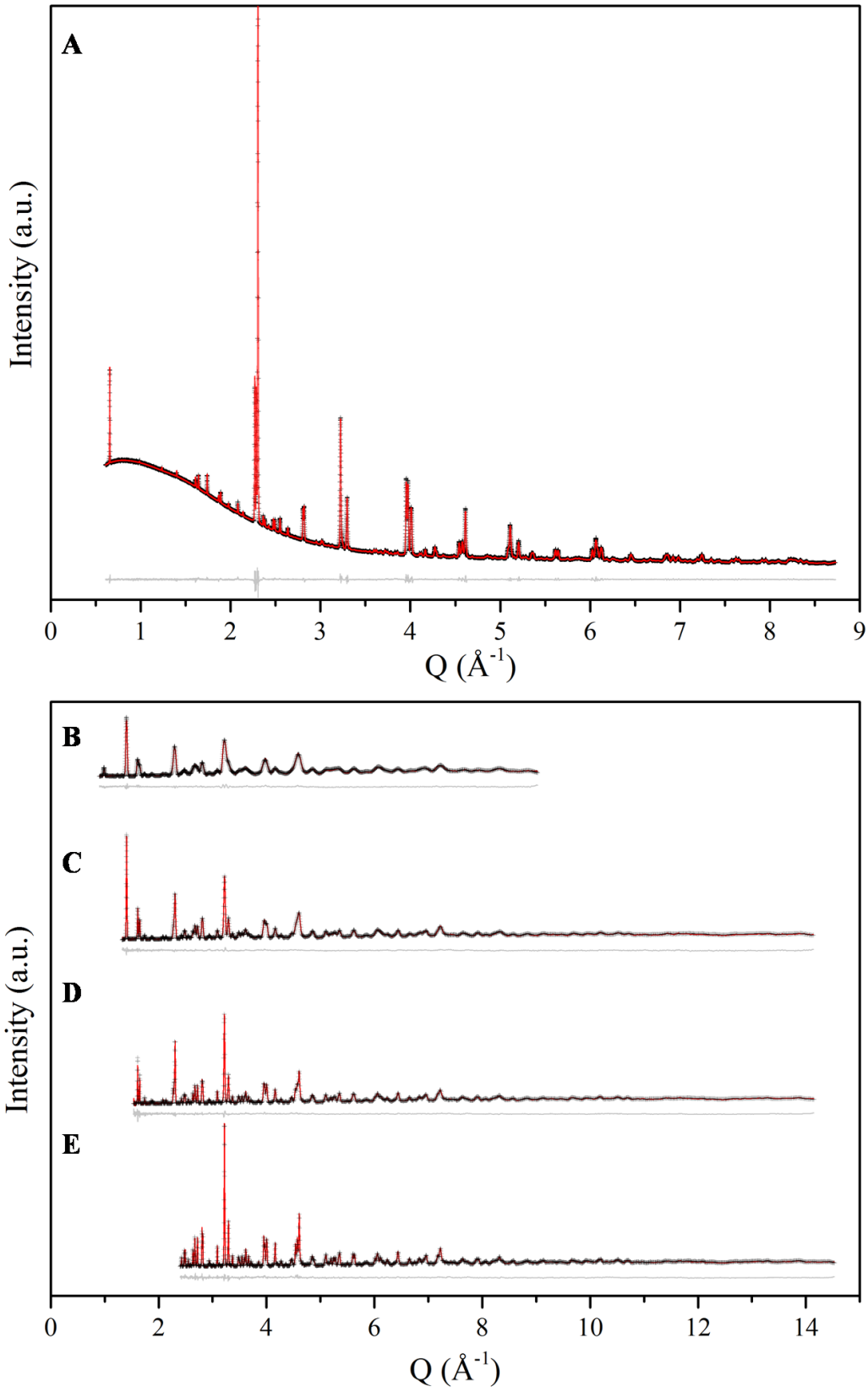

Figure 5.14 Fit data from a combined refinement of SXRD and ND data for x = 1.85(II), showing A) SXRD data together with B) ND bank 2, C) ND bank 3, D) ND bank 4 E) ND bank 5 data.

Unit Cell Parameters						
	a (Å)	5.51848(3)				
	b (Å)	38.00684(8)				
	c (Å)	5.52196(3)				
Site	**Multiplicity**	**Occupancy**	***x***	***y***	***z***	***Biso* (Å^2)**
A1	4*a*	$Y_{0.784(4)}Ca_{0.216(4)}$	0	0	0	0.642(6)
A2	8*h*	$Y_{0.07(4)}Ba_{0.79(1)}Ca_{0.14(5)}$	0	0.59954(1)	0.9968(3)	0.642(6)
A3	8*h*	$Y_{0.35(5)}$ $Ba_{0.06(1)}Ca_{0.59(7)}$	0	069439(2)	0.9825(4)	0.642(6)
B1	8*h*	$Fe_{0.61(1)}Co_{0.39(1)}$	0	0.04979(3)	0.5028(5)	0.333(9)
B2	8*h*	$Fe_{0.707(8)}Co_{0.293(8)}$	0	0.15288(2)	0.5042(5)	0.333(9)
B3	8*i*	$Fe_{0.53(2)}Co_{0.47(2)}$	0.0653(5)	1/4	0.5423(6)	0.333(9)
O1	8*g*	1	1/4	0.0392(1)	1/4	0.79(2)
O2	8*g*	1	1/4	0.9637(1)	1/4	0.79(2)
O3	8*g*	1	1/4	0.1527(1)	1/4	0.79(2)
O4	8*g*	1	1/4	0.6588(1)	1/4	0.79(2)
O5	8*i*	1	0.389(1)	1/4	0.632(2)	0.79(2)
O6	8*h*	1	0	0.0985(1)	0.504(2)	0.79(2)
O7	8*h*	1	0	0.2066(1)	0.4248(7)	0.79(2)

Table 5.5 Refined crystallographic parameters from combined data set of ND, SXRD. Space group - *I*2*mb*. Refined composition $Y_{1.61(16)}$ $Ba_{1.70(3)}Ca_{1.69(22)}Fe_{3.15(3)}Co_{1.85(3)}O_{13}$, including soft chemical composition restraint.

5.3.7 Comparison of refined structures

During the refinements, the structures remain mostly unchanged, with only a few minor differences observed between them. Figure 5.15 shows the refined structures of A) $x = 0$,[35] B) $x = 0.5$, C) $x = 1$, D) $x = 1.85$(I) and E) $x = 1.85$(II). As has already been noted in the sections 5.3.3, 5.3.4, 5.3.5 and 5.3.6, as the Co content is increased, the overall magnetic moments decrease, which relates to the spin states of Fe^{3+} (S = 5/2) and $Co^{3+/2+}$ (S = 2 and 3/2 respectively). Co also shows a slight preference for the T_d *B*3 site, although this does not lead to ordering of the *B*-site cations. For $YBa_2(Fe_{1-z}Co_z)_3O_{8+w}$, Co substituted onto the S_q and O_h sites equally, showing no preference.[266]

The *A*-site cation occupancies do not differ from the parent structure ($x = 0$) significantly, with the *A*2 site in particular remaining mostly Ba, which does not change significantly in

content between samples. *A*1 remains mostly occupied by Y and *A*3 by Ca. The main difference in occupancy of the *A*-sites arises from the difference in composition, which generally involves an increase in Y content and decrease in Ca content with greater amounts of Co doping. In the parent structure ($x = 0$),[35] the greatest mixing of *A*-sites occurs between Y and Ca *A*-site cations, with Ba found mostly on its own site (*A*2). This behaviour is also followed for all Co doped phases studied, with additional Y distributed between the Y site (*A*1) and Ca site (*A*3). The high level of mixing between Ca and Y occurs due to the small difference in ionic radius (Y^{3+} = 1.075 pm, Ca^{2+} = 1.18 pm),[234] while the large difference in ionic radius compared to Ba (Ba^{2+} = 1.47 pm)[234] explains why mixed occupancy with Ba is limited.

The lattice parameter trends of the phases discussed are difficult to compare as changes in Co content is accompanied by changes in the *A*-site ratios (higher Y content for higher Co content), which is required in order to obtain phase pure samples (see Table 5.6). The biggest difference observed in structure and lattice parameters is for x = 1.85(II), which has a stacking axis of 38.00684(8) Å, much smaller than observed for the other compositions, including x = 1.85(I), which has the same Co content, but lower Y content (38.10134(9) Å). The decrease in the stacking direction is attributed to the increase in the presence of the smallest *A*-site cation, Y.

Composition	**Lattice parameters (Å)**		
	a	***b***	***c***
$Y_{0.9}Ba_{1.7}Ca_{2.4}Fe_5O_{13-\delta}$	5.4968(2)	38.183(2)	5.5436(2)
$YBa_{1.8}Ca_{2.2}Fe_{4.5}Co_{0.5}O_{13-\delta}$	5.50323(2)	38.1956(2)	5.54730(2)
$Y_{1.15}Ba_{1.75}Ca_{2.1}Fe_4CoO_{13-\delta}$	5.49546(2)	38.1385(2)	5.53769(2)
$Y_{1.24}Ba_{1.85}Ca_{1.91}Fe_{3.15}Co_{1.85}O_{13-\delta}$	5.50292(1)	38.10134(9)	5.53609(1)
$Y_{1.6}Ba_{1.8}Ca_{1.6}Fe_{3.15}Co_{1.85}O_{13-\delta}$	5.51848(3)	38.00684(8)	5.52196(3)

Table 5.6 Showing lattice parameter changes with composition.

For x = 1.85(II), the *a* and *c* lattice parameters are almost the same, with *a* reduced and *c* increased in length compared to the other compositions (also see Figure 5.5). The change in *a* and *c* can be related to changes in positions of atoms in the T_d polyhedra (*B*3, O5 and O7).

There is also a change in space group from *Imma* with the disordered T_d chains, to *I*2*mb* with ordered T_d chains. Bond lengths from refinements of all materials can be seen in Table 5.7.

Bond	***n* x distance (Å)**			
	***x* = 0.5**	***x* = 1**	***x* = 1.85(I)**	***x* = 1.85(II)**
A1 – O1	4 × 2.462(1)	4 × 2.453(2)	4 × 2.454(3)	4 × 2.456(3)
A1 – O2	4 × 2.401(1)	4 × 2.398(2)	4 × 2.399(3)	4 × 2.397(3)
A2 – O1	2 × 3.016(2)	2 × 3.009(3)	2 × 3.004(4)	2 × 3.002(4)
A2 – O2	2 × 3.113(2)	2 × 3.101(3)	2 × 3.089(4)	2 × 3.094(4)
A2 – O3	2 × 2.768(2)	2 × 2.771(3)	2 × 2.781(4)	2 × 2.773(3)
A2 – O4	2 × 2.965(2)	2 × 2.962(3)	2 × 2.980(4)	2 × 2.987(3)
A2 – O6	2.751(4)	2.757(5)	2.768(7)	2.766(9)
A2 – O6	2 × 2.7530(1)	2 × 2.7487(2)	2 × 2.75919(2)	2 × 2.7616(3)
A2 – O6	2.797(4)	2.782(5)	2.769(7)	2.753(9)
A3 – O3	2 × 2.456(2)	2 × 2.454(3)	2 × 2.467(3)	2 × 2.487(3)
A3 – O4	2 × 2.459(2)	2 × 2.466(2)	2 × 2.453(3)	2 × 2.433(3)
A3 – O5	2 × 2.349(2)	2 × 2.355(3)	2 × 2.340(3)	2 × 2.350(5)
A3 – O7	2.333(3)	2.341(3)	2.366(3)	2.296(4)
A3 – O7	2 × 2.8153(5)	2 × 2.8048(6)	2 × 2.8116(9)	2 × 2.8180(9)
B1 – O1	2 × 1.996(1)	2 × 1.996(2)	2 × 2.002(2)	2 × 2.003(2)
B1 – O2	2 × 2.003(1)	2 × 2.003(2)	2 × 2.000(2)	2 × 2.004(2)
B1 – O6	1.876(2)	1.868(3)	1.859(4)	1.852(4)
B2 – O3	2 × 1.964(1)	2 × 1.963(2)	2 × 1.967(2)	2 × 1.969(2)
B2 – O4	2 × 1.953(1)	2 × 1.947(2)	2 × 1.946(2)	2 × 1.948(2)
B2 – O6	2.098(2)	2.086(3)	2.095(4)	2.066(4)
B2 – O7	2.122(2)	2.100(3)	2.117(4)	2.090(4)
B3 – O5	1.925(5)	1.883 (6)	1.896(8)	1.854(10)
B3 – O5	1.959(5)	1.981(6)	1.961(8)	2.046(11)
B3 – O7	2 × 1.815(2)	2 × 1.812(3)	2 × 1.783(4)	2 × 1.807(4)

Table 5.7 Refined *A*-site to O and *B*-site to O bond lengths for all Co doped $10a_p$ phases from combined refinement of ND and SXRD data.

When refining in the space group *Imma*, the two B3-O5 bond lengths in $x = 1.85$(II) are 1.587(9) Å and 2.371(9) Å, which appear unlikely for Fe-O or Co-O bond lengths. Changing

the space group to *I*2*mb* allowed the bond lengths to refine to chemically sensible positions, whist Fourier difference maps showed no indication that the site should be disordered. Therefore *I*2*mb* appears to model the structure of $x = 1.85$(II) well.

Bond valence sums (BVS) were determined for each of the *B*-sites, calculated for entirely Fe^{3+}, Co^{3+} and Co^{2+} separately. The results from the BVS are shown in Table 5.8. Although there is not a great difference in BVS between different samples, the BVS of $x = 1.85$(II) on site *B*3 is lower than those calculated for the other compositions. This suggests that more Co^{2+} may be occupying the T_d site of $x = 1.85$(II), which should contain more Co of this oxidation state compared to the other compositions. Co^{2+} is larger than both Co^{3+} and Fe^{3+}, which would explain the decrease in BVS.[234]

Site	**Bond Valence Sum**			
	***x* = 0.5**	***x* = 1**	***x* = 1.85(I)**	***x* = 1.85(II)**
Calculated For Fe^{3+} [268]				
B1	2.82	2.83	2.84	2.99
B2	3.11	3.17	3.13	3.17
B3	2.94	3.00	3.14	2.84
Calculated For Co^{3+} [269]				
B1	2.40	2.42	2.42	2.42
B2	2.65	2.70	2.67	2.71
B3	2.51	2.56	2.68	2.55
Calculated For Co^{2+} [268]				
B1	2.35	2.36	2.37	2.37
B2	2.59	2.64	2.61	2.65
B3	2.45	2.50	2.62	2.50

Table 5.8 Bond valence sums calculated for each *B*-site of all Co doped $10a_p$ compositions studied, considering values for Fe^{3+}, Co^{3+} and Co^{2+}.

The refined crystal structures of the Co doped $10a_p$ phases are shown together in Figure 5.15. There is little difference observed between the structures, especially for $x = 0.5$, 1 and 1.85(I), where the main difference is the progressive increase of Co on each of the *B*-sites and Y on sites *A*1 and *A*3. The refined bond angles can be seen in Table 5.9, which shows the only

significant change occurring between *B*3 and the oxygen atoms surrounding the site, O5 and O7.

Bond	Number	Bond angle (°)			
		***x* = 0.5**	***x* = 1**	***x* = 1.85(I)**	***x* = 1.85(II)**
O1-B1-O1	1	87.16(7)	87.0(1)	86.8(1)	87.1(1)
O1-B1-O2	2	87.91(2)	87.71(4)	87.59(5)	87.10(5)
O1-B1-O2	2	156.0(1)	154.7(2)	154.6(2)	154.0(2)
O1-B1-O6	2	101.4(1)	101.9(2)	101.3(2)	101.7(2)
O2-B1-O2	1	86.76(8)	86.63(1)	86.9(1)	87.1(1)
O2-B1-O6	2	103.0(1)	103.41(2)	104.1(2)	104.3(2)
O3-B2-O3	1	88.95(7)	88.85(9)	88.77(9)	89.1(1)
O3-B2-O4	1	90.68(7)	90.58(1)	90.51(2)	90.11(2)
O3-B2-O4	2	176.4(1)	176.4(2)	176.2(2)	174.6(2)
O3-B2-O6	2	88.8(1)	88.8(2)	88.1(2)	88.7(2)
O3-B2-O7	2	84.34(9)	84.5(1)	84.8(2)	82.7(2)
O4-B2-O4	1	89.59(8)	89.8(1)	90.0(1)	90.2(1)
O4-B2-O6	2	94.8(1)	94.8(2)	95.6(2)	96.6(2)
O4-B2-O7	2	92.07(9)	92.0(1)	91.4(2)	91.9(2)
O6-B2-O7	1	170.3(2)	170.5(2)	170.1(3)	167.9(3)
O5-B3-O5	1	108.3(2)	108.3(2)	108.6(2)	103.0(3)
O5-B3-O7	2	103.16(9)	103.4(1)	102.9(1)	102.7(2)
O5-B3-O7	2	107.4(1)	105.9(1)	106.6(2)	106.7(1)
O7-B3-O7	1	126.2(2)	128.8(2)	128.2(3)	131.5(3)
B1-O1-B1	1	158.5(1)	157.4(2)	157.3(3)	156.9(3)
B1-O2-B1	1	152.6(1)	152.1(2)	151.9(3)	151.1(3)
B2-O3-B2	1	176.43(6)	176.75(6)	176.36(9)	177.4(6)
B2-O4-B2	1	169.69(1)	167.7(2)	168.9(3)	166.8(3)
B3-O5-B3	1	122.5(2)	124.7(3)	124.3(4)	133.9(5)
B1-O6-B2	1	178.2(2)	178.7(3)	179.9(4)	179.7(5)
B2-O7-B3	1	143.2(1)	145.0(2)	144.9(2)	144.7(2)

Table 5.9 Refined bond angles for all Co doped $10a_p$ phases from combined refinement of ND and SXRD data.

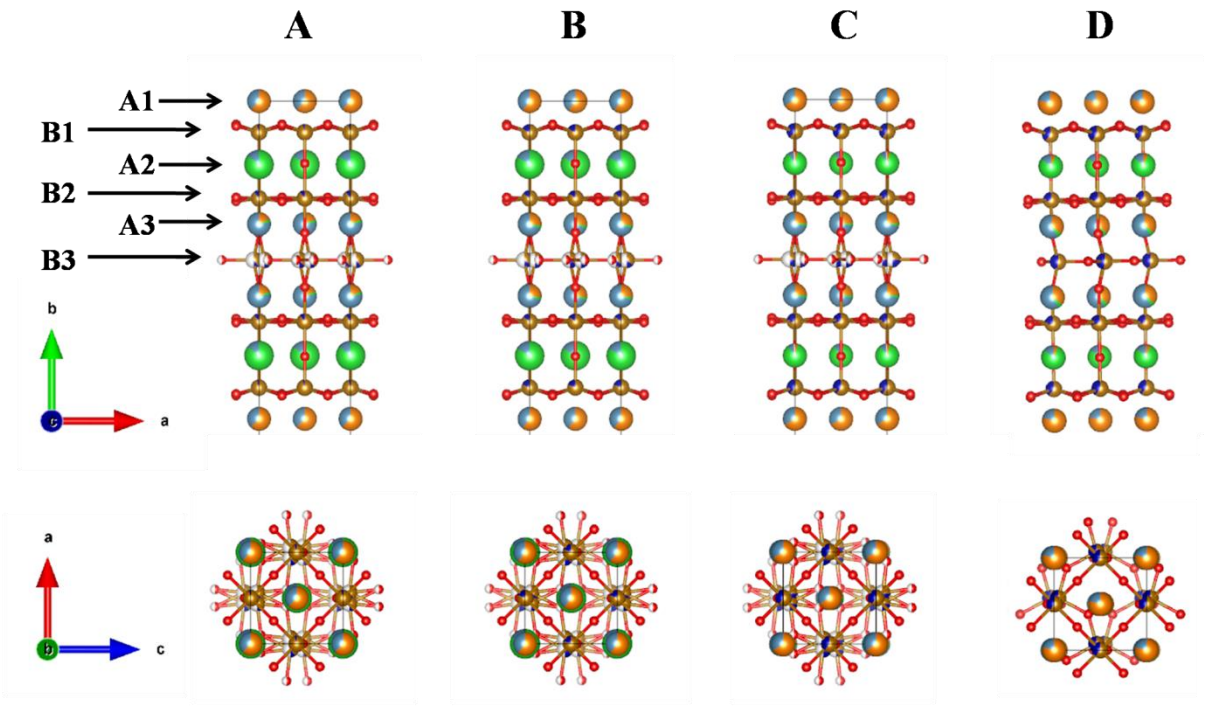

Figure 5.15 Refined crystal structures of A) x = 0.5, B) x = 1 and C) x = 1.85(I), all in *Imma*, and D) x = 1.85(II) in *I2mb*. Colours representing atoms are as follows: Fe (brown), Co (navy blue), Y (orange), Ba (green), Ca (blue) and O (red). Note, showing y = 1/2 (top) at body centring for zoomed in view of structure.

5.4 Physical Properties

5.4.1 Thermal stability and chemical compatibility

In order to assess the performance of the various Co doped $10a_p$ phases as SOFC cathodes, the thermal stability and chemical compatibility with commonly used electrolytes were determined, as for the $16a_p$ and YCSFO phases in the preceding two chapters. Tests were carried out for all samples, with the exception of x = 1.85(I), due to a lack of available sample.

Thermal stability tests were performed on the as-synthesised powders, annealing in air at 750 °C for five days (simulating IT-SOFC operating temperatures) and 950 °C for five hours (more extreme than cathode processing temperatures) and subsequent phase stability was characterised by laboratory PXRD. As can be seen in Figure 5.16, no new phase formation or decomposition was observed for x = 0.5, 1 or 1.85(II), although minor new reflections not

related to the $10a_p$ phase were observed for x = 1.85(II) after annealing at 950 °C. The new reflections were identified as Y_2O_3[201] (0.8 weight%) and $BaCaCo_2Fe_2O_7$[264] (2.8 weight%), nevertheless the major phase present remained the $10a_p$ (96.4 weight%) phase.

Chemical compatibility tests with state-of-the-art electrolytes were carried out as detailed in section 2.7.3 and characterization by PXRD, as shown in Figure 5.16. For these experiments, there was no detectible degradation of any of the phases, and no new reflections were observed within the PXRD patterns, suggesting new phase formation through reactivity with the electrolyte did not occur. It should be noted that although for x = 1.85(II) no new reflections were observed, it is likely that they are present, but had insufficient intensity to resolve under the conditions of the data collection.

The lattice parameters of the Co doped phases before and after the thermal stability and chemical compatibility tests are shown below in Table 5.10. Lattice parameters are generally stable to the fourth significant figure, though for x = 0.5 and 1, there are small decreases in the stacking direction, b. This is a good indication of phase stability of the Co doped $10a_p$ phases, both thermally, and in the presence of the electrolyte GDC. The minor changes to lattice parameters are a likely result of cation diffusion between phases.

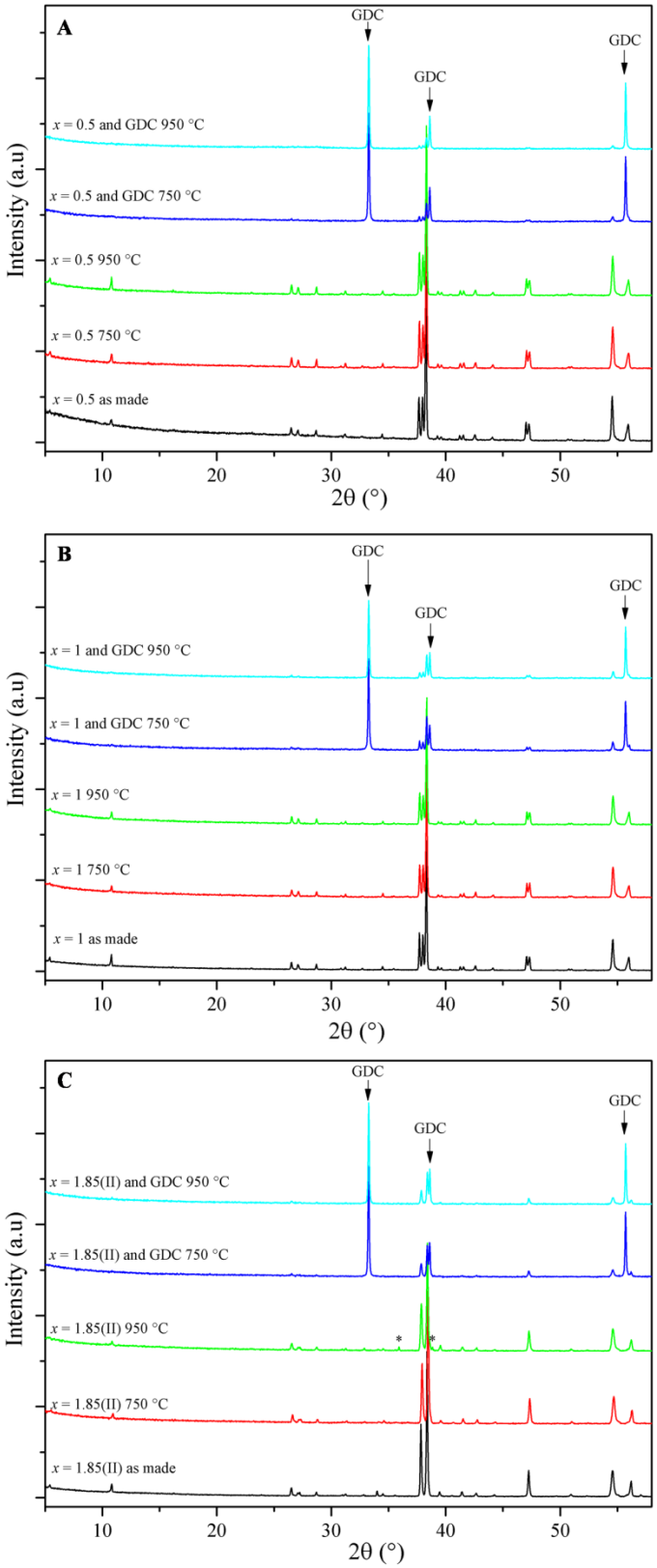

Figure 5.16 PXRD patterns showing the stability of the synthesised A) x = 0.5, B) x = 1 and C) x = 1.85(II) materials at 750 °C for 5 days and 950 °C for 5 hours. The patterns show the materials are compatible with electrolyte materials, GDC.

***x* = 0.5**	**Lattice Parameters (Å)**		
	a	***b***	***c***
As-made	5.5024(2)	38.184(1)	5.5471(2)
750 °C for 5 days	5.5020(3)	38.186(2)	5.5456(2)
950 °C for 5 hours	5.5009(3)	38.180(2)	5.5457(3)
With GDC 750 °C for 5 days	5.4998(5)	38.170(3)	5.5450(5)
with GDC 950 °C for 5 hours	5.4984(7)	38.170(5)	5.5435(7)
***x* = 1**	***a***	***b***	***c***
As-made	5.4971(1)	38.142(1)	5.5389(2)
750 °C for 5 days	5.4959(2)	38.137(2)	5.5371(2)
950 °C for 5 hours	5.4971(2)	38.140(1)	5.5384(2)
With GDC 750 °C for 5 days	5.4972(4)	38.135(2)	5.5383(4)
with GDC 950 °C for 5 hours	5.4965(4)	38.129(1)	5.5376(4)
***x* = 1.85(II)**	***a***	***b***	***c***
As-made	5.517(1)	38.002(1)	5.519(1)
750 °C for 5 days	5.5112(4)	37.993(1)	5.5195(4)
950 °C for 5 hours	5.5123(5)	37.996(2)	5.5200(5)
With GDC 750 °C for 5 days	5.5161(9)	38.003(2)	5.5210(9)
with GDC 950 °C for 5 hours	5.5166(9)	38.007(2)	5.5221(9)

Table 5.10 Lattice parameters of Co doped $10a_p$ phases before and after thermal stability and chemical compatibility tests.

5.4.2 Electrochemical performance

The cathode performance of the Co doped $10a_p$ phases were investigated by measuring the AC impedance of symmetrical cells fabricated on GDC electrolyte substrates, which the materials are chemically compatible with according to the experiments discussed in section 5.4.1. Cathode inks were prepared and symmetrical cells were fabricated as detailed in section 2.10.2.

AC impedance measurements were recorded over the temperature range of 600 °C to 750 °C in static air. The symmetrical cell was held for 90 minutes at each temperature to allow thermal equilibration and measurements were made using ZPlot v.2.9b (Scribner Associates)

every 50 °C. The ASR of the cathodes were calculated by fitting the data using ZView2.[189] The data were fit with an equivalent circuit consisting of an Inductor (I) and two Resistors (R) in series with associated Constant Phase Elements (CPE) in parallel with each resistor. The ASRs were then calculated by normalizing the measured resistance for the electrodes area and dividing by two to take into account the symmetry of the cells.

Figure 5.17 displays Z'-Z" plots of the data obtained for the all of the Co doped 10a_p cathodes on GDC electrolyte substrates. The calculated ASRs versus temperature can be seen for all synthesised Co doped 10a_p phases, along with the published data for x = 0(I),[35] (II)[162] measured on SDC electrolytes for comparison, in Figure 5.18. The data values are also shown in Table 5.11. The difference observed for the two parent material measurements occurred due to changes to cathode processing through altering the milling conditions and lowering the adherence temperature, leading to an improved microstructure.[162] The Co doped samples under investigation here were all subject to the same milling and heating protocols.

As can be seen from the plot in Figure 5.18, as Co content is increased, the ASR for the 10a_p samples is reduced. This same trend is also observed for perovskite cathodes $Sm_{0.5}Sr_{0.5}Co_{1-x}Fe_xO_{3-\delta}$[270] and $Ba_{0.5}Sr_{0.5}Co_{1-y}Fe_yO_{3-\delta}$,[271] in line with the general perception that increased Co improves electrochemical performance. With the target ASR of 0.15 $\Omega.cm^2$,[221] x = 1.85(I) and x = 1.85(II) come close to this objective at 700 °C, with obtained values of 0.23 $\Omega.cm^2$ and 0.19 $\Omega.cm^2$ respectively. This would be well within the IT-SOFC operating range of 500 - 800 °C.[221]

For direct comparison with x = 0(I),[35] (II),[162] x = 1.85(II) was also measured using an SDC electrolyte substrate. The same ASR values were displayed as for the measurement using GDC, showing that the electrolyte did not overly influence the ASR obtained in this case.

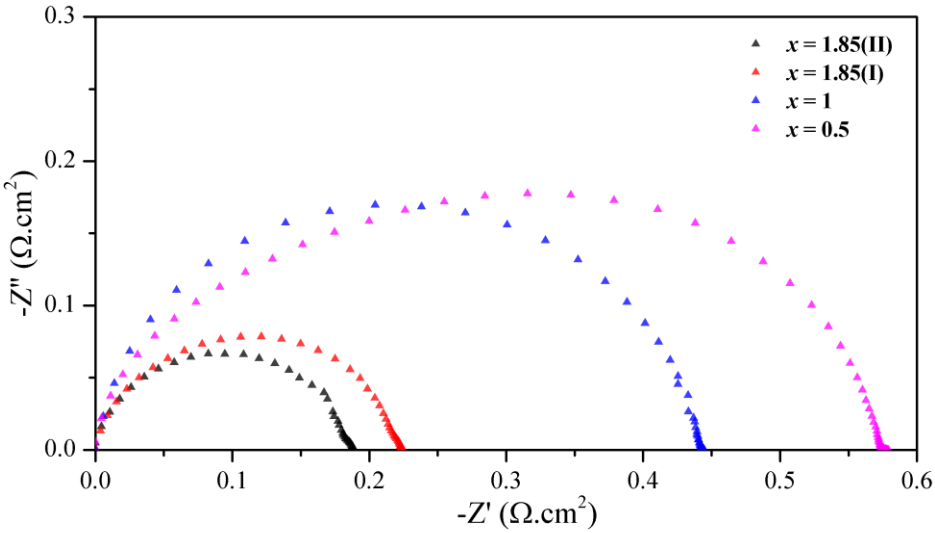

Figure 5.17 Z'-Z'' plot showing cathode performance x = 0.5, 1, 1.85(I) and 1.85(I) in a symmetrical cell on a GDC electrolyte at 700 °C.

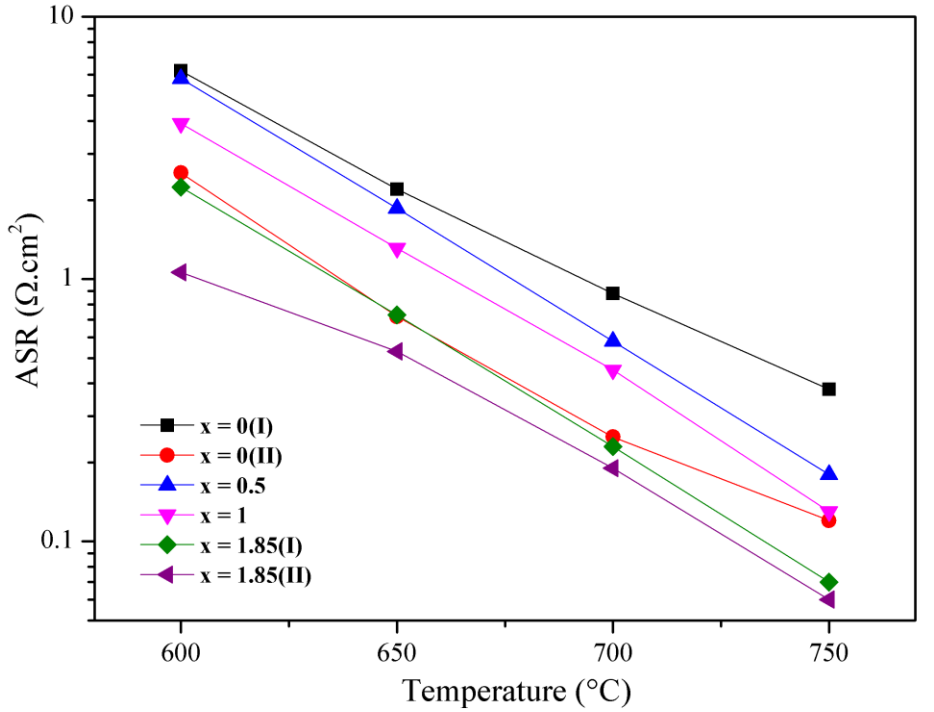

Figure 5.18 Plot showing comparison of ASR versus temperature for x = 0(I) (black), x = 0(II) (red), x = 0.5 (blue), x = 1 (magenta), x = 1.85(I) (green) and x = 1.85(II) (purple).

Temperature (°C)	ASR (Ω.cm^2)					
	x = 0(I)[35]	x = 0(II)[162]	x = 0.5	x = 1	x = 1.85(I)	x = 1.85(II)
750	0.38	0.12	0.18	0.13	0.07	0.06
700	0.88	0.25	0.58	0.45	0.23	0.19
650	2.20	0.72	1.86	1.31	0.73	0.53
600	6.21	2.54	5.81	3.92	2.24	1.06

Table 5.11 Comparison of ASR versus temperature data for all doped 10a_p phases, along with data for the parent phase taken from the original publication[35] and from a second publication[162] after improvements to cell processing.

5.5 Other Dopants

5.5.1 Dopants explored

Below is a short sub-chapter discussing other doping strategies attempted for the 10a_p phase, together with some preliminary electrochemical measurements carried out on a number of successfully doped samples.

As discussed in the 16a_p chapter, section 3.1, the electronic conductivity of the 10a_p phase is inferior when compared to many of the current cathode materials, around 10^{-2} S.cm^{-1} lower than LSCF at IT-SOFC operating conditions.[218] Through appropriate doping, it was hoped that the electronic conductivity would be increased, leading to an improved cathode performance.

Two approaches were considered, the first was doping of the *A*-site, partially substituting Y^{3+} with a more electropositive lanthanide such as La or Pr. This approach has been reported for RBaCo$_2$O$_{5+\delta}$, where R is a lanthanide.[272] The more electropositive the element, the larger the δ value, hence the increased oxygen content would need to be charge balanced, with the transition metal accommodating this requirement, creating charge carriers ($Co^{2+} \rightarrow Co^{3+}$) in the process and enabling a mechanism for an increase in electronic conductivity. For the 10a_p, the expected charge carrier created would be Fe^{4+}.

The second approach considered was the doping of the *B*-site, partially replacing Fe^{3+} with other transition metals of a potentially different oxidation state, which would either become charge carriers directly, or force a change in oxidation state of some Fe^{3+} to Fe^{4+}, thus creating charge carriers for increased conductivity. This has been demonstrated for $LaFe_{1-x}M_xO_3$ (*M* = Mn, Ni or Cu), where doping resulted in an increase in conductivity in all cases.[273]

All syntheses were carried out as described in the $16a_p$ chapter section 3.2.1, in Al_2O_3 crucibles (except Cu doping, where Pt crucibles were used). All successful doping attempts are summarised below in Table 5.12, with the composition required and lattice parameter changes on incorporation of dopant displayed.

Composition	**Lattice parameters (Å)**		
	a	***b***	***c***
$Y_{0.9}Ba_{1.7}Ca_{2.4}Fe_5O_{13\pm\delta}$	5.4968(2)	38.183(2)	5.5436(2)
First approach: Doping by lanthanides in *A*-site			
$La_{0.25}Y_{0.65}Ba_{1.6}Ca_{2.5}Fe_5O_{13\pm\delta}$	5.4945(2)	38.234(1)	5.5428(1)
$La_{0.25}Y_{0.75}Ba_{1.6}Ca_{2.4}Fe_5O_{13\pm\delta}$	5.4972(1)	38.2531(6)	5.5471(1)
$Pr_{0.25}Y_{0.65}Ba_{1.6}Ca_{2.5}Fe_5O_{13\pm\delta}$	5.50004(2)	38.2909(1)	5.54866(2)
Second approach: Doping of *B*-site			
$Y_{1.12}Ba_{1.55}Ca_{2.33}Fe_{4.65}Cu_{0.35}O_{13\pm\delta}$	5.49110(4)	38.2696(3)	5.54141(4)
$Y_{0.9}Ba_{1.7}Ca_{2.4}Fe_{4.75}Zn_{0.25}O_{13\pm\delta}$	5.49418(6)	38.1839(4)	5.54342(6)
$Y_{0.9}Ba_{1.7}Ca_{2.4}Fe_{4.75}Mn_{0.25}O_{13\pm\delta}$	5.49765(4)	38.1039(2)	5.54557(3)
$Y_{0.9}Ba_{1.7}Ca_{2.4}Fe_{4.5}Mn_{0.5}O_{13\pm\delta}$	5.49471(9)	38.1013(7)	5.54199(9)
$Y_{0.9}Ba_{1.7}Ca_{2.4}Fe_{4.25}Mn_{0.75}O_{13\pm\delta}$	5.49111(6)	38.1026(5)	5.53735(6)

Table 5.12 All successfully doped $10a_p$ compositions listed with refined lattice parameters.

For the lanthanide doping, the smaller Y^{3+} (1.019 pm) is replaced with the larger La^{3+} and Pr^{3+} (1.16 and 1.126 pm respectively)[234] cation, leading to an increase in lattice parameters in the stacking direction. The impurity phase observed in this synthesis was $BaFe_2O_4$,[274] which lead to the reduction in Ba content in order to obtain a phase pure sample ($Ba_{1.7} \rightarrow Ba_{1.6}$). This suggests that the lanthanide may have partially occupied the *B*2 Ba site rather than the *B*1 Y site due to the size difference, meaning reduced Ba content was required.

Isolation of the Cu doped sample displayed in Table 5.12 was carried out during the isolation of the 16a_p phase reported on in chapter 3. The *A*-site cation ratios were significantly changed in order to obtain a phase pure sample, with Y^{3+} increased to balance the reduced average *B*-site oxidation state due to Cu^{2+} replacing Fe^{3+}. In this case, Ba^{2+} is mostly substituted for Y^{3+}, rather than Ca^{2+} in the case of Co doping.

Doping with Zn resulted in no real change in the lattice parameters. It may be possible that due to the synthesis being carried out in a Al_2O_3 crucible, no Zn was incorporated and instead it was removed into the crucible. Increases in Mn doping leads to the linear reduction in the unit cell volume, as displayed in Figure 5.19. This is a good indication of incorporation.

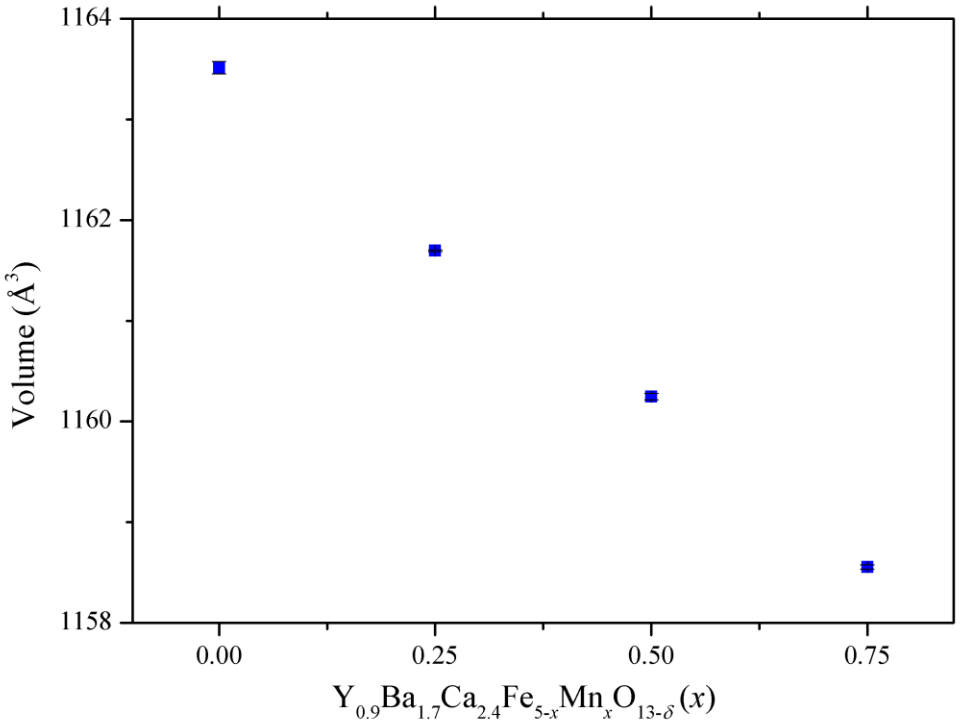

Figure 5.19 Shows the linear volume decrease of the 10a_p with increased Mn substitution (error bars within points).

All doping attempts using Ni and Mg were unsuccessful up to the point of writing this thesis.

5.5.2 Property characterisation

With the isolation of a number of doped 10a_p samples, four-probe DC conductivity was measured to determine whether the electronic conductivity had been improved. The plots in Figure 5.20, show the conductivity versus temperature of the parent 10a_p,[35] together with $La_{0.25}Y_{0.65}Ba_{1.6}Ca_{2.5}Fe_5O_{13\pm\delta}$, $La_{0.25}Y_{0.75}Ba_{1.6}Ca_{2.4}Fe_5O_{13\pm\delta}$, $Y_{0.9}Ba_{1.7}Ca_{2.4}Fe_{4.5}Mn_{0.5}O_{13\pm\delta}$ and $Y_{0.9}Ba_{1.7}Ca_{2.4}Fe_{4.25}Mn_{0.75}O_{13\pm}$. The data shows that while Mn doping did not improve the conductivity, La doping increased the conductivity by approximately 3 times. Despite this, the conductivity is still within the same magnitude as the parent material in the temperature range investigated.

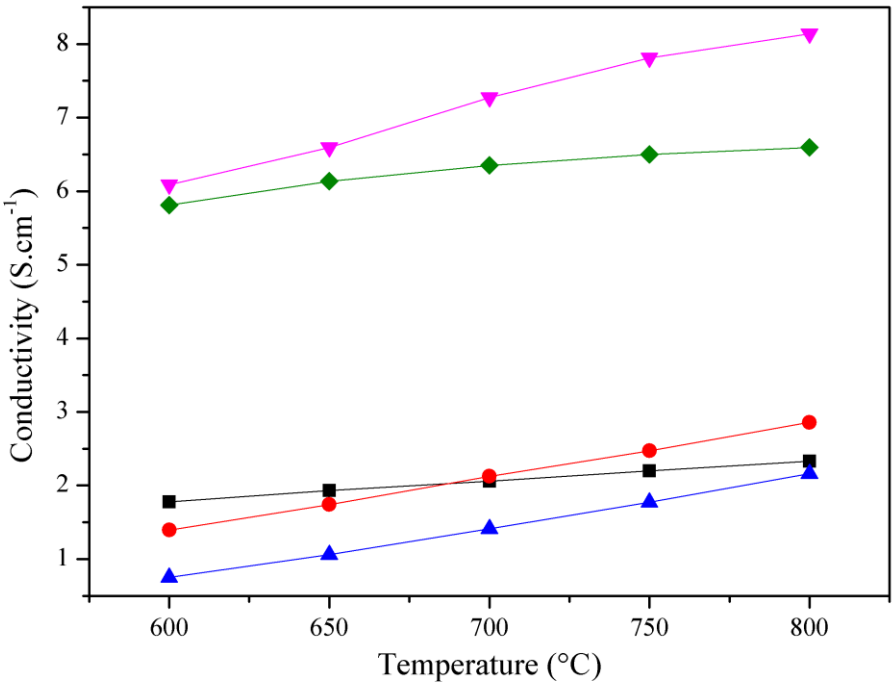

Figure 5.20 Plot of conductivity measured by the four-probe DC method, versus temperature. Compositions displayed include: $Y_{0.9}Ba_{1.7}Ca_{2.4}Fe_5O_{13\pm\delta}$ (black),[35] $La_{0.25}Y_{0.65}Ba_{1.6}Ca_{2.5}Fe_5O_{13\pm\delta}$ (magenta), $La_{0.25}Y_{0.75}Ba_{1.6}Ca_{2.4}Fe_5O_{13\pm\delta}$ (green), $Y_{0.9}Ba_{1.7}Ca_{2.4}Fe_{4.5}Mn_{0.5}O_{13\pm\delta}$ (red) and $Y_{0.9}Ba_{1.7}Ca_{2.4}Fe_{4.25}Mn_{0.75}O_{13\pm\delta}$ (blue).

Symmetrical cell measurements via AC impedance spectroscopy were also carried out for a number of the successfully doped 10a_p phases in order to determine whether doping

improved the overall cathode performance. The ASRs versus temperature for the parent 10a_p,[162] Cu doped, Pr doped and two La doped samples listed in Table 5.12 are displayed in Figure 5.21. The plot shows that the ASR is not decreased for any of the doped samples, with the parent 10a_p phase showing marginally better performance.[162] This may signify (particularly for La doped samples) that either the increase in conductivity was not the limiting factor in the 10a_p performance, or that a substantially improved electronic conductivity is required in order for improvements in overall electrochemical performance to be observed.

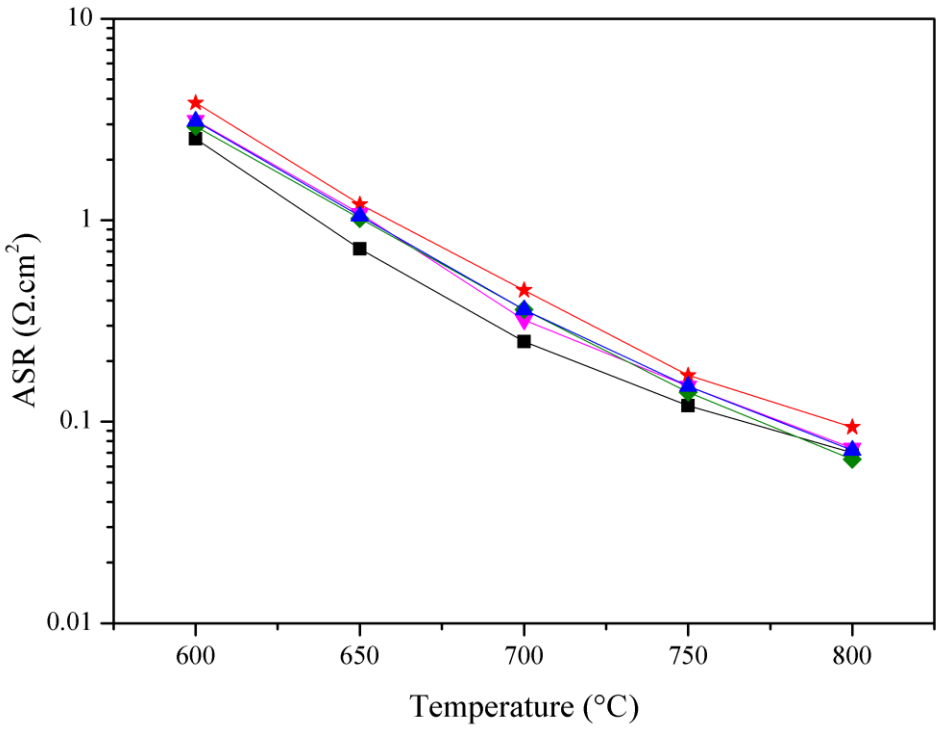

Figure 5.21 ASR versus temperature of $Y_{0.9}Ba_{1.7}Ca_{2.4}Fe_5O_{13\pm\delta}$ (black),[162] $La_{0.25}Y_{0.65}Ba_{1.6}Ca_{2.5}Fe_5O_{13\pm\delta}$ (magenta), $La_{0.25}Y_{0.75}Ba_{1.6}Ca_{2.4}Fe_5O_{13\pm\delta}$ (green), $Pr_{0.25}Y_{0.65}Ba_{1.6}Ca_{2.5}Fe_5O_{13\pm\delta}$ (blue) and $Y_{1.12}Ba_{1.55}Ca_{2.33}Fe_{4.65}Cu_{0.35}O_{13\pm\delta}$ (red).

5.6 Discussion

In this chapter, doping of the 10a_p phase $Y_{0.9}Ba_{1.7}Ca_{2.4}Fe_5O_{13}$, has been explored as an attempt to improve its performance as a cathode operating in the intermediate temperature

range of 500 - 800 °C. As Co is known to show superior catalytic activity,[261] as well as being heavily present in many of the best performing IT-SOFC cathode materials,[63, 127, 185] the partial substitution of Co for Fe was investigated. This work was started with the synthesis of a sample with 50 % Co for Fe substitution in the $10a_p$ phase $Y_{0.9}Ba_{1.7}Ca_{2.4}Fe_{2.5}Co_{2.5}O_{13}$, which produced a multiphasic sample. TEM EDX was carried out on this sample, which resulted in the composition $Y_{1.23(6)}Ba_{1.60(7)}Ca_{2.17(5)}Fe_{3.10(4)}Co_{1.90(4)}O_z$ being determined based on four particles. From this point, synthesis was continued, with the highest Co content aimed for based on the EDX analysis.

After the synthesis of numerous samples, the composition $Y_{1.24}Ba_{1.85}Ca_{1.91}Fe_{3.15}Co_{1.85}O_{13-\delta}$ produced a sample that contained a majority $10a_p$ phase. Titration of a sample with similar composition and comparable impurities resulted in a composition that was deficient in oxygen, $Y_{1.18}Ba_{1.89}Ca_{1.93}Fe_{3.17}Co_{1.83}O_{12.54(5)}$. It has been reported for the $3a_p$ phase $YBa_2(Fe_{1-z}Co_z)_3O_{8+w}$ that annealing in O_2 enabled the increased incorporation of Co, up to $z = 0.47$.[266] Using the same approach, $Y_{1.24}Ba_{1.85}Ca_{1.91}Fe_{3.15}Co_{1.85}O_{13-\delta}$ was annealed in O_2 at its synthesis temperature, resulting in a phase pure sample. It appears that the O_2 atmosphere oxidised Co^{2+} present, enabling the formation of the $10a_p$ with the same oxygen ordering. This was also reported for $YBa_2(Fe_{1-z}Co_z)_3O_{8+w}$, which did not contain any additional oxygen after annealing.[266]

It was observed that when increasing the Co content of the $10a_p$ phase, greater Y^{3+} content (for Ca^{2+}) was also required to form a single phase. For the highest Co content synthesised, greatly increased Y content was used as an approach to achieve pure samples in air. While varying the Y content, it became apparent that the $10a_p$ phase was now forming as a solid solution versus Y content, as shown by lattice parameter evolution in Figure 5.5. This was an unusual behaviour for the $10a_p$ phase, as for the parent Fe only phase, a single phase was only achieved using one specific *A*-site composition ($Y_{0.9}Ba_{1.7}Ca_{2.4}$) Y content.[35]

Accompanying the increase in Y content was a change in lattice parameters, with *a* and *c* moving closer together, becoming almost tetragonal. A Rietveld refinement was carried out on $x = 1.85$(II) ($Y_{1.6}Ba_{1.8}Ca_{1.6}Fe_{3.15}Co_{1.85}O_{13-\delta}$) using combined SXRD and ND data to determine the crystal structure. As the lattice parameters of $x = 1.85$(II) move close to tetragonal, the tilts of the polyhedra were scrutinized as tilts in perovskites often effect symmetry, as discussed in Chapter 1, section 1.6.2. However, there is no significant change

observed in the tilts, which can be seen in the bond angles between B1-O6-B2 and B2-O7-B3 staying the same as for the other compositions. Non-physical bond lengths of 1.587(9) Å and 2.371(9) Å were obtained from a refinement in *Imma*, which led to a change in space group to *I*2*mb*, which has the same reflection conditions and fitted the observed data well, whilst giving chemically sensible bond lengths. Fourier difference maps showed no significant mismatch, indicating the structure was being modelled well.

Rietveld refinements using ND data did not find any excess oxygen, or sites deficient in oxygen for any composition, which suggests some of the Co present in the four compositions must be in its 2+ oxidation state, particularly $x = 1.85$(II), which has a large Y content. BVS of each of the *B*-sites for all of the Co doped $10a_p$ compositions were calculated, considering the sites entirely Fe^{3+}, Co^{3+} and Co^{2+} separately. The results seen in Table 5.8 show that a lower BVS is obtained for the T_d *B*3 site of $x = 1.85$(II) compared to the other composition. This may be due to increased amounts of Co^{2+} present on this site for $x = 1.85$(II), which is likely to contain more Co^{2+} than the other compositions.[234]

One of the major advantages that the parent $10a_p$ phase held over many of the current cathode materials was its stability versus temperature, as well as its chemical compatibility with state-of-the-art electrolyte materials.[35] The Co doped $10a_p$ samples discussed in this chapter appear to share this stability, with the exception of $x = 1.85$(II), which decomposed very slightly under thermal treatment, forming $BaCaCo_2Fe_2O_7$ and Y_2O_3 impurities to < 5 weight%. For application as a cathode however, this may not be a problem as long as the impurity is not detrimental to performance, though further investigation is required. All the other compositions proved both thermally stable and chemically compatible with the electrolyte GDC, with only very minor changes in lattice parameters detected, likely due to cation diffusion.

The $10a_p$ phases with increased Co content demonstrated improved cathode performance, through a reduced ASR. The highest Co content samples $x = 1.85$(I) and $x = 1.85$(II), demonstrated that an ASR below the target value of 0.15 $\Omega.cm^2$ was achievable between 700 - 750 °C, well within the intermediate operating temperature range. This compares favourably to other cathodes with similar Co/Fe ratios, such as $Sm_{0.5}Sr_{0.5}Co_{0.4}Fe_{0.6}O_{3-\delta}$ (0.37 $\Omega.cm^2$),[270] $La_{0.8}Sr_{0.2}Co_{0.5}Fe_{0.5}O_{3-\delta}$ (0.22 $\Omega.cm^2$),[275] $Ba_{0.5}Sr_{0.5}Co_{0.4}Fe_{0.6}O_{3-\delta}$ on LSGM

electrolyte with Pt current collectors (0.21 Ω.cm^2)[276] and on SDC electrolyte with Ag current collectors (0.02 Ω.cm^2),[277] all at 750 °C.

5.7 Conclusion

In summary, successful Co doping of the 10a_p phase was achieved, replacing up to 37 % of Fe on the *B*-site Co. To do this, adjustments to the *A*-site cation ratios were required in order to achieve phase pure samples. At the highest Co content, the Y^{3+} to Ba^{2+}/Ca^{2+} ratios showed a solid solution behaviour, with increasing Y content leading to a progressively more tetragonal geometry. Combined ND and SXRD Rietveld refinements were carried out on four compositions, which showed only minor changes to the structure. Co showed a slight preference for the T_d *B*-site, however the difference in Co occupation of the three *B*-site was not marked.

The Co doped 10a_p phases showed good thermal stability, although x = 1.85(II) did undergo some minor decomposition to Y_2O_3 and $BaCaCo_2Fe_2O_7$. No reactivity was observed between the Co doped samples and electrolyte GDC, though some small deviations in the lattice parameters were observed.

Further work on this project could include a more comprehensive study of the structure of x = 1.85(II). TEM SAED would be useful to determine if the symmetry of the doped phase had changed from the parent structure, possibly identifying a more appropriate space group to use. Rietveld refinements of a range of Y contents at $Fe_{3.15}Co_{1.85}$ may also provide a better understanding of how the structure is changing, possibly highlighting a trend. A range of compositions would be required to be isolated first however, as currently there are none available.

It would also be interesting to see if a 10a_p phase can be made with an increased Co content, possibly full substitution. In this study, the Co limit was determined from a sample containing the parent phases *A*-site cation ratio ($Y_{0.9}Ca_{2.4}Ba_{1.7}$). It may be possible to further increase the Co content through using greater amounts of Y (or a higher valent *A*-site cation), annealing in an O_2 atmosphere, or via partial substitution of a higher oxidation state cation such as Mn, which has previously been successfully doped into the Fe pure 10a_p phase.

A more comprehensive study of the physical properties, particularly at high Co content should be carried out. It is important to discover how any phase instabilities will affect the performance of these doped phases. Although compatibility and stability tests have been carried out, it would be useful to know if performance as a cathode deteriorates during operation. Additionally, further investigation into the processing conditions used for fabricating the symmetrical cells may lead to further improvements to ASR, with the target operating temperature of 700 °C within sight.

6 Summary

The work presented in this thesis focused on the synthesis of long axis *A*-site ordered perovskites, which have been crystallographically characterised by combined powder SXRD and ND respectively. These perovskites, which have ordered oxygen vacancies as a result of the *A*-site ordering, have also been assessed as potential cathodes for solid oxide fuel cells, targeting an intermediate temperature solid oxide (IT-SOFC) operating range of 500 - 800 °C.

The first phase reported on in chapter 3 of this thesis was a $16a_p$ (a_p = 1 perovskite unit) structure that contains the *A*-site cations Y, Ba and Ca, along with *B*-site cations Fe and Cu ($Y_{2.24}Ba_{2.28}Ca_{3.48}Fe_{7.44}Cu_{0.56}O_{21-\delta}$). This phase was discovered whilst attempting to dope a $10a_p$ ($Y_{0.9}Ba_{1.7}Ca_{2.4}Fe_{5-x}Cu_xO_{13-\delta}$) phase with 10 % Cu on the *B*-site in order to improve its electronic conductivity. However, low angle reflections were observed in powder X-ray diffraction (PXRD) patterns collected for this sample, which later led to the indexation of the phase as $a_p \sqrt{2} \times 16a_p \times a_p \sqrt{2}$ by selective area electron diffraction (SAED). The starting model for a Rietveld refinement was identified using a computational method known as the Extended Module Materials Assembly (EMMA), whilst a Rietveld refinement was carried out using combined SXRD and ND data. Mössbauer spectroscopy identified that Fe^{3+} existed in three different coordination environments, whilst an iodometric titration confirmed the oxygen content and therefore the average *B*-site oxidation state. High Angle Annular Scanning Transmission Electron Diffraction (HAADF-STEM) confirmed the *A*-site ordering from the refinement.

The $16a_p$ phase showed good thermal stability and chemical compatibility with state-of-the-art electrolytes (GDC, SDC and LSGM) at operating temperature and symmetrical cell fabrication temperatures, as well as a close matching thermal expansion coefficient (TEC) with the same electrolytes. The phase also showed excellent stability in an atmosphere of 100 % CO_2. Electronic conductivity is ~ 10^{-2} times lower compared to current cathode materials, but despite this the target area specific resistance (ASR) was achieved at 800 °C, within the IT-SOFC operating range.

The second phase discussed in chapter 4 was initially identified while trying to form a $7a_p$ phase. The phase identified was in fact a $10a_p$ phase, and was isolated phase pure with the composition $Y_{0.9}Ca_{2.4}Sr_{1.7}Fe_5O_{13-\delta}$ (YCSFO). SXRD was used to confirm the correct indexing of the phase, as well as being used to identify the starting structure. In combination with ND, the SXRD data was used to identify a suitable space group, *Imma*. A full combined Rietveld refinement was carried out, with the addition of SXRD data collected at the K absorption edge for Sr, so that Sr and Y could be distinguished and therefore located within the structure.

YCSFO showed excellent thermal stability, CO_2 stability and chemical compatibility with state-of-the-art electrolytes, showing no discernable lattice parameters changes under the test conditions. Electronic conductivity was low, of the same magnitude as the $16a_p$, but ASR was 3 times higher, though this can be related to the lack of oxygen vacancy channels that are present in the $16a_p$.

The final phases investigated in chapter 5 of this thesis were that of a Co doped $10a_p$ ($Y_{0.9}Ba_{1.7}Ca_{2.4}Fe_{5-x}Co_xO_{13-\delta}$), although preliminary results from other dopants (La, Pr, Cu, Mn, Zn) were also briefly discussed. Co was successfully doped for x = 0.5, 1 and two different 1.85 compositions (different *A*-site ratios). As a general trend, with increased amounts of Co in the $10a_p$, increased Y was required to obtain a phase pure sample. The limit of Co doping was determined to be x = 1.85 based on transmission electron microscopy electron dispersive X-rays (TEM EDX) analysis of a sample with composition $Y_{0.9}Ba_{1.7}Ca_{2.4}Fe_{2.5}Co_{2.5}O_{13-\delta}$. At x = 1.85, the first sample was isolated phase pure with an *A*-site ratio of $Y_{1.24}Ba_{1.85}Ca_{1.91}$ by annealing in a pure O_2 atmosphere (x = 1.85(I)). The second, with an *A*-site ratio of $Y_{1.6}Ba_{1.8}Ca_{1.6}$ (x = 1.85(II) was isolated through increased Y content, though it became apparent that at the same Co content, a solid solution between Y and Ca/Ba occurs, with higher Y content moving the unit cell from orthorhombic to close to tetragonal. The four doped phases were structurally characterised by combined SXRD and ND Rietveld refinements, with *A*-site order and Co occupancy determined. No additional oxygen, or oxygen vacancies were determined from the refinements for any of the Co doped $10a_p$ phases, with all samples retaining the same oxygen ordering.

Thermal stability and chemical compatibility tests showed the doped phases displayed good stability, especially at operating temperatures of 750 °C for 5 days, which showed no decomposition or reactivity for any of the samples. However for x = 1.85(II), slight

decomposition was observed when annealed at 950 °C for 5 hours. AC impedance measurements carried out on the samples showed that increased Co content reduced the ASR, with the values below the target value, 0.15 $\Omega.cm^2$, observed for both $x = 1.85$ samples at 750 °C, whilst only being slightly higher at 700 °C.

To conclude, the *A*-site ordered perovskites studied in this thesis have displayed potential to be utilised as cathodes for IT-SOFCs due to their good cathode performance, along with great stability at operating and fabrication temperatures. Further modifications to the cathode materials discussed could be pursued in order to improve performance, such as through optimising doping of the phases or through modification of the cathode microstructure through processing conditions. The discovery of new ordered perovskites is also a possibly, conceivably using transition metals other than Fe, which may lead to interesting new structures.

1. I. Dincer, *Renewable and Sustainable Energy Reviews*, 2000, **4**, 157-175.
2. J. Dunderdale, *Energy and the environment: the proceedings of a symposium organized jointly by the Inorganic Chemicals Group and the Environment Group of the Industrial Division of the Royal Society of Chemistry: University of Leeds, 3rd-5th April 1990*, CRC Pr I Llc, 1990.
3. M. S. Dresselhaus and I. L. Thomas, *Nature*, 2001, **414**, 332-337.
4. M. Z. Jacobson, *Journal of Geophysical Research: Atmospheres*, 2002, **107**, 4410.
5. M. Hoel and S. Kverndokk, *Resource and Energy Economics*, 1996, **18**, 115-136.
6. F. S. Sterrett, *Alternative fuels and the environment*, CRC Press, 1994.
7. Varun, I. K. Bhat and R. Prakash, *Renewable and Sustainable Energy Reviews*, 2009, **13**, 1067-1073.
8. M. H. Nehrir, C. Wang, K. Strunz, H. Aki, R. Ramakumar, J. Bing, Z. Miao and Z. Salameh, *Sustainable Energy, IEEE Transactions on*, 2011, **2**, 392-403.
9. A. Chauhan and R. P. Saini, Energy Efficient Technologies for Sustainability (ICEETS), 2013 International Conference on, 2013.
10. R. Baños, F. Manzano-Agugliaro, F. G. Montoya, C. Gil, A. Alcayde and J. Gómez, *Renewable and Sustainable Energy Reviews*, 2011, **15**, 1753-1766.
11. B. C. H. Steele and A. Heinzel, *Nature*, 2001, **414**, 345-352.
12. D. J. L. Brett, A. Atkinson, N. P. Brandon and S. J. Skinner, *Chemical Society Reviews*, 2008, **37**, 1568-1578.
13. C. F. Schœnbein, *Philosophical Magazine Series 3*, 1839, **14**, 43-45.
14. W. R. Grove, *Philosophical Magazine Series 3*, 1839, **14**, 127-130.
15. L. Mond and C. Langer, *Proceedings of the Royal Society of London*, 1889, **46**, 296-304.
16. N. P. Brandon, S. Skinner and B. C. H. Steele, *Annual Review of Materials Research*, 2003, **33**, 183-213.
17. J. Weissbart and R. Ruka, *Journal of The Electrochemical Society*, 1962, **109**, 723-726.
18. A. B. Stambouli and E. Traversa, *Renewable and Sustainable Energy Reviews*, 2002, **6**, 433-455.
19. N. Q. Minh, *J Am Ceram Soc*, 1993, **76**, 563-588.
20. S. Gottesfeld and J. Pafford, *Journal of The Electrochemical Society*, 1988, **135**, 2651-2652.
21. S. W. Tao and J. T. S. Irvine, *Nat Mater*, 2003, **2**, 320-323.
22. K. Huang and J. B. Goodenough, *Solid oxide fuel cell technology: principles, performance and operations*, Elsevier, 2009.
23. N. Q. Minh and T. Takahashi, *Science and technology of ceramic fuel cells*, Elsevier, 1995.
24. J. Larminie, A. Dicks and M. S. McDonald, *Fuel cell systems explained*, Wiley New York, 2003.
25. S. P. Jiang and S. H. Chan, *Journal of Materials Science*, 2004, **39**, 4405-4439.
26. B. C. H. Steele, K. M. Hori and S. Uchino, *Solid State Ionics*, 2000, **135**, 445-450.
27. S. J. Skinner and A. Lashtabeg, *Journal of Materials Chemistry*, 2006, **16**, 3161-3170.
28. E. Siebert, A. Hammouche and M. Kleitz, *Electrochimica Acta*, 1995, **40**, 1741-1753.
29. B. C. Steele, *Solid State Ionics*, 1996, **86**, 1223-1234.
30. J. Van Herle, A. McEvoy and K. R. Thampi, *Electrochimica Acta*, 1996, **41**, 1447-1454.
31. Y. Matsuzaki and I. Yasuda, *Solid State Ionics*, 1999, **126**, 307-313.
32. P. S. Manning, J. D. Sirman and J. A. Kilner, *Solid State Ionics*, 1996, **93**, 125-132.

33. L. Wang, R. Merkle, J. Maier, T. Acartürk and U. Starke, *Applied Physics Letters*, 2009, **94**, 071908.
34. J.-I. Jung, S. Misture and D. Edwards, *J Electroceram*, 2010, **24**, 261-269.
35. A. Demont, M. S. Dyer, R. Sayers, M. F. Thomas, M. Tsiamtsouri, H. N. Niu, G. R. Darling, A. Daoud-Aladine, J. B. Claridge and M. J. Rosseinsky, *Chemistry of Materials*, 2010, **22**, 6598-6615.
36. D. Ding, X. Li, S. Y. Lai, K. Gerdes and M. Liu, *Energy & Environmental Science*, 2014, **7**, 552-575.
37. C. Sun, R. Hui and J. Roller, *J Solid State Electrochem*, 2009, **14**, 1125-1144.
38. A. J. Jacobson, *Chemistry of Materials*, 2009, **22**, 660-674.
39. A. Chroneos, B. Yildiz, A. Tarancon, D. Parfitt and J. A. Kilner, *Energy & Environmental Science*, 2011, **4**, 2774-2789.
40. A. Tarancon, M. Burriel, J. Santiso, S. J. Skinner and J. A. Kilner, *Journal of Materials Chemistry*, 2010, **20**, 3799-3813.
41. S. Adler, J. Lane and B. Steele, *Journal of The Electrochemical Society*, 1996, **143**, 3554-3564.
42. S. B. Adler, *Solid State Ionics*, 1998, **111**, 125-134.
43. S. B. Adler, *Chemical Reviews*, 2004, **104**, 4791-4844.
44. S. Adler, J. Lane and B. Steele, *Journal of The Electrochemical Society*, 1996, **143**, 3554-3564.
45. H. Yokokawa, *Annual Review of Materials Research*, 2003, **33**, 581-610.
46. J. C. Boivin and G. Mairesse, *Chemistry of Materials*, 1998, **10**, 2870-2888.
47. E. Tsipis and V. Kharton, *J Solid State Electrochem*, 2008, **12**, 1367-1391.
48. A. R. West, *Basic solid state chemistry second edition*, Wiley New York, 1999.
49. N. F. Mott and M. Kaveh, *Advances in Physics*, 1985, **34**, 329-401.
50. N. F. Mott and L. Friedman, *Philosophical Magazine*, 1974, **30**, 389-402.
51. N. F. Mott, *Canadian Journal of Physics*, 1956, **34**, 1356-1368.
52. J. Hubbard, *Proceedings of the Royal Society of London. Series A. Mathematical and Physical Sciences*, 1964, **281**, 401-419.
53. J. D. Jorgensen, B. Dabrowski, S. Pei, D. R. Richards and D. G. Hinks, *Physical Review B*, 1989, **40**, 2187-2199.
54. P. Anderson, *Physical Review*, 1950, **79**, 350.
55. W. L. Bragg, *Proceedings of the Royal Society of London. Series A*, 1914, **89**, 468-489.
56. N. Sammes and Y. Du, in *Fuel Cell Technologies: State and Perspectives*, eds. N. Sammes, A. Smirnova and O. Vasylyev, Springer Netherlands, Editon edn., 2005, vol. 202, pp. 19-34.
57. M. Mogensen, D. Lybye, N. Bonanos, P. V. Hendriksen and F. W. Poulsen, *Solid State Ionics*, 2004, **174**, 279-286.
58. A. Tarancón, A. Morata, F. Peiró and G. Dezanneau, *Fuel Cells*, 2011, **11**, 26-37.
59. R. H. Mitchell, *Perovskites: modern and ancient*, Almaz Press Thunder Bay, 2002.
60. V. Goldschmidt, *Akad. I. Mat.-nat. Kl*, 1927.
61. A. Glazer, *Acta Crystallographica Section B: Structural Crystallography and Crystal Chemistry*, 1972, **28**, 3384-3392.
62. L. R. Moras, *Journal of Inorganic and Nuclear Chemistry*, 1974, **36**, 3876-3878.
63. Z. Shao and S. M. Haile, *Nature*, 2004, **431**, 170-173.
64. A. A. Colville and S. Geller, *Acta Crystallographica Section B*, 1971, **27**, 2311-2315.
65. P. Karen, E. Suard and F. Fauth, *Inorganic Chemistry*, 2005, **44**, 8170-8172.
66. A. Orera and P. R. Slater, *Chemistry of Materials*, 2009, **22**, 675-690.

67. H. G. Scott, *J Mater Sci*, 1975, **10**, 1527-1535.
68. J. W. Fergus, *Journal of Power Sources*, 2006, **162**, 30-40.
69. D. W. Strickler and W. G. Carlson, *Journal of the American Ceramic Society*, 1964, **47**, 122-127.
70. B. C. H. Steele, *Solid State Ionics*, 2000, **134**, 3-20.
71. N. P. Brandon, S. Skinner and B. C. Steele, *Annual Review of Materials Research*, 2003, **33**, 183-213.
72. R. Casselton, *Journal of applied Electrochemistry*, 1974, **4**, 25-48.
73. V. Kharton, F. Marques and A. Atkinson, *Solid State Ionics*, 2004, **174**, 135-149.
74. D. Kuščer, J. Holc, M. Hrovat, S. Bernik, Z. Samardžija and D. Kolar, *Solid State Ionics*, 1995, **78**, 79-85.
75. H.-K. Lee, *Materials Chemistry and Physics*, 2003, **77**, 639-646.
76. C. Clausen, C. Bagger, J. B. Bilde-Sørensen and A. Horsewell, *Solid State Ionics*, 1994, **70–71, Part 1**, 59-64.
77. C. Brugnoni, U. Ducati and M. Scagliotti, *Solid State Ionics*, 1995, **76**, 177-182.
78. G. Chiodelli and M. Scagliotti, *Solid State Ionics*, 1994, **73**, 265-271.
79. Y. Ji, J. A. Kilner and M. F. Carolan, *Solid State Ionics*, 2005, **176**, 937-943.
80. H. Y. Tu, W. Y. Sun, Y. J. Yang, Z. Y. Lu, D. Q. Wang and T. L. Wen, *Journal of the European Ceramic Society*, 2000, **20**, 2421-2425.
81. G. Stochniol, E. Syskakis and A. Naoumidis, *Journal of the American Ceramic Society*, 1995, **78**, 929-932.
82. H. Grübmeier, A. Naoumidis, G. Stochniol and A. Tsoga, *Fresenius J Anal Chem*, 1995, **353**, 393-398.
83. S. P. S. Badwal, *Solid State Ionics*, 2001, **143**, 39-46.
84. Y. Mizutani, M. Tamura, M. Kawai and O. Yamamoto, *Solid State Ionics*, 1994, **72, Part 2**, 271-275.
85. K. Nomura, Y. Mizutani, M. Kawai, Y. Nakamura and O. Yamamoto, *Solid State Ionics*, 2000, **132**, 235-239.
86. O. Yamamoto, *Electrochimica Acta*, 2000, **45**, 2423-2435.
87. R. Chiba, T. Ishii and F. Yoshimura, *Solid State Ionics*, 1996, **91**, 249-256.
88. K. Schwarz, *P Natl Acad Sci USA*, 2006, **103**, 3497.
89. D. A. Andersson, S. I. Simak, N. V. Skorodumova, I. A. Abrikosov and B. Johansson, *P Natl Acad Sci USA*, 2006, **103**, 3518-3521.
90. H. Yahiro, K. Eguchi and H. Arai, *Solid State Ionics*, 1989, **36**, 71-75.
91. B. Dalslet, P. Blennow, P. Hendriksen, N. Bonanos, D. Lybye and M. Mogensen, *J Solid State Electrochem*, 2006, **10**, 547-561.
92. N. Sakai, Y. P. Xiong, K. Yamaji, H. Kishimoto, T. Horita, M. E. Brito and H. Yokokawa, *Journal of Alloys and Compounds*, 2006, **408–412**, 503-506.
93. D. Waller, J. A. Lane, J. A. Kilner and B. C. H. Steele, *Solid State Ionics*, 1996, **86–88, Part 2**, 767-772.
94. V. Dusastre and J. A. Kilner, *Solid State Ionics*, 1999, **126**, 163-174.
95. J. M. Ralph, C. Rossignol and R. Kumar *Journal of The Electrochemical Society*, 2003, **150**, A1518-A1522.
96. A. Tsoga, A. Gupta, A. Naoumidis and P. Nikolopoulos, *Acta Mater*, 2000, **48**, 4709-4714.
97. A. Martínez-Amesti, A. Larrañaga, L. M. Rodríguez-Martínez, A. T. Aguayo, J. L. Pizarro, M. L. Nó, A. Laresgoiti and M. I. Arriortua, *Journal of Power Sources*, 2008, **185**, 401-410.
98. G. Corbel, S. Mestiri and P. Lacorre, *Solid state sciences*, 2005, **7**, 1216-1224.

99. T. Ishihara, H. Matsuda and Y. Takita, *Journal of the American Chemical Society*, 1994, **116**, 3801-3803.
100. P. n. Huang and A. Petric, *Journal of The Electrochemical Society*, 1996, **143**, 1644-1648.
101. K. Huang, M. Feng, J. B. Goodenough and M. Schmerling, *Journal of The Electrochemical Society*, 1996, **143**, 3630-3636.
102. W. X. Chen, H. W. Nie, W. H. Huang, R. Zheng, H. Y. Tu, Z. Y. Lu and T. L. Wen, *Journal of Materials Science Letters*, 2003, **22**, 651-653.
103. V. Kharton, A. Yaremchenko, A. Viskup, M. Patrakeev, I. Leonidov, V. Kozhevnikov, F. Figueiredo, A. Shaulo, E. Naumovich and F. Marques, *Journal of The Electrochemical Society*, 2002, **149**, E125-E135.
104. S. Schmidt, F. Berckemeyer and W. Weppner, *Ionics*, 2000, **6**, 139-144.
105. M. Lerch, H. Boysen and T. Hansen, *J Phys Chem Solids*, 2001, **62**, 445-455.
106. P. R. Slater, J. T. S. Irvine, T. Ishihara and Y. Takita, *Solid State Ionics*, 1998, **107**, 319-323.
107. J. B. Goodenough and Y.-H. Huang, *Journal of Power Sources*, 2007, **173**, 1-10.
108. T. Setoguchi, K. Okamoto, K. Eguchi and H. Arai, *Journal of The Electrochemical Society*, 1992, **139**, 2875-2880.
109. B. de Boer, M. Gonzalez, H. J. M. Bouwmeester and H. Verweij, *Solid State Ionics*, 2000, **127**, 269-276.
110. S. Tao and J. T. S. Irvine, *Journal of The Electrochemical Society*, 2004, **151**, A252-A259.
111. S. Tao and J. T. S. Irvine, *Nature Materials*, 2003, **2**, 320-323.
112. E. Lay, G. Gauthier and L. Dessemond, *Solid State Ionics*, 2011, **189**, 91-99.
113. S. Jiang, *J Mater Sci*, 2008, **43**, 6799-6833.
114. J. H. Kuo, H. U. Anderson and D. M. Sparlin, *Journal of Solid State Chemistry*, 1990, **87**, 55-63.
115. A. Hammouche, E. J. L. Schouler and M. Henault, *Solid State Ionics*, 1988, **28–30, Part 2**, 1205-1207.
116. J. Mizusaki, Y. Yonemura, H. Kamata, K. Ohyama, N. Mori, H. Takai, H. Tagawa, M. Dokiya, K. Naraya, T. Sasamoto, H. Inaba and T. Hashimoto, *Solid State Ionics*, 2000, **132**, 167-180.
117. A. Berenov, H. Wood and A. Atkinson, *ECS Transactions*, 2007, **7**, 1173-1181.
118. S. Kuharuangrong, T. Dechakupt and P. Aungkavattana, *Materials Letters*, 2004, **58**, 1964-1970.
119. A. Endo, M. Ihara, H. Komiyama and K. Yamada, *Solid State Ionics*, 1996, **86–88, Part 2**, 1191-1195.
120. S. P. Jiang, *Solid State Ionics*, 2002, **146**, 1-22.
121. J.-D. Kim, G.-D. Kim, J.-W. Moon, Y.-i. Park, W.-H. Lee, K. Kobayashi, M. Nagai and C.-E. Kim, *Solid State Ionics*, 2001, **143**, 379-389.
122. Y. Takeda, R. Kanno, M. Noda and O. Yamamoto, *Bulletin of the Institute for Chemical Research, Kyoto University*, 1986, **64**, 157-169.
123. H. Ullmann, N. Trofimenko, F. Tietz, D. Stöver and A. Ahmad-Khanlou, *Solid State Ionics*, 2000, **138**, 79-90.
124. K. Huang, H. Y. Lee and J. B. Goodenough, *Journal of The Electrochemical Society*, 1998, **145**, 3220-3227.
125. K. T. Lee and A. Manthiram, *Journal of The Electrochemical Society*, 2006, **153**, A794-A798.

126. F. Tietz, I. Arul Raj, M. Zahid and D. Stöver, *Solid State Ionics*, 2006, **177**, 1753-1756.
127. L. Tai, M. Nasrallah and H. Anderson, *Journal of Solid State Chemistry*, 1995, **118**, 117-124.
128. Y. Teraoka, H. Zhang, K. Okamoto and N. Yamazoe, *Materials Research Bulletin*, 1988, **23**, 51-58.
129. E. Perry Murray, M. J. Sever and S. A. Barnett, *Solid State Ionics*, 2002, **148**, 27-34.
130. F. Tietz, A. Mai and D. Stöver, *Solid State Ionics*, 2008, **179**, 1509-1515.
131. S. P. Simner, M. D. Anderson, M. H. Engelhard and J. W. Stevenson, *Electrochemical and Solid-State Letters*, 2006, **9**, A478-A481.
132. S. McIntosh, J. F. Vente, W. G. Haije, D. H. Blank and H. J. Bouwmeester, *Chemistry of Materials*, 2006, **18**, 2187-2193.
133. M. Arnold, H. Wang and A. Feldhoff, *Journal of Membrane Science*, 2007, **293**, 44-52.
134. A. Yan, M. Cheng, Y. Dong, W. Yang, V. Maragou, S. Song and P. Tsiakaras, *Applied Catalysis B: Environmental*, 2006, **66**, 64-71.
135. A. Yan, V. Maragou, A. Arico, M. Cheng and P. Tsiakaras, *Applied catalysis. B, Environmental*, 2007, **76**, 320-327.
136. A. Yan, M. Yang, Z. Hou, Y. Dong and M. Cheng, *Journal of Power Sources*, 2008, **185**, 76-84.
137. V. V. Kharton, A. A. Yaremchenko, A. V. Kovalevsky, A. P. Viskup, E. N. Naumovich and P. F. Kerko, *Journal of Membrane Science*, 1999, **163**, 307-317.
138. M. F. Carolan, P. N. Dyer, S. M. Fine, J. M. LaBar Sr and R. M. Thorogood, Google Patents, Editon edn., 1993.
139. B. Gharbage, R. Baker and F. M. Marques, *Journal of Materials Science Letters*, 1998, **17**, 75-77.
140. D. N. Mueller, R. A. De Souza, T. E. Weirich, D. Roehrens, J. Mayer and M. Martin, *Physical Chemistry Chemical Physics*, 2010, **12**, 10320-10328.
141. P. Müller, H. Störmer, M. Meffert, L. Dieterle, C. Niedrig, S. F. Wagner, E. Ivers-Tiffée and D. Gerthsen, *Chemistry of Materials*, 2013, **25**, 564-573.
142. P. Müller, H. Störmer, L. Dieterle, C. Niedrig, E. Ivers-Tiffée and D. Gerthsen, *Solid State Ionics*, 2012, **206**, 57-66.
143. C. Niedrig, S. Taufall, M. Burriel, W. Menesklou, S. F. Wagner, S. Baumann and E. Ivers-Tiffée, *Solid State Ionics*, 2011, **197**, 25-31.
144. A. Demont, R. Sayers, M. A. Tsiamtsouri, S. Romani, P. A. Chater, H. Niu, C. Martí-Gastaldo, Z. Xu, Z. Deng, Y. Bréard, M. F. Thomas, J. B. Claridge and M. J. Rosseinsky, *Journal of the American Chemical Society*, 2013, **135**, 10114-10123.
145. S. N. Ruddlesden and P. Popper, *Acta Crystallographica*, 1958, **11**, 54-55.
146. B. Grande and H. Müller-Buschbaum, *Zeitschrift für anorganische und allgemeine Chemie*, 1977, **433**, 152-156.
147. Z. Zhang and M. Greenblatt, *Journal of Solid State Chemistry*, 1995, **117**, 236-246.
148. E. Boehm, J. M. Bassat, P. Dordor, F. Mauvy, J. C. Grenier and P. Stevens, *Solid State Ionics*, 2005, **176**, 2717-2725.
149. R. Sayers, R. De Souza, J. Kilner and S. Skinner, *Solid State Ionics*, 2010, **181**, 386-391.
150. F. Mauvy, C. Lalanne, J.-M. Bassat, J.-C. Grenier, H. Zhao, L. Huo and P. Stevens, *Journal of The Electrochemical Society*, 2006, **153**, A1547-A1553.
151. R. Sayers, J. Liu, B. Rustumji and S. J. Skinner, *Fuel Cells*, 2008, **8**, 338-343.

152. G. Amow, P. S. Whitfield, I. J. Davidson, R. P. Hammond, C. N. Munnings and S. J. Skinner, *Ceramics International*, 2004, **30**, 1635-1639.
153. A. A. Taskin, A. N. Lavrov and Y. Ando, *Applied Physics Letters*, 2005, **86**, 091910-091910.
154. G. Kim, S. Wang, A. J. Jacobson, Z. Yuan, W. Donner, C. L. Chen, L. Reimus, P. Brodersen and C. A. Mims, *Applied Physics Letters*, 2006, **88**, 024103.
155. C. Frontera, J. Garcia-Munoz, A. Llobet and M. Aranda, *Physical Review B*, 2002, **65**, 180405.
156. K. Zhang, L. Ge, R. Ran, Z. Shao and S. Liu, *Acta Mater*, 2008, **56**, 4876-4889.
157. N. Li, Z. Lü, B. Wei, X. Huang, K. Chen, Y. Zhang and W. Su, *Journal of Alloys and Compounds*, 2008, **454**, 274-279.
158. A. Tarancón, J. Peña-Martínez, D. Marrero-López, A. Morata, J. C. Ruiz-Morales and P. Núñez, *Solid State Ionics*, 2008, **179**, 2372-2378.
159. A. Tarancón, A. Morata, G. Dezanneau, S. J. Skinner, J. A. Kilner, S. Estradé, F. Hernández-Ramírez, F. Peiró and J. R. Morante, *Journal of Power Sources*, 2007, **174**, 255-263.
160. J. Peña-Martínez, A. Tarancón, D. Marrero-López, J. C. Ruiz-Morales and and P. Núñez, *Fuel Cells*, 2008, **8**, 351-359.
161. J.-H. Kim and A. Manthiram, *Journal of The Electrochemical Society*, 2008, **155**, B385-B390.
162. R. Sayers, F. Schiffmann, S. Fearn, J. A. Kilner, B. Slater, S. Romani, D. J. Tatham, J. B. Claridge, F. Corà and M. J. Rosseinsky, *Chemistry of Materials*, 2013, **25**, 3441-3457.
163. S. Shin, M. Yonemura and H. Ikawa, *Materials Research Bulletin*, 1978, **13**, 1017-1021.
164. H. Yamamura, Y. Yamada, T. Mori and T. Atake, *Solid State Ionics*, 1998, **108**, 377-381.
165. Y. Takeda, R. Kanno, T. Takada, O. Yamamoto, M. Takano and Y. Bando, *Zeitschrift für anorganische und allgemeine Chemie*, 1986, **540**, 259-270.
166. Y. S. Touloukian and D. P. DeWitt, *Thermophysical Properties of Matter-The TPRC Data Series. Volume 7. Thermal Radiative Properties-Metallic Elements and Alloys*, DTIC Document, 1970.
167. P. Y. Z. V.K. Pecharsky, *Fundamentals of Powder Diffraction and Structural Characterisation of Materials*, Springer, 2008.
168. V. F. Sears, *Neutron News*, 1992, **3**, 29-37.
169. C. G. Shull, W. A. Strauser and E. O. Wollan, *Physical Review*, 1951, **83**, 333-345.
170. D. B. Williams and C. B. Carter, in *Transmission Electron Microscopy*, Springer, Editon edn., 2009.
171. M. Hellenbrandt, *Crystallography Reviews*, 2004, **10**, 17-22.
172. H. Rietveld, *Journal of Applied Crystallography*, 1969, **2**, 65-71.
173. H. Rietveld, *Acta Crystallographica*, 1967, **22**, 151-152.
174. B. Toby, *Journal of Applied Crystallography*, 2001, **34**, 210-213.
175. A. Coelho, *Topas Academic v5, Coelho Software*, 2012.
176. D. Schwarzenbach, S. C. Abrahams, H. D. Flack, E. Prince and A. J. C. Wilson, *Acta Crystallographica Section A*, 1995, **51**, 565-569.
177. D. Schwarzenbach, S. C. Abrahams, H. D. Flack, W. Gonschorek, T. Hahn, K. Huml, R. E. Marsh, E. Prince, B. E. Robertson, J. S. Rollett and A. J. C. Wilson, *Acta Crystallographica Section A*, 1989, **45**, 63-75.

178. A. Le Bail, H. Duroy and J. L. Fourquet, *Materials Research Bulletin*, 1988, **23**, 447-452.
179. G. Pawley, *Journal of Applied Crystallography*, 1981, **14**, 357-361.
180. S. P. Thompson, J. E. Parker, J. Potter, T. P. Hill, A. Birt, T. M. Cobb, F. Yuan and C. C. Tang, *Rev Sci Instrum*, 2009, **80**, 075107.
181. R. Ibberson, W. David and K. Knight, *The High Resolution Powder Diffractometer (HRPD) at ISIS: A User Guide*, Rutherford Appleton Laboratory, 1992.
182. S. Hull, R. I. Smith, W. I. F. David, A. C. Hannon, J. Mayers and R. Cywinski, *Physica B: Condensed Matter*, 1992, **180–181, Part 2**, 1000-1002.
183. M. Knoll and E. Ruska, *Z. Physik*, 1932, **78**, 318-339.
184. R. Mössbauer, *Z. Naturforsch. A*, 1959, **14**, 211.
185. R. C. D. A. I. Vogel. J. Mendham, J.D. Barnes and M. Thomas, *Vogel's textbook of quantitative chemical analysis, fifth edition revised by G. H. Jeffery et al.*, 2000.
186. D. K. Schroder, *Semiconductor material and device characterization*, John Wiley & Sons, 2006.
187. J. R. Macdonald and E. Barsoukov, *History*, 2005, **1**, 8.
188. J. T. S. Irvine, D. C. Sinclair and A. R. West, *Advanced Materials*, 1990, **2**, 132-138.
189. D. Johnson, *ZPlot, ZView Electrochemical Impedance Software, 2.3b, Scribner Associates*, 2000.
190. P. Berastegui, S. G. Eriksson and S. Hull, *Materials Research Bulletin*, 1999, **34**, 303-314.
191. A. A. Taskin, A. N. Lavrov and Y. Ando, *Appl Phys Lett*, 2005, **86**, 091910.
192. A. A. Taskin, A. N. Lavrov and Y. Ando, *Progress in Solid State Chemistry*, 2007, **35**, 481-490.
193. H. Yahiro, Y. Eguchi, K. Eguchi and H. Arai, *J Appl Electrochem*, 1988, **18**, 527-531.
194. T. Ishihara, H. Matsuda and Y. Takita, *J Am Chem Soc*, 1994, **116**, 3801-3803.
195. L. W. Tai, M. M. Nasrallah, H. U. Anderson, D. M. Sparlin and S. R. Sehlin, *Solid State Ionics*, 1995, **76**, 273-283.
196. H.-C. Wang, C.-L. Wang, J.-L. Zhang, M.-L. Zhao, J. Liu, W.-B. Su, N. Yin and L.-M. Mei, *Chinese Physics Letters*, 2009, **26**, 7301.
197. M. S. Dyer, C. Collins, D. Hodgeman, P. A. Chater, A. Demont, S. Romani, R. Sayers, M. F. Thomas, J. B. Claridge, G. R. Darling and M. J. Rosseinsky, *Science*, 2013, **340**, 847-852.
198. H. T. Stokes and D. M. Hatch, *Journal of Applied Crystallography*, 2005, **38**, 237-238.
199. K. Momma and F. Izumi, *Journal of Applied Crystallography*, 2008, **41**, 653-658.
200. A. S. Wills, *Physica B: Condensed Matter*, 2000, **276–278**, 680-681.
201. A. M. Kevorkov, V. F. Karyagin and A. I. Munchaev, *Crystallography Reports*, 1995, **40**, 23-26.
202. P. Stephens, *Journal of Applied Crystallography*, 1999, **32**, 281-289.
203. A. Nemudry, M. Weiss, I. Gainutdinov, V. Boldyrev and R. Schöllhorn, *Chemistry of Materials*, 1998, **10**, 2403-2411.
204. A. Nemudry, E. L. Goldberg, M. Aguirre and M. Á. Alario-Franco, *Solid state sciences*, 2002, **4**, 677-690.
205. H. Kruger, S. Stober, T. R. Welberry, R. L. Withers and J. D. Fitz Gerald, *Acta Crystallographica Section B*, 2011, **67**, 476-485.
206. C. Koch, Thesis, Editon edn., 2008.
207. G. C. Kostogloudis, C. Ftikos, A. Ahmad-Khanlou, A. Naoumidis and D. Stöver, *Solid State Ionics*, 2000, **134**, 127-138.

208. O. Schulz and M. Martin, *Solid State Ionics*, 2000, **135**, 549-555.
209. S. Švarcová, K. Wiik, J. Tolchard, H. J. M. Bouwmeester and T. Grande, *Solid State Ionics*, 2008, **178**, 1787-1791.
210. M. Arnold, T. M. Gesing, J. Martynczuk and A. Feldhoff, *Chemistry of Materials*, 2008, **20**, 5851-5858.
211. K. Efimov, Q. Xu and A. Feldhoff, *Chemistry of Materials*, 2010, **22**, 5866-5875.
212. K. Wang, R. Ran, W. Zhou, H. Gu, Z. Shao and J. Ahn, *Journal of Power Sources*, 2008, **179**, 60-68.
213. C. Meingast, O. Kraut, T. Wolf, H. Wühl, A. Erb and G. Müller-Vogt, *Physical Review Letters*, 1991, **67**, 1634-1637.
214. C. A. M. dos Santos, J. J. Neumeier, Y.-K. Yu, R. K. Bollinger, R. Jin, D. Mandrus and B. C. Sales, *Physical Review B*, 2006, **74**, 132402.
215. V. Prashanth Kumar, Y. S. Reddy, P. Kistaiah, G. Prasad and C. Vishnuvardhan Reddy, *Materials Chemistry and Physics*, 2008, **112**, 711-718.
216. L. Vasylechko, V. Vashook, D. Savytskii, A. Senyshyn, R. Niewa, M. Knapp, H. Ullmann, M. Berkowski, A. Matkovskii and U. Bismayer, *Journal of Solid State Chemistry*, 2003, **172**, 396-411.
217. S. Carter, A. Selcuk, R. J. Chater, J. Kajda, J. A. Kilner and B. C. H. Steele, *Solid State Ionics*, 1992, **53–56, Part 1**, 597-605.
218. A. Petric, P. Huang and F. Tietz, *Solid State Ionics*, 2000, **135**, 719-725.
219. A. L. Shaula, Y. V. Pivak, J. C. Waerenborgh, P. Gaczyñski, A. A. Yaremchenko and V. V. Kharton, *Solid State Ionics*, 2006, **177**, 2923-2930.
220. J. Larminie and A. Dicks, *Fuel cell systems explained*, Wiley, 2003.
221. B. C. H. Steele, *Solid State Ionics*, 1996, **86–88, Part 2**, 1223-1234.
222. Y. Bando, Y. Sekikawa, H. Yamamura and Y. Matsui, *Acta Crystallographica Section A*, 1981, **37**, 723-728.
223. M. Arnold, H. Wang and A. Feldhoff, *Journal of Membrane Science*, 2007, **293**, 44-52.
224. Z. Yáng, A. S. Harvey and L. J. Gauckler, *Scripta Materialia*, 2009, **61**, 1083-1086.
225. S. Singhal, *High-temperature Solid Oxide Fuel Cells: Fundamentals, Design and Applications: Fundamentals, Design and Applications*, Elsevier, 2003.
226. M. M. R. Barfod, T. Klemensoe, A. Hagen, Y. Liu, *Proc. SOFCIX, 1*, 2005, 524-533.
227. E. Ivers-Tiffée, A. Weber and D. Herbstritt, *Journal of the European Ceramic Society*, 2001, **21**, 1805-1811.
228. H. Y. Tu, Y. Takeda, N. Imanishi and O. Yamamoto, *Solid State Ionics*, 1997, **100**, 283-288.
229. J. Holc, D. Kuščer, M. Hrovat, S. Bernik and D. Kolar, *Solid State Ionics*, 1997, **95**, 259-268.
230. S. P. Jiang, *Materials Science and Engineering: A*, 2006, **418**, 199-210.
231. C. Xia, W. Rauch, F. Chen and M. Liu, *Solid State Ionics*, 2002, **149**, 11-19.
232. A. Chang, S. J. Skinner and J. A. Kilner, *Solid State Ionics*, 2006, **177**, 2009-2011.
233. R. Sayers, N. L. O. Flack, J. Alaria, P. A. Chater, R. G. Palgrave, S. R. C. McMitchell, S. Romani, Q. M. Ramasse, T. J. Pennycook and M. J. Rosseinsky, *Chemical Science*, 2013, **4**, 2403-2412.
234. R. Shannon, *Acta Crystallographica Section A*, 1976, **32**, 751-767.
235. A. K. Azad, A. K. M. Zakaria, F. U. Ahmed, S. K. Paranjpe and A. Das, *Journal of Magnetism and Magnetic Materials*, 2000, **214**, 251-257.
236. R. W. Grant, *The Journal of Chemical Physics*, 1969, **51**, 1156-1162.
237. P. Coppens and M. Eibschutz, *Acta Crystallographica*, 1965, **19**, 524-531.

238. J. Hudspeth, D. Goossens, A. Studer, R. Withers and L. Norén, *Journal of Physics: Condensed Matter*, 2009, **21**, 124206.
239. Y. Bando, H. Yamamura and Y. Sekikawa, *Journal of the Less Common Metals*, 1980, **70**, 281-284.
240. J. Hadermann, A. M. Abakumov, H. D'Hondt, A. S. Kalyuzhnaya, M. G. Rozova, M. M. Markina, M. G. Mikheev, N. Tristan, R. Klingeler, B. Buchner and E. V. Antipov, *Journal of Materials Chemistry*, 2007, **17**, 692-698.
241. E. Sullivan, J. Hadermann and C. Greaves, *Journal of Solid State Chemistry*, 2011, **184**, 649-654.
242. H. Kruger and V. Kahlenberg, *Acta Crystallographica Section B*, 2005, **61**, 656-662.
243. G. J. Redhammer, G. Tippelt, G. Roth and G. Amthauer, *American Mineralogist*, 2004, **89**, 405-420.
244. E. Asenath-Smith, S. T. Misture and D. D. Edwards, *Journal of Solid State Chemistry*, 2011, **184**, 2167-2177.
245. P. H. Fuoss, P. Eisenberger, W. K. Warburton and A. Bienenstock, *Physical Review Letters*, 1981, **46**, 1537-1540.
246. D. Coleman, A. Berghuis, E. Lee, M. Linder, A. Gilman and Sprang, *Science*, 1994, **265**, 1405-1412.
247. W. Hendrickson, *Science*, 1991, **254**, 51-58.
248. W. A. Hendrickson and M. M. Teeter, *Nature*, 1981, **290**, 107-113.
249. P. Lee, Y. Gao, H. S. Sheu, V. Petricek, Restori, R., P. Coppens, A. Darovskikh, J. C. Phillips, A. W. Sleight and M. A. Subramanian, *Science*, 1989, **244**, 62-63.
250. R. S. Howland, T. H. Geballe, S. S. Laderman, A. Fischer-Colbrie, M. Scott, J. M. Tarascon and P. Barboux, *Physical Review B*, 1989, **39**, 9017-9027.
251. L. Reinhard, J. L. Robertson, S. C. Moss, G. E. Ice, P. Zschack and C. J. Sparks, *Physical Review B*, 1992, **45**, 2662-2676.
252. D. T. Cromer, *Acta Crystallographica*, 1965, **18**, 17-23.
253. I. D. Brown, A. Dabkowski and A. McCleary, *Acta Crystallographica Section B*, 1997, **53**, 750-761.
254. M. Harder and H. Müller-Buschbaum, *Zeitschrift für anorganische und allgemeine Chemie*, 1980, **464**, 169-175.
255. M. Schmidt and S. J. Campbell, *Journal of Solid State Chemistry*, 2001, **156**, 292-304.
256. T. Takeda, Yamaguch.Y, Tomiyosh.S, M. Fukase, M. Sugimoto and H. Watanabe, *J Phys Soc Jpn*, 1968, **24**, 446-452.
257. L. M. Corliss, J. M. Hastings, W. Kunnmann and E. Banks, *Acta Crystallographica*, 1966, **21**, 95.
258. D. du Boulay, E. N. Maslen, V. A. Streltsov and N. Ishizawa, *Acta Crystallographica Section B*, 1995, **51**, 921-929.
259. K. Jacob, G. Rajitha and N. Dasgupta, *Indian Journal of Engineering and Materials Sciences*, 2012, **19**, 47-53.
260. M. Koyama, C.-j. Wen, T. Masuyama, J. Otomo, H. Fukunaga, K. Yamada, K. Eguchi and H. Takahashi, *Journal of The Electrochemical Society*, 2001, **148**, A795-A801.
261. I. Kojima, H. Adachi and I. Yasumori, *Surf Sci*, 1983, **130**, 50-62.
262. E. Ivers-Tiffee, A. Weber, K. Schmid and V. Krebs, *Solid State Ionics*, 2004, **174**, 223-232.
263. J. Piao, K. Sun, N. Zhang, X. Chen, S. Xu and D. Zhou, *Journal of Power Sources*, 2007, **172**, 633-640.

264. M. Valldor, *Solid state sciences*, 2004, **6**, 251-266.
265. B. Raveau, V. Pralong, V. Caignaert and A. Maignan, *Zeitschrift für anorganische und allgemeine Chemie*, 2011, **637**, 1079-1087.
266. Q. Z. Huang, V. Lynn Karen, A. Santoro, A. Kjekshus, J. Lindén, T. Pietari and P. Karen, *Journal of Solid State Chemistry*, 2003, **172**, 73-80.
267. M. Wilke, F. Farges, P.-E. Petit, G. E. Brown and F. Martin, *American Mineralogist*, 2001, **86**, 714-730.
268. I. Brown and D. Altermatt, *Acta Crystallographica Section B: Structural Science*, 1985, **41**, 244-247.
269. N. Brese and M. O'keeffe, *Acta Crystallographica Section B: Structural Science*, 1991, **47**, 192-197.
270. H. Lv, Y.-j. Wu, B. Huang, B.-y. Zhao and K.-a. Hu, *Solid State Ionics*, 2006, **177**, 901-906.
271. Z. Chen, R. Ran, W. Zhou, Z. Shao and S. Liu, *Electrochimica Acta*, 2007, **52**, 7343-7351.
272. E. L. Rautama and M. Karppinen, *Journal of Solid State Chemistry*, 2010, **183**, 1102-1107.
273. X. D. Zhou, J. B. Yang, E. C. Thomsen, Q. Cai, B. J. Scarfino, Z. Nie, G. W. Coffey, W. J. James, W. B. Yelon, H. U. Anderson and L. R. Pederson, *Journal of The Electrochemical Society*, 2006, **153**, J133-J138.
274. H. Mitsuda, S. Mori and C. Okazaki, *Acta Crystallographica Section B*, 1971, **27**, 1263-1269.
275. J. Chen, F. Liang, B. Chi, J. Pu, S. P. Jiang and L. Jian, *Journal of Power Sources*, 2009, **194**, 275-280.
276. J. Peña-Martínez, D. Marrero-López, J. C. Ruiz-Morales, P. Núñez, C. Sánchez-Bautista, A. J. Dos Santos-García and J. Canales-Vázquez, *International Journal of Hydrogen Energy*, 2009, **34**, 9486-9495.
277. Z. Chen, R. Ran, W. Zhou, Z. Shao and S. Liu, *Electrochimica Acta*, 2007, **52**, 7343-7351.